Dynamics and structure analysis of coherent turbulent structures at the boundary of toroidally confined plasmas

vorgelegt von

Golo Fuchert

aus Varel

*It is difficult to say what is impossible,
for the dream of yesterday is the hope
of today and reality of tomorrow.*
– Robert H. Goddard (1882 – 1945)

Zusammenfassung

Einleitung

Die sichere und finanzierbare Deckung des steigenden Energiebedarfs ist eine der größten Herausforderungen unseres Jahrhunderts. Kernfusionskraftwerke nach dem Prinzip des magnetischen Einschlusses können möglicherweise einen entscheidenden Beitrag dazu leisten, die Energieversorgung in Zukunft klimaschonend und ohne die Risiken der Kernspaltung zu gewährleisten. Derzeit verhindern jedoch Energieverluste des Fusionsplasmas einen effizienten Betrieb. Insbesondere die Plasmaturbulenz spielt hierbei eine zentrale Rolle, da turbulente Fluktuationen in Fusionsplasmen in hohem Maße zu Energie- und Teilchenverlusten führen. Nahe der Wand, in der sogenannten *Abschälschicht* (engl.: scrape-off layer, SOL), wird der Transport dominiert von sogenannten *Blobs* oder *Filamenten*: Lokalisierte Strukturen erhöhten Drucks, die Energie und Teilchen in Richtung der Wand transportieren. Es kommt zu einer erhöhten Erosion der Innenwand des Fusionsreaktors und damit auch zu einer Verunreinigung des Plasmas. Diese Blobs werden in praktisch allen Fusions- und in vielen Grundlagenexperimenten beobachtet, was auf ein fundamentales Phänomen mit sehr robustem Entstehungsmechanismus hindeutet. Der Transport hängt unter anderem von der Größe, Geschwindigkeit und Entstehungsrate der Blobs ab. Für einfache Geometrien des einschließenden Magnetfelds existiert ein analytisches Modell, welches die Größe und Geschwindigkeit der Blobs vorhersagt. Da das Modell die Dynamik von bereits in der Abschälschicht existierenden Blobs untersucht, macht es keine Aussage über den Entstehungsmechanismus und enthält damit auch keine Vorhersage der Entstehungsrate. Experimentelle Beobachtungen deuten auf eine Beteiligung der *Randschichtturbulenz* in der Nähe der letzten geschlossenen Flussfläche (der Grenze zwischen eingeschlossenem Plasma und der Abschälschicht) bei der Blobentstehung hin, was sich vor allem in der Entstehungsrate widerspiegeln sollte, möglicherweise aber auch weitere Blobeigenschaften beeinflusst.

Ein umfassendes Verständnis der Blobs ist nötig um den Transport in der Abschälschicht vorherzusagen und möglicherweise zu beeinflussen. Diese Arbeit soll zu diesem Verständnis der Blobentstehung und Dynamik beitragen und beant-

wortet hierfür vorrangig zwei Fragen: Beschreiben die oben erwähnten Modelle für einfache Magnetfeldgeometrien auch die Blobdynamik in komplexen Geometrien tatsächlicher Fusionsexperimente (Tokamaks und Stellaratoren) und welchen Einfluss hat die Randschichtturbulenz auf die Blobeigenschaften?

Hierfür werden mittels Hochgeschwindigkeitsfotografie Größe, Geschwindigkeit und Entstehungsrate der Blobs im Stellarator TJ-K und dem Tokamak ASDEX Upgrade untersucht und mit analytischen Vorhersagen verglichen. Zusätzliche Diagnostiken ermöglichen es ein möglichst umfassendes Bild der physikalischen Eigenschaften der Blobs zu erhalten und helfen bei der Interpretation der Kameradaten. Im Falle von TJ-K handelt es sich insbesondere um vergleichende Langmuirsondenmessungen, welche an ASDEX Upgrade aufgrund der höheren Plasmatemperatur in der Abschälschicht nicht in dem Umfang möglich sind.

Während eine grundsätzliche Übereinstimmung mit den Vorhersagen besteht, konnte im Experiment TJ-K zum ersten Mal gezeigt werden, dass die Randschichtturbulenz die untersuchten Eigenschaften klar beeinflusst. Die Messungen beinhalten den ersten systematischen Vergleich der Strukturgrößen innerhalb und außerhalb der letzten geschlossenen Flussfläche. Es zeigt sich, dass die charakteristische Größe der Driftwellenturbulenz im eingeschlossenen Plasma die Blobgröße in der Abschälschicht beeinflusst. Außerdem zeigt sich, dass die Blobentstehungsrate eindeutig von der Driftwellenturbulenz im Randschichtplasma bestimmt wird. Für die radiale Auswärtsgeschwindigkeit der Blobs (in Richtung der Wand), zeigt sich eine gute Übereinstimmung mit den theoretischen Vorhersagen. Die Übereinstimmung lässt sich noch weiter verbessern, wenn zusätzlich der Einfluss der *Kreuzphase* zwischen Potential und Dichte berücksichtigt wird. Darüber hinaus wird mit Sondenmessungen die dreidimensionale Struktur der Blobs in einem Stellarator vermessen und gezeigt, dass die Blobs mehr als 50 % des lokalen und mehr als 20 % des totalen turbulenten Transports in der Abschälschicht ausmachen. Mithilfe der verwendeten Multisondenanordnung kann die Gültigkeit eines weiteren Aspekts des Blobmodells in Stellaratorgeometrie gezeigt werden: In Übereinstimmung mit dem Blobmodell treten die Blobs gerade in den Bereichen der Abschälschicht auf, in denen die gemittelte Normalenkrümmung $\langle \kappa_{\mathrm{n}} \rangle$ negativ ist. Messungen eines Stroms entlang der Filamente (parallel zum magnetischen Feld) bestätigen, dass das analytische Modell die relevanten physikalischen Prozesse beinhaltet. Hierfür wird ein bestehendes Modell erweitert, welches Erkenntnisse aus der Geschwindigkeitsuntersuchung beinhaltet, um den physikalischen Gegebenheiten des TJ-K Plasmas gerecht zu werden.

In ASDEX Upgrade werden Blobeigenschaften bestimmt und in zwei Einschlussregimen, der sogenannten L- und H-Mode, verglichen. Die H-Mode zeichnet sich durch eine starke Reduktion der Turbulenz am Plasmarand aus und hat damit eine wesentliche Bedeutung für die Realisierung eines zukünftigen Fusionskraftwerks. Welche Rolle diese Turbulenzreduktion für die Blobentstehung spielt, ist bislang unklar. Die durchgeführten Kameramessungen zeigen, dass die Anzahl an beobachteten Blobs in L- und H-Mode nahezu identisch ist. Dieser Befund deutet auf einen nur geringen Einfluss der veränderten Randschichtdynamik in der H-Mode auf die

Blobentstehung hin. Die Blobdynamik in Fusionsplasmen ist im Wesentlichen vergleichbar mit der in kalten Plasmen wie etwa im Experiment TJ-K. Unterschiede treten jedoch vor allem durch den Beitrag der Ionentemperatur zur Drucküberhöhung des Blobs auf. Dieser Einfluss wurde bisher weder experimentell noch in den Modellen ausführlich untersucht. Der Vergleich gemessener Blobeigenschaften mit einem kürzlich veröffentlichten Blobmodell ist daher ein wichtiger Teil der Untersuchungen an ASDEX Upgrade. Wie schon in TJ-K zeigt sich eine weitgehende Übereinstimmung mit den analytischen Vorhersagen. Insbesondere bei der Blobgröße findet sich eine sehr gute Übereinstimmung, welche auf einen klaren Einfluss der hohen Ionentemperatur auf die Blobdynamik hinweist. Bei der Interpretation der beobachteten Radialgeschwindigkeit bleiben allerdings auch einige Fragen offen, die in zukünftigen Experimenten geklärt werden sollten. Unter anderem wird von dem analytischen Modell ein großer Unterschied in der Radialgeschwindigkeit für die L- und H-Mode vorhergesagt, welcher im Experiment nicht beobachtet wird. Überhaupt zeigt sich eine überraschend geringe Variation der Blobeigenschaften zwischen den zwei Einschlussregimen. Insbesondere wird beobachtet, dass trotz der drastischen Reduzierung der Turbulenz im eingeschlossenen Plasma die Detektionsrate der Blobs in der Abschälschicht praktisch unverändert bleibt oder sogar leicht zunimmt. Dies schränkt den räumlichen Bereich ein, der Einfluss auf die Blobenstehung hat.

Die oben aufgeführten Resultate werden im Folgenden ausführlicher besprochen.

Experimente an TJ-K

Ein Ziel der vorliegenden Arbeit ist die Einführung der Hochgeschwindigkeitsfotografie als Diagnostik für das Experiment TJ-K. Hierzu wurden grundlegende Experimente durchgeführt, um die diagnostischen Möglichkeiten zu untersuchen. Es konnte gezeigt werden, dass mittels einer Hochgeschwindigkeitskamera turbulente Strukturen in der Randschicht des TJ-K Plasmas quasi-lokalisiert detektiert werden können. Dank der nachgeprüften Linearität der Antwortfunktion der Kamera (Linearität der gespeicherten Zählrate mit der eingestrahlten Lichtintensität), können die beobachteten Strukturen mit Dichtestörungen identifiziert werden. Allerdings erscheinen die Strukturen in den Kameradaten aufgrund der dreidimensionalen Geometrie des Stellaratorplasmas verzehrt, was die Interpretation der Kameradaten erschwert. Vergleichende Experimente mit Langmuirsonden konnten jedoch zeigen, dass die für diese Arbeit relevanten Größen mittels eines Strukturerkennungsalgorithmus korrekt aus den Kameradaten bestimmt werden können. Hierbei handelt es sich insbesondere um die Position, die Größe und die Trajektorie der beobachteten Strukturen.

Vor den eigentlichen Untersuchungen zu den Blobeigenschaften wurden Experimente durchgeführt zur Ermittlung der dreidimensionalen Struktur der Blobs und dem durch sie hervorgerufenen Transport. Diese Untersuchungen sind bereits für sich von Interesse zum Verständnis der Struktur und der Dynamik der Blobs, vor

allem aber sind die Kenntnisse über das Auftreten und die Geometrie eine notwendige Voraussetzung für das Design der Untersuchungen zur Entstehungsrate, Größe und Geschwindigkeit der Filamente. Durch gleichzeitige Messungen mit der Hochgeschwindigkeitskamera und poloidalen Multisondenanordnungen kann die dreidimensionale Struktur der Blobs und insbesondere ihre Orientierung bezüglich des Magnetfelds bestimmt werden. Die Analysen zeigen, dass die Blobs in der SOL von TJ-K eine Länge von mindestens $l_\parallel = 1.85\,\mathrm{m}$ aufweisen (der Verbindungslänge zwischen den zwei verwendeten Sondenanordnungen), und sich damit vermutlich über die gesamte SOL-Verbindgunslänge von $l_{\mathrm{SOL}} \approx 2.79\,\mathrm{m}$ erstrecken (der Länge der Feldliniensegmente zwischen zwei eingebrachten Limitern). Die Filamente sind außerdem im Rahmen der experimentellen Auflösung perfekt entlang der Feldlinien ausgedehnt. Die verwendeten Diagnostiken erlauben es die Bereiche in der SOL zu ermitteln, in denen überhaupt Blobs beobachtet werden. Es zeigt sich, dass dieser Bereich bestimmt wird durch eine negative Normalenkrümmung der Feldlinien $\langle \kappa_{\mathrm{n}} \rangle$, gemittelt über das vom Filament beanspruchte Feldliniensegment. Dies ist ein Hinweis darauf, dass die wesentlichen Aussagen des Blobmodells auch in der Stellaratorgeometrie von TJ-K gültig sind. Darüber hinaus kann der turbulente Transport, der durch die Blobs hervorgerufen wird, vom turbulenten Gesamttransport separiert und somit quantifiziert werden. Es zeigt sich hierbei, dass der Anteil der Blobs am turbulenten Transport lokal bis zu 90 % und global bis zu 20 % beiträgt. Da die verwendeten Analysen nur Blobs oberhalb eines Dichteschwellwerts detektieren, könnte der tatsächliche Anteil am turbulenten Transport sogar noch größer ausfallen. Dieser Fund unterstreicht die Bedeutung einer umfassenden Untersuchung der Blobstruktur und Dynamik.

Der durch Blobs induzierte Transport richtet sich im Wesentlichen nach ihrem internen Druck, der geometrische Größe, ihrer Geschwindigkeit und der Entstehungsrate. Bezüglich des Plasmadrucks innerhalb der Filamente existieren experimentelle Untersuchungen, dass dieser im Wesentlichen durch den Druck in der Entstehungsregion bestimmt wird. In dieser Arbeit richtet sich der Fokus deshalb auf die Größe, Geschwindigkeit und Entstehungsrate.

Die Entstehungsrate sollte im Wesentlichen durch den Mechanismus vorgegeben werden, der zur Blobentstehung führt. Da die Blobentstehung bislang nicht im Detail verstanden ist, existiert derzeit auch noch keine quantitative Vorhersage. Es zeigt sich jedoch in verschiedenen Experimenten, dass die Turbulenz in der Plasmarandschicht eine zentrale Rolle bei der Blobentstehung spielt. Die charakteristischen Zeitskalen der entsprechenden Instabilitäten sollten sich deshalb in der typischen Wartezeit zwischen zwei Ereignissen widerspiegeln. Im Falle von TJ-K haben frühere Experimente gezeigt, dass kohärente Strukturen der sogenannten Driftwellenturbulenz die Dichte für die Blobentstehung bereitstellen. Aus diesem Grund werden in dieser Arbeit vergleichende Wartezeitstatistiken für diese kohärenten Strukturen innerhalb des eingeschlossenen Plasmas und der Blobs in der SOL aufgestellt. Es zeigt sich hierbei, dass nicht nur die Wahrscheinlichkeitsverteilung der beobachteten Wartezeiten (*Wartezeitverteilung*) für beide Strukturarten iden-

tisch ist, sondern auch die absoluten Zählraten übereinstimmen sind. Dieses Ergebnis bestätigt die Beobachtung, dass die Driftwellenturbulenz maßgeblich an der Blobentstehung beteiligt ist. Darüber hinaus zeigt die Übereinstimmung der Zählraten, dass praktisch jede kohärente Struktur der Driftwellenturbulenz über einem bestimmten Dichteschwellwert zur Blobentstehung führt.

Bezüglich der Blobgröße wurden Skalierungsuntersuchungen mit der sogenannten Driftskala

$$\rho_\mathrm{s} = \frac{\sqrt{m_\mathrm{i} T_\mathrm{e}}}{eB}$$

durchgeführt. Hier ist m_i die Ionenmasse, T_e die Elektronentemperatur, e die Elementarladung und B die Magnetfeldstärke. Das eingangs erwähnte Blobmodell sagt voraus, dass die Größe der Blobs senkrecht zum magnetischen Feld δ_b mit $\rho_\mathrm{s}^{4/5}$ skaliert. Wie man der obigen Formel entnehmen kann, lässt sich der Parameter ρ_s durch Veränderung der Gasart (m_i), der Heizleistung (T_e) und der Magnetfeldstärke B variieren. Der experimentell gefundene Skalierungsexponent $\alpha \approx 0.2 \pm 0.05$ weicht deutlich von dem vorhergesagten Wert $\alpha = 0.8$ ab. Stattdessen zeigt sich eine deutliche Übereinstimmung mit dem Skalierungsexponenten, der in den selben Experimenten für die durch die Driftwellenturbulenz hervorgerufenen kohärenten Strukturen beobachtet wird. Da das Blobmodell die Entwicklung bereits bestehender Stukturen ohne Einbeziehung des Entstehungsmechanismus untersucht, können die Ergebnisse dahingehend interpretiert werden, dass die Blobgröße zunächst durch den Entstehungsprozess vorgegeben wird und sich möglicherweise in der späteren Entwicklung der Blobs stärker dem theoretischen Wert annähert. Da die von den Blobs in TJ-K zurückgelegte Strecke bis zum Wandkontakt jedoch nur wenig größer ist als die Blobgröße selber, lässt sich die letztgenannte Vermutung zunächst nicht überprüfen. Eindeutig ist jedoch der Einfluss der Driftwellenturbulenz auf die Blobgröße. Dieser lässt sich mit Hilfe der Hochgeschwindigkeitskamera auch für Einzelstrukturen nachweisen. Dieser Einfluss ist auch deshalb relevant, weil das Blobmodell eine größenabhängige Geschwindigkeit voraussagt. Indirekt würde dies also über die Blobgröße einen Einfluss der Driftwellenturbulenz auf die Blobgeschwindigkeit bedeuten. Voraussetzung hierfür ist die Gültigkeit der Geschwindigkeitsvorhersage für TJ-K, welche im Folgenden überprüft wird.

Unter der Voraussetzung, dass die Ionentemperatur vernachlässigbar ist gegenüber der Elektronentemperatur ($T_\mathrm{e} \gg T_\mathrm{i}$), sagt das bestehende Blobmodell die Blobgeschwindigkeit voraus. Unter anderem hängt die radiale Geschwindigkeit von δ_b und ρ_s ab. Da die Messung der Geschwindigkeit eine große Genauigkeit in der Positionsbestimmung verlangt, wird die Blobgeschwindigkeit aus zweidimensional aufgelösten Sondenmessungen bestimmt. Wie bereits für die Größenmessung beschrieben, wird der Parameter ρ_s durch Veränderung der Gasart, der Heizleistung und der Magnetfeldstärke variiert. Für die meisten untersuchten Gase zeigt sich in TJ-K eine gute Übereinstimmung zwischen der gemessenen Radialgeschwindigkeit und der theoretisch vorhergesagten. Die Ergebnisse deuten daraufhin, dass der

Ionenpolarisationsstrom die entscheidende Rolle für die Reduktion der Blobpolarisation spielt. Für Deuterium und insbesondere Wasserstoff gibt es jedoch auch deutliche Abweichungen von der Vorhersage: Die beobachteten Geschwindigkeiten sind deutlich geringer als die berechneten Werte erwarten lassen. Diese Abweichungen lassen sich durch die sogenannte Kreuzphase zwischen Potential und Dichte $\alpha^{\phi,n}$, welche die räumliche Anordnung der Dichte und des Plasmapotentials zueinander beschreibt, erklären. Plasmastörungen die, wie es im Blobmodell der Fall ist, durch einen Mechanismus vergleichbar der Austauschinstabilität hervorgerufen werden, sollten eine Kreuzphase von $\alpha^{\phi,n} = \pi/2$ aufweisen. Im Experiment werden jedoch Werte kleiner als $\pi/4$ gemessen, was eine reduzierte Geschwindigkeit zur Folge hat. In Wasserstoff und Deuterium sind die gemessenen Kreuzphasen am niedrigsten, was zu den deutlichen Abweichungen führt. Dies bedeutet, dass die Blobdynamik nicht ausschließlich von der Austauschinstabilität bestimmt wird, sondern ein zusätzlicher Driftwellen-artiger Charakter entlang der Magnetfeldlinien vorliegt.

Um die Behauptung zu überprüfen, dass das Blobmodell die wesentlichen physikalischen Mechanismen zur Beschreibung der Blobdynamik enthält, wird eine experimentell unabhängige Größe benötigt, die aus dem selben Modell vorhergesagt werden kann. Ein Beispiel hierfür ist der Parallelstrom, der entlang der Filamente fließt um die Polarisation innerhalb des Blobs zu reduzieren und die Quasineutralität im Plasma zu gewährleisten. Basierend auf dem Standardblobmodell existiert eine Vorhersage für diesen Parallelstrom unter der Annahme, dass es keine weiteren Reduktionsmechanismen für die Blobpolarisation gibt. Diese Annahme ist nicht verträglich mit den Geschwindigkeitsmessungen, die einen dominanten Einfluss des Ionenpolarisationsstroms erkennen lassen. In der vorliegenden Arbeit wird deshalb dem Modell zur Berechnung des Parallelstroms der Einfluss des Ionenpolarisationsstroms hinzugefügt. Messungen mit einer speziellen Stromsonde zeigen eine gute Übereinstimmung mit den berechneten Werten. Dies bestätigt, dass das Blobmodell die wichtigsten physikalischen Effekte zur Beschreibung der Blobdynamik in TJ-K enthält.

Die Experimente am Stellarator TJ-K haben damit zum einen gezeigt, dass unter Verwendung von feldliniengemittelten Größen die Vorhersagen des Standardmodells die experimentell beobachtete Blobdynamik im Wesentlichen erklären können. Es konnte darüber hinaus ein starker Einfluss der Turbulenz in der Randschicht des eingeschlossenen Plasmas auf die Blobeigenschaften gezeigt werden.

Experimente an ASDEX Upgrade

Eine weitere Zielsetzung der vorliegenden Arbeit ist die Etablierung von "Gas-puff imaging" (GPI) als Diagnostik für Turbulenzuntersuchungen am Tokamak ASDEX Upgrade: Durch die im Vergleich zu TJ-K deutlich höheren Plasmatemperaturen ist das Plasma selbst in der SOL weitgehend ionisiert und es wird nur wenig sichtbares Licht emittiert. Beim GPI wird lokal durch Gaseinblasen die Neutralgas-

dichte erhöht, was aufgrund von Stößen mit den Plasmaelektronen eine stark erhöhte Lichtemission zur Folge hat. Aufgrund des steilen Temperaturprofils in der SOL von Fusionsplasmen beschränkt sich die Lichtemission auf einen Bereich in der SOL. Dieser wird mittels einer Hochgeschwindigkeitskamera beobachtet und somit werden Fluktuationen von Plasmatemperatur und Dichte sichtbar gemacht, welche sich zunächst nicht trennen lassen. Üblicherweise wird hierfür entweder Deuterium oder Helium verwendet. Deuterium hat den Vorteil stark im sichtbaren Spektrum abzustrahlen und stellt für die üblichen Deuteriumplasmen keine Verunreinigung dar. Helium zeichnet sich hingegen durch eine sehr hohe Ionisierungsenergie aus und kann somit weiter in das Plasma eindringen, bevor es ionisiert wird. Um eine Kontamination des Plasmas mit Helium und damit eine Veränderung der zu untersuchenden Dynamik zu verhindern, sind jedoch nur relativ kurze Gaseinlassintervalle von ca. 300 ms möglich. Von Vorteil bei den Experimenten an ASDEX Upgrade sind, verglichen mit TJ-K, die deutlich größeren Abmessungen des Experiments im Vergleich zum Abbildungsvolumen, was zu einer deutlich verbesserten Lokalisierung der Strukturen führt.

Alle durchgeführten Entladungen begannen mit einer rein ohmschen L-Mode Phase, bevor durch zusätzliche ECR-Heizung der Übergang in die H-Mode stattfand. Dadurch können die Blobeigenschaften in beiden Einschlussregimen untersucht werden. Die Detektionsrate, Blobgröße δ_b und Geschwindigkeit (poloidal und radial) werden in beiden Phasen bestimmt und verglichen, wobei die Analyse sich in der H-Mode auf die inter-ELM Phasen beschränkt um die zu untersuchenden Blobeigenschaften nicht durch Detektion von ELMs zu verfälschen.

Es wird beobachtet, dass die Blobgröße in der H-Mode zunimmt und gleichzeitig die radiale Geschwindigkeit abnimmt. Beide Effekte sind jedoch gering, maximal 20 % in den analysierten Entladungen, und deuten nicht auf eine dramatische Veränderung der Blobdynamik zwischen beiden Einschlussregimen hin. Hiermit im Einklang steht die Beobachtung, dass auch die Detektionsraten und die Wartezeitverteilung sich nach dem L-H-Übergang kaum verändern. Die Detektionsrate steigt in der H-Mode leicht an, was aber möglicherweise auf die erhöhte Blobgröße und damit eine steigende Detektionswahrscheinlichkeit zurückzuführen ist. In jedem Fall macht dieses Ergebnis deutlich, dass sich die drastische Turbulenzreduktion in der Randschicht von H-Mode Plasmen nicht in der Blobentstehungsrate widerzuspiegeln scheint, was den für die Entstehung relevanten Bereich im Plasma deutlich auf die Region rund um die Separatrix einschränkt.

Deutliche Unterschiede in der Blobdynamik lassen sich hingegen in der poloidalen Propagation der Strukturen erkennen. In der äußeren SOL ($\rho_{pol} \gtrsim 1.06$) wird in den untersuchten L-Mode Phasen eine Umkehr der poloidalen Propagationsrichtung beobachtet, im Gegensatz zu den inter-ELM H-Mode Phasen. Es ist anzunehmen, dass dieses Verhalten auf Unterschiede im radialen elektrischen Feld zurückzuführen ist, verursacht durch Veränderungen im Druckprofil nach dem L-H-Übergang. Weiter im Inneren werden Blobs in der L-Mode sogar mit unterschiedlichen poloidalen Propagationsrichtungen detektiert. Folglich sollten Resultate von konditionellen

Mittelungsanalysen mit größter Vorsicht interpretiert werden und mit Analysen von Einzelereignissen überprüft werden.

Unabhängig vom Einschlussregime wird eine Abnahme der radialen Geschwindigkeit $v_{r,\mathrm{b}}$ der Filamente während ihrer Auswärtspropagation beobachtet. Dieses Verhalten wurde bereits als Vermutung formuliert um Beobachtungen in Ionentemperaturmessungen zu erklären und ist auch von anderen Fusionsexperimenten bekannt. Hierbei dürften parallele Verluste und senkrechte Diffusion eine wichtige Rolle spielen, durch die der interne Druckgradient der Filamente abgebaut und damit ihr Antrieb reduziert wird.

Zusätzlich werden die Abhängigkeiten der Blobgröße δ_b und Auswärtsgeschwindigkeit $v_{r,\mathrm{b}}$ untersucht und mit theoretischen Vorhersagen verglichen. Hierbei wird neben dem Standardmodell eine aktuelle Erweiterung untersucht, die den Einfluss der Ionentemperatur berücksichtigt. Im Bereich von $\rho_\mathrm{s} = 1.07$ zeigt sich für δ_b eine gute Übereinstimmung mit den theoretischen Vorhersagen, wobei die beste Übereinstimmung unter Berücksichtigung der endlichen Ionentemperatur erreicht wird. Beide Modelle erklären korrekt die ähnliche aber leicht erhöhte Blobgröße in den H-Mode Phasen. Im Falle der Blobgeschwindigkeit ist die Interpretation der gefundenen Resultate weniger eindeutig. Aufgrund einer erhöhten Elektrontemperatur in den H-Mode Phasen, sagt das Blobmodell eine erhöhte Radialgeschwindigkeit in diesem Einschlussregime vorher. Dies widerspricht dem experimentellen Resultat, dass $v_{r,\mathrm{b}}$ nach dem L-H-Übergang im Wesentlichen konstant bleibt und sogar eine Tendenz zu einer leichten Reduktion von $v_{r,\mathrm{b}}$ beobachtet wird (maximal $20\,\%$). Mittels Regressionsanalyse zeigt sich, dass auch für Einzelereignisse eine Abhängigkeit von $v_{r,\mathrm{b}}$ mit δ_b beobachtet wird. Kleine Korrelationskoefizienten zeigen hierbei jedoch, dass δ_b nicht der einzige Skalierungsfaktor für $v_{r,\mathrm{b}}$, wie es vom Blobmodell auch erwartet wird.

Abgesehen von den physikalischen Ergebnissen der Experimente an ASDEX Upgrade zeigt sich, dass GPI ein wertvolles Werkzeug zur Untersuchung turbulenter Strukturen in der SOL darstellt. Von besonderem Interesse sind die zweidimensional aufgelösten Daten zu jedem Messzeitpunkt, mit denen die Form und Orientierung der Strukturen bestimmt werden können. Diese Eigenschaften sind unter anderem wichtig für die Interpretation nicht ortsaufgelöster Diagnostiken, bei deren Interpretation oft auf Annahmen über die räumliche Struktur der Filamente zurückgegriffen werden muss. Im Gegenzug lassen sich aus den Kameradaten zunächst keine Rückschlüsse über Dichte, Temperatur und Potential im Plasma ziehen. Deshalb werden zukünftige Blobuntersuchungen an ASDEX Uprade sich auf einen multidiagnostischen Ansatz stützen.

Zusammenfassung und Ausblick

Die wichtigsten Erkenntnisse der vorliegenden Arbeit lassen sich in folgenden Punkten zusammenfassen:

Gültigkeit des Blobmodells in Stellaratorgeometrie: Obwohl die meisten Blobmodelle von sehr einfachen Magnetfeldgeometrien ausgehen (in der Regel dem *Simple Magnetized Torus*), können die wesentlichen Blobeigenschaften im Stellarator TJ-K korrekt vorhergesagt werden, wenn die Magnetfeldstärke und Normalenkrümmung κ_n entlang der Magnetfeldlinien gemittelt werden. Insbesondere die Blobgeschwindigkeit, ein Strom entlang der Filamente parallel zum Magnetfeld und das Auftreten von Blobs in Regionen mit $\langle \kappa_\mathrm{n} \rangle < 0$ entsprechen den theoretischen Vorhersagen. Im Gegensatz zu den Experimenten am Tokamak ASDEX Upgrade zeigt sich keine gute Übereinstimmung mit der vorhergesagten Größe der Blobs δ_b. Ein wesentlicher Unterschied zwischen beiden Experimenten ist, dass die Blobs in TJ-K nur unwesentlich kleiner sind als die Strecke, die sie bis zur Wand zurücklegen. Da das Blobmodell den Entstehungsmechanismus nicht beinhaltet, könnte die Erklärung für die Abweichungen darin begründet sein, dass δ_b direkt nach ihrem Auswurf noch durch den Entstehungsmechanismus beeinflusst ist. In TJ-K ist die beobachtete Größenverteilung deshalb stark durch den Entstehungsmechanismus beeinflusst, während in ASDEX Upgrade nur Blobs die stabil gegen Sekundärinstabilitäten sind die Beobachtungsregion erreichen können.

Bedeutung der Kreuzphase für die Radialgeschwindigkeit: In TJ-K konnte gezeigt werden, dass die Kreuzphase zwischen Potential und Dichte $\alpha^{\phi,n}$ einen entscheidenden Einfluss auf die Radialgeschwindigkeit $v_{r,\mathrm{b}}$ hat. Diese Beobachtung ist in perfekter Übereinstimmung mit grundlegenden Überlegungen zur Plasmaturbulenz, der Effekt ist aber nicht in den aktuellen Blobmodellen enthalten, in denen $\alpha^{\phi,n} = \pi/2$ vorausgesetzt wird. Auch in ASDEX Upgrade wurde in früheren Messungen beobachtet, dass $\alpha^{\phi,n} < \pi/2$. Dies könnte die Ursache für die unklare Interpretation von $v_{r,\mathrm{b}}$ an ASDEX Upgrade sein. Durch gleichzeitige Sondenmessungen wird diese Vermutung in zukünftigen Experimenten überprüft werden.

Beobachtung von Einflüssen der Ionentemperatur auf die Blobdynamik: Ein erster Vergleich der Blobgröße und Geschwindigkeit in ASDEX Upgrade mit theoretischen Vorhersagen eines Modells, welches den Einfluss der Ionentemperatur berücksichtigt, zeigt in der Tat einen Einfluss auf die Blobdynamik.

Starker Einfluss der Randschichtdynamik auf die Blobeigenschaften: Zum ersten Mal konnte durch die Experimente am TJ-K gezeigt werden, dass einige Eigenschaften von Blobs in der Abschälschicht beeinflusst werden durch die Turbulenz am Rand des eingeschlossenen Plasmas. Insbesondere die Entstehungsrate und die Blobgröße zeigen einen klare Kopplung an die entsprechenden Eigenschaften kohärenter Dichtestrukturen in der Plasmarandschicht. Da am ASDEX Upgrade mittels *Gas-Puff Imaging* nur die Abschälschicht untersucht werden kann, steht eine Bestätigung dieser Ergebnisse für Fusionsplasmen noch aus. Gerade im Hinblick auf die Detektionsrate werden in Fusionsplasmen jedoch sehr ähnliche Werte gefunden, was ebenfalls auf einen Einfluss von Instabilitäten in der Randschicht hindeuten könnte. Eine wichtige Folgerung aus dem Einfluss der Turbulenz auf die Blobs ist, dass die Blobdynamik nicht nur durch Änderungen der Plasmaparameter in der Abschälschicht beeinflusst werden kann, sondern auch durch eine Kontrolle

der Turbulenz nahe der LCFS.

Vergleichbare Blobdynamik in L- und H-Mode: Es wurden für ASDEX Upgrade keine Hinweise darauf gefunden, dass es fundamentale Unterschiede in der Entstehungsrate, Größe und Radialgeschwindigkeit zwischen Blobs in L- und H-Mode Plasmen gibt. Dies deutet darauf hin, dass die grundlegenden physikalischen Mechanismen der Blobentstehung und Dynamik unabhängig vom jeweiligen Einschlussregime sind. Nur für das Profil der Poloidalgeschwindigkeit können zwischen den einzelnen Phasen große Unterschiede auftreten, die vermutlich auf Änderungen des radialen elektrischen Feld (und der damit einhergehenden Änderung in der $\mathbf{E} \times \mathbf{B}$-Drift) zurückzuführen sind und die sogar eine Umkehr der Propagationsrichtung bewirken können.

Abschließend wird erläutert, welche weiterführenden Untersuchungen angestellt werden sollten. Einige dieser Experimente befinden sich bereits in Planung.

Ein wichtiger Schritt an TJ-K wird es sein, gezielt nach Abweichungen von dem Standardblobmodell zu suchen, die sich durch die Stellaratorgeometrie ergeben sollten. Dies steht nicht im Widerspruch zur obigen Aussage, dass im Wesentlichen eine gute Übereinstimmung zwischen Modell und Experiment besteht: Im Detail sollten Unterschiede zu beobachten sein, die von der komplexen Feldgeometrie hervorgerufen werden. In einem Experiment das derzeit in Vorbereitung ist, wird zunächst der Einfluss der geodätischen Krümmung auf die Blobtrajektorie untersucht. Analog zur radialen Propagation der Filamente durch die Normalenkrümmung, sollte die geodätische Krümmung eine poloidale Propagation hervorrufen.

In zukünftigen Experimenten an ASDEX Upgrade wird ein multidiagnostischer Ansatz verfolgt, um einen vollständigen Satz von Blobeigenschaften zu erhalten, welcher Notwendig ist um offene Fragen der Blobdynamik in Fusionsplasmen zu beantworten. Unter anderem die Rolle der Ionentemperatur und die Ähnlichkeit der Blobdynamik in den unterschiedlichen Einschlussregimen wird hierbei eine Rolle spielen. Mit dem erhaltenen Datensatz können umfassende Vergleiche mit theoretischen Modellen angestellt werden, was zu einem fundamentalen Verständnis der Blobdynamik unter fusionsrelevanten Bedingungen führen wird.

Abstract

The safe and reliable satisfaction of the world's increasing energy demand at affordable costs is one of the major challenges of our century. Nuclear fusion power plants following the magnetic confinement approach may play an essential role in solving this issue. The energy loss of the fusion plasma due to plasma turbulence reduces the efficiency and poses a threat to the first wall of a fusion reactor. Close to the wall, in the *scrape-off layer*, this transport is dominated by *blobs* or *filaments*: Localized structures of increased pressure, which transport energy and particles towards the wall by propagating radially outwards. Their contribution to the transport depends on their size, propagation velocity and generation rate. An analytical model for the evolution of blobs predicts their velocity and size, but not the generation rate. Experiments indicate that *edge turbulence* in the vicinity of the last closed flux surface (the boundary between the confined plasma and the scrape-off layer) is involved in the blob generation process and should influence the generation rate.

The present thesis aims at answering two main questions: How well do the blob properties predicted from the simple model compare to experimental observations in more complex magnetic field configurations of actual fusion experiments and does the edge turbulence influence the blob properties during the generation process.

A fast camera was used to measure blob properties in two devices, TJ-K and ASDEX Upgrade. In TJ-K, blob sizes and velocities were determined together with the generation rate. An overall agreement with the predictions from the simple model is found. For the first time a clear influence of the edge dynamics on the analyzed blob properties is demonstrated. These measurements include the first systematic comparison of the structure-size scaling inside and outside of the last closed flux surface. Furthermore, measurements with a multi-probe array are used to reconstruct the blob shape in a stellarator and to show that the blobs account for more than $50\,\%$ of the local and more than $20\,\%$ of the total scrape-of layer transport. Measurements of a current along the filaments directly show that the simple model contains the relevant physical processes.

In the tokamak ASDEX Upgrade, blob properties are compared for two confinement regimes, the so-called L- and H-mode. As in TJ-K, the blob properties can to a good extent be understood from available blob models. Size measurements indicate an influence of the finite ion temperature on the blob properties. Furthermore, a surprisingly low difference in the blob dynamics is observed between L- and H-mode.

Contents

Chapter 1

Introduction

Since the first power plant for public electricity supply went online in 1881 in the British town *Godalming* [1] to feed a few dozen streetlights, the global electricity consumption has increased considerably, reaching $18.4\,\mathrm{PWh}$ in the year 2011 [2]. Today, electricity is a basic requirement for our modern society. Its large-scale production, however, consumes a substantial amount of non-renewable resources and poses a threat to mankind and nature. $79.7\,\%$ of the world electricity production in 2011 was provided by fossil and nuclear fuels [2] and it is considered necessary to find a replacement for this large fraction in order to avert global warming or to avoid the risk of nuclear disasters. This challenge becomes even more pressing by the expectation that the global electricity consumption will grow further within this century [3]. Considering the dimensions of this project, it is indispensable to explore the potential of all possible alternatives. One of these alternatives is nuclear fusion.

Nuclear fusion can occur if two nuclei collide with high energy. At very short distances the attractive strong nuclear force exceeds the repulsive electromagnetic force and a single nucleus can be generated. During this process, the binding energy is released as gamma radiation or kinetic energy of escaping particles. Ion energies high enough for nuclear fusion are found in hot ionized gases, so-called plasmas. From the beginning of the research on nuclear fusion, the energy production was one of the key issues. Initially, however, not with the aim of exploiting a new energy source on earth, but to show that nuclear fusion is responsible for the enormous energy production of the stars. This was proposed by Eddington [4] in the 1920s and quantitatively treated by Bethe in the late 1930s. Bethe identified two reaction paths, the *CNO cycle* and the *proton-proton chain reaction*, in which ^{4}He is built up from four protons by fusion reactions as the dominant energy source of regular stars [5]. Eddington speculated that mankind might use nuclear fusion as an energy source one day. Early experiments studied the confinement of plasmas with magnetic fields, but challenging technical issues and the political conditions during World War II prevented nuclear fusion from getting much attention as a possible energy source on earth. Instead, research focused on the development of nuclear fission power plants and nuclear weapon techniques [6].

An important achievement in this early time of fusion research was the identification of the deuterium-tritium fusion reaction as particularly interesting for high fusion rates at technically achievable plasma densities and temperatures [7]. However, no magnetic field geometry had been identified to stably confine a fusion plasma and reach *ignition*. Ignition refers to the point at which the fusion reaction becomes self-sustaining, i. e. when the energy production from fusion reactions compensates all losses. At that point, no further external heating of the fusion plasma is needed and, hence, ignition is a prerequisite for a competitive fusion power plant.

An important step in the search for optimum magnetic field configurations (with respect to energy losses) was the switch from linear devices to *toroidal configurations* with a helical magnetic field: In toroidal configurations, the field lines wind around a central axis (see Fig. 1.1) and constitute the so-called *confinement region*, where the field lines are either closed or feature an infinite length and never leave the confinement region. Closed field lines can lead to instabilities and are avoided as far as possible. Close to the walls, the magnetic field lines intersect the wall or other plasma facing components and there the plasma is not confined. This region is called *scrape-off layer* (SOL). It is separated from the confinement region by the *last closed flux surface* (LCFS). The transport of particles and especially energy across the LCFS constitutes one of the most important loss channels in fusion experiments and has to be minimized. It has been found, though, that a purely toroidal field leads to unstable plasma confinement due to curvature-induced drifts. This problem can be solved by substituting the toroidal field with a *helical field*, where the field lines are twisted around the magnetic axis as illustrated in Fig. 1.1. Two promising
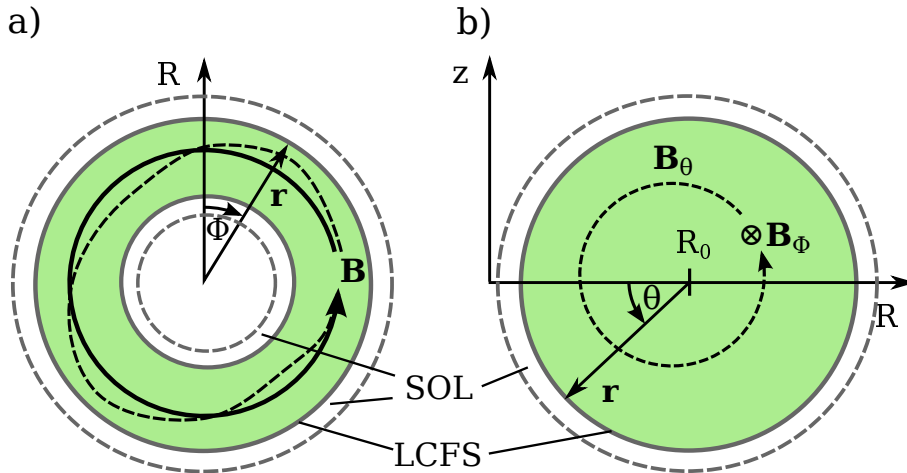
Figure 1.1: *Drawing of the magnetic field in toroidal configurations. a) shows a toroidal cross section. The closed line indicates a field line in a purely toroidal (ϕ) field, the dashed line in a helical field. b) shows a poloidal cross section. The toroidal field points into the paper, the poloidal (θ) field (to generate the helical field) is depicted as dashed line. The location of the scrape-off layer (SOL) and the last closed flux surface (LCFS) are indicated.*

concepts to realize the required helical field have been proposed in the early 1950s,
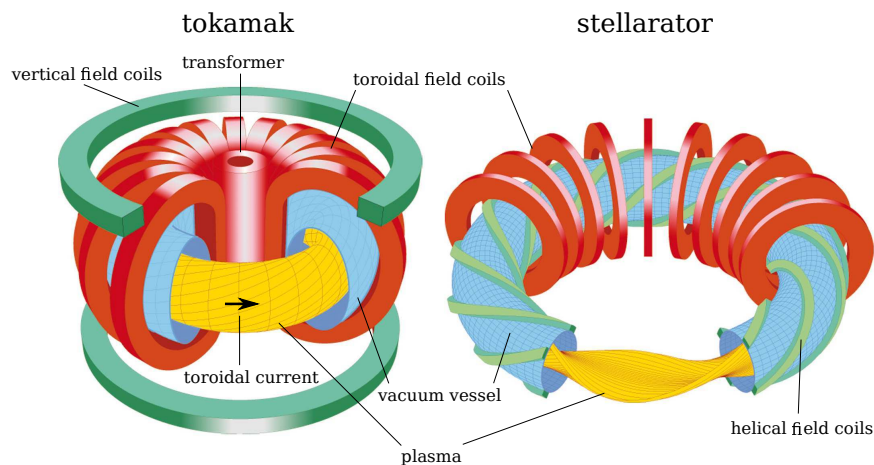
Figure 1.2: *Illustration of the different magnetic field coil sets and the resulting plasma shape in a tokamak (left) and a stellarator (right) [8].*

the tokamak [9] and the stellarator [10]. In a tokamak (left in Fig. 1.2), a toroidal field is generated by a set of toroidal field coils. In order to obtain a helical field, an additional poloidal field is required. This poloidal field is generated by a central solenoid that induces a toroidal current in the plasma, which acts as the secondary coil of a transformer. In contrast, the stellarator (right in Fig. 1.2) uses a set of toroidal and helical field coils to generate the helical field directly. It is also possible to combine the two coil systems into a set of complexly shaped magnetic field coils, as it has e. g. been done for the W7-X stellarator [11]. While both concepts feature characteristic challenges concerning the plasma stability (see Ref. [12] for a comparison of tokamaks and stellarators), one of the most important loss mechanisms is common to both configurations: Plasma turbulence.

Plasma turbulence is caused by instabilities in a plasma. The evolution and coupling of these instabilities is governed by non-linear processes, which give rise to turbulent fluctuations in e. g. the density, temperature, and potential in the plasma. These fluctuations have a huge impact on the dynamics of many different physical processes like e. g. star formation [13]. In fusion experiments, turbulence leads to an extensive transport of particles and energy, which reduces the energy confinement and, if the losses are too high, prevents ignition. Furthermore, the heat load to the wall is significantly increased, which poses a severe threat to the first wall and other plasma facing components and contaminates the plasma.

In magnetized plasmas, pressure perturbations are equilibrated much faster along the magnetic field lines than in the perpendicular direction. This gives rise to highly elongated structures, extended along the magnetic field lines. Such filamentary structures or *filaments* are e. g. found in solar flares [14], but are also a feature commonly found in the turbulence in magnetized plasmas. In fusion experiments, filaments are observed in the SOL. These filaments are often referred to as *blobs* due

to the appearance of the filaments in the cross section perpendicular to the magnetic field. They are generated in the vicinity of the LCFS and in most experiments propagate radially outwards towards the wall. Experiments indicate that blobs dominate the turbulent transport in the SOL. The particle transport due to blobs can be estimated by the contribution of a single blob times the so-called packing fraction f_p [15]:

$$\Gamma \propto n_b \cdot v_{r,b} \cdot f_p .\tag{1.1}$$

n_b is the average density in a blob and $v_{r,b}$ its radial propagation velocity while f_p depends on $v_{r,b}$, the blob size δ_b, and the waiting time between subsequent blobs t_w: $f_p = 2\delta_b/v_{r,b}t_w$ [16, 17]. This simple model already illustrates which blob properties influence directly the transport caused by blobs. Consequently, knowledge of the physical processes determining n_b, $v_{r,b}$, δ_b and t_w is essential to predict and possibly control the blob transport and reduce the wall erosion. Present analytical models predict $v_{r,b}$ and δ_b in a simple magnetic field geometry with purely toroidal field lines. The waiting time t_w and the density n_b cannot be predicted yet. There are indications that n_b is determined mainly by the background density in the birth region of blobs [15]. The experimental observation that blobs are generated from turbulent fluctuations in the vicinity of the LCFS indicates that the dynamics in this region should determine t_w. The generation process is not part of the analytical model and, hence, it is not clear if also other blob properties are influenced by the turbulence around the LCFS. The experiments presented in this thesis aim at answering two main questions:

1. Does the simple model predict experimentally observed blob properties in more complex magnetic field configurations of actual fusion experiments correctly?

2. Are the blob properties influenced by turbulence in the vicinity of the LCFS during the generation process?

To this end, measurements with a fast camera were performed in the stellarator TJ-K and the tokamak ASDEX Upgrade. In the low temperature plasma of TJ-K, additional probe measurements are available to get detailed information about the spatial structure of the filaments and the induced transport.

The thesis is organized as follows: First, a brief overview on turbulent transport and involved instabilities is given in Ch. 2 and on an analytical blob model in Ch. 3. Then, the experiments and diagnostics are presented in Ch. 4 and the analysis methods in Ch. 5. The subsequent chapters cover the experiments performed at TJ-K. Chapter 6 describes the results from basic experiments to investigate the capabilities of fast imaging to measure blob properties in TJ-K. A 3D analysis of the structure of blobs and the induced transport is shown in Ch. 7. Then, results of measurements of the generation rate, size, and radial velocity of the filaments are shown in Ch. 8 and observations concerning blob generation in Ch. 9. The experiments in the tokamak ASDEX Upgrade are discussed in Ch. 10. Finally, Ch. 11 gives a summary of the insights obtained from the presented experiments.

Chapter 2

Microscopic instabilities and turbulent transport

Small fluctuations in the plasma (e.g. in the temperature $\tilde{T}$, density $\tilde{n}$, plasma potential $\tilde{\phi}_{\mathrm{p}}$, and magnetic field strength $\tilde{B}$) can grow due to different types of plasma instabilities. In fusion plasmas many of these instabilities are driven by gradients in the background profiles (n and T) that typically peak in the center and decay towards the wall. During this growth process, energy is transferred from the background profiles to the instabilities. Furthermore, the instabilities can cause radial transport (i.e. towards the wall) of particles and energy.

Instabilities that occur in the plasma can influence each other. Since the evolution of density and potential is governed by non-linear processes, the *coupling* of different instabilities gives rise to turbulent fluctuations in the plasma. In the edge of fusion plasmas, the dominant instability that is responsible for the turbulence is the so-called drift-wave instability [18], while in the scrape-off layer the interchange instability (or interchange-like instabilities) is important [19, 20]. In this chapter a general picture of turbulent transport is given before the interchange and drift-wave instability are introduced. Both instabilities affect pressure perturbations $\tilde{p} = \tilde{n}T + n\tilde{T}$, but for simplicity reasons they are discussed for the constant temperature case, where $\tilde{p} = \tilde{n}T$.

2.1 Turbulent transport

Due to the gyro motion of charged particles in magnetized plasmas, an external force $\mathbf{F}_{\mathrm{ext}}$ induce a drift of the particles perpendicular to the magnetic field $\mathbf{B}$ and $\mathbf{F}_{\mathrm{ext}}$ with the drift velocity

$$\mathbf{v}_{\mathrm{drift}} = \frac{\mathbf{F}_{\mathrm{ext}} \times \mathbf{B}}{qB^2} \, . \tag{2.1}$$

where q is the charge of the particle. A very important example is the $\mathbf{E} \times \mathbf{B}$ drift due to electrical fields with the Coulomb force $\mathbf{F}_c = q\mathbf{E}$:

$$\mathbf{v}_{\mathrm{E} \times \mathrm{B}} = \frac{\mathbf{E} \times \mathbf{B}}{B^2}\,. \tag{2.2}$$

Electrical fields can arise due to turbulent potential fluctuations ($\tilde{\mathbf{E}} = -\nabla \tilde{\Phi}$), which
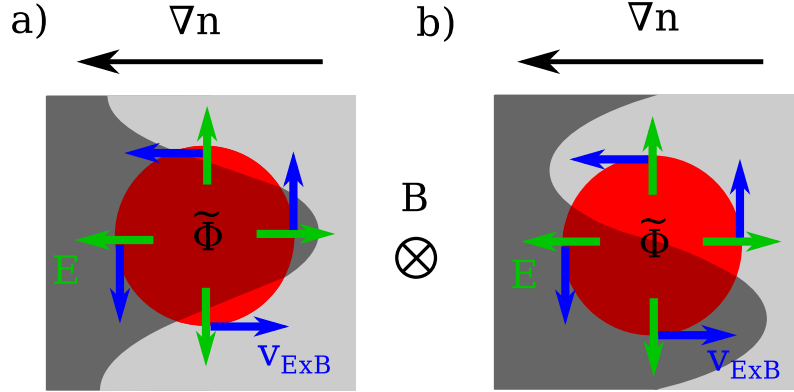
Figure 2.1: *Depending on the phase between potential fluctuations $\tilde{\Phi}$ (red circle) and density fluctuations $\tilde{n}$ (dark area: high density, bright area: low density), eddies in the $\mathbf{E} \times \mathbf{B}$ flow can cause a net outward transport. In a) the phase shift between is zero and the outward transport of density in the lower half of the eddy is compensated by inward transport of the same amount of density in the bottom half, resulting in a zero net transport. In b), however, outward transport from the high density region is not compensated by inward transport from the low density region resulting in a net outward transport.*

lead to eddies in the $\mathbf{E} \times \mathbf{B}$ flow as depicted in Fig. 2.1. Together with a density perturbation $\tilde{n}$ these eddies can lead to outward particle transport Γ, depending on the orientation of $\tilde{n}$ and $\tilde{\Phi}$. In Fig. 2.1 two different situations are compared. In a) $\tilde{n}$ and $\tilde{\Phi}$ are perfectly aligned and the net transport is zero. In b), however, a positive $\tilde{\Phi}$ is located between a positive and a negative $\tilde{n}$. The resulting eddy in the $\mathbf{E} \times \mathbf{B}$ flow transports density from the high density region to the low density region, which is not compensated by the back flow of plasma from the low density region to the high density region. The time averaged ($\langle \cdot \rangle_t$) turbulent transport at one location can be calculated as

$$\Gamma = \langle \tilde{n} \tilde{v}_r \rangle_t \overset{(2.2)}{=} \left\langle \tilde{n} \frac{E_\theta}{B} \right\rangle_t \,. \tag{2.3}$$

This can also be written in the Fourier representation with wavenumber k as

$$\Gamma \sim \Re \left\{ \left\langle \Sigma_k \hat{n}(k) \hat{E}^*(k) \right\rangle \right\} = \sum_k |\hat{n}(k)||\hat{E}(k)| \cdot \cos(\alpha^{n,E}(k))\,. \tag{2.4}$$

In the last step, the cross phase between density and electrical field $\alpha^{n,E}(k)$ is introduced. In the Fourier representation there is a phase shift between $\tilde{\Phi}$ and $\tilde{E}$ of

$\pi/2$, hence the cross phase between density and potential is $\alpha^{\Phi,n} = \alpha^{n,E} + \pi/2$ and Eq. (2.4) can be written as

$$\Gamma = \frac{1}{B} \sum_k |\hat{n}(k)||\hat{E}(k)| \cdot \sin(\alpha^{\Phi,n}(k)) \,. \tag{2.5}$$

The net transport Γ is zero for $\alpha^{\Phi,n} = 0$, corresponding to Fig. 2.1 a), and reaches its maximum for $\alpha^{\Phi,n} = \pi/2$, Fig. 2.1 b).

2.2 Interchange instability

The interchange instability requires a pressure gradient and curved magnetic field lines. To illustrate the driving mechanism, a density perturbation is considered. In Fig. 2.2 a) the background density gradient is parallel to the curvature radius of the magnetic field line $\mathbf{R}_c$ and in b) antiparallel. The curvature of the field induces curvature and gradient drifts with the drift velocities

$$v_c = \frac{2W_\parallel}{qR_c^2} \frac{\mathbf{R}_c \times \mathbf{B}}{B^2} \qquad , \qquad v_{\nabla B} = -\frac{W_\perp}{q} \frac{\nabla B \times \mathbf{B}}{B^3} \,. \tag{2.6}$$

$W_\parallel$ and $W_\perp$ are the kinetic energies of the particle parallel and perpendicular to $\mathbf{B}$ and q is the charge of the particle. Since both drift velocities depend on q they point in the opposite direction for electrons and ions. In Fig. 2.2, the ions are moving upwards and the electrons are moving downwards. This leads to a polarization of regions of different densities and, hence, electrical fields. This electrical field introduces an $E \times B$ drift due to the background magnetic field. The direction of the $E \times B$ drift is the same for electrons and ions and, hence, is the same for the two cases in Fig. 2.2. This leads to a damping of the density perturbation in a) and an amplification in b). Therefore, regions where ∇n is parallel to $\mathbf{R}_c$ are called *good curvature* regions and in the antiparallel case *bad curvature* regions. As an example, in a tokamak good curvature regions are found on the inboard side and bad curvature regions on the outboard side.

In the ideal case described above, the interchange modes feature a cross phase between density and potential of $\alpha^{\Phi,n} = \pi/2$ and the perturbation is homogeneous along the magnetic field ($k_\parallel = 0$). In the confinement region, ideal interchange modes with $k_\parallel = 0$ are only possible on rational flux surfaces. In the SOL, however, the field lines intersect the vessel at some point and the character of turbulent fluctuations is more interchange-like. Furthermore, in tokamaks and stellarators the curvature is not constant. The curvature vector $\boldsymbol{\kappa} = -\mathbf{R}_c$ is defined as

$$\boldsymbol{\kappa} = (\hat{\mathbf{b}} \cdot \nabla)\hat{\mathbf{b}} \,, \tag{2.7}$$

with $\hat{\mathbf{b}} = \mathbf{B}/B$. With the normal vector of the flux surfaces $\hat{\mathbf{n}}$ the normal curvature is given by

$$\kappa_n = \boldsymbol{\kappa} \cdot \hat{\mathbf{n}} \,. \tag{2.8}$$
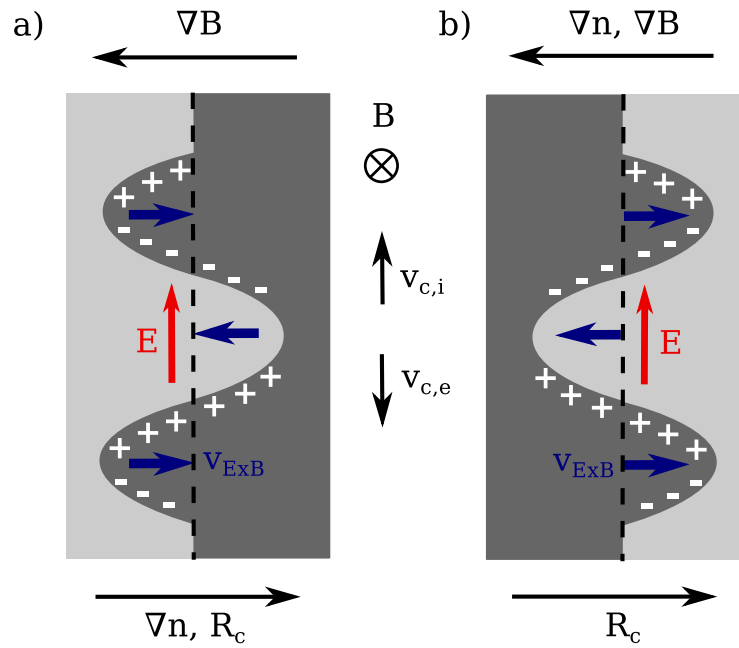
Figure 2.2:   *Illustration of the interchange mechanism. Regions of higher density are shown as dark areas and regions of lower density as bright areas. In a) the stable situation in a good curvature region is shown, while b) shows the unstable case in a bad curvature region. The space charge distribution is shown together with the resulting electrical field E and drift velocity $v_{E \times B}$.*

Bad curvature regions, where interchange instabilities are driven, are characterized by $\kappa_n < 0$. Due to the helical magnetic field geometry, field lines pass through both, good and bad curvature regions. Interchange-like instabilities are observed [21] for density perturbations on field lines with

$$\langle \kappa_n \rangle < 0 \,, \tag{2.9}$$

where $\langle \cdot \rangle$ denotes the average along the field line segment covered by the density perturbation.

2.3 Drift-wave instability

Drift waves arise from pressure fluctuations $\tilde{p}$ in magnetized plasmas with a background pressure gradient. The mechanism behind the drift wave is illustrated in Fig 2.3. Regions of increased density strive to equilibrate parallel to the magnetic
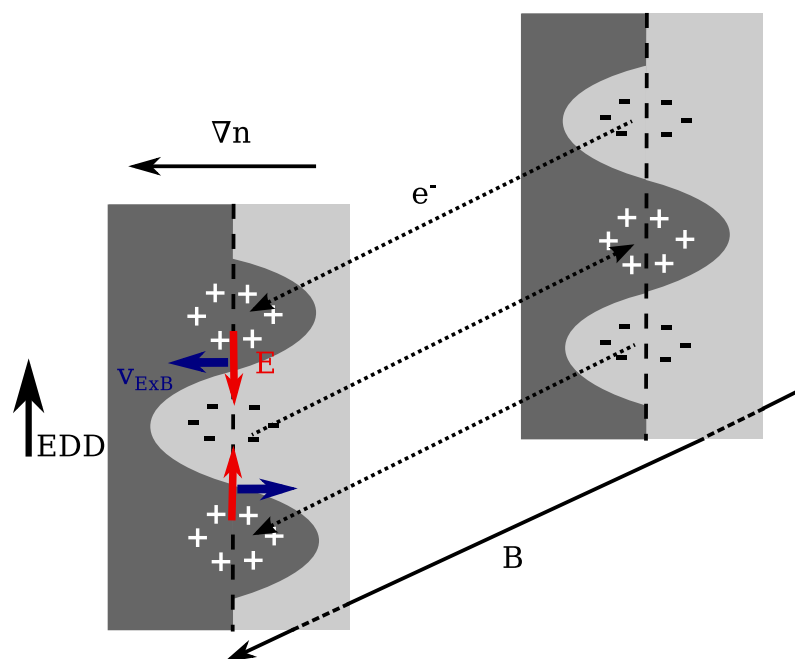
Figure 2.3: *Illustration of the mechanism behind drift waves. Regions of higher density are shown as dark area and regions of lower density as bright area. The space charge distribution is shown together with the resulting electrical field E and drift velocity $v_{E \times B}$.*

field. Due to their higher mobility, electrons leave the region of increased density faster than the heavier ions, which leads to a charge separation with a surplus of electrons in low-density regions and ions in high-density regions of the drift wave. Therefore, the drift wave inherently features a parallel structure with $k_\parallel \neq 0$ and potential fluctuations $\tilde{\Phi}$ arise from the charge separation. For the ideal drift wave

the electrons can be considered as *adiabatic*, i.e. they follow the density perturbation instantly. Hence, for a drift wave positive $\tilde{\Phi}$ coincide exactly with regions of positive $\tilde{p}$ and vice versa, leading to a cross phase between density and potential of $\alpha^{\Phi,n} = 0$. According to Eq. 2.5 no transport is caused by an ideal drift wave. The drift-wave instability arises when the electrons are not adiabatic. This can happen because of a parallel resistivity, Landau damping, or trapped particles [22]. Then, $\alpha^{\Phi,n} \neq 0$ and radial transport is caused by the unstable drift wave.

Another important characteristic of the drift wave is a proper motion in the poloidal direction. As depicted in Fig. 2.3, a fluctuating electrical field $\tilde{E}$ is caused by $\tilde{\Phi}$. The resulting radial $\tilde{E} \times B$ drift leads to an outward particle flux on one side and an influx on the other side of the density perturbation, leading to a poloidal displacement of the whole structure in the direction of the diamagnetic drift velocity of the electrons

$$v_{\mathrm{dia,e}} = \frac{\nabla p \times B}{enB^2} \,, \tag{2.10}$$

where e is the elementary charge and n the density. Equation (2.10) defines the electron diamagnetic drift direction (EDD) and the counter part in the opposite direction, the ion diamagnetic drift direction (IDD).

Chapter 3

Theory of blob dynamics

It was motivated in the introduction that filaments of increased pressure, so-called *blobs*, contribute significantly to the transport of energy and particles in the scrape-off layer (SOL), which in turn leads to increased wall erosion. The term blob is not always used very strictly in the literature, since there is no precise definition. Mostly it is used to refer to structures that fulfill the following criteria (according to Ref. [16]):

- The density perturbation is a monopole with a peak density higher than the standard deviation of the density fluctuations of the background plasma.

- The filament is aligned to the magnetic field with almost no pressure variations along the field and a cross-field size much smaller than the parallel length.

- The filament propagates due to the $\mathbf{E} \times \mathbf{B}$ drift caused by an associated dipole structure in the potential transverse to the direction of the propagation.

The dynamics of blobs in the SOL is governed by non-linear phenomena. That makes the analytical description challenging even for a single filament. As soon as blobs change the background plasma or interact with other blobs, numerical simulations are mandatory. Nevertheless, it is worthwhile to study reduced models to gain insight in the mechanism of blob evolution and to get simple scaling laws to estimate the induced transport. Simple scaling laws are important for the design of new fusion experiments or future fusion reactors. Since numerical simulations of turbulence are very time-consuming, it is necessary to identify the useful parameter range for the simulations and, hence, the machine design. In most of the experiments where blobs occur, three common features of these structures are observed:

1. Blobs are relatively long-living quasi-coherent structures with lifetimes typically larger than $100\,\mu s$ [23].

2. Blobs feature a much larger extension parallel to the magnetic field than perpendicular to it [24] ($l_\perp \ll l_\parallel$). It is often assumed that density and plasma

potential do not vary along the filament or in other words that the parallel wave number $k_\parallel = 0$. Possible parallel variations are treated as perturbation or secondary instability [25]. In contrast to the confinement region, a perturbation can have a $k_\parallel$ of zero in the SOL due to the finite connection length between plasma facing components [26, 27].

3. The blobs feature a radial outward propagation. One of the earliest descriptions of the radial movement of blobs can be found in Ref. [28] and an extensive review of experimental observations is given in Ref. [16] . There are, however, also experiments where no or almost no radial propagation of the filaments has been found (e. g. in the stellarator W7-AS [29]).

The dynamics of these objects are discussed in this chapter. When the parallel length $l_\parallel$ is close to the SOL connection length L_{SOL} the filaments end at the sheath of a plasma facing component (wall or limiter) and sheath physics becomes important. Hence, this chapter starts with a brief overview of sheath physics. Then, model predictions for the radial blob velocity $v_{r,\mathrm{b}}$ and the blob size δ_{b} are given. Expectations for the blob generation rate are discussed and a prediction for parallel currents along the filament is presented.

3.1   Sheath physics

In the plasma, quasi-neutrality holds ($n_{\mathrm{e}} = n_{\mathrm{i}}$). Close to a wall, the space charge distribution is changed ($n_{\mathrm{e}} < n_{\mathrm{i}}$). This region is called the sheath. It is caused by particle fluxes to the wall: Due to their smaller mass, the thermal velocity of the electrons is large compared to that of the ions, which results in a higher electron flux to the walls. An isolated wall will charge up negatively and, hence, repel further electrons and attract ions until the electron and ion flows are equal and a stable situation is reached. At this point, the wall is charged to the floating potential Φ_{f} (Sec. 4.4). Due to Debye shielding, the electrical field from the charged wall cannot penetrate far into the plasma. In order to attract ions to the sheath region, a transition region called pre-sheath exists where the potential decreases slightly towards the wall from the plasma potential Φ_{p} to the sheath entrance potential Φ_{se}. In this pre-sheath the plasma can be approximated to be quasi-neutral ($n_{\mathrm{e}} \lesssim n_{\mathrm{i}}$). In Fig. 3.1 the potential is shown as a function of the distance from the wall. The sheath entrance is located at about 10 Debye lengths λ_{D}, depending on the ion species, the density, and the temperature (Ref. [30]).

In the equilibrium state described above the wall is charged to Φ_f and there is no net current to the wall. In the presence of potential fluctuations $\tilde{\Phi}_{\mathrm{p}}$ in the plasma, however, net currents $\tilde{\mathbf{j}}$ flow to the wall. In a magnetized plasma this current follows the magnetic field lines ($|\tilde{\mathbf{j}}| = \tilde{j}_\parallel$) and at the sheath holds [30]

$$j_{\parallel,\,\mathrm{sheath}} = -nec_{\mathrm{s}} \left(1 - \mathrm{e}^{-e(\Delta\phi - \phi_{\mathrm{f}})/T_{\mathrm{e}}}\right) , \tag{3.1}$$

where $\Delta\phi = \phi_{\mathrm{p}} - \phi_{\mathrm{wall}}$ is the potential drop from the plasma potential to the actual wall potential and $\phi_f \approx 3T_{\mathrm{e}}$ [31] is the floating potential. This can be rewritten in terms of the difference of the plasma potential to a reference potential ϕ_*:

$$j_{\parallel,\,\mathrm{sheath}} = -nec_{\mathrm{s}}\left(1 - \mathrm{e}^{-e(\phi_{\mathrm{p}} - \phi_*)/T_{\mathrm{e}}}\right) \approx \frac{ne^2 c_{\mathrm{s}}(\phi_{\mathrm{p}} - \phi_*)}{T_{\mathrm{e}}}\,, \tag{3.2}$$

with the ion sound speed $c_{\mathrm{s}} = \sqrt{T_{\mathrm{e}}/m_{\mathrm{i}}}$. In the absence of temperature fluctuations, however, ϕ_* is only a constant reference potential and it will be seen below that its numerical value has no influence on the blob dynamics.
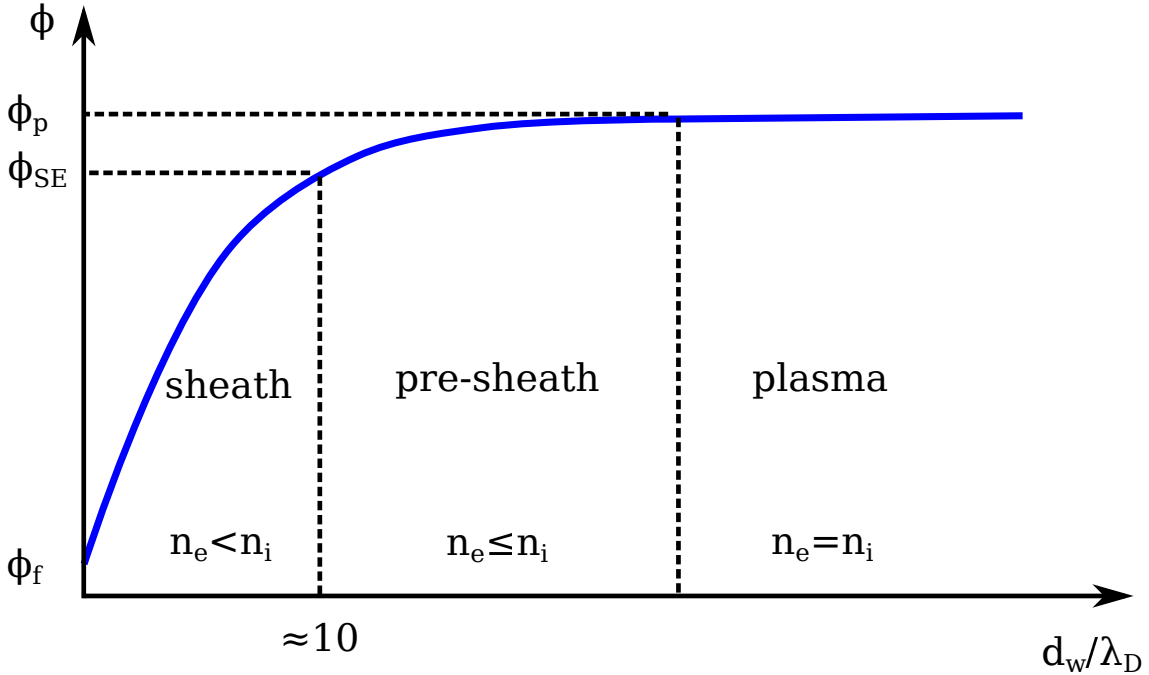
Figure 3.1: *The potential in the presence of a wall as a function of the distance d_{w} in units of the Debye length λ_{D}. Towards the wall, the potential drops from the plasma potential Φ_{p} to the sheath entrance potential Φ_{se} in the approximately quasi-neutral pre-sheath and drops further until it reaches the floating potential Φ_{f} at the wall.*

3.2 Radial blob propagation

The basic mechanism of this radial motion is as follows: Due to charge-separating drifts, the blob is polarized. The resulting electrical field $\tilde{\mathbf{E}}$ then leads to $\tilde{\mathbf{E}} \times \mathbf{B}$ drifts in the background magnetic field $\mathbf{B}$ with a radial velocity component of up to ten percent of the ion sound velocity c_{s} [16].

To estimate the radial blob velocity $v_{\mathrm{r,b}}$ the first two features stated above are used (long lifetime and $k_{\parallel} = 0$). Since the blobs seem to be stable on turbulence

time scales it is assumed that the polarization has reached an equilibrium state and no further charges are accumulated. The current perpendicular to the magnetic field $\mathbf{j}_\perp$ (the currents arising from charge separating drifts that are responsible for the blob polarization and currents counteracting this polarization) are balanced by a current parallel to the magnetic field $j_\parallel$ leading to the vanishing divergence of the total current:

$$-\nabla_\perp \cdot \mathbf{j}_\perp = \nabla_\parallel j_\parallel \,. \tag{3.3}$$

It is shown below how the radial blob velocity can be derived using this model. It is clear that the solution depends on the choice of the dominant contributions to $\mathbf{j}_\perp$ and $j_\parallel$. Different drifts have been identified to cause charge separation in blobs [16] and, hence, radial propagation. However, in magnetized toroidal plasmas the dominant drift is almost always caused by the magnetic field geometry [16, 32, 33]. In the literature often the single particle drifts are discussed for the blob polarization namely the curvature and gradient drift. The same results are obtained in the fluid picture, where the divergence of the diamagnetic drift is used. For the balancing of the polarization caused by these drifts, often the ion-polarization current and a parallel current flowing along the filament to the sheath in front of a limiter (more general a plasma facing component) are considered. In Ref. [34] it is shown that in this case Eq. (3.3) can be written as

$$\frac{m_i}{B^2} \nabla \cdot \left(n \frac{\mathrm{d}}{\mathrm{d}t} \nabla_\perp \phi + n\nu_{\mathrm{in}} \nabla_\perp \phi \right) = \nabla_\parallel j_\parallel + \frac{2}{B} \hat{\mathbf{b}} \cdot \boldsymbol{\kappa} \times \nabla p \,, \tag{3.4}$$

with $\mathrm{d}/\mathrm{d}t = (\partial/\partial t + \mathbf{v}_{E\times B} \cdot \nabla)$, the plasma potential ϕ, the unit vector in the direction of the magnetic field $\hat{\mathbf{b}} = \mathbf{B}/B$, the curvature vector $\boldsymbol{\kappa} = (\hat{\mathbf{b}} \cdot \nabla)\hat{\mathbf{b}}$, the neutral-ion collision frequency ν_{in} and the plasma pressure $p = p_e + p_i = n_e T_e + n_i T_i$. It should be noted that in contrast to Ref. [34] Eq. (3.4) is given in SI units and the term accounting for ion-neutral collisions from Ref. [35] has been added. The terms describe from left to right the divergence of the ion-polarization current, the divergence of perpendicular currents due to collisions, the divergence of the parallel sheath currents (which will be treated in more detail in Sec. 3.5) and the divergence of the diamagnetic current. The last term is responsible for the polarization of the filament and is, therefore, sometimes called *forcing term* or *blob drive*. To solve this equation analytically a number of approximations are employed in Ref. [34]:

1. The Boussinesque approximation:

$$\nabla \cdot \left(n \frac{\mathrm{d}}{\mathrm{d}t} \nabla_\perp \phi \right) = n \frac{\mathrm{d}}{\mathrm{d}t} \nabla_\perp^2 \phi \,. \tag{3.5}$$

This approximation assumes low fluctuation amplitudes $\tilde{n}/n \ll 1$, the absence of a background electrical field and structure sizes much smaller than the background profile scale length. The discussion in Ref. [34] shows that these requirements are not strictly fulfilled for blobs in the SOL, but that the approximation is adequate to describe the blob danymics.

2. The assumption of a simple magnetic field geometry with a local coordinate system where $\mathbf{B} = B\hat{\mathbf{e}}_z$ and $\boldsymbol{\kappa} = -\hat{\mathbf{e}}_x/R$ (R is the major radius).

3. No pressure variations in the blob parallel to the magnetic field ($\partial_z p = 0$).

With these approximations Eq. (3.4) can be written as

$$\frac{2}{RB}\frac{\partial p}{\partial y} = \frac{nm_i}{B^2}\left(\frac{\partial}{\partial t} + \mathbf{v}_{E\times B}\cdot\nabla\right)\nabla^2\phi - \nabla_\parallel j_\parallel + n\nu_{\mathrm{in}}\nabla_\perp^2\phi\,. \tag{3.6}$$

Figure 3.2 illustrates the meaning of the different terms in this equation.
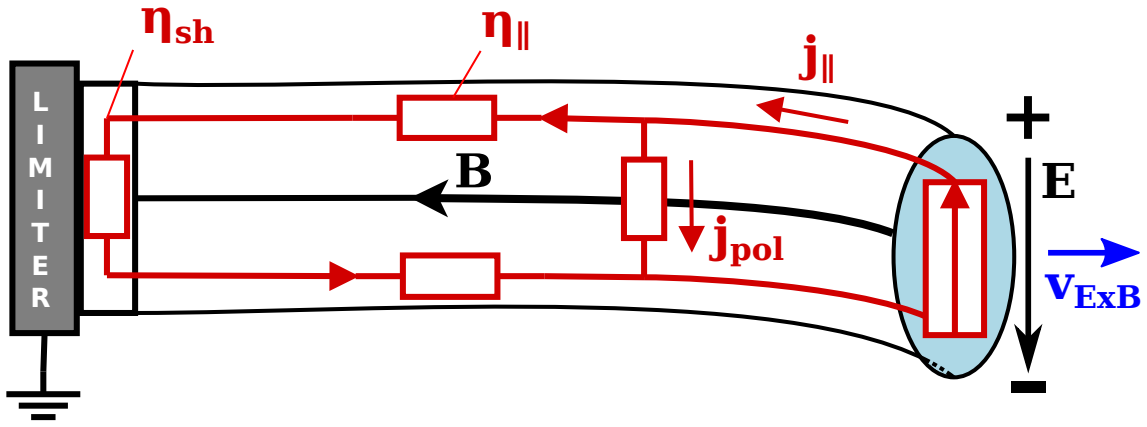
Figure 3.2:   *Illustration of a blob extended along a curved magnetic field line. Curvature induced drifts polarize the filament. The polarization is balanced by parallel currents $j_\parallel$, which are damped due to sheath resistivity η_{sh}, neutral-ion collisions $\eta_\parallel$ and ion-polarization currents perpendicular to the field line. The resulting poloidal (upwards in the figure) electrical field gives rise to radial $\mathbf{E}\times\mathbf{B}$ drifts. Reproduced after [34, 36].*

Blobs are observed in plasmas with very different conditions. Hence, usually not all of the terms in Eq. (3.6) are of equal importance and further approximations can be used to find simple solutions. Two such solutions are briefly presented in the following, one for plasmas with cold ions as in TJ-K and one for warm ions as in ASDEX Upgrade.

3.2.1   Cold plasmas

Equation (3.6) can be simplified when the ions are cold ($T_i \ll T_e$) and electron temperature fluctuations can be neglected ($\tilde{T}_e = 0$). Then $\tilde{p} = \tilde{p}_e + \tilde{p}_i \approx \tilde{p}_e \approx T_e\tilde{n}_e$. To derive the radial blob velocity $v_{r,\mathrm{b}}$ a model for $j_\parallel$ is required. In Refs. [32, 33] it is assumed that the parallel current flowing along the blob filament matches the sheath current at the sheath of the wall/limiter (see Sec. 3.1). Since it is assumed that $k_\parallel = 0$ for the density and potential perturbation associated with the blob

and that the filament extends between two plasma facing components (i. e. sheath contact at both ends of the filament), the parallel derivative of $j_\parallel$ is [34]

$$\nabla_\parallel j_\parallel = \frac{2}{l_\parallel} j_{\parallel,\,\text{sheath}} \,. \tag{3.7}$$

In Refs. [35, 37, 38] a number of approximations are applied to simplify Eq. (3.6):

1. The blob drive is explained by the interchange mechanism. Hence, the growth rate of the ideal interchange instability is used to replace the total time derivative in the first term of Eq. (3.6): $\mathrm{d}/\mathrm{d}t \approx \sqrt{2}c_{\mathrm{s}}/\sqrt{R\delta_{\mathrm{b}}}$ with the blob size δ_{b}.

2. It is assumed that at the position of the positive potential pole $\partial p/\partial y = -T_{\mathrm{e}}\delta n/\delta_{\mathrm{b}}$, where $\delta n = n_{\max} - n_0$ is the difference between maximum and background density.

3. Linearization of the derivatives [35, 38]: $\nabla_\perp \phi \approx 0$, $\nabla^2 \phi \approx -\phi^*/\delta_{\mathrm{b}}^2$, and $\phi^* \approx Bv_{r,\mathrm{b}}\delta_{\mathrm{b}}$ (approximating the $\mathbf{E} \times \mathbf{B}$ velocity).

With these approximations Eq. (3.6) can be solved for $v_{r,\mathrm{b}}$:

$$v_{r,\mathrm{b}} = \frac{\sqrt{\frac{2\delta_{\mathrm{b}}}{R}}c_s}{1 + \frac{1}{\rho_s^2 l_\parallel}\sqrt{\frac{R}{2}}\delta_{\mathrm{b}}^{5/2} + \frac{\nu_{\mathrm{in}}\sqrt{R\delta_{\mathrm{b}}}}{\sqrt{2}c_s}} \frac{\delta n}{n_0} \,, \tag{3.8}$$

with $l_\parallel$ the parallel length of the blob (e. g. the distance between two limiter plates) and ρ_{s} the drift scale:

$$\rho_{\mathrm{s}} = \frac{\sqrt{m_{\mathrm{i}}T_{\mathrm{e}}}}{eB} \,. \tag{3.9}$$

An agreement with this predicted velocity has been found in experiments in the magnetized torus TORPEX [35]. It should be noted that this model assumes a density perturbation like for the interchange instability, described in Sec. 2.2, to obtain the velocity calculated above. This implies a pure interchange instability with a cross phase between density and potential of $\alpha^{\phi,n} = \pi/2$.

The three terms in the denominator of Eq.(3.8) describe from left to right the influence of the ion-polarization current, the parallel currents through the sheath and neutral-ion collisions. If one of the three terms dominates the denominator, three different branches or regimes of Eq.(3.8) can be identified that were derived independently before (references given below). Assuming $\delta n/n_0 = 1$, these are the sheath limited regime [33, 34]

$$v_{r,\text{sheath}} \approx 2c_{\mathrm{s}} \left(\frac{\rho_{\mathrm{s}}}{\delta_{\mathrm{b}}}\right)^2 \frac{l_\parallel}{R} \,, \tag{3.10}$$

the so-called inertial regime [37, 39]

$$v_{r,\text{inertial}} = \sqrt{\frac{2\delta_{\text{b}}}{R}} c_{\text{s}} \, , \tag{3.11}$$

and a regime dominated by neutral friction [40]

$$v_{r,\text{fric.}} = \frac{2c_{\text{s}}^2}{\nu_{\text{in}} R} \, . \tag{3.12}$$

All three regimes predict a different dependence of $v_{r,\text{b}}$ on the blob size δ_{b}.

3.2.2 Warm plasmas

The approximations justified for cold plasmas are no longer valid in fusion plasmas, where in the SOL it is usually the case that $T_i > T_e$ together with a fluctuating part $\tilde{T}_{e,i} \neq 0$ [41]. While there are numerical simulations taking this into account, not much effort has been spent yet to find scaling laws for the blob velocity as those shown above for the cold ion case. Only very recently this problem has been treated analytically in Ref. [42]. In analogy to Eq. (3.6) the evolution of the charge separation is described by

$$\frac{\mathrm{d}\nabla_{\perp}^2(\phi + \tau_{\text{i}}\tilde{p}_{\text{e}})}{\mathrm{d}t} = \nabla_{\parallel}j_{\parallel} - (1 + \tau_{\text{i}})\frac{2L_{\perp}}{R}\frac{\partial\tilde{p}_{\text{e}}}{\partial y} \, . \tag{3.13}$$

Here, $\tau_{\text{i}} = T_{\text{i}}/T_{\text{e}}$, $\tilde{p}_{\text{e}}$ is the pressure amplitude normalized to the background pressure $p_{\text{e},0}$ and $L_{\perp}$ is the mean profile scale length. Additional equations to describe the electron pressure evolution $\mathrm{d}p_{\text{e}}/\mathrm{d}t$ and to predict the parallel current $j_{\parallel}$ are needed, which depend on the dominant reduction mechanism for the blob polarization and are given in Ref. [42]. For the sheath dissipation regime, where parallel currents to the walls are important, the following velocity scaling is obtained:

$$v_{r,\text{sheath}} \approx (1 + \tau_i)c_{\text{s}} \left(\frac{\rho_{\text{s}}}{\delta_{\text{b}}}\right)^2 \frac{l_{\parallel}}{R} \, , \tag{3.14}$$

which agrees with the cold ion scaling according to Eq. (3.14) beside an additional factor $(1 + \tau_i)/2$ describing the pressure contribution by the ions. If, however, collisions get important, the following scaling is obtained

$$v_{r,\text{b}} = \Lambda\frac{(1 + \tau_i)}{R} \left(\frac{l_{\parallel}}{L_{\text{SOL}}}\right)^2 \left(\frac{\rho_{\text{s}}}{\delta_{\text{b}}}\right)^2 \, , \tag{3.15}$$

with the SOL connection length L_{SOL} and the collision parameter [43]

$$\Lambda = \frac{\nu_{\text{ie}}L_{\text{SOL}}}{\Omega_{\text{ce}}\rho_{\text{s}}} \approx 1.7 \cdot 10^{-22}\frac{n_{\text{e}}\,[\text{m}^{-3}]L_{\text{SOL}}\,[\text{m}]}{T_{\text{e}}\,[\text{eV}]^2} \, . \tag{3.16}$$

Here, ν_{ie} is the electron-ion collision frequency and Ω_{ce} the cyclotron frequency of the electrons. Eq. (3.15) has the same size dependence as Eq. (3.14), but is much more sensitive to the background density n_{e} and electron temperature T_{e}. According to Refs. [15, 42], the collisional scaling is valid for $\Lambda > 1$.

3.3   Blob size

The blob size is treated theoretically by two different approaches. One approach is to study the stability of blobs that already exist in the SOL against secondary instabilities (see e. g. Refs. [44, 45]). The results depend on the secondary instabilities considered. Starting point of the stability analysis is often an equation comparable to the model equation (3.4). As in the case of the blob velocity, the result for the blob size δ_b also depends strongly on the regime of blob dynamics (Sec. 3.2). If the ions are cold and the blob dynamics are thus well described by Eq. (3.6) (neglecting the neutral collision term), Ref. [34] reports a most stable blob size δ_* (with respect to secondary instabilities) of

$$\delta_* = \rho_\mathrm{s} \left(\frac{l_\parallel^2}{\rho_\mathrm{s} R} \right)^{1/5} \propto \rho_s^{4/5} . \tag{3.17}$$

For the warm-ion case, the size dependent growth rate is analyzed in Ref. [42] and, again neglecting collisions, the width δ of largest growth rate is found:

$$\delta = \rho_\mathrm{s} \left(8(1 + \tau_i) \right)^{1/5} \cdot \left(\frac{l_\parallel^2}{\rho_\mathrm{s} R} \right)^{1/5} \propto \rho_s^{4/5} , \tag{3.18}$$

which is comparable to the most stable blob size δ_* in the cold-ion case, but includes a contribution of the ion temperature.

It can be expected that the blob size distributions observed in experiments, which usually are rather broad, are influenced by the physics of the blob generation (characteristic size of the generating edge turbulence structures), the size dependent growth rate of the newly formed structure and, after having evolved for some time, also the stability. Hence, a quantitative prediction of the blob size distribution is a challenging task and still remains an unresolved issue.

3.4   Generation rate

The generation rate of blobs depends on the generation mechanism. The understanding of blob generation has increased a lot over recent years [46–50]. Different instabilities have been identified that trigger blob generation. As an example, there are observations that isolated blobs are detaching from drift waves [48] or interchange modes [47]. There are controversial discussions whether turbulent eddies can break up or not, but concerning blob generation close to the last closed flux surface (LCFS) it is observed in some experiments that parts of the initial density perturbation reside inside of the LCFS. These experiments were e. g. done by gas-puff imaging in Alcator C-Mod [51], NSTX [52], and TEXTOR [53], but also by probe measurements in TJ-K [48]. Therefore, although no quantitative prediction for the generation rate exists so far it can be expected that it should depend strongly

on the typical frequency band of the blob generating instability in the edge plasma. These expectations are supported by observations from the tokamak Alcator C-Mod and the linear device PISCES: In Ref. [32] it is shown that in Alcator C-Mod the birth rate of blobs is connected to the typical drift-wave frequency band. In the linear device PISCES it was observed that large amplitude density fluctuations in the *source free region* (limiter shadow) are correlated with density bursts in the main plasma column. In both regions, the waiting-time distribution (WTD) was investigated, i. e. the distribution of time intervals between two subsequent events of the same type (see Sec. 5.3). The WTDs have been found to be comparable, which points to a direct coupling between turbulent fluctuations in the main plasma and blobs in the source free region of this device [54].

3.5 Parallel current

The blob model presented in this chapter includes currents flowing along the filament to the sheath in front of a limiter (or other plasma facing components) that reduce the blob polarization. In Ref. [55], Eq. (3.4) is solved for the parallel current density at the sheath entrance $j_\parallel\big|_{\mathrm{sheath}}$. The assumptions made are that the ions are cold and that the parallel current is the only effective reduction mechanism of the polarization. In this case Eq. (3.4) reads

$$\frac{2c_s^2 m_i}{RB}\frac{\partial n}{\partial y} = -\nabla j_\parallel \approx \frac{2j_{\mathrm{sheath}}}{l_\parallel} \ . \tag{3.19}$$

The current density at the sheath entrance $j_\parallel\big|_{\mathrm{sheath}}$ is obtained by integrating this equation along the magnetic field line. Since the simple model assumes $k_\parallel = 0$, the integration is accomplished by multiplying with $l_\parallel$:

$$\frac{l_\parallel c_s^2 m_i}{RB}\frac{\partial n}{\partial y}\bigg|_{l_\parallel/2} = j_\parallel\big|_{\mathrm{sheath}} \ . \tag{3.20}$$

Due to the $\partial n/\partial y$ term, Eq. (3.20) predicts a parallel current with a dipole structure in the poloidal direction (y-direction) centered around the density peak. This is schematically shown in Fig. 3.3.

The magnetic field points into the paper (z-direction), the blob is polarized in the poloidal (y-direction) direction, which causes the dipolar parallel current and a radial (R-direction) $\mathbf{E} \times \mathbf{B}$ propagation. A qualitative agreement with the prediction according to Eq. (3.20) has been found at TORPEX, however, the observed currents were significantly smaller than expected, indicating that the parallel current is not solely responsible for reducing the blob polarization. An improved prediction including the ion-polarization current is presented in Sec. 8.4.1.
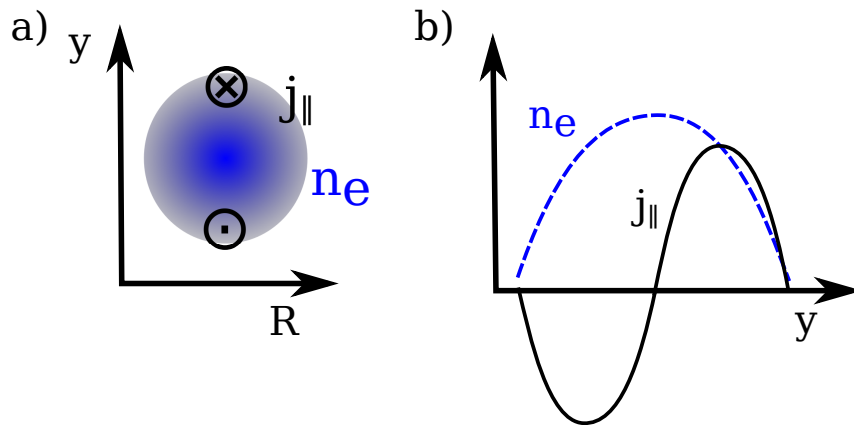
Figure 3.3: *According to Eq. (3.20), a blob is polarized in the poloidal (y) direction. In the sheath limited case, this polarization leads to parallel currents flowing along the filament (see Fig. 3.2). In a) a density blob (blue circle) is shown in a poloidal cross section and the direction of the current is indicated. In b) a poloidal cut of $j_\parallel$ and n_e is shown.*

Chapter 4
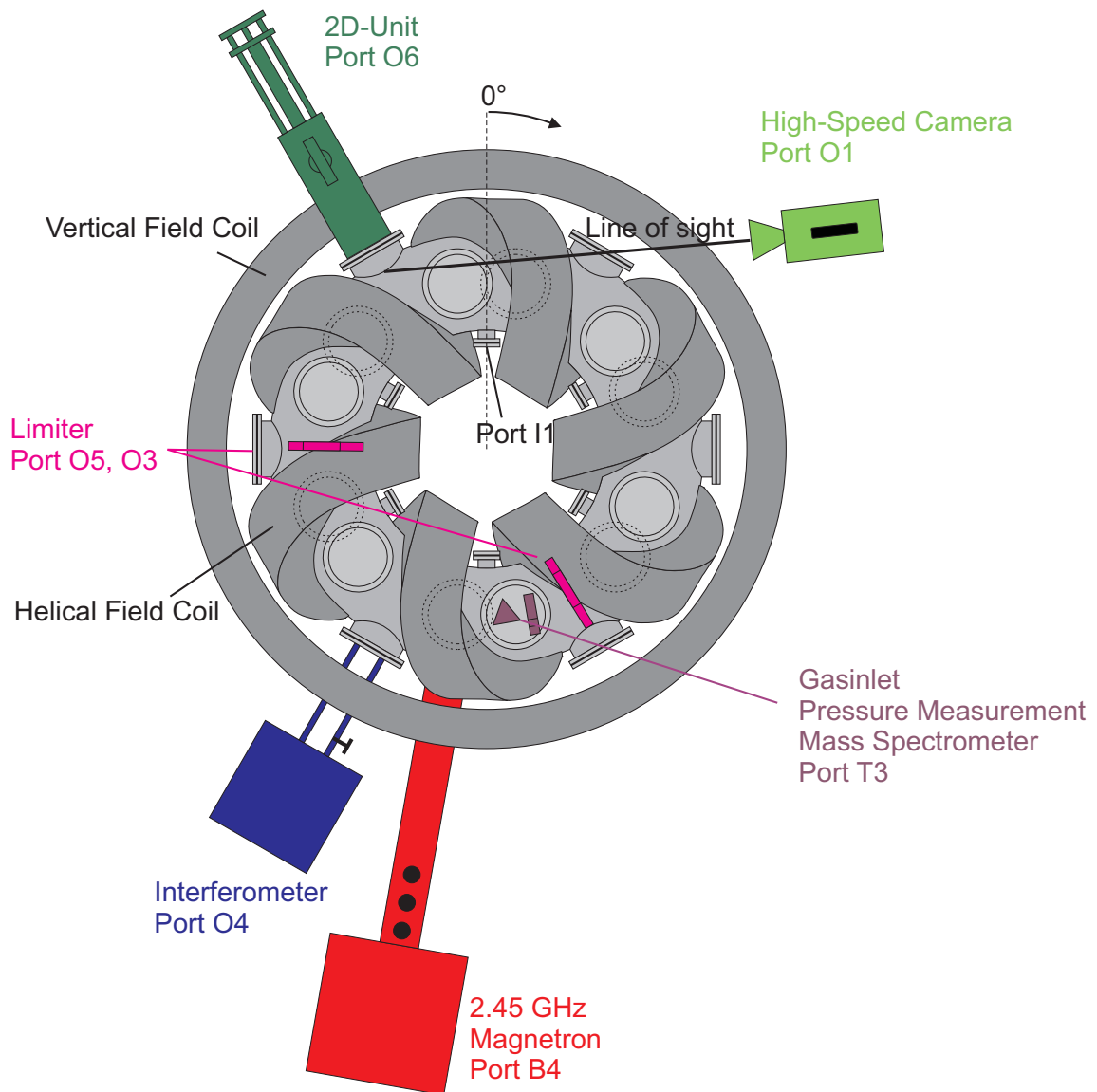
Experiments and diagnostics

4.1 The stellarator TJ-K

The experiment TJ-K is a stellarator with an $l = 1$ helical field coil, which produces a magnetic field with a six-fold toroidal symmetry ($m = 6$). An additional pair of vertical field coils (Helmholtz coils) is used to shape and position the flux surfaces. Originally designed and built at CIEMAT in Madrid as TJ-1U [56–58], the experiment was moved first to Kiel, where it was renamed to TJ-K [59, 60] and later moved to Stuttgart, where it is operated today at the IGVP at the University of Stuttgart. The experiment is shown in Fig. 4.1 as a schematic drawing and in Fig. 4.2 on a photograph.

The stellarator TJ-K features a minor radius of $a = 0.1\,\mathrm{m}$ and a major radius of $R_0 = 0.6\,\mathrm{m}$. After the latest upgrade of the power supply system, a maximum current of $I_\mathrm{c} = 2\,\mathrm{kA}$ allows to reach a magnetic field strength of $B_{\mathrm{t,\,max}} = 500\,\mathrm{mT}$. The location of the flux surfaces can be varied by changing the current ratio r_vh between the currents through the vertical and the helical field coils. The standard value for TJ-K is $r_\mathrm{vh} = 0.57$, which is chosen for all experiments presented in this work.

The plasmas in TJ-K are generated and heated by microwaves. In Ref. [61] an extensive review of the heating schemes employed at TJ-K is given. Three different microwave frequencies are available to heat the plasma corresponding to different characteristic magnetic field ranges. Typical temperatures are $T_e \approx 10\,\mathrm{eV}$ for the electrons and $T_i \approx 1\,\mathrm{eV}$ for the ions [62, 63]. By using different working gases (hydrogen, deuterium, helium, neon, and argon) the ion mass m_i can be varied and, hence, the drift scale

$$\rho_\mathrm{s} = \frac{\sqrt{m_\mathrm{i} T_\mathrm{e}}}{eB}\,. \tag{4.1}$$

In order to study the plasma from the outside, the vacuum vessel has 24 access ports. These access ports allow to position diagnostics inside or close to the plasma or to provide a line-of-sight (LOS) for measurements of the radiation emitted or

Figure 4.1:   *Schematic drawing of the experiment TJ-K showing the vacuum vessel, the magnetic field coils, and the diagnostics employed. The toroidal angle coordinate ϕ is defined as indicated in the figure.*
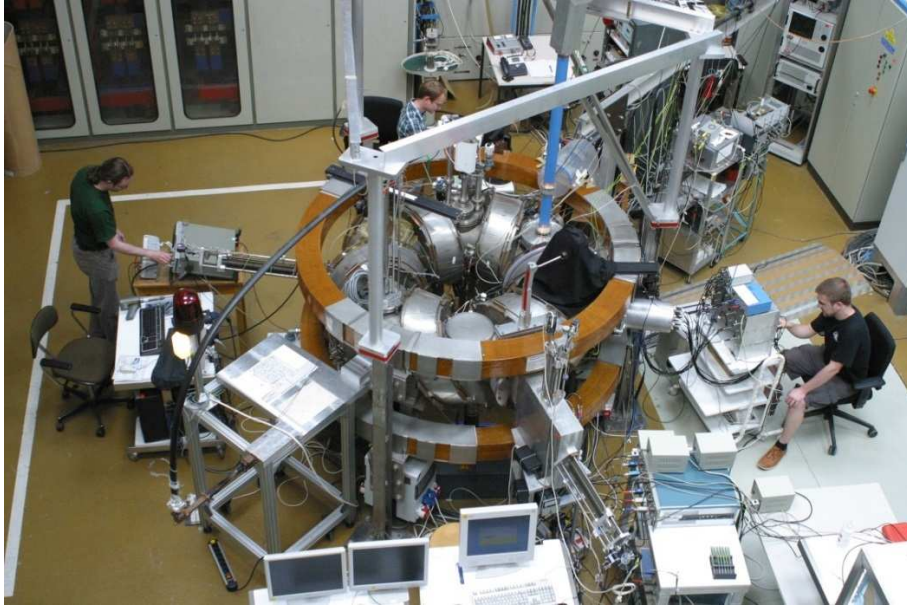
Figure 4.2: *The stellarator TJ-K operated at the IGVP, University of Stuttgart.*

reflected from the plasma, e.g. diagnostics for microwaves or visible light. According to the six-fold toroidal symmetry of the magnetic field coils, the ports are arranged in six identical segments around the torus. Each segment has four ports at different toroidal locations that allow to study the plasma from the top (top port), the bottom (bottom port), the inside of the torus (inner port) and the outside of the torus (outer port). The bottom-, outer-, and top ports are DN 250 ISO-K flanges, while the inner ports are smaller DN 63 ISO-K flanges because of the limited space available at the inside of the torus. For the interpretation of measurements at the different access ports, the shape and position of the magnetic flux surfaces must be known. Poincaré plots of the flux surfaces at arbitrary toroidal positions can be determined with the Gourdon code [64]. Due to the six-fold symmetry of the vessel design and magnetic field the result is the same for all ports of the same type (apart from small imperfections in the magnetic field). The Poincaré plots of the flux surfaces are shown in Fig. 4.3 for the four different types of access ports.

The main subjects of study at TJ-K are plasma turbulence and plasma-microwave interaction, including, but not limited to microwave heating, and the technical realization of microwave heating schemes.

4.1.1 Edge turbulence and blobs in TJ-K

The edge turbulence in TJ-K has been studied extensively in prior experiments. The results that are important for the interpretation of the experiments presented in this work are briefly summarized in this section. Furthermore, results from prior experiments on blobs in the SOL of TJ-K are presented.
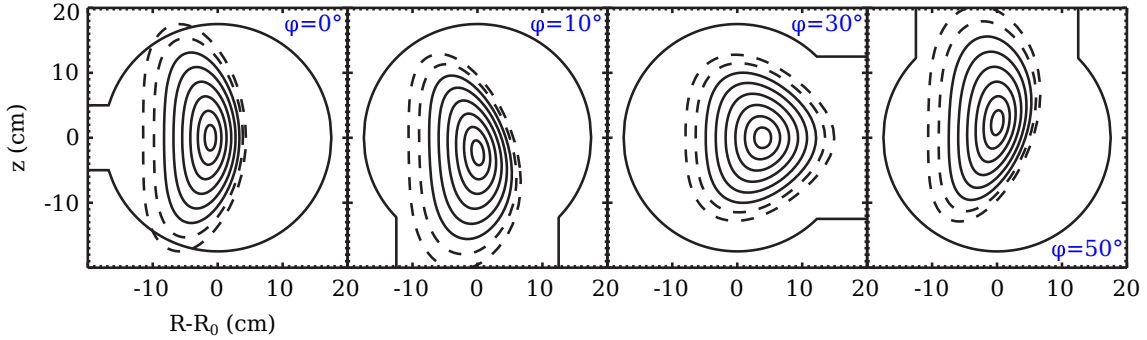
Figure 4.3:   *Poincaré plots of the flux surfaces for the different types of access ports (from left to right): Inner-, bottom-, outer- and top port. ϕ is the toroidal angle according to Fig. 4.1.*

The edge turbulence in TJ-K is dominated by electrostatic drift-wave turbulence. This has been demonstrated by a number of experiments. Indicators for the drift-wave character of observed density and potential fluctuations are cross phases $\alpha^{\Phi,n}$ close to zero [65, 66], a finite parallel wavelength [67, 68], a poloidal propagation of coherent structures in the electron diamagnetic drift direction (EDD) [69], and a scaling of the structure size with the drift scale ρ_s [70–72]. In Refs. [48, 73] it was shown that blobs are generated around the last closed flux surface (LCFS) by coherent structures arising from the drift-wave turbulence. Studies of the waiting-time distribution (WTD, Sec. 5.3) revealed a connection between the typical time scales on which subsequent blobs are generated and the characteristic frequency band of the drift-wave turbulence in TJ-K [74, 75].

4.1.2   Setup of diagnostics at TJ-K

The measurements presented were performed in hydrogen, deuterium, helium, neon and argon discharges with low (70 mT) and high (300 mT) magnetic field strength in order to vary the plasma parameters over a broad range. All discharges were heated with microwaves at 2.45 and 8 GHz for the low field and high field, respectively. To broaden the scrape-off layer (SOL) with constant connection lengths (the length of a field line segment in the SOL between the intersections with in-vessel components like limiter disks or the wall), two limiter disks were introduced. One of the two identical limiter disks was located at port O3 and the other at port O5 (see Fig. 4.1). Fig. 4.4 shows a poloidal cross section of TJ-K at port O6, depicted is the LCFS in the standard setup of TJ-K (dashed line) and the LCFS with limiter disks installed (closed line). A detailed description of the limiter disks can be found in Ref. [73]. From the set of standard diagnostics at TJ-K a pressure gauge at port T3 and a microwave interferometer at port O4 are used for the experiments presented in this work. The blob properties were studied with Langmuir probes and a high-speed camera. A 2D movable probe measured floating potential and ion-saturation
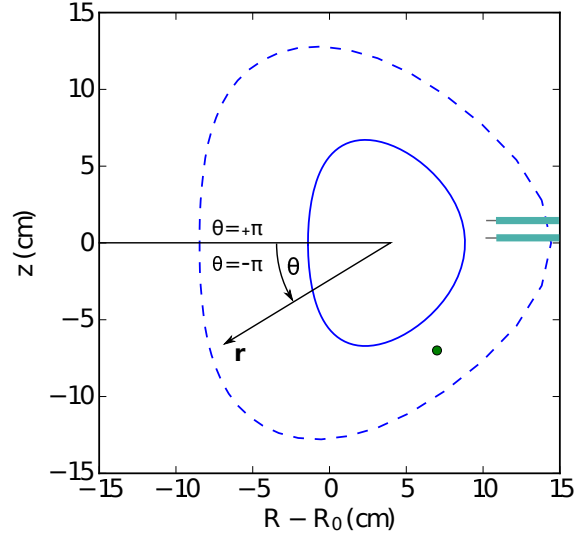
Figure 4.4: *Poloidal cross section of TJ-K at port O6. Shown is the separatrix in the standard setup of TJ-K (dashed line) and with the limiter disks installed (closed line). For the measurements presented, a fixed reference probe was located at $(R - R_0, z) = (7, -7)$. A movable 2-pin probe (right) was used to measure the ion-saturation current $I_{\text{i,sat}}$ and floating potential Φ_{f}. Also shown is the TJ-K definition of the poloidal angle θ.*

current over a whole poloidal cross section of the torus at port O6 with a step size of typically 1 cm in both directions (exceptions noted explicitly). An additional fixed reference probe close to O6 was used as trigger source for conditional averaging (see Sec. 5.1). The reference probe measured the floating potential and was located in the lower outboard side in the SOL region, where the camera detects the majority of blob events [76]. Temperature fluctuations are negligible in TJ-K [77], since the T_{e} profile is relatively flat. Therefore, 2D fluctuation data from plasma potential and density can be deduced from the data. Langmuir probe characteristics were recorded during a radial scan at port O2 in order to obtain the radial profile of the electron density n_{e} and electron temperature T_{e}. Typical values are $n_{\text{e}} \approx 10^{18}\,\text{m}^{-3}$ and $T_{\text{e}} \approx 10\,\text{eV}$. The fast camera observes the plasma almost tangentially at port O6. Details about the optical setup are given in the following section.

4.1.3 Optical setup at TJ-K

The high-speed camera used is a Photron Fastcam SA-5 with a frame rate up to 750 kfps (kilo frames per second). The camera was located close to port O1 and observed the plasma column almost tangential at port O6 (see Fig. 4.1), where the plane of focus was located. The object distance is $g = 2.06\,\text{m}$ and is needed in order to project magnetic field lines or the LCFS to the image data: Since g and the focal length f of the lens system are known, the image distance b can be calculated using

the lens equation

$$\frac{1}{f} = \frac{1}{g} + \frac{1}{b}.$$
(4.2)

With these three quantities the path of a light ray can be traced from the observed plasma volume to the image sensor of the camera (see Fig. 4.5). Since the pixel width of the image sensor of the Photron Fastcam SA-5 is known ($20\,\mu$m), ray tracing is sufficient to determine the position of the pixel that detects a specific light ray.
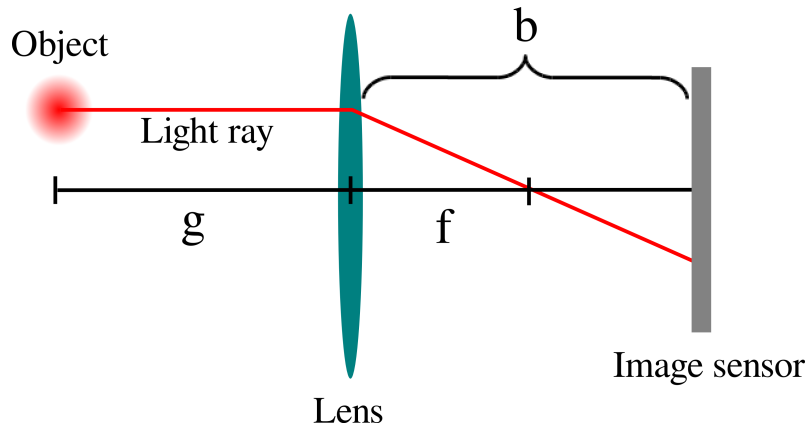
Figure 4.5:   *The position of a pixel on the image sensor that will detect a specific light ray can be calculated if the image distance b and the focal length f are known. Using Eq. (4.2), b can be calculated from f and the object distance g.*

Due to the low temperature, the plasma in TJ-K is not completely ionized and, hence, visual light is emitted by the whole plasma. This allows for measurements in the confinement region and the SOL without neutral gas injection. In contrast to the probe measurement, the 2D fluctuation data are obtained instantaneously over the whole cross section, which allows for a proper statistical treatment of the investigated quantities. To minimize effects due to the integration along the line-of-sight, the depth of focus has to be small. In order to achieve this, a camera lens with focal length $f = 50\,$mm and the aperture ratio $D/f = 0.75$ (D is the effective aperture) was used.

4.2   The tokamak ASDEX Upgrade

The divertor tokamak ASDEX Upgrade is a fusion experiment in Garching near Munich operated by the Max Planck Institute of Plasma Physics (IPP). ASDEX Upgrade went into operation in 1991 as the predecessor of the experiment ASDEX. ASDEX Upgrade is the largest fusion experiment in Germany. Among other research topics ASDEX Upgrade is dedicated to study different first-wall materials under ITER-like plasma conditions [78]. The major radius is $R = 1.65\,$m and the minor

radius is about $a = 0.6\,\mathrm{m}$, depending on the shaping of the plasma. Details about ASDEX Upgrade can be found in Ref. [79].

The experiments presented in this work were all run in the lower single null configuration with a magnetic field strength B_t around $-2.5\,\mathrm{T}$. The toroidal current was $I_\mathrm{p} = 0.8\,\mathrm{MA}$ and the line averaged density n_e was about $7 \cdot 10^{19}/\mathrm{m}^3$. These parameters were chosen to obtain comparable discharges to prior measurements of blob properties in ASDEX Upgrade presented in Refs. [80–82]. A cross section of the experiment can be seen in Fig. 4.6. The flux surfaces are shown in red, the separatrix (the LCFS in a divertor experiment) in blue and the field-of-view (FOV) of the camera is shown as green patch (see Sec. 4.2.2 for details on the optical setup). To make discharges with differently shaped flux surfaces comparable, the poloidal
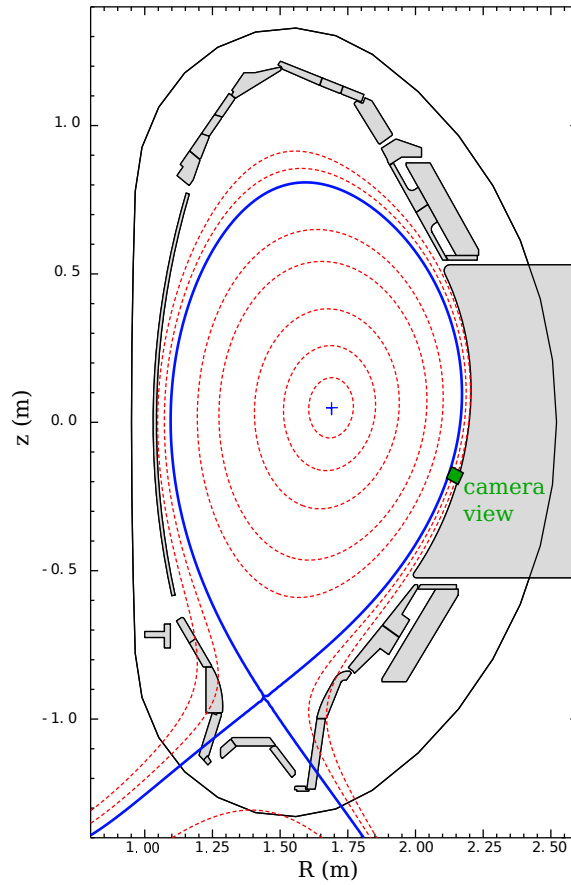
Figure 4.6: *Cross section of the experiment ASDEX Upgrade with magnetic flux surfaces (red), the separatrix (blue) and the field-of-view of the camera (green patch).*

magnetic flux Ψ_θ is used to define a normalized radial coordinate ρ_pol as

$$\rho_\mathrm{pol} = \frac{\Psi_\mathrm{p}(\mathbf{r}) - \Psi_\mathrm{p,0}}{\Psi_\mathrm{p,sep} - \Psi_\mathrm{p,0}} \,, \tag{4.3}$$

where $\Psi_\mathrm{p,0}$ is the poloidal magnetic flux in the center and $\Psi_\mathrm{p,sep}$ the one at the

separatrix. Hence, ρ_{pol} is 0 in the center, 1 at the separatrix, and larger than 1 in the SOL.

4.2.1 Modes of confinement

In the earlier experiment ASDEX the H-mode was discovered in 1982 [83]. If the heating power is increased above a threshold power, which depends on the plasma parameters [84], a sudden increase of the pressure gradient in the edge plasma is observed, which causes higher densities and temperatures in the core (see Fig. 4.7) and the formation of an *edge transport barrier* is observed [85], where the radial electrical field changes drastically over a narrow region in the plasma edge [86]. The initial standard discharge condition is called L-mode (for low confinement) and the condition after the transition is called H-mode (for high confinement). The names refer to the observation that after the *L-H transition* turbulence level in the edge [87] is reduced. This reduction is regarded as the reason for the steepening of the profiles and, hence, the dramatic increase of the confinement. A lot of progress has been made to understand the L-H transition [88], but so far the exact physical interpretation remains an open question. Nevertheless, the H-mode is considered today as a crucial prerequisite for a successful fusion power plant [89].
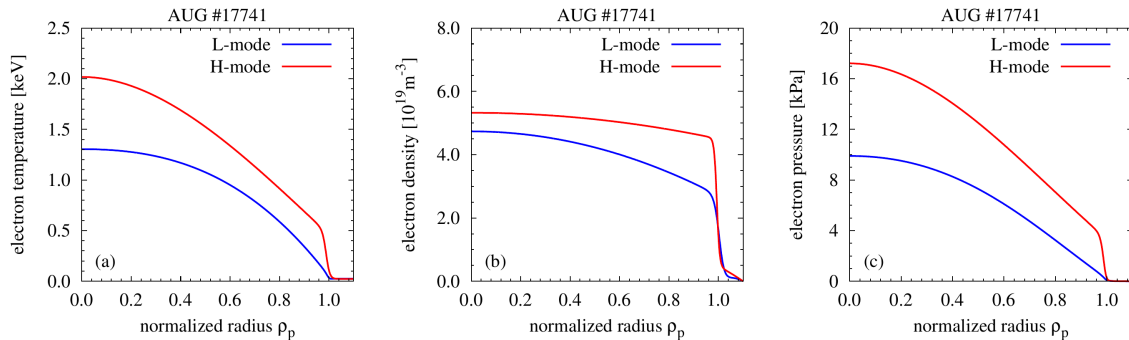
Figure 4.7: *Temperature, density and pressure profiles (from left to right) in L- and H-mode plasmas of ASDEX Upgrade [90].*

A further characteristic of the H-mode is the existence of the so-called *Edge-Localized Modes* [91], a violent instability that leads to a sudden collapse of the steepened H-mode pressure profile and can release a significant fraction of the energy stored in the plasma up to several tens of percent. These energy releases severely deteriorate the condition of the first wall. There are methods to suppress or mitigate ELMs, but a lot of work remains to be done on this [92]. One aspect of the ELM instability is the occurrence of filaments in the SOL that are clearly visible in camera measurements [93]. Since these filaments may have a different origin than the turbulence generated blobs, the camera data are only evaluated in phases where no ELM activity is present (*inter-ELM phases*).

4.2.2 Optical setup at AUG

To study blob properties in the SOL of ASDEX Upgrade, a gas-puff imaging (GPI) setup was designed. GPI is a well established technique in many experiments [94–97]. Usually, a gas puff of deuterium or helium is used to increase the neutral pressure locally. The radiation emitted by the gas cloud as a consequence of collisions of plasma electrons with the neutral gas is observed by a camera. Care has to be taken that the increasing plasma density due to ionization of neutral atoms originating from the gas puff does not change the plasma dynamics.

The fast camera used at ASDEX Upgrade is a Phantom v7.3. The optical setup is described in the following and depicted in Fig. 4.8 (top). To shield the camera from ionizing radiation it is located in a shielding box next to the vacuum vessel. The light emitted by the gas cloud for gas-puff imaging (GPI) is observed via a mirror inside an immersion tube inside of the vacuum vessel. The lens system is located close to the mirror and the resulting image is focused on one end of a coherent fibre bundle, which transmits the image to the shielding box. In the shielding box, the fast camera observes the other end of the coherent fibre bundle with a second lens system to capture the image. Using this optical setup, an image of the illuminated vessel interior was captured. By comparing it to a 3D model of the vessel interior, the camera view can be reconstructed, which is a prerequisite to measure size and velocity of light emitting structures in the laboratory frame. This is shown in the bottom of Fig. 4.8.

4.2.3 Experiments at AUG

Like most of the current fusion experiments, ASDEX Upgrade can be operated in two confinement regimes, the L- and the H-mode (Sec. 4.2.1). One of the main goals of the experiments performed at ASDEX Upgrade in the course of this work was to study differences in the blob dynamics in L- and H-mode. Hence, the discharges start with a purely ohmically heated L-mode phase, before additional electron cyclotron resonance heating (ECRH, see Ref. [98]) triggers the L-H transition. In Fig. 4.9 the time traces of the line averaged electron density n_e together with the heating power and the deuterium puff rate are shown. In the H-mode the blob properties are only studied in phases where no ELM activity is present. The phases of ELM activity were determined from D_α light emission from the divertor, which increases significantly in intensity during ELM activity.

4.3 Fast imaging diagnostics

State-of-the-art commercially available digital cameras reach very high frame rates in the range of one million frames (images) per second. These cameras are often called high-speed or fast cameras. The upper limit for the frame rate is currently determined by the time needed to read-out the image sensor and the limited data
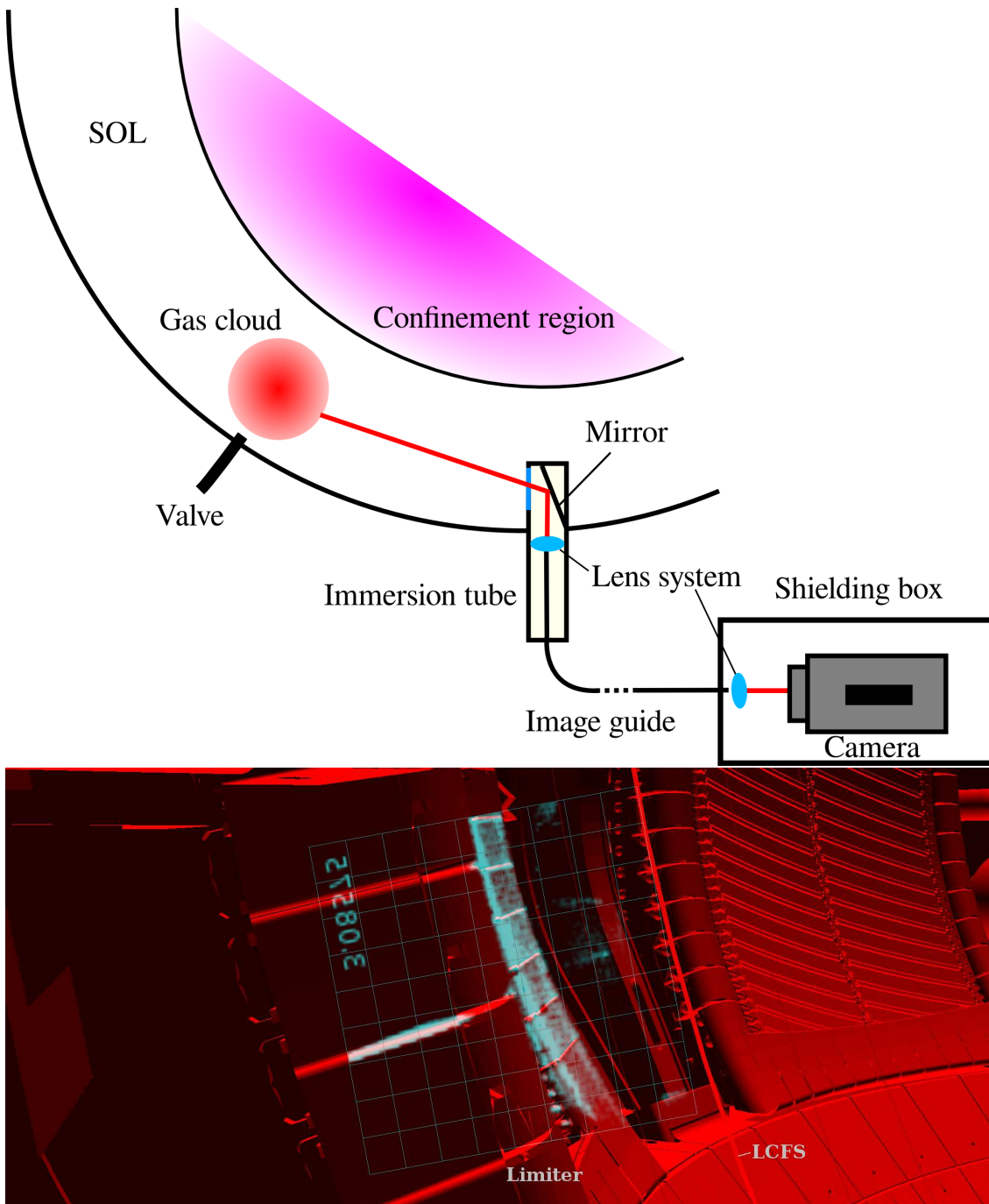
Figure 4.8: *The optical setup at ASDEX Upgrade is illustrated in the top (see the text for a detailed description). In the bottom an image of the illuminated vessel interior (without plasma) is shown (blue square). In order to reconstruct the camera view, the in-vessel components captured in the image data are matched to a 3D model of the vessel interior (red background image).*
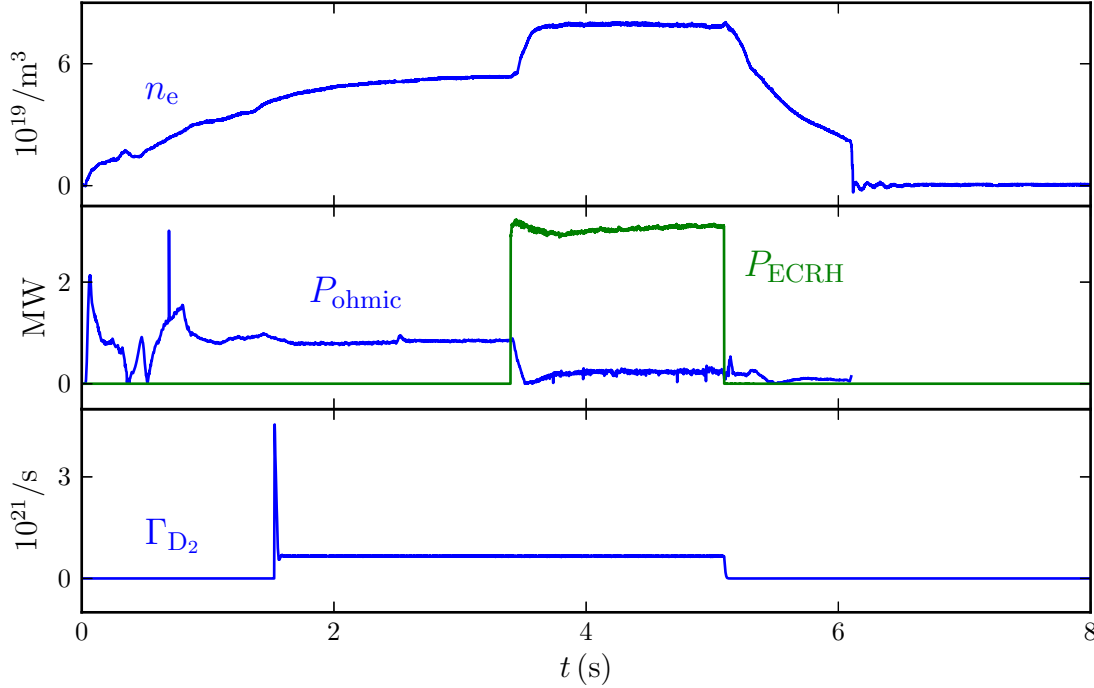
Figure 4.9: *Time traces of the line averaged core density n_{e0} (top), the ohmic and ECRH heating power (middle), and the deuterium puff rate (bottom) for #28769.*

throughput of the read-out electronics. To meet these constraints and in order to record sufficiently high signal strengths in the short exposure times, fast cameras usually have an image sensor with a relatively low resolution and a large pixel size compared to regular digital cameras. The fast camera employed at TJ-K, a Photron Fastcam SA5, features a CMOS image sensor [99] with 1024×1024 pixels and a pixel size of $20\,\mu\text{m}$. Due to the limited data throughput, however, the full resolution is only available for low frame rates. For high frame rates, only a fraction of the image sensor, the *active region of interest*, is read out. Hence, designing a fast imaging experiment always involves to find the best trade-off between time resolution (frame rate), spatial resolution (region of interest), and signal-to-noise ratio (since the exposure time is limited by the inverse frame rate). The ascertainment of the corresponding camera settings for the fast imaging experiments at TJ-K is shown in Sec. 6.2.

4.3.1 Image noise

There are two main sources for noise in the image data recorded by digital cameras [100]: The so-called *photon shot noise* and the electronic noise due to the technical realization of digital cameras. Typically, the camera specific noise is dominated by *dark noise* and *read noise*. The photon shot noise is caused by statistical fluctuations in the amount of incident photons. Hence, photon shot noise is due to

the quantum properties of light and cannot be eliminated. Dark noise is caused by electrons created in the silicon lattice of the image sensor due to thermal effects, while read noise arises in the process of quantifying and digitalizing the charge accumulated by a certain pixel due to light exposure. The noise characteristics of the different sources are reflected in the corresponding variances σ_i^2. The photon arrival leading to the shot noise is described by a Poisson process, which means that the standard deviation $\sigma_{\mathrm{p}} = \sqrt{N}$, where N is the amount of incident photons. Dark and read noise do not depend significantly on the signal strength [101], hence σ_{d} and σ_{r} are constants. Therefore, for intensities above a certain threshold, the image noise is dominated by the shot noise:

$$\sigma_{\mathrm{tot}} = \sqrt{\sigma_{\mathrm{d}}^2 + \sigma_{\mathrm{r}}^2 + \sigma_{\mathrm{p}}^2} = \sqrt{c_1 + N} \overset{N \gg c_1}{\approx} \sqrt{N} \,, \tag{4.4}$$

with the constant $c_1 = \sigma_{\mathrm{d}}^2 + \sigma_{\mathrm{r}}^2$. In practice, however, the number of incident photons N is unknown and the quantity of interest is the *bit count* or *count rate* I in the resulting image data. Since the count rate is proportional to the number of incident photons (see Ref. [99] and Sec. 6.1.1), the standard deviation of I can be written as

$$\tilde{\sigma}_{\mathrm{tot}} \approx \sqrt{\tilde{c}_1 + \tilde{c}_2 I} \overset{I \gg 1}{\approx} \sqrt{\tilde{c}_2 I} \,. \tag{4.5}$$

The constants $\tilde{c}_1$ and $\tilde{c}_2$ are determined experimentally in Sec. 6.1.2. It can be seen from Eq. (4.5) that the image noise scales as $\sqrt{I}$, while I is proportional to N. Hence, the relative importance of the noise decreases with longer exposure time. This is quantified by the signal-to-noise ratio (SNR): Let μ a signal recorded by the camera, then the SNR is defined as [101]

$$\mathrm{SNR} = \mu / \tilde{\sigma}_{\mathrm{tot}} \,. \tag{4.6}$$

The experimentally motivated *Rose criterion* [102] for image data states that a feature can reliably be identified as *real* (i. e. not caused by noise) if the SNR ≥ 5.

4.3.2   Visual light emitted by the TJ-K plasma

The radiation emitted by the TJ-K plasma in the visible spectrum is dominated by line radiation, as was shown in Ref. [103]. Low temperature plasmas with $T_{\mathrm{e}} \lesssim 10\,\mathrm{eV}$ typically feature low degrees of ionization (e. g. in the edge and SOL of TJ-K typically 10–30 %) and, hence, a background density of neutral atoms or molecules n_{n} larger or comparable to the electron density n_{e} is present. The neutrals can be excited by collisions with the plasma electrons and absorption of photons with the excitation energy. The de-excitation happens mainly due to photon emission, electron impact de-excitation, and ionization. Radiation models that include these mechanisms, and eventually further higher-order processes (see Ref. [104]), are called collisional-radiative models. The emitted light intensity of a specific emission line can then be calculated from a differential equation balancing all processes that either excite or

de-excite a specific energy level. In the most general case, the light intensity emitted from that emission line is [104]

$$I \propto n_\mathrm{n} n_\mathrm{e}^\alpha T_\mathrm{e}^\beta, \tag{4.7}$$

with the neutral and electron density n_n and n_e and the electron temperature T_e. The non-linear dependence on n_e arises from the fact that the population density of the energy levels itself depends on n_e. Both cases $\alpha = 1$ (e. g. in Ref. [105]) and $\alpha \neq 1$ (e. g. in Refs. [95, 106]) are observed in different experiments. In the experiments performed at TJ-K the full visible spectrum is observed and, hence, the light of different spectral lines is captured. As a consequence, the exact n_e dependence of the emitted light intensity is not clear. That the size of density structures can nevertheless be deduced from the image data is shown in Sec. 6.3.4.

4.4 Langmuir probe diagnostics

Langmuir probes [107–109] are electrostatic probes that are commonly used to diagnose low-temperature plasmas. Under certain circumstances that are discussed below they allow measurements of the local electron density n_e, electron temperature T_e, and *floating potential* ϕ_f. Typically, the Langmuir probe consists of a tungsten wire, which is insulated by e. g. a ceramic tube apart from a small probe tip of a few millimeters length, which is exposed to the plasma. Electrons and ions from the plasma flow to the probe tip, creating an electron and ion current (I_e and I_i). These currents can be influenced by applying a bias voltage U to the probe and they further depend on the plasma parameters. The dependence of the net current drawn by the Langmuir probe on the bias voltage is called the *characteristic* of the Langmuir probe. Figure 4.10 shows an illustration of this characteristic for different probe tip geometries (spherical, cylindrical and planar). The characteristic consists of three distinct regions with different U dependence that are discussed in the following. In region A, the probe is biased strongly negative and, hence, repels the electrons from the plasma ($I_\mathrm{e} = 0$) and only ions are flowing to the probe. Since the plasma shields the probe (see Sec. 3.1), the amount of ions that can reach the probe is limited and the current drawn by the probe is limited by the ion-saturation current $I = I_\mathrm{i,sat}$. Assuming a Maxwellian energy distribution and a collisionless unmagnetized plasma, $I_\mathrm{i,sat}$ can be calculated as [31]

$$I_\mathrm{i,sat} = 0.61 \cdot e n_\mathrm{e} S \sqrt{\frac{T_\mathrm{e}}{m_\mathrm{i}}}. \tag{4.8}$$

Here, e is the electron charge, n_e the electron density, S the effective probe surface, T_e the electron temperature, and m_i the ion mass. When the bias voltage is increased (region B), ions can still reach the probe, but more and more electrons are collected, depending on their energy. Hence, in region B the current drawn by the probe is

$$I = I_\mathrm{i,sat} \left[1 - \exp\left(-\frac{e(\phi_\mathrm{f} - U)}{T_\mathrm{e}} \right) \right]. \tag{4.9}$$
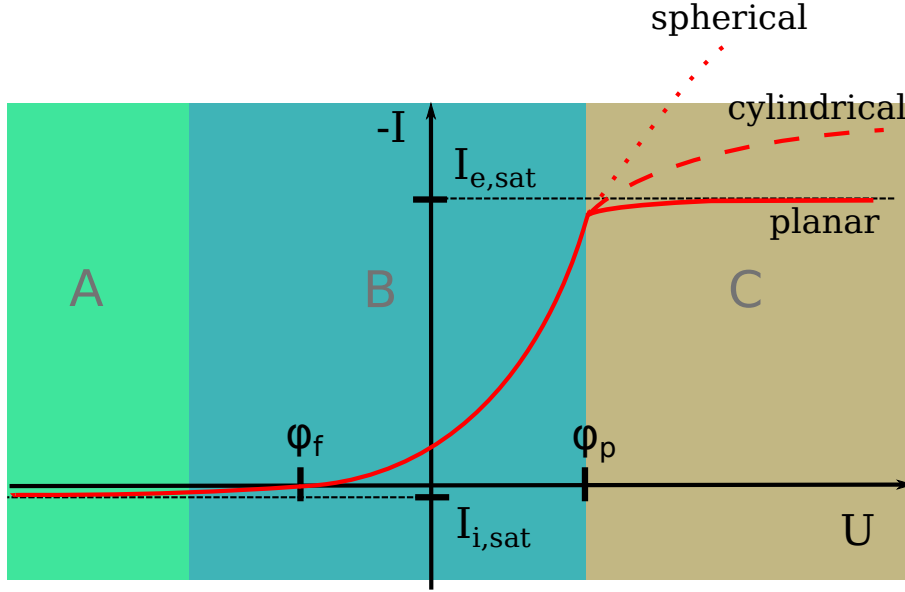
Figure 4.10: *Illustration of the U-I characteristic of a Langmuir probe with planar, cylindrical, or spherical shaped probe tip with $I_{e,sat}$ and $I_{i,sat}$ the electron- and ion-saturation current and the floating and plasma potential Φ_f and Φ_p.*

At the floating potential

$$\phi_f = \phi_p + \frac{T_e}{e}\ln\left(0.61\sqrt{2\pi}\frac{m_e}{m_i}\right), \tag{4.10}$$

I_e and I_i exactly cancel each other out to $I = 0$. A probe without any external bias will be charged by the plasma until Φ_f is reached. This is due to the high mobility of the electrons, which reach the probe before the heavier ions. As a consequence, the negatively charged probe attracts ions and repels electrons until $I_e = -I_i$. If the probe bias reaches the plasma potential ϕ_p, the probe repels the ions and attracts the electrons. Hence, in region C $I_i = 0$ and the electron current reaches the electron-saturation current $I = I_{e,sat}$ with

$$I_{e,sat} = -en_e S\sqrt{\frac{T_e}{2\pi m_e}}. \tag{4.11}$$

For non-ideal probes, however, I_e also depends on the probe geometry and saturation does not occur as depicted in Fig. 4.10.

The Langmuir probe characteristic can be measured by sweeping the bias voltage and measuring the current drawn. By fitting the measured characteristic to Eq. (4.9), n_e, T_e and ϕ_f can be obtained. Since the sweeping of the bias voltage requires time and should preferably be repeated several times to increase the quality of the fit, this method is especially useful to measure average values. In order to measure time dependent phenomena like fluctuations, e. g. due to turbulence, a

fixed bias voltage is chosen. Ion-saturation current fluctuations $\tilde{I}_{\mathrm{i,sat}}$ are measured by applying a negative voltage to the probe (at TJ-K typically $-90\,\mathrm{V}$) and floating potential fluctuations $\tilde{\phi}_{\mathrm{f}}$ are measured with no external bias voltage is applied. If temperature fluctuations $\tilde{T}_{\mathrm{e}}$ are negligible (as in TJ-K [77]), $\tilde{I}_{\mathrm{i,sat}}$ is proportional to density fluctuations $\tilde{n}_{\mathrm{e}}$ and $\tilde{\phi}_{\mathrm{f}}$ agrees with plasma potential fluctuation $\tilde{\phi}_{\mathrm{p}}$. In magnetized, collisional plasmas, the numerical values in Eq. (4.8) vary. Hence, to deduce $\tilde{n}_{\mathrm{e}}$ from $\tilde{I}_{\mathrm{i,sat}}$, it is rewritten as

$$I_{\mathrm{i,sat}} = Cn\,, \tag{4.12}$$

where the constant C is determined by comparison with the line-averaged density obtained by interferometry [73]. Note that this equation is only valid for constant T_{e} and that the numerical value of C depends on the ion species.
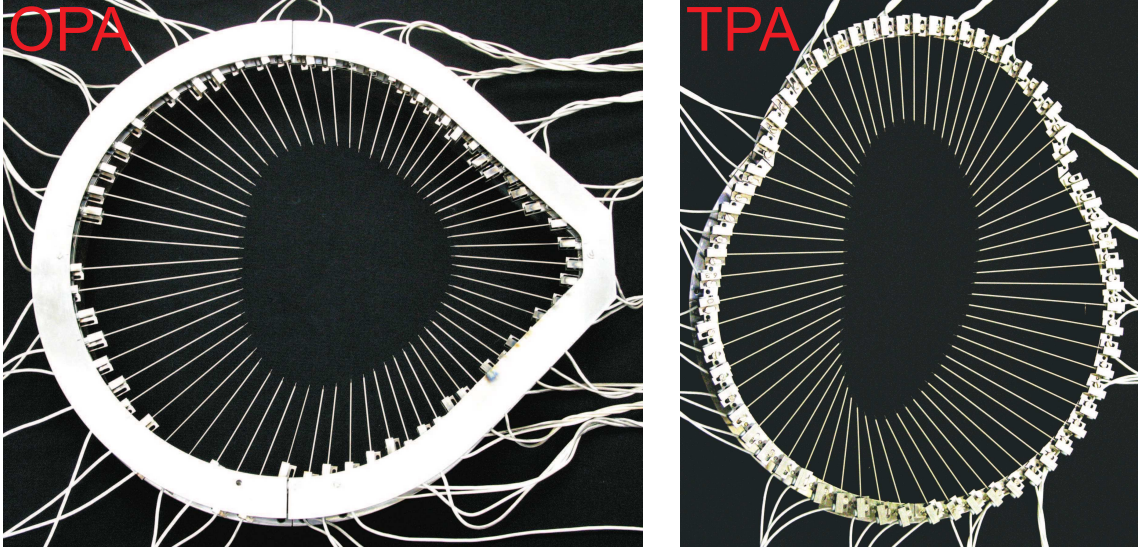
4.4.1 Poloidal probe arrays

In the low temperature plasmas of TJ-K, Langmuir probes show no severe degradation even after being exposed to the plasma for several hours. Since the discharges last between 1 and 45 minutes, Langmuir probes are ideally suited to measure $\tilde{I}_{\mathrm{i,sat}}$ and $\tilde{\phi}_{\mathrm{f}}$ at arbitrary positions in the plasma with a high resolution in both space and time. This facilitates the usage of multi-probe arrays in TJ-K.

In Refs. [110, 111], two poloidal probe arrays (PPA) are introduced that consist of 64 Langmuir probes each. The probes of the outer port array (OPA) are aligned to a flux surface (assuming $r_{\mathrm{vh}} = 57\,\%$) at the outer port position and the probes of the top port array (TPA) are aligned to the same flux surface but at the top port position (see Fig. 4.11). Each probe can either be biased or not to measure the ion-saturation current $I_{\mathrm{i,sat}}$ or floating potential ϕ_{f}, respectively. As was shown in the previous section this allows to measure fluctuation in density $\tilde{n}_{\mathrm{e}}$ and plasma potential $\tilde{\phi}_{\mathrm{p}}$. A typical application is the measurement of $I_{\mathrm{i,sat}}$ or ϕ_{f} with all probes. Since the probes of the arrays are aligned to a flux surface it is possible to study the poloidal and parallel dynamics of turbulent structures e.g. by means of cross-correlation analysis (Sec. 5.2). Another application choses a setting, where the probes are measuring $I_{\mathrm{i,sat}}$ and ϕ_{f} alternately so that every probe measuring $I_{\mathrm{i,sat}}$ is surrounded by two probes measuring ϕ_{f} and vice versa. The probes measuring ϕ_{f} (e.g. probe number i and $i+2$) can be used to assess the fluctuations in the poloidal electrical field $\tilde{E}_{\theta}$ in between, i.e. at the position of probe $i+1$:

$$\tilde{E}_{\theta} = -\nabla_{\theta}\tilde{\phi}_{\mathrm{p}} \approx \frac{\tilde{\phi}_{\mathrm{f}}^{i+2} - \tilde{\phi}_{\mathrm{f}}^{i}}{2\delta}\,, \tag{4.13}$$

with the probe distance δ. Since the probe $i+1$ measures $\tilde{I}_{\mathrm{i,sat}}$, the turbulent particle transport Γ (see Sec. 2.1) can be calculated as

$$\Gamma := \langle \tilde{n}\tilde{v}_r \rangle_t = \left\langle \tilde{n}\frac{\tilde{E}_{\theta}}{B} \right\rangle_t \propto -\left\langle \tilde{I}_{\mathrm{i,sat}}\frac{\tilde{\phi}_{\mathrm{f}}^{i+2} - \tilde{\phi}_{\mathrm{f}}^{i}}{B2\delta} \right\rangle_t . \tag{4.14}$$

Figure 4.11: *Photograph of the outer port array (OPA, left) and the top port array (TPA, right) consisting of 64 Langmuir probes each aligned on a flux surface [110].*

Here, $\tilde{v}_r$ is expressed as the $\mathbf{E}_\theta \times \mathbf{B}$ drift velocity. Further details on how to evaluate Eq. (4.14) can be found in Ref. [110].

When the limiters are installed, the field lines that cross the probe arrays intersect the limiters and, hence, the probes are located in the SOL. In the frame of a bachelor's thesis [112], such a configuration was used to study blob properties in the SOL. In the present work the data acquired in Ref. [112] are further analyzed with respect to turbulent transport and the 3D structure of the blob filaments. The experimental setup together with the results is presented in Ch. 7.

4.4.2 Sheath current probe

In Sec. 3.5 it is shown that currents can flow parallel to the magnetic field along blob filaments. If the parallel extension of the blob filament is limited by plasma facing components (e. g. the wall or a limiter), the parallel currents enter the sheath where the current circuit is closed. In Ref. [55] it is shown that in the vicinity of a limiter, currents parallel to the magnetic field lines can be measured with a single-sided Langmuir probe. In order to achieve this, the probe is positioned near the limiter and oriented perpendicular to the field lines. Furthermore, the probe potential is kept as close as possible to the limiter potential. Therefore, a current that would flow to the sheath of the limiter takes the alternate current path along the probe and the current density parallel to the field line $j_\parallel$ is

$$j_\parallel = I_0/A_{\mathrm{LP}} \,, \tag{4.15}$$

where I_0 is the total current collected by the probe and $A_{\mathrm{LP}} = 6.4 \pm 0.4 \, \mathrm{mm}^2$ is the area of the probe surface. To verify that this setup indeed measures a parallel

current to the limiter and that this current is not altered by the probe itself, Ref. [55] presents a comparative measurement of the described probe setup and a specially designed current probe. This current probe consists of an array of three tri-axial pick up coils (indexed by $i = 1, 2, 3$) that measure the fluctuating magnetic field components $\tilde{B}_{z,i}$ and $\tilde{B}_{r,i}$. The current is obtained by integrating Ampere's law, $\tilde{\mathbf{j}} = 1/\mu_0 \cdot \nabla \times \tilde{\mathbf{B}}$, over the triangular surface enclosing the three probes, arranged in a plane perpendicular to the magnetic field. For both measurement techniques, a qualitative and quantitative agreement has been obtained. This result indicates that the single-sided Langmuir probe indeed can be used to measure parallel currents in blob filaments.

In the frame of a bachelor's thesis at TJ-K [36], a 3-pin probe has been designed and built to measure the ion-saturation current, the parallel blob current and the floating potential simultaneously. Two of the probe tips are regular Langmuir probes, while the third one is a single-sided Langmuir probe that is connected to the limiter. The basic setup and probe geometry are displayed in Fig. 4.12, further details can be found in Ref. [36].
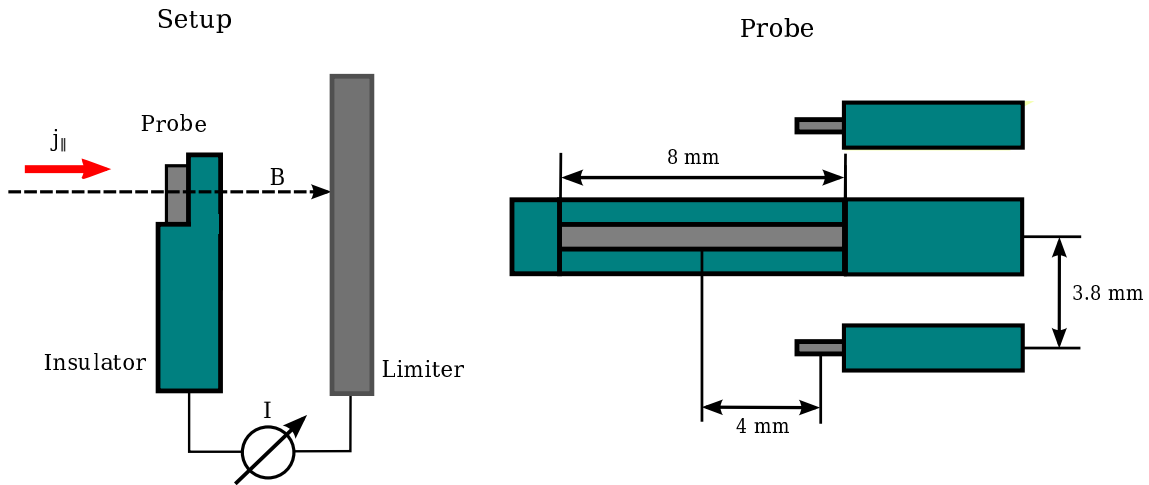
Figure 4.12: *Illustration of the setup and the probe to measure parallel currents in the vicinity of the limiter.*

Chapter 5

Data analysis

5.1 Conditional averaging

The conditional averaging technique is used to study the evolution of coherent structures [113]. In a reference signal $\tilde{x}(t)$, with a sampling interval of Δt, large fluctuation amplitudes are used as trigger events $(\tilde{x}(t_i) \geq x_0 > \tilde{x}(t_i - \Delta t))$ at times t_i. A time window $\tau \in [-T/2, T/2]$ of fixed length T is stored from the same or another signal $\tilde{y}(t)$ around each trigger event t_i. From all subsequences, the average is calculated for each time lag τ resulting in the conditional average (CA) $y_c(\tau)$ of the signal $\tilde{y}(t) = y_c(t) + y_n(t)$ as the coherent contribution while incoherent noise $y_n(t)$ cancels. With the CA technique, 2D resolved measurements are possible by using a fixed reference probe and a movable probe, which scans a poloidal cross section of the plasma [114]. By combining the CAs for every probe position, the 2D time resolved CA is obtained.

5.2 Cross correlation

The cross-correlation function (CCF) is used to quantify the similarity of two time dependant mean free $(\langle \cdot \rangle_t = 0)$ signals $\tilde{u}(t)$ and $\tilde{v}(t)$ as a function of the time lag τ between the two signals. The CCF is defined as

$$C_{\tilde{u},\tilde{v}}(\tau) = \frac{\langle \tilde{u}(t)\tilde{v}(t + \tau)\rangle}{\sigma_u \sigma_v} \,, \tag{5.1}$$

with the standard deviations σ_u and σ_v of the respective signal. The CCF is defined on a range of $[-1, 1]$, where high values indicate a large similarity of the signals, high negative values indicate a high similarity of $u(t)$ and $-v(t)$, called *anti-correlation*, and values close to zero indicate uncorrelated signals. In this work the cross-correlation function is used to detect turbulent structures that extend between two probes connected by a field-line segment (see Sec. 7.1.3).

5.3   Waiting-time distribution

For events repetitive in time, where periodicity is not required, the waiting-time distribution (WTD) can be defined. Every event i has an occurrence time t_i and the waiting time t_w is defined as the time interval between two subsequent events:

$$t_\mathrm{w} = t_{i+1} - t_i \,. \tag{5.2}$$

The WTD is the distribution function that determines the probability of an event to occur with a waiting time t_w in the time interval $[n\Delta t, (n+1)\Delta t)$ with the natural number n and a time bin width Δt. In order to approximate the WTD from experimental data, it is determined how often a t_w is observed in the time interval $n\Delta t \leq t_\mathrm{w} < (n+1)\Delta t$. Signals which are dominated by periodic events show a WTD dominated by one or more peaks corresponding to the period of the signal, while broad WTDs indicate random events and a process without a memory.

In the WTD analysis of the camera data (Sec. 8.1), the occurrence time t_i of a structure is defined as the time when the count rate in a small predefined area of the image reaches its maximum during an ongoing event.

5.4   Pulsed-Light Velocimetry

Pulsed-Light Velocimetry (PLV) [115] is used to deduce velocities from image data. The main idea is to define *regions* in the image data and represent the regions by *markers* at distinct locations in the image. By recognizing a specific region in two or more pictures over a time interval of Δt, the *velocity* of this region can be obtained by tracking the position $\mathbf{x}$ of the representative marker. The velocity $\mathbf{u}$ is defined as

$$\mathbf{u}(\mathbf{x}, t) = \frac{\Delta \mathbf{x}(\mathbf{x}, t)}{\Delta t} \,. \tag{5.3}$$

Depending on the lifetime of the chosen regions and their typical number per image different methods for the identification and recognition of these regions exist. A common realization of Pulsed-Light Velocimetry is to add tracer particles to the system. If the trajectory of the particles is determined by a flowing quantity in the system, the respective flow field can be reconstructed by tracking these particles. If the amount of tracer particles is small enough so that their images do not overlap, single particles can unambiguously be identified in any image. This special case is called *Particle Image velocimetry* (PIV). If the number of particles per unit cell in the image data is small, the *nearest neighbour* approximation can be used, where particles are paired with the nearest neighboring particle in the subsequent image. In its mathematical representation, particle i in an image at time t is recognized as particle j from all particles k in the subsequent image at $t+1$ if for their spatial distance $\Delta_{i,j}$ holds:

$$\Delta_{i,j} = \|\mathbf{X}_{j,t+1} - \mathbf{X}_{i,t}\| = \min_k \|\mathbf{X}_{k,t+1} - \mathbf{X}_{i,t}\| \,. \tag{5.4}$$

The velocity of particle i at time t can then be determined by Eq. (5.3). Since in this case single particles are tracked, this method is also called *Particle Tracking Velocimetry* (PTV). In the edge and SOL of TJ-K, the number of simultaneously visible quasi-coherent structures is small enough to justify the use of PTV.

5.5 Moment method

If the size of a particle image for PTV is of the order of the pixel size, it is easy to determine the position of this particle. However, the measured velocity for that particle may be influenced by *pixel locking*. Pixel locking describes the phenomenon, that measured positions are concentrated at certain favored positions with respect to the pixel edges. The simplest example is a particle, which has an image that fits into one single pixel [116]. The location of this particle can only be determined with an accuracy of the pixel width, which leads to discrete velocity values. If the image of a particle is larger than one pixel, the location of the particle can be determined with sub-pixel precision by using the *moment method* summarized below.

The first step of the moment method is to decide which pixels image the particle. The particle itself is detected by choosing a threshold intensity I_{th} and searching the image data for pixel $(x_p,\ y_p)$ that exceed this threshold. All pixels around $(x_p,\ y_p)$ with a count rate of at least $I \geq I(x_p, y_p)/2$ are considered as part of the imaged structure. The next step is to determine the amplitude weighted center of the structure. In analogy to mass distributions in classical mechanics this is called the *center of mass* (COM) of the intensity structure and is defined as [116]

$$\mathbf{R_{cm}} = \frac{\sum_i \mathbf{R}_i I_i}{\sum_i I_i}\,,\tag{5.5}$$

where $\mathbf{R}_i$ is the position of pixel i and I_i is its count rate.

The moment method helps further to fit an ellipse to the intensity structure. Since the geometrical parameters of the ellipse are obtained directly from the fitting algorithm they can be used to describe the shape and location of the object [117]. An often applied fitting algorithm is the reconstruction of the *ellipse of inertia*, which employs the image moments: The $(p+q)$th order two-dimensional geometric moment of the intensity function $I(x,y)$ of a digital image is defined as [117]

$$m_{pq} = \sum_{\xi} x^p y^q I(x, y)\,.\tag{5.6}$$

ξ is the image region for which the image moments are evaluated, i.e. the region representing the analysed object. The center of mass position can be expressed in terms of the geometric moments (compare Eq. 5.5):

$$\mathbf{R}_{\text{cm}} = \begin{pmatrix} m_{10}/m_{00} \\ m_{01}/m_{00} \end{pmatrix}\,.\tag{5.7}$$

To characterize the shape of an intensity structure in the image it is useful to transform the image to a binary image, i. e. all pixels which image the structure are set to one, while all other pixels are set to zero. Then Eq. (5.6) simplifies to

$$\tilde{m}_{pq} = \sum_{\xi} x^p y^q \,, \tag{5.8}$$

which is the defining equation for the so-called *silhouette moments* $\tilde{m}_{pq}$. In analogy to the center of mass, the silhouette moments define the *centroid* of the structure

$$x_c = \frac{m_{10}}{m_{00}}, \; y_c = \frac{m_{01}}{m_{00}} \,. \tag{5.9}$$

The silhouette moments itself have no clear geometrical interpretation since they are not translation invariant. Therefore, the *central moments* are defined with respect to the object's centroid

$$\mu_{pq} = \sum_{\xi} (x - x_c)^p (y - y_c)^q \,. \tag{5.10}$$

Using these moments, the *ellipse of inertia* is defined with the major and minor semi axes (w, l) and the angle θ describing the orientation of the major axis. They are [117]

$$w = 2\sqrt{\frac{I_1}{\mu_{00}}}, \qquad l = 2\sqrt{\frac{I_2}{\mu_{00}}}, \qquad \theta = \frac{1}{2}\arctan\left\{\frac{2\mu_{11}}{\mu_{20} - \mu_{02}}\right\}, \tag{5.11}$$

with

$$I_1 = \frac{(\mu_{20} + \mu_{02}) + \left[(\mu_{20} - \mu_{02})^2 + 4\mu_{11}^2\right]^{\frac{1}{2}}}{2}\,, \tag{5.12}$$

$$I_2 = \frac{(\mu_{20} + \mu_{02}) - \left[(\mu_{20} - \mu_{02})^2 + 4\mu_{11}^2\right]^{\frac{1}{2}}}{2}\,. \tag{5.13}$$

5.6   Object recognition

Turbulent structures in the edge and SOL are captured by the camera as more or less elliptical shaped structures. Typical detection rates of similar events are in the range of a few thousand blobs per second together with a comparable number of density structures in the edge arising from drift-wave turbulence. Hence, an object recognition method is needed to detect these structures, distinguish between blobs and the coherent structures in the edge and measure their location and size:

In a first step, the mean value $\langle I \rangle$ is calculated for every pixel (x, y) and subtracted from the image data to obtain the intensity fluctuations (here intensity refers to the count rate of the pixel)

$$\tilde{I}(x,y) = I(x,y) - \langle I \rangle(x,y) \,. \tag{5.14}$$

The characteristic amplitudes of the observed intensity fluctuations change depending on the location of the experiment that is imaged due to variations in the background electron and neutral density (n_e and n_n). In order to make the intensity fluctuations comparable across the whole image, normalized intensity fluctuations $\tilde{I}_n$ are defined, where the fluctuations are normalized pixelwise to the mean value

$$\tilde{I}_n(x,y) = \frac{I(x,y) - \langle I \rangle(x,y)}{\langle I \rangle(x,y)}.$$

(5.15)

It is demonstrated in Sec. 6.3.4 that the structure sizes determined from $\tilde{I}_n$ indeed represent the size of the density perturbations.

In a second step the data is searched pixelwise for intensity fluctuations larger than the standard deviation $\sigma(x,y)$. These fluctuations are either caused by structures in the plasma or by image noise. To deal with the image noise an area threshold of n pixels is introduced: For every detected local fluctuation maximum $\tilde{I}_{n,max}$ detected at pixel (x_{max}, y_{max}) the surrounding area of this pixel is analyzed. A fluctuation maximum is considered as *real* (i. e. not noise) if it is surrounded by a cluster of at least n directly connected pixels that fulfill the criterion given in Sec. 5.5. The area threshold n can be small and is determined by starting with $n = 1$ and increasing it stepwise until no obvious noise events are triggering the object recognition. For the analyses in this work, a value of $n = 20$ was chosen.

The third step is to describe the analyzed cluster by an ellipse obtained from the moment method and thereby obtain the location and size of the structure. For the TJ-K measurements, the center of mass is used to localize the picture, while for the measurements in ASDEX Upgrade the centroid is used. The reason is that for the measurements in ASDEX Upgrade an image guide was used to transmit the light signal to the fast camera and the different fibres of the image guide all have an individual transmittance which may introduce errors when comparing amplitudes observed through neighbouring fibres.

The object recognition has to distinguish between density perturbations caused by the drift-wave turbulence in the edge plasma and blobs in the SOL of TJ-K. The edge structures detected by the object recognition are the density maxima of quasi-coherent drift waves in the edge plasma. In the following these density maxima are referred to as *coherent edge structures*. The main difference between coherent edge structures and blobs is the position of the center of mass (COM), which is either located inside or outside of the LCFS, respectively. The other difference is the direction of the poloidal propagation, which points in the electron diamagnetic direction for the drift waves and in the opposite direction for blobs. In principle, these two conditions are already sufficient to decide the nature of completely isolated structures. It is, however, also necessary to detect intensity fluctuations captured during close encounters of blobs and coherent edge structures, which overlap in the image data and cannot be resolved as single structures, since meaningful location and size measurements are not possible in these cases.

The object recognition developed in the course of this work detects an overlap by determining the orientation of the major axis of the fitted ellipse. As shown in Sec. 6.3.4, the major axis of structures in the camera data is oriented approximately parallel to the projection of the magnetic field lines on to the image. If two structures overlap in the data, the orientation of the major axis changes notably. This circumstance is depicted in Fig. 5.1. In both images, two turbulent structures S1 and S2 are shown. In a) the two structures are correctly resolved by the object recognition code and the orientation of the major axis of the fitted ellipse agrees with the projection of the magnetic field lines (see Sec. 6.3.2). In b), however, the structures overlap in the image data and the orientation of the major axis is changed noticeably. This is quantified by introducing a minimum and a maximum threshold angle α_{min} and α_{max}. No overlap is detected if $\alpha_{\mathrm{min}} \leq \alpha \leq \alpha_{\mathrm{max}}$. The threshold angles are determined for every discharge by running the object recognition code, visually searching for overlapping structures in the first few events and determine the characteristic values for the orientation angle for overlapping structures. The list of the threshold parameters is documented in Appendix A.
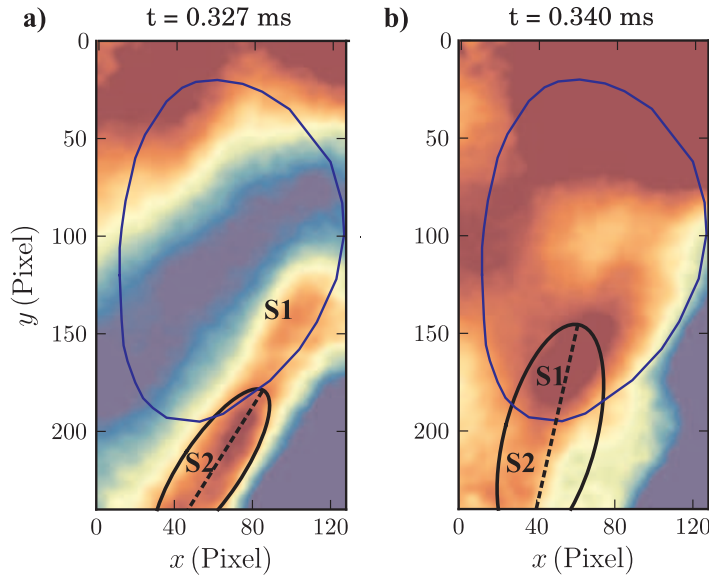
Figure 5.1: *Normalized intensity fluctuations $\tilde{I}_{\mathrm{n}}$ showing coherent structures in the edge (S1) and blobs in the SOL (S2). In a) both structures are detected as isolated structures, for S2 the fitted ellipse is shown as an example. In b) the same two structures overlap and cannot be resolved as isolated and the orientation of the ellipse is changed.*

If overlap is detected, this still indicates the presence of a blob in the SOL, which should be considered when analyzing the waiting-time distribution. The obtained structure sizes and velocities are, however, not reliable and should be discarded.

Chapter 6

Fast imaging at TJ-K

This chapter discusses prospects and limitations of fast imaging measurements at TJ-K. In a first step, the accessible range of the frame rates and resolutions to obtain reliable measurements is investigated. Furthermore, it is examined how well the camera measurements can be localized despite the light integration along the line-of-sight (LOS) by adjusting the experimental setup and by means of data analysis. For this purpose, results from fast imaging and Langmuir probes are compared. This includes studies about the possibilities to determine meaningful structure sizes and velocities from the fast imaging data. The standard optical setup presented in Sec. 4.1.3 is designed to satisfy the requirements deduced from the analysis presented in this chapter. Some parts of the experiments shown were performed in the course of a diploma thesis at TJ-K [118] dealing with the comparability of fast imaging and Langmuir probe measurements.

6.1 Camera characteristics and settings

6.1.1 Linearity of the camera response

It was shown in Sec. 4.3.1 that the signal-to-noise ratio (SNR) increases with the recorded light intensity. Hence, in principle one wants to capture as much light as possible. A high signal-to-noise ratio (SNR) is important to detect faint structures in the image data. In scientific imaging, however, there are reasons to avoid too high count rates: In this work, relative fluctuation amplitudes are of interest, e.g. to define the spatial extent of structures in order to measure their size and track their propagation. This means that overexposure has to be avoided and, hence, the maximum available count rate of the camera must be larger than the sum of the background signal and the highest occurring fluctuation amplitude. Even more restrictive is the fact that for very large signals the count rate of a particular pixel is no longer linear to the number of photons impinging on that pixel (see Ref. [99]). The relation between the bit count stored in the final image and the incoming light intensity is described by the *response*. To prevent detection rates in the non-linear

response range the exposure rate can be decreased or the frame rate can be increased further, as long as the area of pixels which are actually read out, the so-called region of interest (ROI), stays large enough. However, since the internal memory of the camera is a limiting factor, just reducing the exposure time without going to higher frame rates facilitates longer recording times.

In the following, an experiment to determine the linear response range for the chip of the Photron Fastcam SA-5 is described. The experimental setup is shown in Fig. 6.1. The main idea is to capture an image series from a light source emitting constantly over time and dim it by putting different filters between the light source and the camera. Due to the fact that the transmittance even of a neutral density filter is not perfectly constant over the whole wavelength range, it is more accurate to carry out this measurement for a single wavelength. The transmittance of a filter for a certain wavelength can be determined accurately using a spectrophotometer[1].

The light source is a 40 Watt light bulb, operated with a DC power source for temporal constance. The brightness of the light source is chosen so that no pixel is overexposed at any time. To deal with the statistical fluctuations due to the photon shot noise averaging over a series of 100 images was performed. The diaphragm prevents scattered light from being detected. The ground glass ensures the even illumination of the camera chip. Different filters are used to attenuate the intensity of the incoming light. Finally, the dichroic filter selects the wavelength λ of the detected light for the reason described above.

To test the general behavior of the camera, the experiment was performed for a blue and a red wavelength (437.7 and 656.4 nm). The measured response curves are shown in Fig. 6.2. The behavior is qualitatively comparable for both wavelengths. Between 2000 and 3000 counts there is a first deviation from a linear response. However, the slope of the response curves stays close to the one in the linear regime. At about 3500 counts saturation occurs, making amplitude measurements meaningless. Since apparently the exact position of the salient points of the different regimes depends on the wavelength, it can be concluded from this measurement that for white light measurements (i.e. without filters) a bit count of about 2000 can be considered as safe for relative amplitude measurements. For measurements with interference filters the setup described above can be used to determine the exact response function for that wavelength.
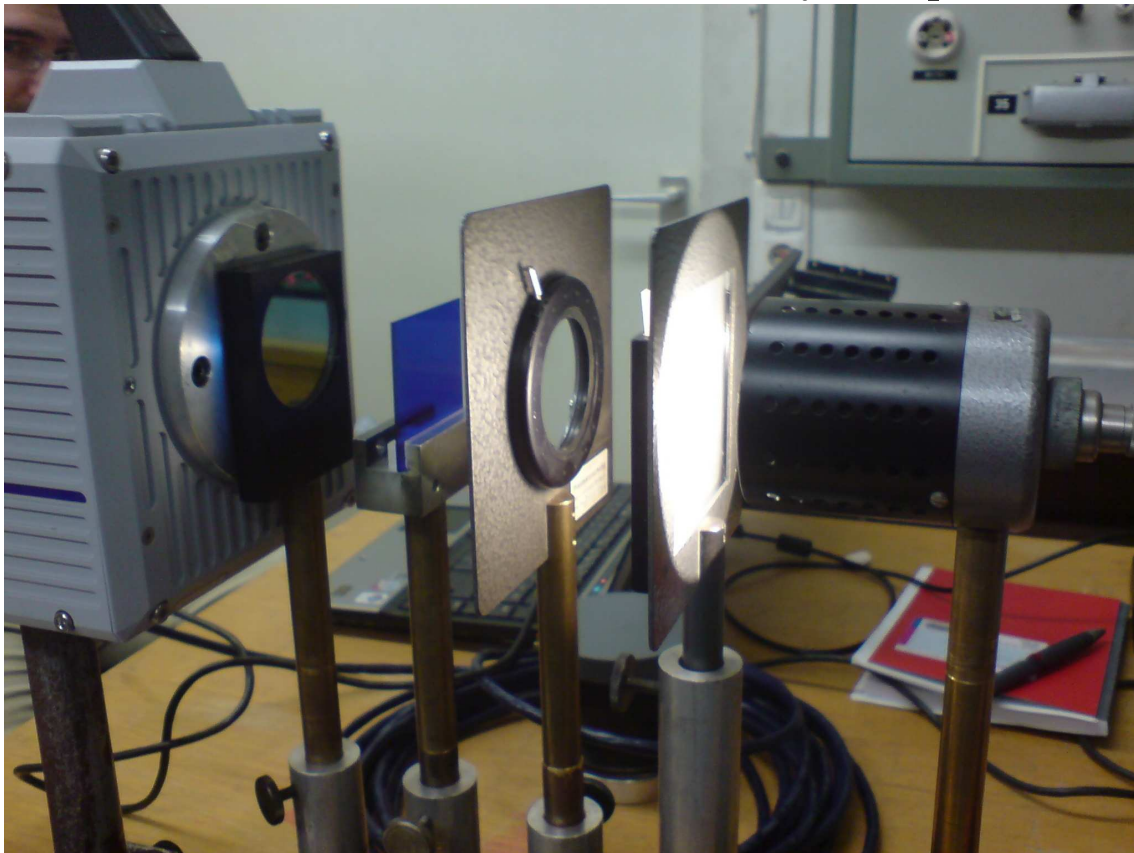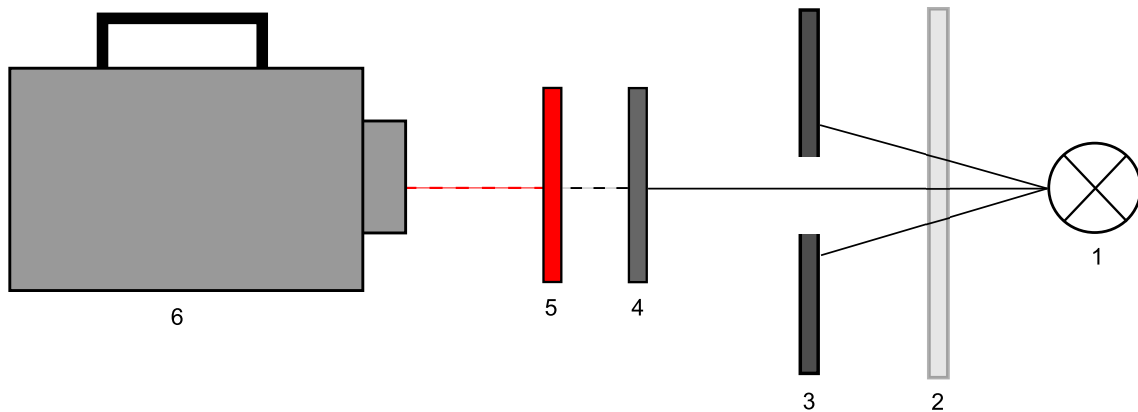
6.1.2   Image noise

In Sec. 4.3.1 the following noise model is introduced

$$\tilde{\sigma}_{\text{tot}} \approx \sqrt{\tilde{c}_1 + \tilde{c}_2 I} \overset{I \gg 1}{\approx} \sqrt{\tilde{c}_2 I} \,.$$

Here, $\tilde{\sigma}_{\text{tot}}$ is the standard deviation of the count rate I and the constants $\tilde{c}_1$ and $\tilde{c}_2$ are determined in the following. Note that Eq. (4.5) is only valid in the linear regime

---

[1]In this case the spectrophotometer *UV-3101* by Shimadzu Corp. was used.

Figure 6.1: *Setup to measure the count rate response to the intensity of the incident light. The top image shows a schematic view of the experiment, while the image on the bottom shows the realization in the lab. A light bulb (1) is powered with DC voltage to emit light with a constant intensity. The ground glass (2) is used to diffuse the light in order to illuminate the camera chip evenly, while the diaphragm (3) prevents scattered light to reach the camera chip. The light passes through an attenuating filter (4) with a transmission precisely known for the measured wavelength and is detected by the camera after passing through a dichroic filter (5) to select that wavelength.*
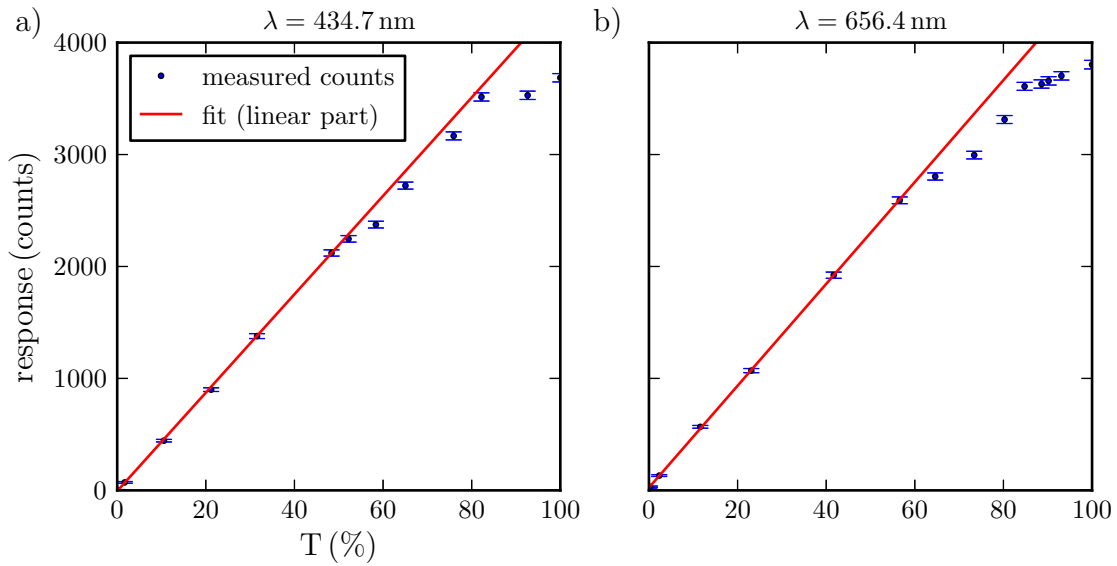
Figure 6.2: *Measurement of the bit count response in dependence of the relative photon flux (represented by the transmission T of the setup) for a) $\lambda = 434.7$ nm and b) $\lambda = 656.4$ nm. The response is qualitatively comparable for both wavelengths. It was ensured that no pixel saturated at 4095, the maximum count rate achievable with the 12-bit chip of the Photron Fastcam SA-5, which would have distorted the result.*
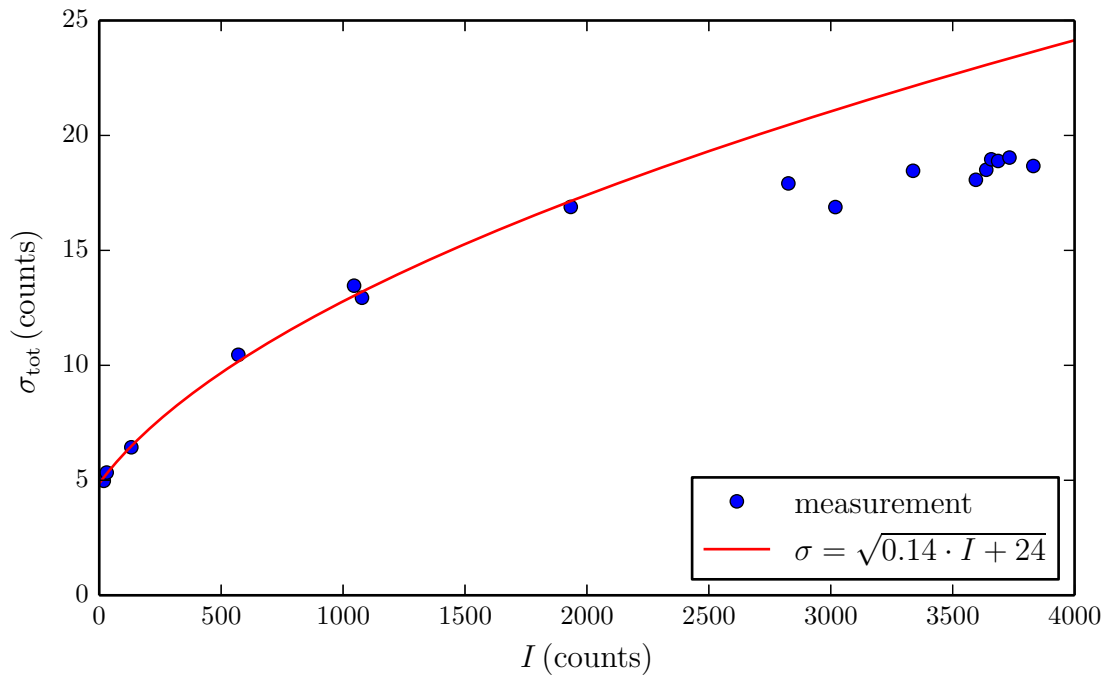
Figure 6.3: *Comparison of the measured standard deviation of the count rate as a function of the light intensity with a fitted noise model. The observed deviations from the model in the non-linear regime (count rates > 2000) are expected for digital cameras.*

of the response curve since otherwise I is not proportional to the number of incident photons N any longer. This noise model can be compared to the experimental data from the response measurements. For a single pixel the standard deviation is determined from a time series of 100 images. The noise model according to Eq. (4.5) is fitted to the obtained standard deviations, considering only data points in the linear regime of the response (i.e. for the mean value of the analyzed pixel holds $\langle I \rangle < 2000$ counts, see Sec. 6.1.1). The resulting empirical noise model is

$$\tilde{\sigma}_{\text{tot}} = \sqrt{0.14 \cdot I + 24} \,. \tag{6.1}$$

It is illustrated in Fig. 6.3 that this noise model indeed describes the observed standard deviations quite well in the linear response regime. In the non-linear regime for count rates above 2000, the observed standard deviations are smaller than predicted. This behavior is expected for digital cameras, since due to the saturation of the count rate, statistical fluctuations in the amount of incident photons are not completely resolved [99].

6.2 Frame rate

In Sec. 4.3 it is explained that a trade-off between time resolution (frame rate), spatial resolution (region of interest), and signal-to-noise ratio has to be found. In the following it is estimated what frame rates are needed to study blobs in the SOL and it is checked whether such frame rates yield sufficient light and a good signal-to-noise ratio for typical TJ-K discharges.

6.2.1 Estimation of the useful frame rate range

With the optical system presented in Sec. 4.1.3, a spatial resolution of approximately $1\,\text{mm/pixel}$ is obtained. The typical propagation velocity is of the order of $1\,\text{km/s} = 1\,\text{mm/µs} \approx 1\,\text{pixel/µs}$. To resolve the trajectory of the blobs they need to change their position by at least one pixel per image. Since the structures are spatially extended and hence cover an area of several pixels, the tracking accuracy will be improved by slower frame rates, where the structures move across several pixels between two subsequent images. Yet it should still be possible to recognize the same structure in subsequent images unambiguously. Therefore, the displacement should not be larger than the typical distance between different structures. The distances between different structures are usually of the same order as the structure size, which is in the range of a few tens of pixels. Hence, with the resolution and propagation velocity stated above and an intended displacement of the structure between subsequent images of 2 to 20 pixels, frame rates between 50 and $500\,\text{kfps}$ are considered useful.

6.2.2 Experimentally available frame rates

This estimation takes the contrary approach than the one presented above. The idea is to determine the frame rate range in which conclusive measurements are possible considering where a sufficient light intensity is recorded from the plasma discharges with a good signal-to-noise ratio (SNR) regardless of the exact application.
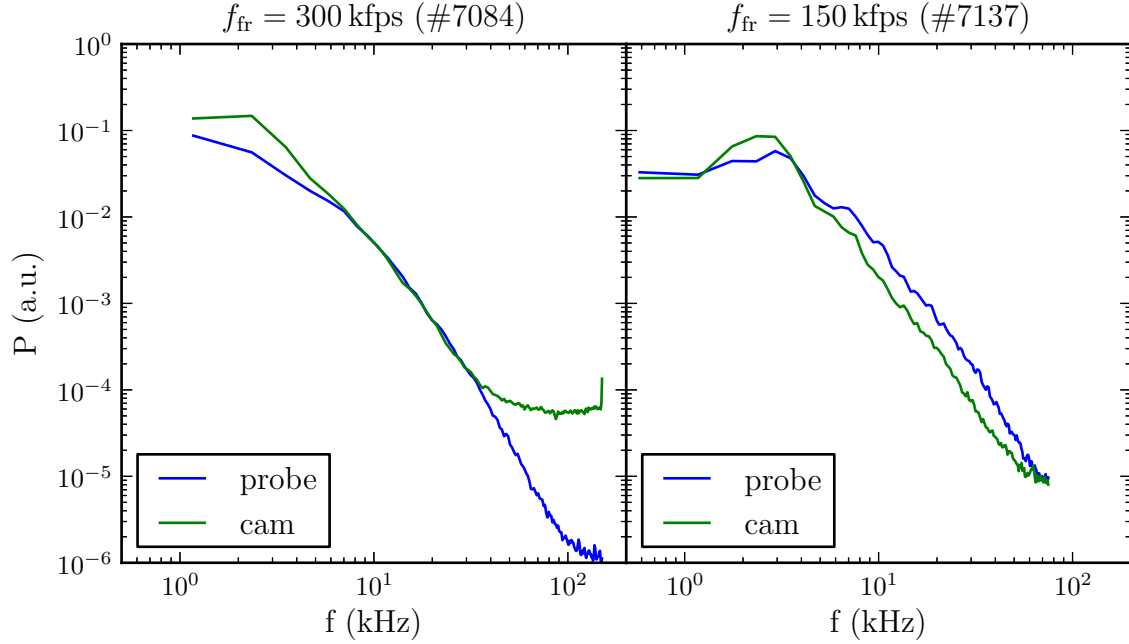

Figure 6.4: *Power spectra are compared for probe and camera measurements. The Langmuir probe measures the ion-saturation current, while the camera images the plasma in the vicinity of the probe. The analysis is done for the frame rates* 300 kfps *(left) and* 150 kfps *(right). For the higher frame rate, saturation occurs for frequencies higher than about* 30 kHz. *Such behavior is not observed for* $f_{\mathrm{fr}} = 150$ kfps. *Reproduced after Ref. [118].*

A first analysis to asses the influence of image noise on camera measurements with the fast camera Photron Fastcam SA-5 was performed in Ref. [118]. The plasma was imaged with different frame rates in the vicinity of a Langmuir probe measuring the ion-saturation current with a sampling rate of 1 MHz. Due to the reduction of the exposure time for increasing frame rates the image noise becomes more important and the SNR decreases. The auto power spectrum of light fluctuations was determined for different plasmas with different frame rates for both the camera and the probe data. Figure 6.4 shows two different measurements, one with a frame rate of 300 kfps for a hydrogen plasma and one with 150 kfps for a helium plasma. The spectra are compared to the ones from the probe measurements to elucidate the role of image noise in the power spectra. Although there are some differences between both diagnostics, which are discussed in Ref. [118] in more detail, there is a

satisfying overall agreement. However, in the power spectrum for the camera measurement with 300 kfps the power saturates at about 30 kHz. This effect is probably due to image noise, since it vanishes for frame rates about 150 kHz. Therefore, it was concluded that frame rates above 150 kHz are not resolving very fast processes in the plasma correctly. In the course of this work, further analysis is undertaken by investigating the SNR for a frame rate of 150 kHz. The estimated camera noise is given by Eq. (6.1). If the camera captures a count rate I as the sum of a fluctuating part $\tilde{I}$ and a background signal $\langle I \rangle$, the fluctuation can be recognized as a real feature when the Rose criterion $\tilde{I} > 5 \cdot \tilde{\sigma}_{\text{tot}}(I)$ (Sec. 4.3.1) is fulfilled. If the same physical situation is imaged with different exposure times, the fluctuation $\tilde{I}$ will scale linearly with the total count rate I, while the noise level will scale with $\sqrt{I}$ according to Eq. (4.5). Hence, the scaling of the SNR reads

$$\text{SNR} = \frac{\tilde{I}}{\tilde{\sigma}_{\text{tot}}} \propto \frac{I}{\sqrt{I}} \propto \sqrt{I} \,. \tag{6.2}$$

The consequence is that by increasing the frame rate (decreasing exposure time) the SNR is reduced, making object recognition less reliable. In Fig. 6.5, three images are
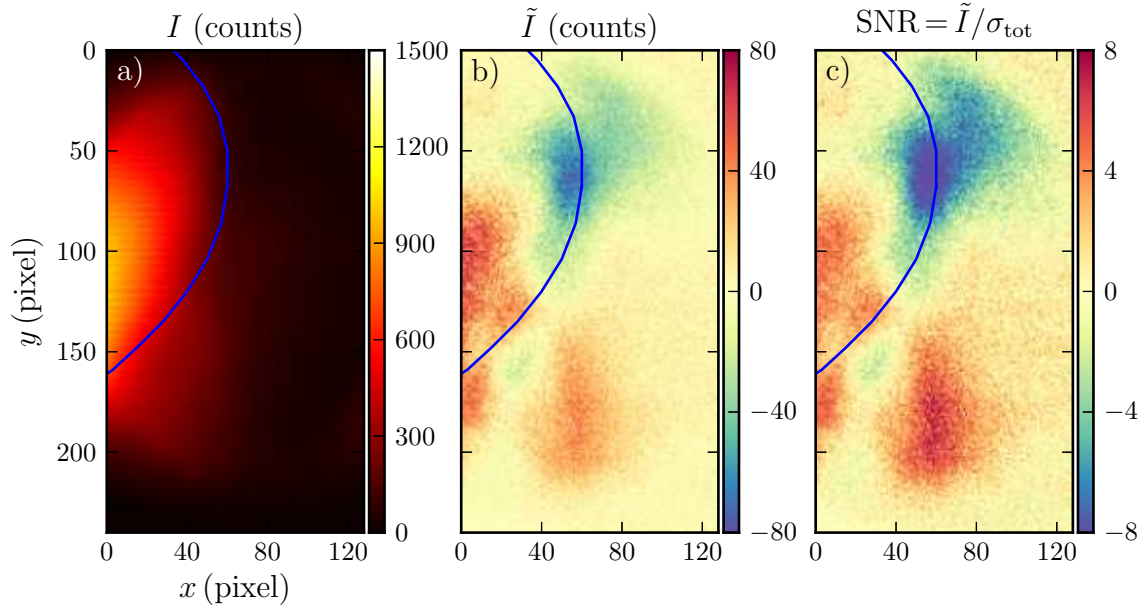
Figure 6.5: *Shown here is a colorized raw image I (a), the fluctuations $\tilde{I} = I - \langle I \rangle$ (b), and the SNR of the fluctuations. While the raw image is dominated by the brightly glowing confined plasma, a structure outside of the LCFS (blue line) is visible in the fluctuation image together with a large intensity fluctuation in the edge of the confined plasma. The relative fluctuations are for both structures in the range of $5\text{-}10 \cdot \tilde{\sigma}_{\text{tot}}$.*

shown captured during a plasma discharge with a frame rate of 150 kHz. Figure 6.5 a) shows an exemplary colorized raw image. The maximum intensity is below 1500

and, hence, in the linear response regime. The image is dominated by the brightly glowing confined plasma, which is seen left of the LCFS (blue line). Figure 6.5 b) shows the fluctuating part of the same image, i. e. after subtracting the mean image averaged over the 10 previous images. Positive intensity variations are shown in red, negative ones in blue. Two structures are visible, one in the edge of the confined plasma (left of the LCFS) and one in the SOL. That these structures in the light fluctuations are connected to real plasma phenomena can be seen in Fig. 6.5, where the SNR is shown. For both structures the SNR peaks at about 8, which well fulfills the Rose criterion, meaning that the meso-scale turbulent fluctuations are clearly distinguishable from noise for the chosen setup.

The analysis presented in this section revealed that frame rates up to about 150 kfps allow a reliable detection of turbulent structures in the image data. This result, together with those from the previous section, show that the applicable frame rate range to study blobs in TJ-K ranges from 50 to 150 kHz.

6.2.3 Frame rate constraints due to required resolution

The lens system used (Sec. 4.1.3) has an exceptional small depth of focus due to a low aperture ratio, which goes along with a very high brightness of the images. Also, the spatial resolution achieved with this lens for the used setup of about 1 mm/pixel is favorable to resolve blob sizes of a few cm sufficently well to measure even small size differences. Therefore, if possible, the available field-of-view should not be adjusted by choosing a different lens. The camera should ideally capture at least a region in the SOL, which spans from the LCFS to the outer wall with a poloidal extension as large as possible. It will prove necessary to also capture the outer part of the confinement region, where the drift-wave turbulence causes pronounced density structures. Therefore, in the radial direction, the field-of-view should cover about 10 cm (from the center of the plasma column to the outer wall) and in the vertical direction it should at least cover 10 cm as well to track the propagation of single structures in the image data. Favorably, the whole cross section of the vacuum vessel should be captured at once with approximately 20 cm in the vertical direction. With the obtained spatial resolution of 1 mm/pixel, the active ROI on the chip should cover about 100 pixels in the radial direction and between 100 and 200 pixels in the vertical direction. For the employed Photron Fastcam SA5 a suitable resolution close to this is 128×240 pixels. This resolution can be used for frame rates up to 150 kHz, which is compatible with the frame rate range determined above.

6.2.4 Resulting standard settings

The presented analysis indicates that there is an optimal camera setting for the Photron Fastcam SA5 to satisfy the different constraints arising from the employed experimental and optical setup. In particular, a horizontal and vertical resolution of 128 and 240 pixels, respectively, is chosen to observe almost the full extent of the

poloidal cross section in the vertical direction and the outboard side from almost the center to the wall in R-direction simultaneously with a spatial resolution that ensures the detection and accurate size measurement of blobs. The frame rate is set to 150 kfps, which guarantees the appropriate detection of the displacement of the structures between two images with an adequate signal-to-noise ratio to distinguish the structures clearly from the background plasma.

6.3 Comparison with probe measurements

The spatial resolution achieved with the camera setup is about 1 mm/pixel. Since the size of turbulent structures in TJ-K is of the centimeter scale the resolution is well suitable to resolve turbulent structures. The camera delivers measurements of the full field-of-view (FOV) with that resolution and, therefore, turbulent structures can be traced appropriately. On the other hand, the fast imaging suffers from the fact that the measured light signal is integrated along the line of sight (LOS) and, thus, care has to be taken in the interpretation of the obtained image data. The effect of this can be reduced by using a lens system with a small aperture ratio D/f, which ensures a small depth of focus. In the following the data obtained with the chosen setup (Sec. 4.1.3) is compared to measurements of the ion-saturation current, which is, especially in TJ-K, a measure for density fluctuations. In Ref. [118] it was shown that in TJ-K due to the line integration the localization of the structures is not trivial and the observed shape is distorted. However, since the structures are elongated along the magnetic field with a parallel length $l_\parallel$ longer than the part of the plasma column captured by the fast camera, the toroidal location of the structures is no longer a degree of freedom (illustrated schematically in Fig. 6.6) and a localization of the structure part in the imaged volume should be possible.

This section is dedicated to the demonstration that the localization is indeed possible and that certain properties of turbulent structures can be determined reliably from the fast imaging data. First, a qualitative comparison of the conditional average (CA) of probe and camera measurements will illustrate the issues one has to deal with in order to reconstruct the shape and location of the structures. By determining the trajectory of the CA blob event for both diagnostics using the particle tracking velocimetry (PTV) method (Sec. 5.4) it will be shown also quantitatively that positions and velocities can be determined, with some restrictions, for SOL structures using the imaging data from the fast camera. Finally, a quantitative comparison of size measurements will be given, where it will be seen that perpendicular to the magnetic field sizes can be determined from the image data.

6.3.1 Qualitative comparison

In Ref. [48], the generation and dynamics of blobs have been studied with Langmuir probes. In the present section, the comparability of probe and camera measurements

○ center of mass (real)

● center of mass (observed)
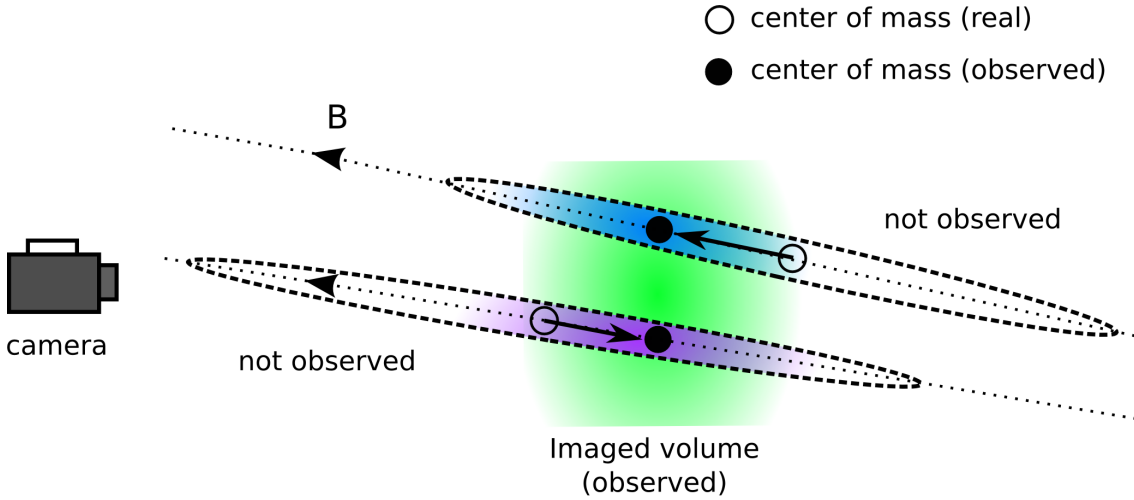
Figure 6.6: *This drawing illustrates the situation when the imaged structures are much longer than the depth of view. Since the structures extend over more than the observed region, the center of mass of their image does not correspond to the center of mass of the real structure. Since the structures are elongated along the magnetic field lines, the observed center of mass is sufficient to reconstruct the structure part in the imaged volume and a localization to a certain field line is possible.*

for similar experiments is examined. Figures 6.7 a-c) show an image series of a propagating structure as obtained by conditionally averaging fluctuations in the ion-saturation current. The dot in the lower right corner indicates the position of the reference probe. In the confined plasma of TJ-K, drift-wave turbulence is accompanied by coherent structures with lifetimes in the range of 10-100 µs [70]. These structures propagate into the electron diamagnetic drift direction (clockwise in the figures). Such a structure with a poloidal mode number of $m = 3$ can be seen in Fig. 6.7 a) at $\tau = -0.02$ ms. The density structure extends partly over the last closed flux surface (LCFS, depicted as solid line) into the SOL. As shown in Ref. [48], the part of the structure extending into the SOL can grow when a turbulent potential fluctuation advects density outwards by the resulting $\mathbf{E} \times \mathbf{B}$-drift. Following the next few µs in Fig. 6.7 b) and c), one can see the structure near the reference propagate and grow. It detaches from the bulk and forms a blob. Figures 6.7 d-f) show the CA of intensity variations from the image data of the fast camera for the same discharge. A pixel in the region where the blobs are observed is used as reference signal (dot). Comparing Figs. 6.7 a) and d) it can be seen that the intensity variations are similar to the density fluctuations. In the confinement region the mode structure can be seen in the first image of Fig 6.7 d), but it is blurred due to the integration along the line of sight and the longer integration time compared to the sampling time of the probes measurement. In the SOL, where the blob properties are studied, the agreement is much better. This can be seen by comparing the structures in the top and bottom right for both diagnostics at
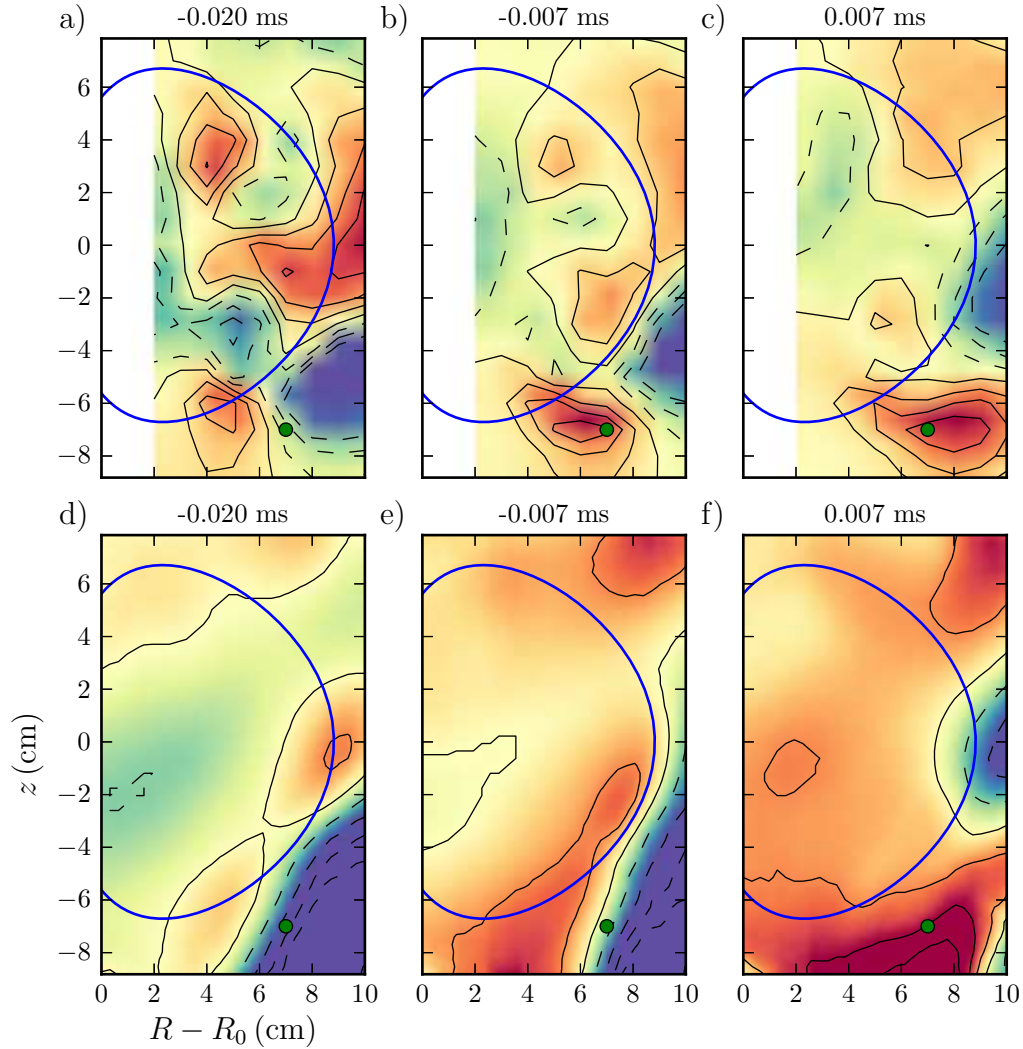
Figure 6.7: *Three time instances of the conditional average of density fluctuations from probes (a-c) and camera (d-f) during blob events in a hydrogen plasma (#8213). The solid line depicts the LCFS, the dot (green) is the location of the reference probe. Positive fluctuations are shown as solid contour lines (red) and negative ones as dashed contour lines (blue). Both diagnostics reveal turbulent fluctuations inside the confined plasma and in the SOL. While the integration along the line of sight distorts the structures, there is an overall agreement of the observed dynamics.*

$\tau = 0.007\,\mathrm{ms}$. To show this agreement systematically, the PTV method is used to locate the blobs and measure their velocities.

6.3.2   Comparison of PTV results

In order to compare the camera and probe measurements, two identical plasma discharges were conducted. The probe measurement featured a 2D scan to obtain a CA of the dynamics in the poloidal plane. The fast camera images the same poloidal cross section and can be conditionally averaged using the same reference probe as for the probe measurements, but with a sampling rate matched to the frame rate of the camera. Compared to Fig. 6.7, the camera view captures a region in the poloidal cross section closer to the wall. Therefore, the propagation of structures can be tracked over long distances in the SOL. Figures 6.8 a-c) show an image series of the CA of the probe data and d-f) of the camera data. In both data sets a blob is clearly visible in the SOL. Compared to the probe measurement, the shape of the blob is significantly distorted by the integration along the LOS. Object recognition (see Sec. 5.6) is used to determine the center of mass of the blob for every time step and the resulting blob positions are used as "particles" to determine the blob velocity using PTV. The result is shown in Fig. 6.9, where the dots mark the measured structure positions together with the velocity (color-coded). It becomes apparent that in the lower parts of the SOL the agreement is remarkably good, both for the center of masses in the poloidal plane and for the determined velocities, while in the upper SOL the line integration has a noticeable influence on the measurements. Around the midplane the poloidal velocity as seen by the camera is higher compared to the probe data by a factor of two. Accordingly, above the midplane the structure shows a displacement to more outward positions (upper right). This is due to the parallel extension of the filaments as will be shown in the following.

Instead of studying just the conditionally averaged dynamics, the camera data can be used to explore the dynamics of single structures in the raw data. Since the poloidal propagation of drift waves in the edge plasma and blobs in the SOL point in opposite directions, the two regions can be recognized in the images by determining the mean velocity field. For this purpose the data set of the same camera measurement used for the CA above is processed using the object recognition. For every detected structure a counter in a 2D histogram is incremented to analyze where structures occur in the poloidal cross section.

Such a 2D histogram is displayed in Fig. 6.10 a). Plotted on top are the positions of the LCFS projected from different toroidal angles on the camera data. There are two regions in the histogram. In the upper left, the structures are distributed rather homogeneously, while in the rest of the histogram, the detected structures tend to cluster. It was assumed that the border between those regions may be the LCFS, since it fits to the projected LCFS 5° in front of the focused plane (towards the camera). The velocity field was determined to check this.

Whenever one of these structures can clearly be recognized again in the subse-
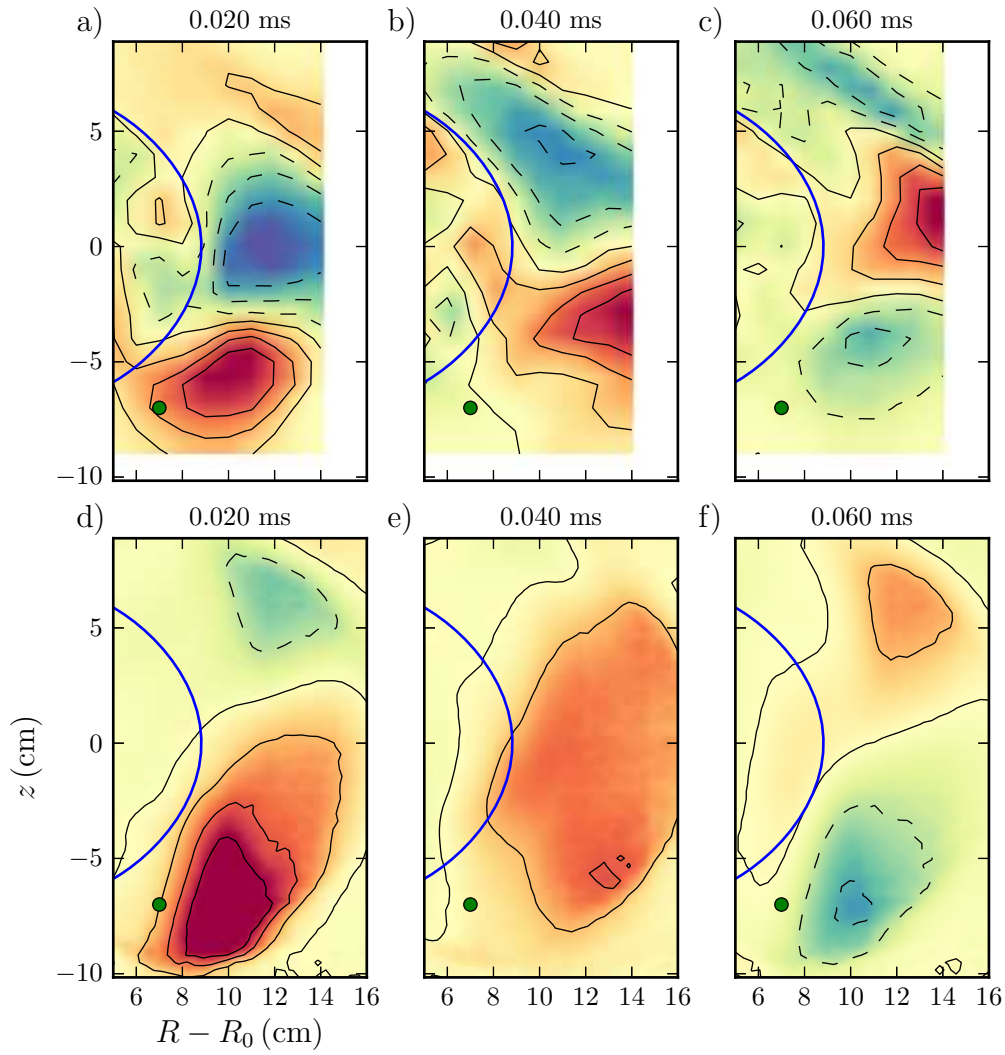
Figure 6.8: *Qualitative comparison of three time instances of the conditionally averaged density (top row) and intensity fluctuations (bottom row) in a helium plasma (camera: #7508, probe: #7509). The reference probe is shown as green dot. The dynamics is captured comparably with both diagnostics. Above the mid-plane, the observed structures are shifted upwards as compared to the localized probe measurements due to line integration.*
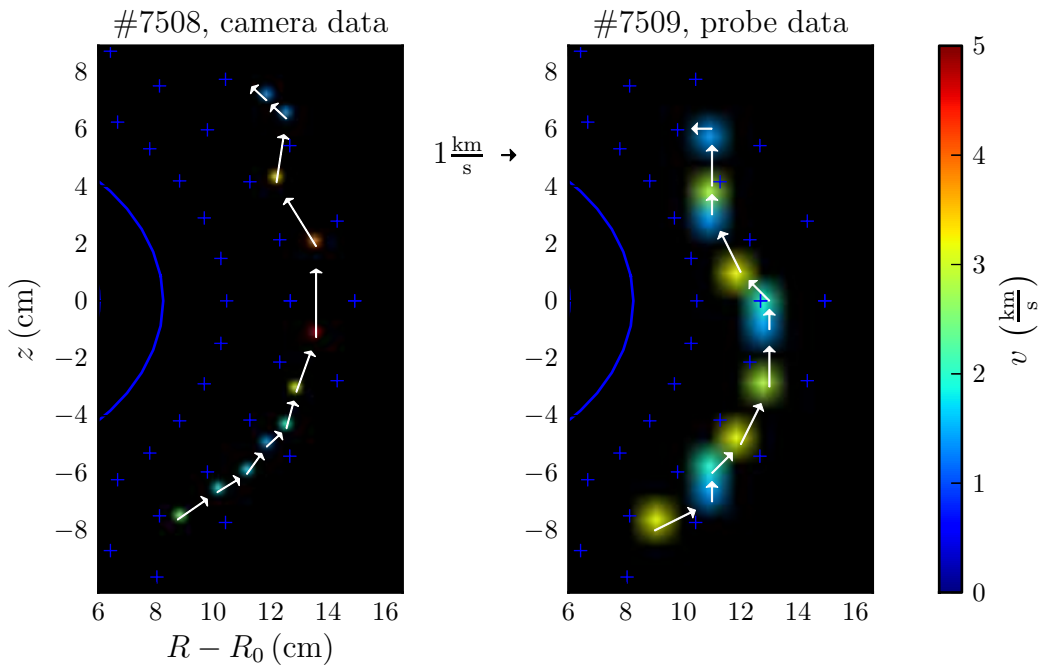
Figure 6.9: *Comparison of the trajectories of a blob in the SOL as measured with the fast camera (left) and Langmuir probes (right). The observed structure positions and velocities agree almost perfectly in the lower half of the SOL. Around the midplane the integration along the LOS reduces the agreement, but still the trajectory is well reproduced by the fast imaging. The reason for this positive result is that the parallel elongation of the structures is typically larger than the observed plasma volume (see Fig. 6.6).*
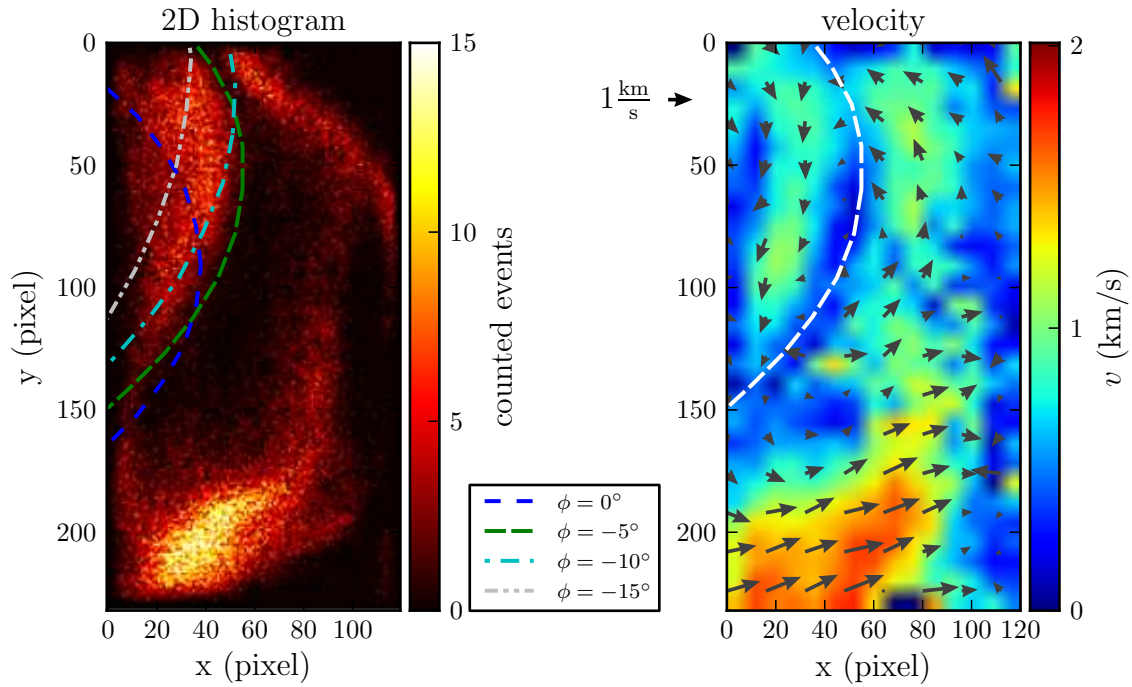
Figure 6.10: *On the left, a 2D histogram of structures detected in the image data of #7508 is shown. The different lines depict projections of the LCFS from different toroidal positions, where 0° stands for the focused plane at port O6 and negative toroidal angles are counted towards the camera. Structures are detected both in the edge and the SOL. While they appear to be distributed homogeneously in the edge, in the SOL most of the structures are observed only in distinct regions. The edge seems to be limited by the LCFS projected from 5° in front of the focused plane (green line on the left). This assumption is supported by the velocity field displayed on the right together with the assumed LCFS (white line). Directly at the LCFS the poloidal propagation direction is reversed as expected.*

quent image, the velocity can be determined by the PTV method (Sec. 5.4). The velocities are then averaged, first over all structures for every single pixel and second, in order to smooth the results for visualization, a spatial averaging over 8×8 pixels (roughly $1 \times 1\,\mathrm{cm}^2$) is performed; the result is displayed in Fig. 6.10 b). Plotted on top is the assumed LCFS position in the image data. The expected reversal of the poloidal propagation velocity is observed exactly in the vicinity of that curve. Hence, this is the LCFS as seen by the camera. By comparing the LCFS position in the focused plane and in the plane where the LCFS is actually seen, it becomes clear why the agreement in structure positions in Fig. 6.9 varies over the poloidal cross section. In the lower half, both curves are close together and then deviate more and more with increasing poloidal angle (counterclockwise) as the two LCFS projections depart from each other.

6.3.3   Influence of the non-locality on shape reconstruction

The qualitative comparison of camera and probe data in Sec. 6.3.1 illustrates that due to the integration along the LOS the shape of visible structures is altered in the image data. In the frame of a diploma thesis at TJ-K [118] this was treated more quantitatively by fitting an ellipse to density maxima of structures arising from drift-wave turbulence in the edge plasma. The results indicated that the ellipses were tilted as compared to Langmuir probe measurements. To illustrate that this is in fact due to the integration along the LOS the shape of the observed structures is compared to the course of the magnetic field lines.

Figure 6.11 a) shows the cross correlation of the image data with a reference probe measuring the ion-saturation current inside the confinement region of a plasma discharge without limiters installed (standard setup). The cross correlation reveals a drift wave in the plasma. Also shown in the figure is the projection of a magnetic field line (dashed line) going through the reference probe. The size of the drift wave, as seen by the camera, is much smaller perpendicular to the magnetic field and it is apparent that the parallel extension of the turbulent structure along the magnetic field influences the light signal recorded by the camera. A similar situation is shown in Fig. 6.11 b) for a blob in the SOL of a limited plasma. Similarly to the case above, the elongation of the structure along the magnetic field stretches the shape of the imaged structure along the projection of the magnetic field line. It will be shown quantitatively in the following section that the structure size perpendicular to the magnetic field can be measured in good agreement with the probe measurements.

6.3.4   Size measurements

Due to the parallel elongation of the structures, the structure position measurement is reduced by one degree of freedom. This enables a reliable localization and velocity measurement as it was shown above. It is, however, also apparent from different analyses that the shape of the structures as captured by the camera is distorted
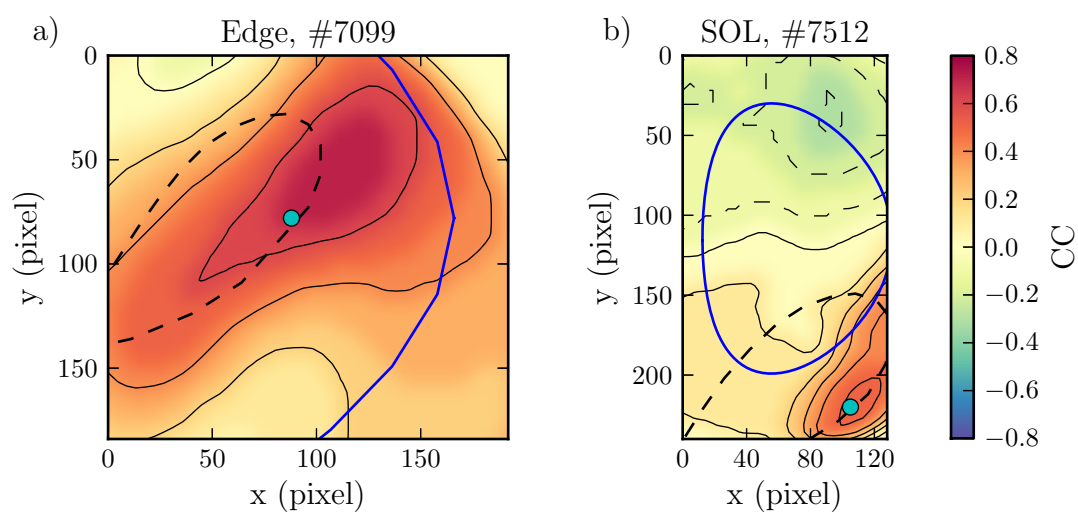
Figure 6.11: *Shown in a) is the cross correlation (CC) of an $I_{i,sat}$ reference signal (probe position: cyan dot) with the image data of a plasma discharge without limiter disks installed. The closed line (blue) depicts the LCFS in the focused plane, the dashed line (black) is the magnetic field line through the reference probe. The equivalent situation is shown in b) for a plasma discharge with the limiters installed and a reference probe in the SOL. In both cases, the shape of detected structures, drift wave in a) and blob in b), is elongated along the projected field direction.*

due to the light integration. Therefore, the structure size is not readily available
from the camera measurements. However, since the imaged structures are mainly
blurred along the course of the magnetic field lines, it should be possible to determine
the structure size perpendicular to the field line. Due to the elongation along the
projected field line, this size coincides with the length of the minor axis of the fitted
ellipse, while the major axis is oriented parallel to the magnetic field. This can be
seen in Fig. 6.12. From the probe measurements it is known that the structures do
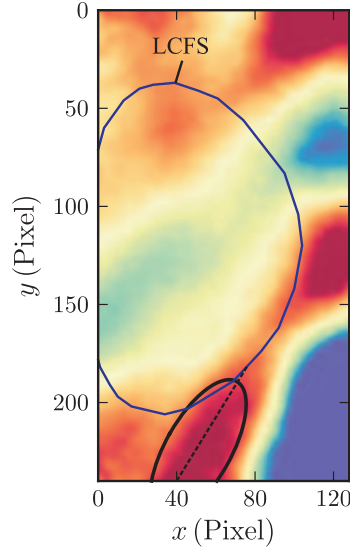
Figure 6.12: *An ellipse (closed black line) is fitted to intensity fluctuations in the image
data during a blob event. The dashed black line shows the projection of a magnetic field
line going through the blob. Due to the elongation of the filament along the field, the
structure is stretched into the projected field direction. Hence, the major radius of the
ellipse is oriented parallel to the magnetic field direction.*

not have a circular shape, but are better described by an ellipse. Hence, the size has
to be measured in at least two different directions. Two distinguished directions of
special interest are the radial and poloidal direction with the respective structure
sizes δ_r and δ_p. In this work the structure size is defined as the full width at half
maximum (FWHM) of the analyzed structures, exceptions are stated explicitly.
Additionally, the effective size can be determined, which is the radius of a circle
with the same area as the structure, i. e.

$$\delta_{\text{eff}} = \sqrt{\delta_r \delta_p} \,. \tag{6.3}$$

As can be seen from the comparison of probe and camera measurements, the imaged
shape of the filaments is blurred along the magnetic field lines, while the perpen-
dicular direction seems to agree quite well. Hence, it is not immediately clear how
the structure sizes determined from the camera images compare to the probe mea-
surements. To elucidate this connection, comparative measurements of structure
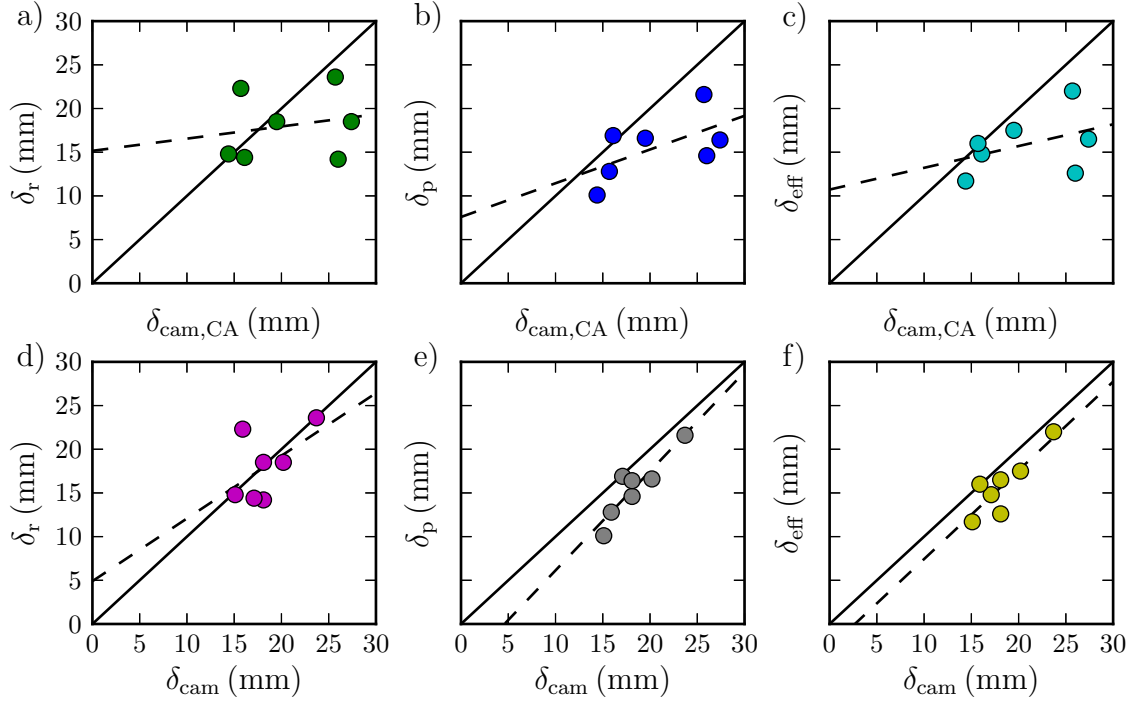
Figure 6.13: *Comparison of different blob sizes in the SOL determined from the CA of probe measurements (radial, poloidal and effective size δ_r, δ_p and δ_{eff}) and fast imaging data ($\delta_{cam,CA}$ determined from the CA and δ_{cam} averaged over single events). By plotting the different probe sizes as a function of $\delta_{cam,CA}$ or δ_{cam} and fitting a line to the data (dashed lines), the agreement for the different combinations can be assessed. While there is a relatively large scatter for all comparisons with $\delta_{cam,CA}$ (a-c) and for the comparison of δ_{cam} with δ_r (d), δ_p and δ_{eff} are in almost equally good agreement with δ_{cam} (e and f).*
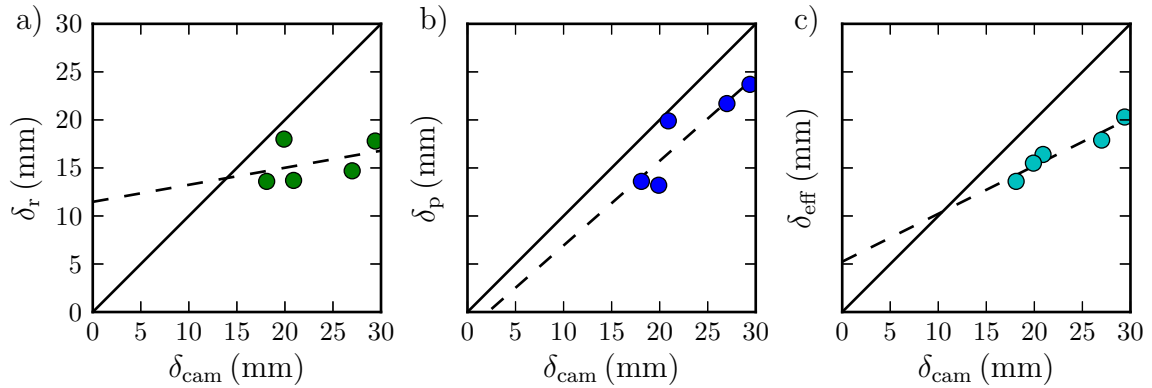
Figure 6.14: *Same representation as in Fig. 6.13, but for sizes of drift-wave density maxima in the edge of the confined plasma in TJ-K. While comparison a) with δ_r shows no convincing agreement, δ_p and δ_{eff} are showing a better agreement with δ_{cam} (b and c). δ_{eff} shows the smallest scatter, but the absolute values are affected by the light integration along the LOS.*

sizes with Langmuir probes and the fast camera were performed for both, blobs in the SOL and density maxima of drift waves in the edge. For every discharge, $\delta_{\rm r}$, $\delta_{\rm p}$, $\delta_{\rm eff}$, and $\delta_{\rm cam,CA}$ are determined from the CA blob structure and, if available, also a drift-wave density maxima in the edge plasma. Due to the limited discharge duration for the high-field discharges it was not possible to scan the SOL and the edge plasma in the same discharge. Additionally the sizes of single structures can be determined from the camera data. These sizes can be averaged at certain positions, yielding the size measurement $\delta_{\rm cam}$. The results are depicted so that the different sizes determined from the probe data are shown as function of the size determined from the fast imaging data. A straight line points to a linear relationship between the different measurements, which is already sufficient for scaling studies as presented in Sec. 8.2. If the slope is close to one also the absolute values agree. Such a comparison is shown for blobs in the SOL in Fig. 6.13. While the sizes determined from the CA of the image data show a relatively large scatter, the agreement with the size averaged over single events is much better. The close relation between $\delta_{\rm cam}$ and $\delta_{\rm p}$ and $\delta_{\rm eff}$ implies that these quantities can be determined from the image data. The close match with $\delta_{\rm p}$ can be understood by looking at the projection of the field lines in Fig. 6.12, which is oriented mainly in the radial direction. Hence, the poloidal direction is scarcely influenced by the light integration.

In the case of the drift waves, the CA of the image data shows very blurred structures (as seen in Fig. 6.7), rendering a reliable determination of sizes impossible. Hence, only $\delta_{\rm cam}$ is compared in Fig. 6.14 to the sizes of the probe measurement. The overall agreement is worse than in the SOL, especially the absolute values are differing between both diagnostics. Nevertheless, in principle the same results as for the blobs are obtained, namely that in the observed region the sizes as determined by the camera are matching $\delta_{\rm p}$ and $\delta_{\rm eff}$.

It has to be noted that this result depends on the observed region in the image data as well as the exact optical setup, since both change the image of the course of the field lines. The analyses presented are conducted for the setup and observation region that will be used for the studies of blob properties in Ch. 8.

6.4   Conclusions of camera measurements

The analyses presented in this chapter revealed that quasi-localized camera measurements are possible in the SOL of TJ-K. By imaging the plasma with a small depth of view and the right choice of camera settings, turbulent phenomena can be resolved with a sufficient spatiotemporal resolution. In the SOL, the center of mass of the detected structures agrees quite well with probe measurements in the focused plane, reliable position measurements allow for a determination of the velocities and structure sizes.

Chapter 7

Characterization of filaments and SOL transport in TJ-K

In order to study blobs (filaments) in TJ-K, it has to be known where in the SOL they exist. The shape of the filaments enters the equations which describe their dynamics (e.g. via the filament length $l_\parallel$). Hence, the knowledge about the shape of the filament is essential in order to predict the blob properties and dynamics. This chapter begins with the characterization of the three dimensional shape of the filaments and the region in the SOL in which blobs occur in the setup with two limiter disks (Sec. 4.1). It is shown that this region is determined by the magnetic field geometry, which can be understood from the blob model summarized in Sec. 3.2. In addition, indications of turbulence spreading in the SOL of TJ-K are presented. After that, a generation region is identified, where the majority of all blob events is observed. Finally, the transport induced by blobs is characterized and the role of blobs for the total transport is assessed.

7.1 Blob filament shape and occurrence region

7.1.1 Parallel extension

In order to determine the parallel length of the blobs $l_\parallel$, experiments with both poloidal probe arrays (see Sec. 4.4.1) are performed. The setup is shown schematically in Fig. 7.1. In a first step, the field-line segments between the *outer port array* (OPA) and the *top port array* (TPA) are determined for each probe on the OPA. Since the field line segments that cross a probe at the OPA do not exactly cross any probe on the TPA (see Fig. 7.1), any OPA probe is associated with the three TPA probes with the smallest distance from the field line (three since a possible misalignment of the arrays may also introduce a radial displacement). Finally, for any OPA probe i the cross correlation functions (CCFs) are evaluated with these three associated TPA probes. The maximum of these three CCFs is determined for $\tau = 0 \pm t_s$ ($t_s = 1\,\mu s$ is the sampling time of the measurement). Correlation values,
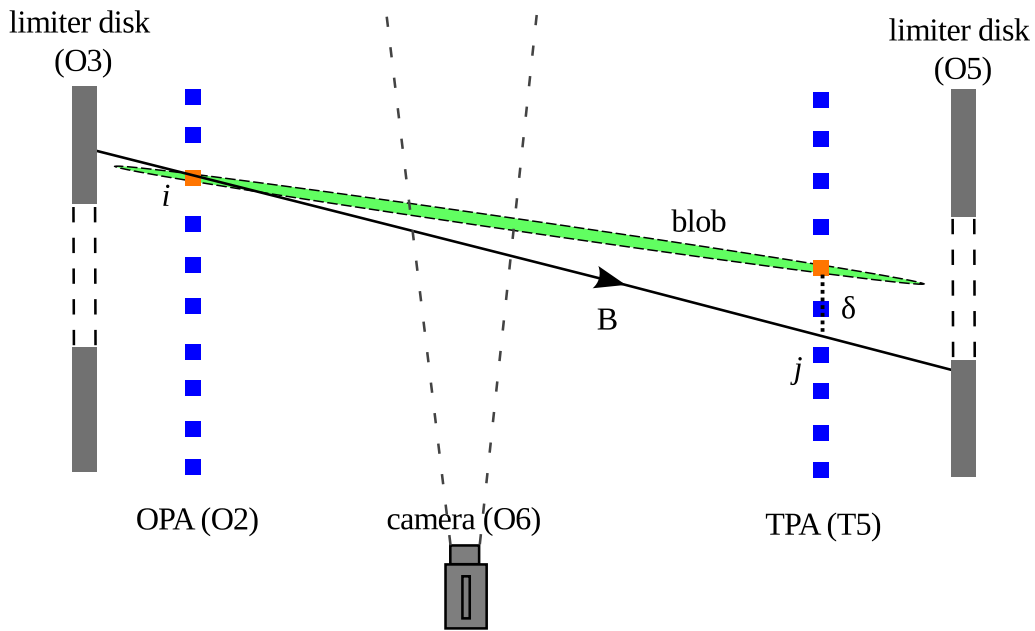
Figure 7.1:   *Setup with two poloidal probe arrays between the limiter disks. The* outer port array *(OPA) is located at port O2, the* top port array *(TPA) at port T5. The probes are depicted by squares (blue). The camera observes the plasma tangentially at port O6 (not perpendicular as shown in the simplified drawing). By cross correlating the signals for all probes i and j, blobs (green) which extend between both arrays are detected. Furthermore, it is possible to detect a tilt of the structures to the field lines by analyzing the deviation δ between TPA probe closest to the field line and the correlation maximum (orange).*

larger than 0.5 indicate the existence of turbulent structures in the SOL that have a parallel extent larger than the connection length between the two probe arrays. As it is seen in Fig. 7.2, values larger than 0.5 are observed in the region between approximately $\theta = -\pi/2$ and $\theta = 3\pi/4$. The high correlation values are caused by blobs, as shown in the following.
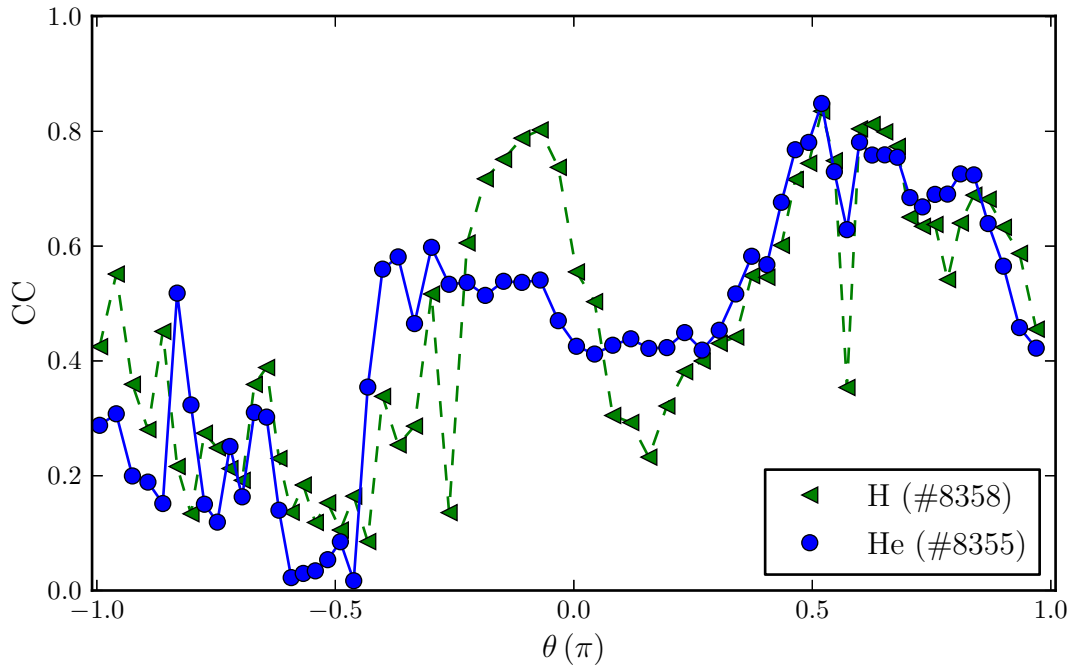
Figure 7.2: *For each probe on the OPA, measuring ion-saturation current fluctuations, the cross correlation functions (CCFs) are evaluated with a set of approximately field line connected TPA probes (see the text for details). The maxima of these CCFs are plotted here for hydrogen and helium discharges against the poloidal angle of the OPA probes.*

The fast camera is used in addition to the probe arrays to observe the plasma tangentially at port O6. The CCF is evaluated for the probe arrays as described above, but also for each probe i on the OPA with every pixel (x_k, y_k) of the image data. The CC of the image data with three exemplary OPA probes is shown in Fig. 7.3. The three reference probes are chosen from different regions in Fig. 7.2: Figure 7.3 a) shows the CC at $\tau = \tau_{\mathrm{max}}$, i.e. when the highest CC value is found, for a reference probe at $\theta = -0.54\pi$ (left of the region of high correlation values in Fig. 7.2). It can be seen that also no significant correlation is found between probe and image data, indicating that no elongated structures exist in that region of the SOL. The second reference probe is located in the region of high correlation values between both PPAs ($\theta = -0.35\pi$). At $\tau_{\mathrm{max}} = 40\,\mu$s, a blob is seen in the CC as displayed in Fig. 7.3 b). The positive time lag means that the structure first appears in the viewing range of the camera and then reaches the OPA probe. For the third reference probe (right from the region with high correlation values in Fig. 7.2), at

$\tau_{\mathrm{max}} = -100\,\mu\mathrm{s}$, the same blob structure is observed in c) as it was the case for the second reference probe, but this time it is visible in the image data before it reaches the reference probe.
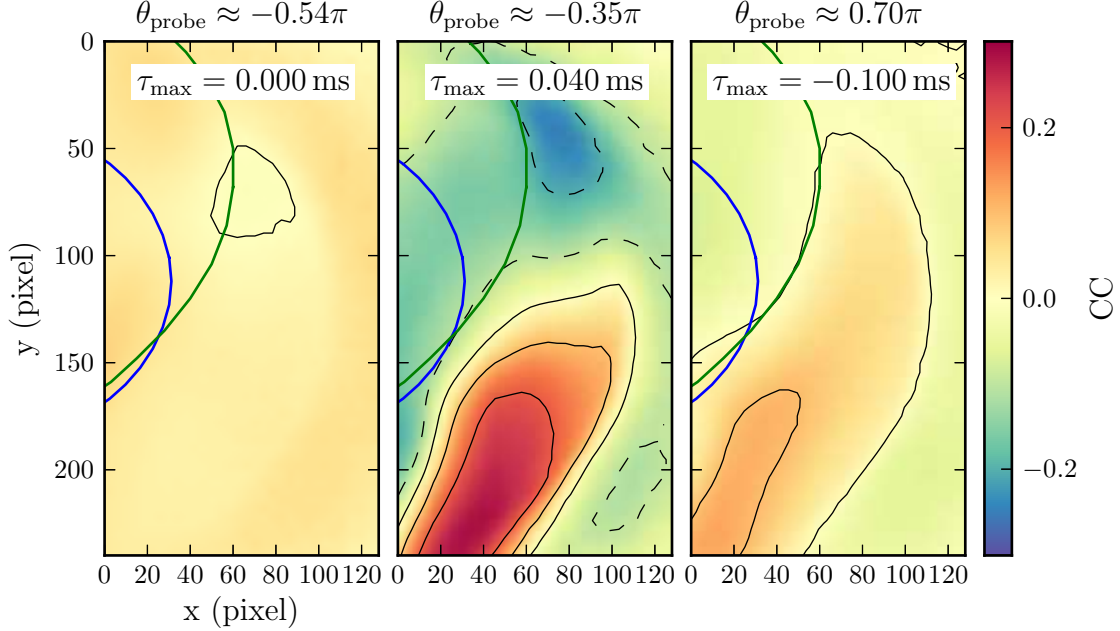
Figure 7.3: *Cross correlation (CC) of the image data with three OPA probes at different poloidal angles (stated on top of the images). All three images show the time lag τ_{max}, where the highest CC is found. The first reference probe shows no significant CC with the image data (a). In the CC of the image data with the second reference probe, a blob is seen in the SOL at $\tau_{\mathrm{max}} = 40\,\mu\mathrm{s}$ (b). The third reference probe shows a lower CC maximum in the image data at $\tau_{\mathrm{max}} = -100\,\mu\mathrm{s}$ (c).*

These observations can be summarized as follows: In the region of low correlation between OPA and TPA, no significant CC with the camera data is found as well. For reference probes in the region of high correlation values between the probe arrays, the dominant feature observed in the camera data is a blob, which leaves the confined plasma at a low poloidal angle (bottom of the images) living longer than $100\,\mu\mathrm{s}$ and propagating over large poloidal distances. Hence, the high correlation between both probe arrays is indeed caused by blobs with $l_{\parallel} > l_{\mathrm{OPA}\to\mathrm{TPA}} \approx 1.85\,\mathrm{m}$. Since the connection length between both limiter disks is of the same order of magnitude ($l_{\mathrm{SOL}} \approx 2.79\,\mathrm{m}$) it is assumed that $l_{\parallel} = l_{\mathrm{SOL}}$.

7.1.2   Field alignment

It was found that blobs in the SOL are extended along the magnetic field lines between the two limiter disks. Using the PPAs it is possible to check if these

structures are perfectly aligned with the magnetic field lines or if there is a resolvable tilt (indicated schematically in Fig. 7.1), as was found for drift waves in the confined plasma of TJ-K [110].
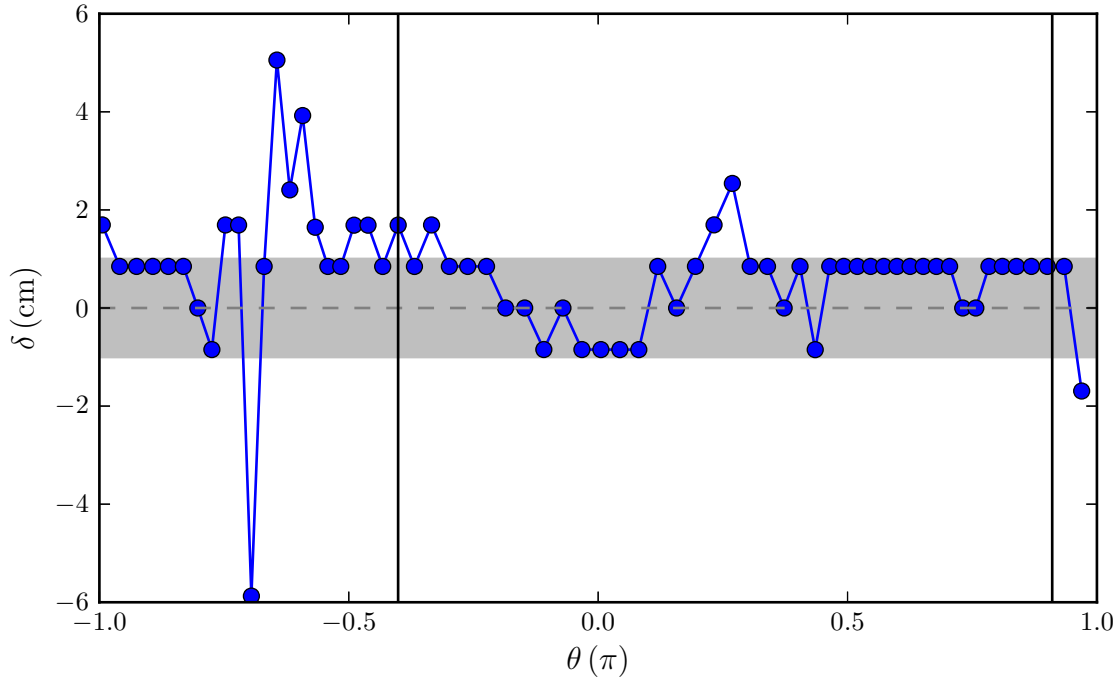

Figure 7.4: *The CC maxima between ion-saturation current measurements (#8355) from each OPA probe to every TPA probe are determined and the distance δ to the field line that connects the OPA probe to the TPA plane is deduced. Perfectly field aligned structures have a δ = 0. The accuracy of the measurement is ≈ 1 cm. The vertical lines mark the region where high correlation values (> 0.5) are found between both PPAs. In this region, most of the points are showing a deviation smaller than 1 cm.*

To this end, the CCF($\tau = 0$) was evaluated for each OPA probe with every TPA probe as before and the TPA probe position with the highest correlation was identified. The distance δ was computed between the probes showing the highest CC values and the point where the magnetic field line crosses the poloidal plane at the toroidal position of the TPA (see Fig. 7.1) with an uncertainty of 1 cm due to the probe spacing. The result of this analysis is shown in Fig. 7.4. The two vertical lines mark the region where a high correlation between the two arrays was found in Fig. 7.2. Outside of this region, the results of this analysis are not reliable, since no clear structures exist. For almost all points inside this region the measured deviation from the field line is smaller than the accuracy of 1 cm. Hence, within the experimental resolution no tilt between the field lines and filaments is found in contrast to drift waves in the edge, for which a δ of about 2 cm is reported for comparable distances in Refs. [110, 119].

7.1.3   Blob region in the SOL of TJ-K

The measurements with the poloidal probe arrays revealed that blobs are observed in specific parts of the SOL. This section is dedicated to the systematic investigation of this effect. The method chosen for this was demonstrated in a bachelor's thesis performed at TJ-K [112] and makes use of the fact that the blobs propagate both radially and poloidally. After a blob is generated it propagates radially outwards and is detected as soon as it reaches a probe i on one of the probe arrays. Due to the poloidal propagation, the blob also travels to another probe on the same probe array. This leads to characteristic traces in the correlation data when evaluating the cross correlation functions (CCF) for one probe with all other probes on the same probe arrays. The resulting CCFs can be visualized as a function of time and poloidal angle of the probe. The traces are then seen as stripe-like patterns as shown in Fig. 7.5 a). The tilt of the stripes reflects the poloidal propagation. By varying the reference probe position i, it can be determined at what probe positions blobs do exist. A comparison of the CCFs for different reference probes and for the OPA as well as the TPA is shown in Figure 7.5. In the top row, the results for the OPA are shown, where in a) the reference probe is located at the inboard side and in b) at the outboard side. In agreement with the correlation analysis with the OPA and the fast camera presented in Fig. 7.3, no quasi-coherent structures are observed for the reference probe on the inboard side. The same situation is shown in the bottom row for the TPA, again for a reference probe at the inboard side in c) and one on the outboard side in d). A similar analysis for the reversed magnetic field direction is shown in Fig. 7.6. It can be seen that blobs are observed at different poloidal angles as in the standard field case and that the poloidal propagation direction is reversed, which is in agreement with a poloidal propagation according to the $\mathbf{E} \times \mathbf{B}$ background drift. The region in TJ-K where blobs are observed, the *blob region*, is marked for the OPA and the TPA by the horizontal lines in Fig. 7.5. The blob region is observed at different poloidal angles at the OPA and the TPA. Due to their poloidal propagation, the blobs enter the blob region from one edge and propagate to the other. For the blob region, the beginning is the point the blobs move poloidally away from and the end is the point the blobs move towards. Hence, in the standard magnetic field case, the beginning is at negative poloidal angles and in the reversed field case at positive poloidal angles. Field line tracing reveals that in both magnetic field configurations, the beginnings of the blob region observed at the OPA and the TPA are connected via a field line. This is not the case, however, for the ends of the blob region, which is probably a detection issue, since the radial position and shape of the blob changes over time.

It can be concluded that the region in the SOL of TJ-K where blobs are observed, is a poloidally extended band that twists toroidally around the plasma, following roughly the helical magnetic field lines. This is in agreement with the observation, that the blobs are elongated along the magnetic field. Hence, there is a toroidal asymmetry in the sense that poloidally resolved measurements in the SOL give
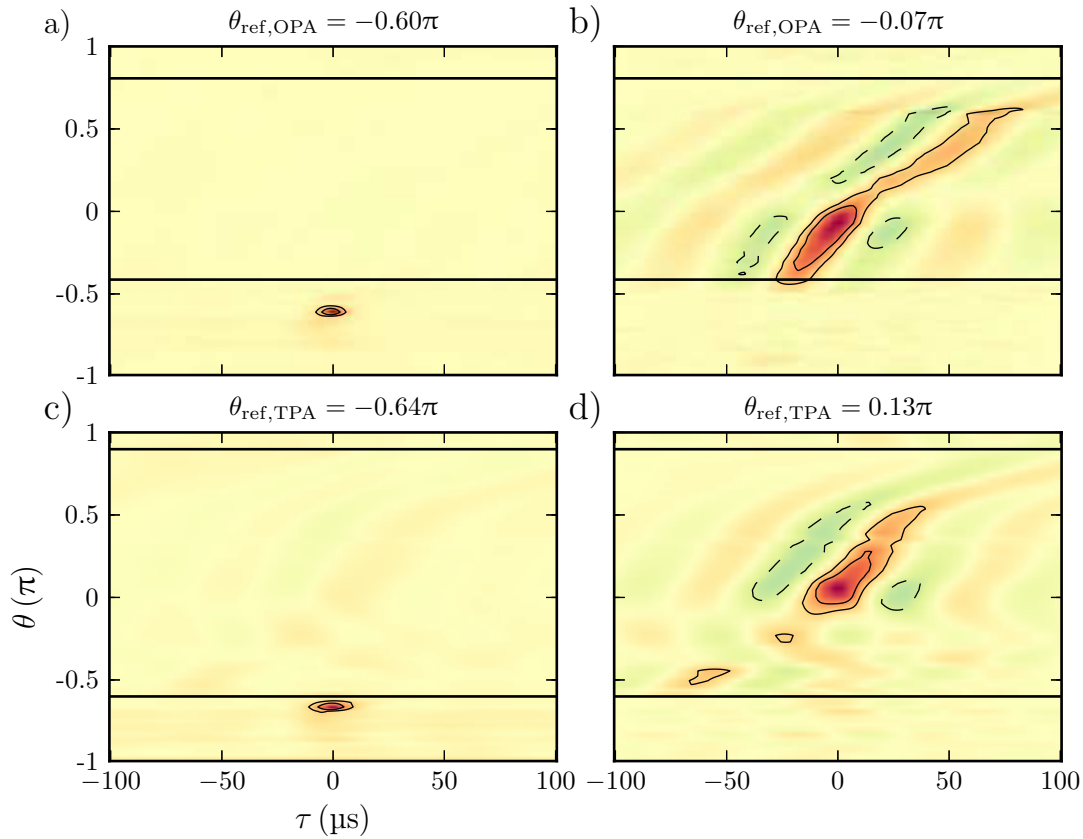
Figure 7.5: *CC of different reference probes on the OPA (top row) and TPA (bottom row) with all other probes on the same probe array (#8355). Positive CC values are shown in red with closed contour lines, negative ones in blue with dashed contour lines. Stripe-like patterns point to the existence of blobs as was explained in the text. In a) and c) the results for reference probes are displayed where no blob activity is observed. In b) and d) the reference probes are located in the region inside of the horizontal lines, the range of poloidal angles where blobs do occur.*
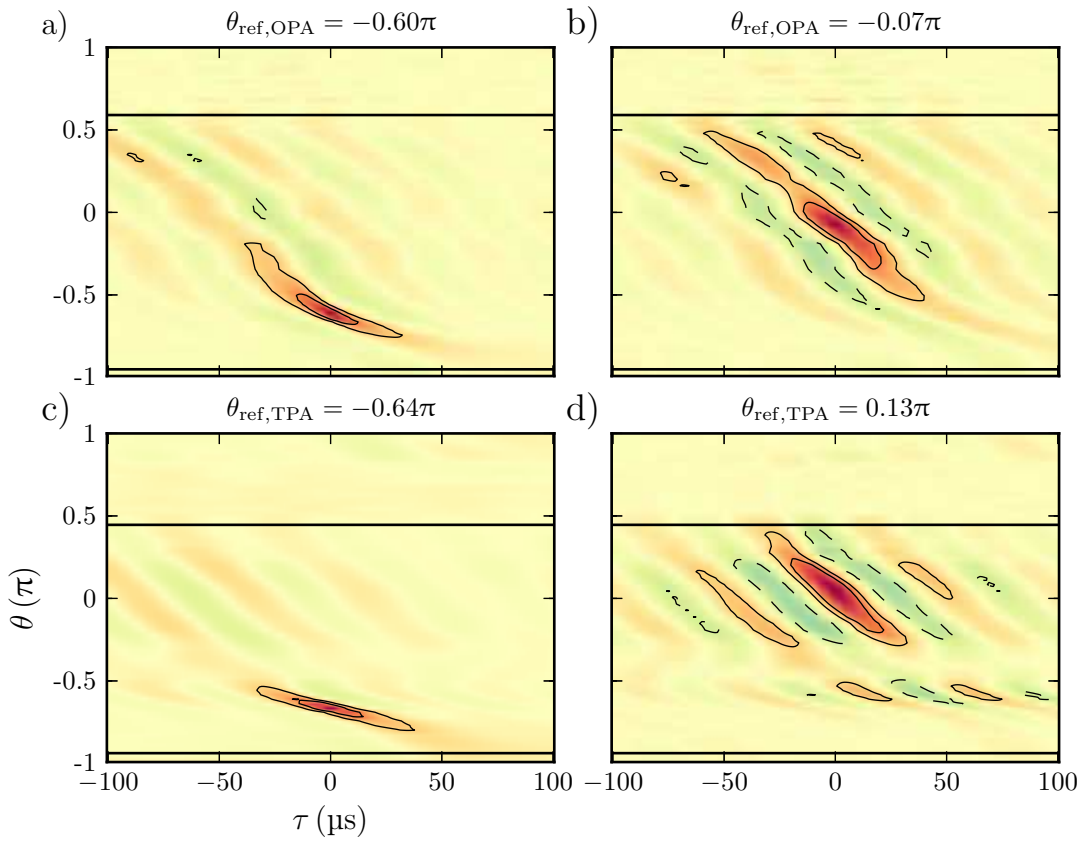
Figure 7.6: *Same representation as in Fig. 7.5, but this time with reversed magnetic field. Using the same reference probes, it can be seen in a) and c) that blobs are present in regions where they are not observed in the forward field case. For the reference probes in b) and d), the results are comparable to the standard field case, only the poloidal propagation direction is reversed.*

different results depending on the toroidal position.

7.1.4   Role of the mean normal curvature

According to the blob theory summarized in Sec. 3.2, blobs are driven by the interchange mechanism, which can exist in regions of negative normal curvature κ_{n} (see Sec. 2.2). If blob generation would be driven mainly by local quantities, the SOL region where blobs occur should feature the same six-fold toroidal symmetry as the magnetic field of TJ-K. As was illustrated in Sec. 7.1.3, this is not the case. Instead, the blob region follows the magnetic field lines, implying that field line averaged quantities are of major importance. The information that the blob length is comparable to the SOL connection length is necessary to specify the boundary conditions for averaging the normal curvature along a filament. To determine the corresponding field line and the normal curvature, field lines were traced numerically with the code MCC [120]. The mean normal curvature was approximated by the following discrete definition

$$\langle \kappa_{\mathrm{n}} \rangle \approx \frac{\sum_{j=1}^{N} \kappa_{\mathrm{n},j} \cdot |(\mathbf{r}_{j+1} - \mathbf{r}_j)|}{\sum_{j=1}^{N} |(\mathbf{r}_{j+1} - \mathbf{r}_j)|} \, , \tag{7.1}$$

where the $\mathbf{r}_j$ denote the locations of the N discrete grid points of the traced field line segment between the limiter disks (ordered by ascending toroidal angle) and $\kappa_{\mathrm{n},j}$ is the normal curvature of the magnetic field at $\mathbf{r}_j$. Both the local κ_{n} and the averaged $\langle \kappa_{\mathrm{n}} \rangle$ are shown as a function of the poloidal angle in Fig. 7.7 a) at the toroidal position of the OPA and in b) for the TPA. It can be seen that for both probe arrays, neither the region of negative κ_{n} nor $\langle \kappa_{\mathrm{n}} \rangle$ matches the blob detection region identified in the last section.

The poloidal propagation direction is marked in the figures by the black arrow. Hence, the left edge of the blob region (gray area) marks the beginning of the blob region and the right edge the end. The beginning of the blob region, at low poloidal angles θ, is for both poloidal probe arrays located close to the zero crossing of $\langle \kappa_{\mathrm{n}} \rangle$, while κ_{n} is positive for the TPA and negative for the OPA. For both arrays, the beginning of the blob region is shifted in the poloidal propagation direction. The end of the blob region is located in regions where both $\langle \kappa_{\mathrm{n}} \rangle$ and κ_{n} are positive at the same time, i. e. where according to theory the blobs should be damped.

According to 7.7 b), blobs can be generated in regions where κ_{n} is positive. A possible explanation is that blobs are generated in regions where $\langle \kappa_{\mathrm{n}} \rangle < 0$, but due to their poloidal propagation, they can then enter stable regions where $\langle \kappa_{\mathrm{n}} \rangle > 0$. That this propagation in stable regions indeed happens can be seen in Fig. 7.3 c). There, a high correlation is found between a reference probe outside of the region of $\langle \kappa_{\mathrm{n}} \rangle < 0$ and the image data, which shows a blob originating from low poloidal angles (inside the region of $\langle \kappa_{\mathrm{n}} \rangle < 0$). The hypothesis that blobs are generated where $\langle \kappa_{\mathrm{n}} \rangle$ is negative was checked by reversing the direction of the magnetic field.
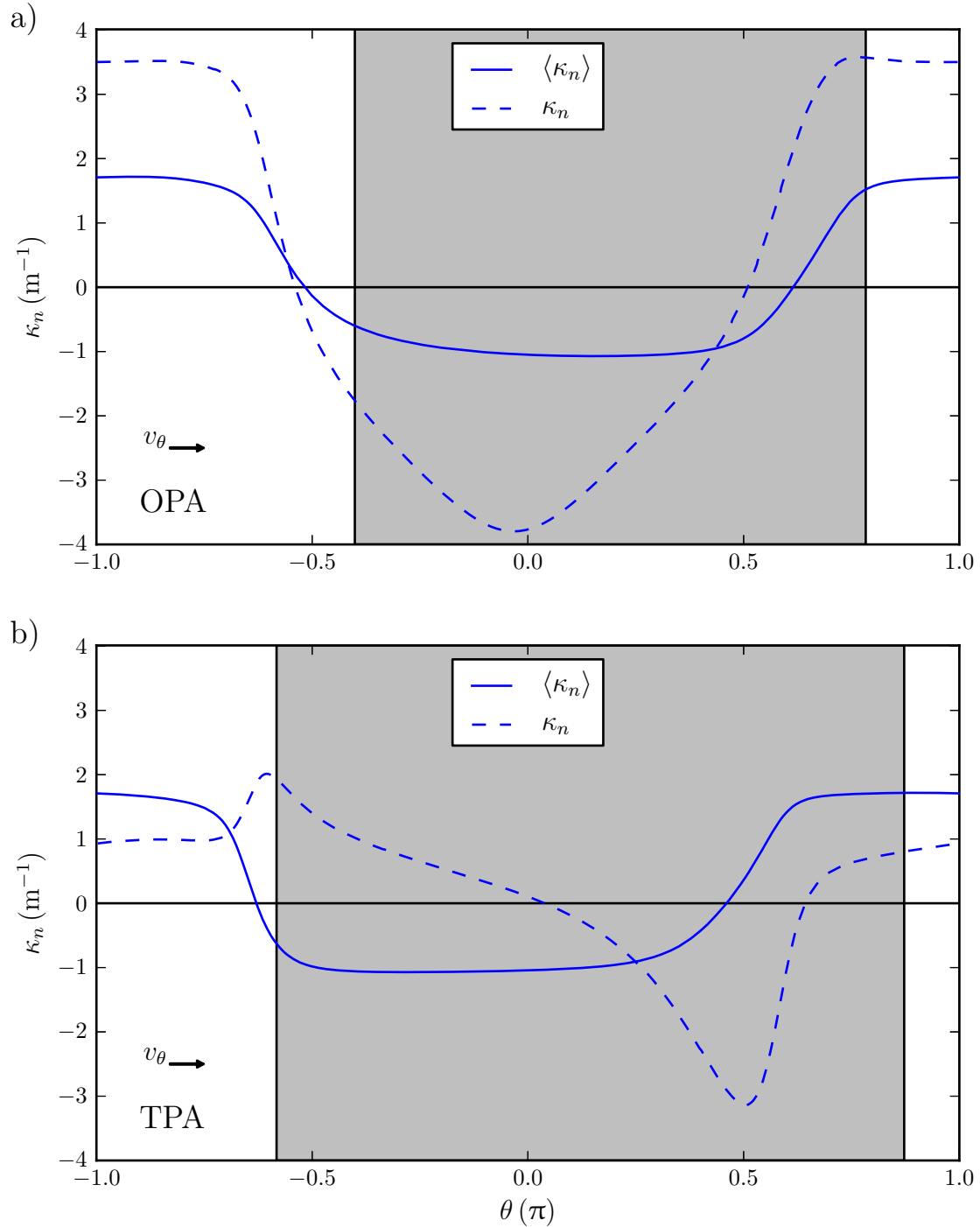
Figure 7.7:   *Local and averaged normal curvature (κ_n and $\langle\kappa_n\rangle$) as a function of the poloidal angle at the OPA (a) and TPA (b). The gray area marks the region where blobs are observed in #8355. The poloidal propagation velocity of the structures is to the right as indicated by the black arrow.*
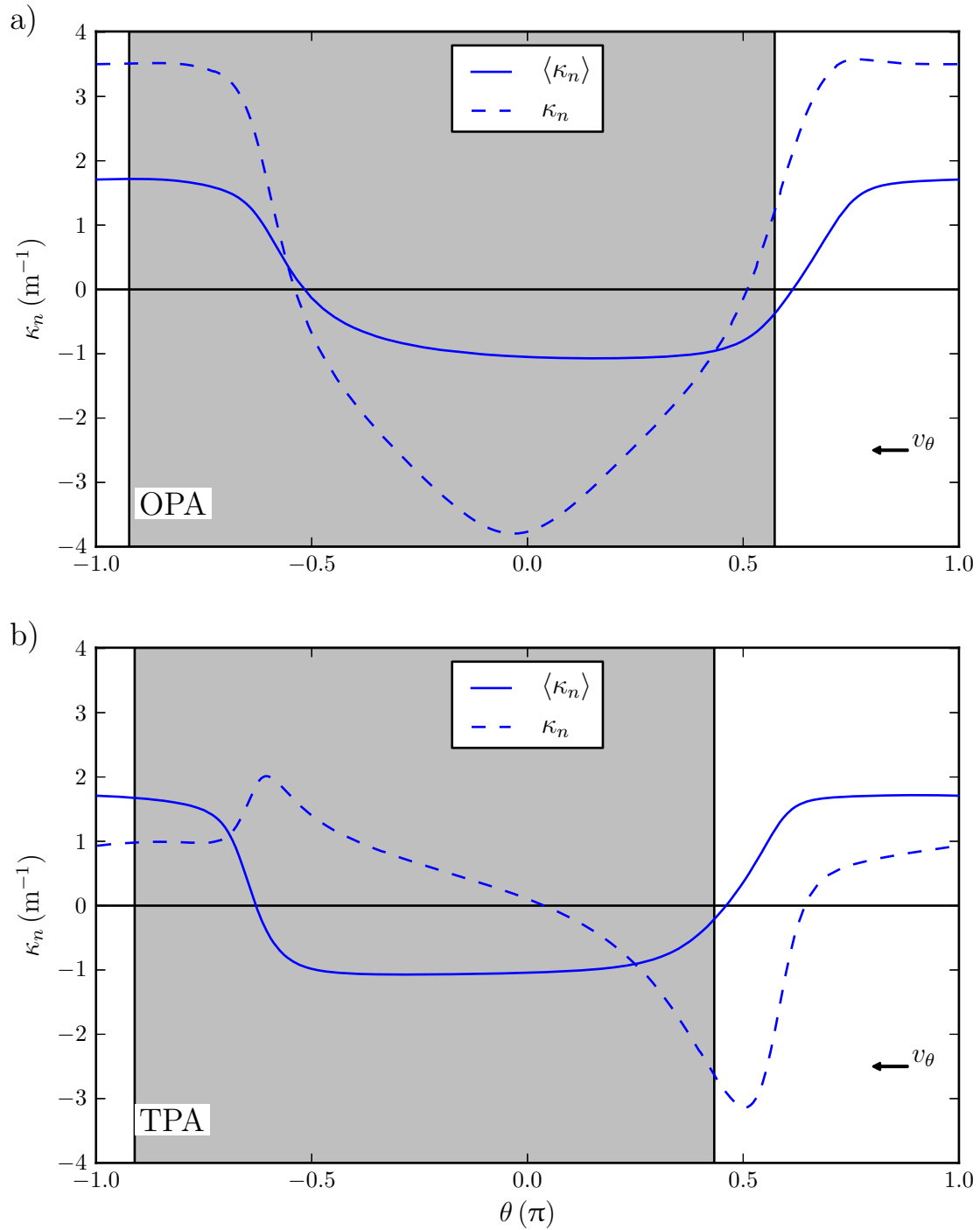
Figure 7.8: *Same representation as in Fig. 7.7, but for the reversed field case (#8352).*

While the normal curvature is unaffected by the field reversal, the poloidal propagation direction of the blobs is reversed. The blob region should then start at higher poloidal angles (right side) close to the zero crossing of $\langle \kappa_n \rangle$ and end at smaller poloidal angles in a region, where $\langle \kappa_n \rangle$ is positive again. Figure 7.8 shows for the OPA in a) and the TPA in b) that this is indeed the case. The propagation of turbulent structures from unstable into stable regions is an effect related to turbulence spreading. Here, turbulence spreading refers to the propagation of turbulent structures into regions, which themselves are stable against this kind of instability (according to Refs. [121, 122]).

Local variations of $\langle \kappa_n \rangle$ explain the observed blob region and in particular its toroidal asymmetry. The location of the limiter disks determines $\langle \kappa_n \rangle$ at a specific location in the SOL and, hence, the limiters are breaking the toroidal symmetry of blob generation.

7.1.5   Generation region

As described above, blobs occur in a specific region in the SOL, defined as the blob region. However, it was already seen in Sec. 6.3.2 that even in this region the blobs are distributed very inhomogeneously. There exists a relatively small region where the majority of all events is detected. The poloidal probe array measurements revealed that the blob filaments are elongated along the magnetic field and extend between the two limiter disks installed for the measurements. Due to the helical field the observed poloidal asymmetry varies depending on the toroidal position of the measurement. Figure 7.9 shows two 2D histograms of structures detected by the object recognition method in the camera data of discharges #7508 and #7512 (see Sec. 6.3.2 for a detailed description of how these histograms are obtained). The left histogram shows a more outward view than compared to the right histogram. The dashed line (blue) in the left histogram and the line (blue) in the right histogram depict the LCFS projected from the focused plane. As was shown in Sec. 6.3.2, in the lower parts of the SOL the LCFS in the focused plane is well captured by the camera. Both histograms show a large number of detected events in the lower right part of the image. It seems that many blobs are generated around $(R - R_0, z) \approx (7, -7)$ (at port O6), which then propagate poloidally upwards (counterclockwise in the images), until they reach the outer SOL parts. Hence, in the poloidal cross-section, a small area seems to exist, where most of the blobs originate from. This region is referred to as generation region in the following. Possible explanations for the existence of the generation region will be discussed in Sec. 9.1.

The existence of the generation region has a huge influence on measurements of blob properties in TJ-K, since the large number of blobs in this region guarantees sufficient detection rates for a statistical treatment of the measured quantities. Note that the optical setup analyzed in Ch. 6 is already specifically designed for measurements in the generation region.
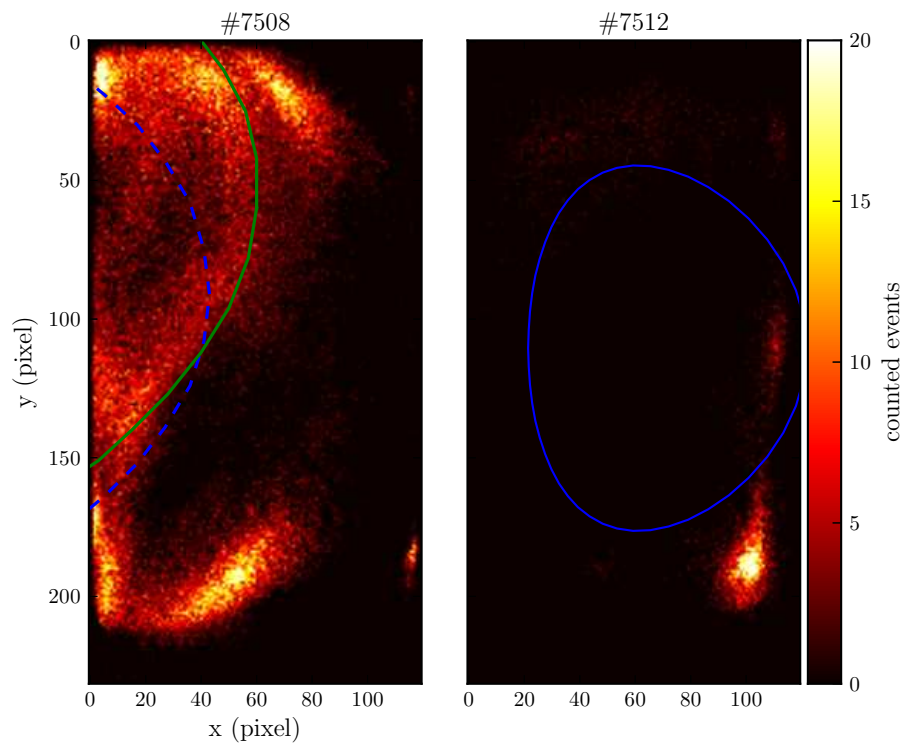
Figure 7.9: *2D histograms of events detected with the object recognition method in two similar helium discharges. The left histogram shows a more outward view compared to the right one. In the left, the dashed line (blue) represents the LCFS in the focused plane and the green line the LCFS as seen by the camera. In the right histogram, only the LCFS in the focused plane is shown, since in the lower parts of the image the two coincide.*

7.1.6 Poloidal cross section

So far, it was possible to reveal a distinct region, where filaments with a parallel extension in the range of the SOL connection length exist, which feature both a poloidal and radial propagation. To complete the characterization of the blobs in TJ-K, their poloidal cross section at an outer port position is determined.

In the conditional average of 2D probe scans, three characteristic phases in the evolution of the blob can be identified. In the growth phase, the blob is very small and shows a circular or elliptical cross section. This growth can be seen by comparing Fig. 7.10 a) and b). In a), a scarcely noticeable positive density structure is seen in the lower part of the SOL (near the bottom left edge of the figure), which has grown in size in b). In the detachment phase, Fig. 7.10 c) and d), the blob has grown in size and detaches from the confined bulk plasma. In the laboratory frame the isolated SOL structure propagates in the ion diamagnetic direction, which agrees with the direction of the $\mathbf{E} \times \mathbf{B}$ background drift. This indicates a change in the dynamics of the structure from drift-wave like dynamics to a predominant interchange-like behaviour. Additionally, the blob moves radially outwards and its size and shape vary only marginally. In a third phase, the blob reaches the outer SOL region, where the connection length is no longer constant because the filament has direct contact to the outer walls. This is associated to a dramatic change in the shape of the blob, which form a complex, wedge-like shape, as can be seen in Fig. 7.10 e) and f). The blob continues to propagate poloidally in the ion diamagnetic direction. It is observed in the conditional average, Fig. 7.10 f), that during this prolonging propagation, the density blob spreads out and covers a large area in the poloidal cross section of the SOL. The single blob is no longer clearly distinguishable from surrounding perturbations, which renders an exact assessment of the radial propagation velocity impossible. The second phase is best suited for a comparison of the blob dynamics with the analytical theory described in Sec. 3.2. The blob properties can clearly be determined in that phase and seem to be relatively constant on the propagation time scale $\delta_{\mathrm{b}}/v_{\mathrm{b}}$. In this detached phase, the perpendicular blob size is on the centimeter scale, i. e. $\delta_{\mathrm{b}}/l_{\parallel} \approx 10^{-2}$ and $\delta_{\mathrm{b}}/\rho_s \approx 10$. A systematic study of the blob size, velocity, and its scaling with ρ_s is presented in Ch. 8.

7.1.7 3D visualization of blobs

This section gives a graphical summary of the results of the blob shape presented above. From the fact that filaments in TJ-K expand between the limiter disks and are aligned with the field lines it follows that from a measurement of density fluctuations over a poloidal cross section of the SOL, it is possible to reconstruct the whole filament. In order to do such a reconstruction, the center of mass of the density structure in the 2D CA data of the probe measurements is deduced and the field line which crosses this center of mass in the scanned 2D plane is traced between
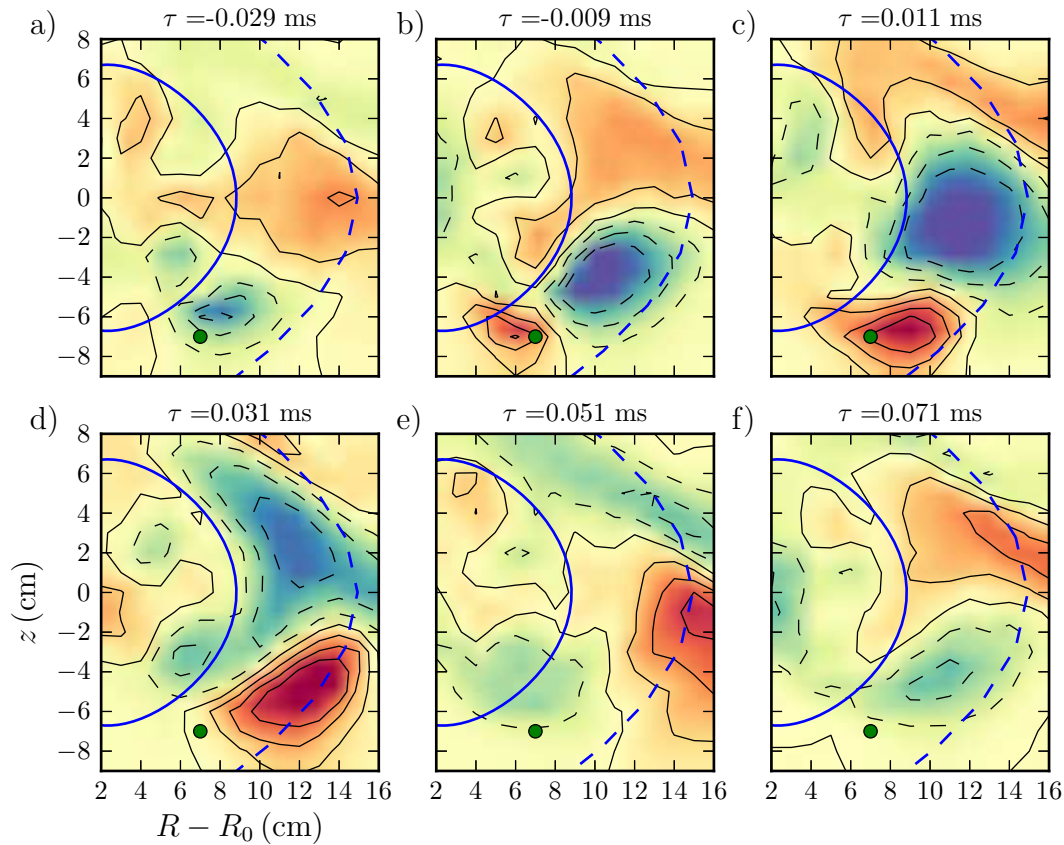
Figure 7.10: *CA of ion-saturation current fluctuations during blob events in a hydrogen discharge (#8213). Positive density fluctuations are shown in red (closed contour lines), negative ones in blue (dashed contour lines). The reference probe is marked as a dot (green), the LCFS as closed line (blue) and the edge of the L-SOL as dashed line (blue). From a) to b), a blob grows near the reference probe. In c) and d) this blob propagates radially outwards and poloidally in the ion diamagnetic drift direction. In e) and f) the blob reaches the region with open field lines, which end on the wall and not on the limiters. The shape of the blob changes drastically in this last phase.*

the two limiter disks. A circular cross section of the blob is assumed and is also traced along the magnetic field. Figure 7.11 shows such a 3D reconstruction from a conditionally averaged 2D measurement of ion-saturation current fluctuations, which gives an impression of the spatial structure of a blob and its propagation. The filament is visible in the SOL and as the time proceeds, it propagates radially outwards and poloidally into the ion diamagnetic drift direction.
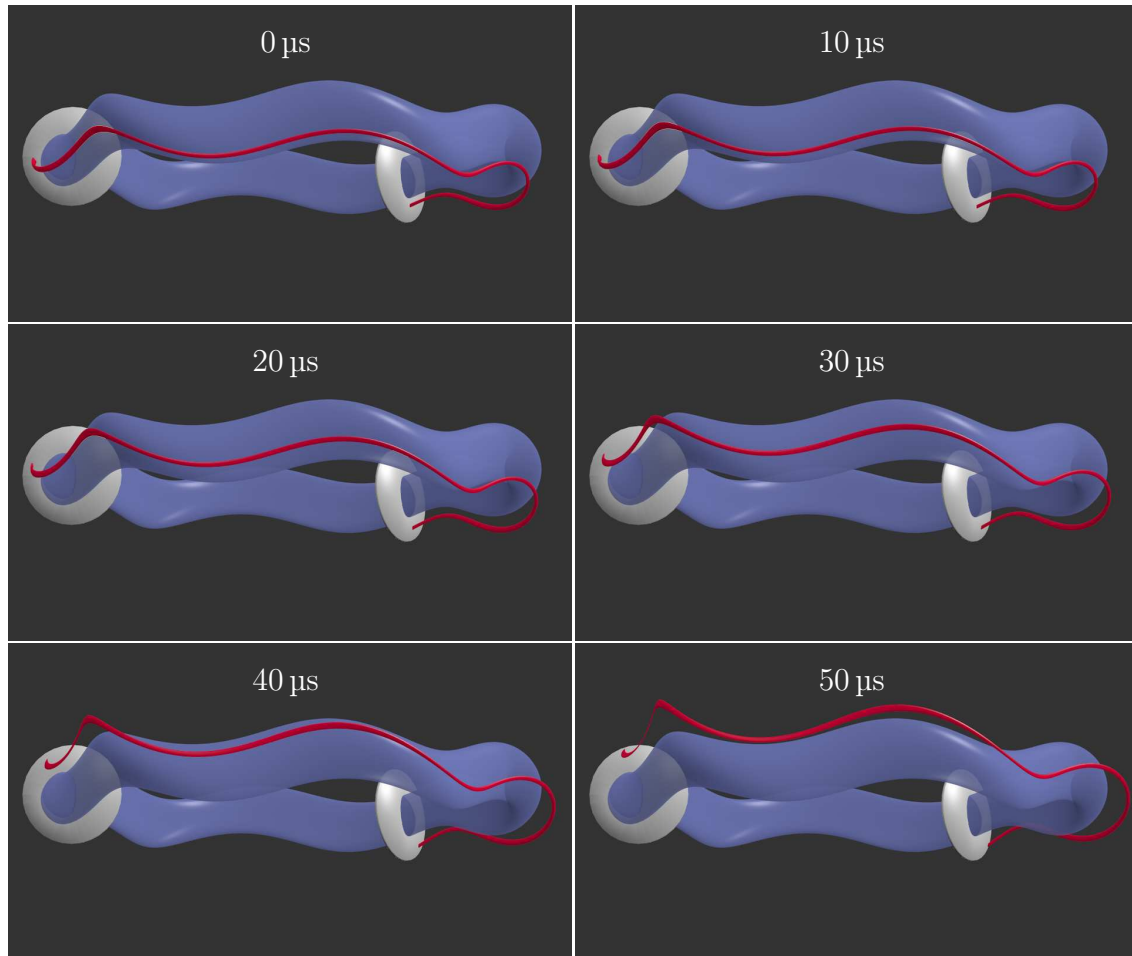
Figure 7.11: *3D reconstruction of a blob from 2D CA probe data. The confined plasma of TJ-K in the limiter configuration is shown in blue, the two limiter disks in gray, and the blob filament is shown in red. Depicted is the blob evolution in* 10 µs *steps. The blob features a poloidal and radial propagation.*

7.2   Blob induced transport

It is shown in Sec. 4.4.1 that the probe arrays can be used to measure the turbulent transport. In this section the contribution of blobs to the local and total (summed

over the whole probe array) transport is investigated. Both the peak transport and the transport averaged over a blob event can be deduced.

One possibility to do this is to conditionally average the transport over all events exceeding a specific density fluctuation threshold. This way, the time duration of all averaged events together, T_{CA}, is recorded (number of trigger events multiplied by the chosen time interval length around the trigger events). This CA is then compared to the transport averaged over the complement of the time trace ($\bar{T}_{\mathrm{CA}}$), where no large amplitude events occur. The relative importance of blobs to the transport can than be estimated by

$$f_{\mathrm{blob}} = \frac{\langle\Gamma\rangle_{T_{\mathrm{CA}}} - \langle\Gamma\rangle_{\bar{T}_{\mathrm{CA}}}}{\langle\Gamma\rangle} \cdot \frac{T_{\mathrm{CA}}}{T_{\mathrm{CA}} + \bar{T}_{\mathrm{CA}}} \; . \tag{7.2}$$

The difference $\langle\Gamma\rangle_{T_{\mathrm{CA}}} - \langle\Gamma\rangle_{\bar{T}_{\mathrm{CA}}}$ estimates the contribution of blobs by removing the background transport without blobs.

It is shown that high amplitude peaks in both the local and total SOL transport are caused by blobs and that these peaks contribute significantly to the turbulent transport.

7.2.1 Local transport

In order to assess the contribution of blobs to the turbulent transport, in a first step the camera was used to detect blobs originating from the generation region and conditionally average the corresponding transport as measured by the OPA. The result is illustrated in Fig. 7.12. The CA of the image data (right) shows a blob in the SOL. At the same time, the transport is increased very localized at poloidal angles around $\theta = 0$-0.25π at port O2 (left). The maximum in the local transport occurs at the OPA probe 32, which is located at $\theta = 0.07\pi$. Figure 7.13 shows the CA local transport Γ_{32} measured at that probe position. For a short time during the blob event, the local transport increases by a factor of nine. Of course, the relative importance of blobs depends on the rate with which blobs occur in that region. As described above, this can be estimated by storing T_{CA} during the conditional averaging and compare the transport in blob phases with the average transport. At the OPA probe 32 the fraction that blobs have on the local transport is 95 % for hydrogen and 53 % for helium. Locally, the transport is clearly dominated by blobs.
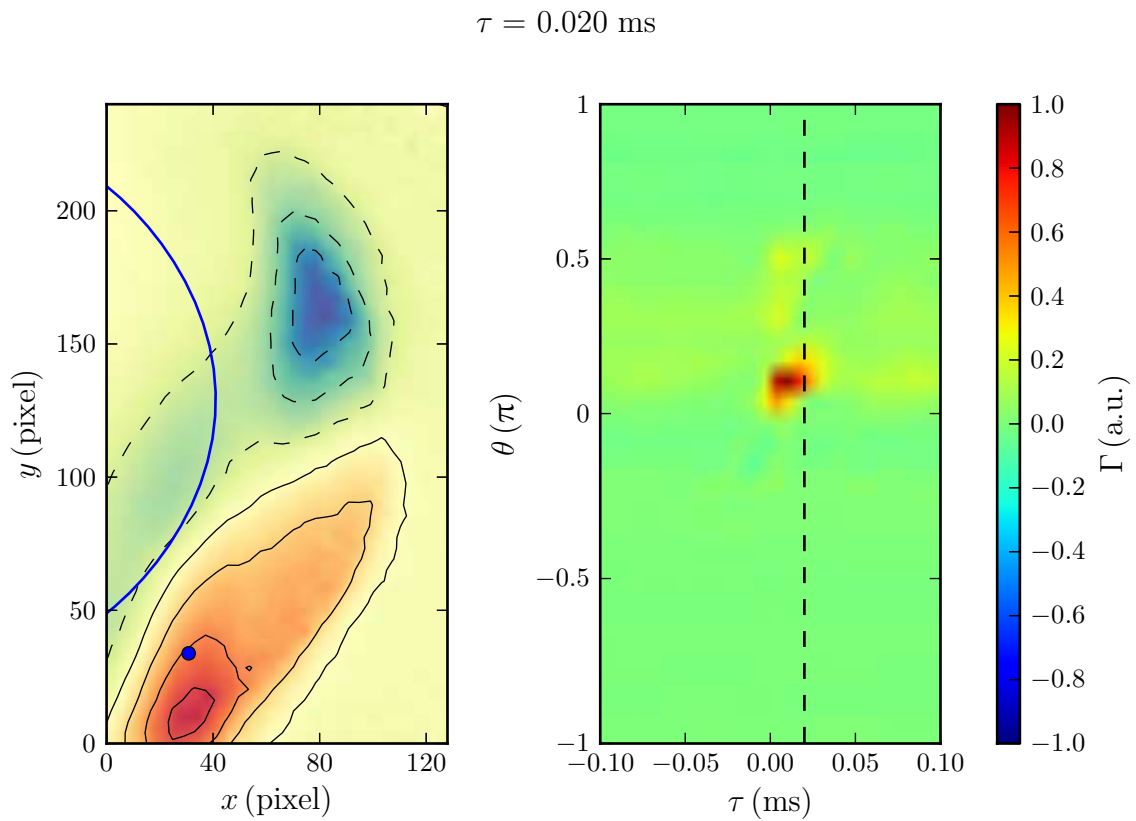
7.2.2 Total transport

The transport measured with the OPA summed over all probes can be used to estimate the total transport $\Gamma \approx \Sigma_i \Gamma_i$. Γ was used to conditionally average normalized intensity fluctuations $\tilde{I}_{\mathrm{n}}$ recorded by the fast camera. The trigger condition was set to two times the standard deviation. The result is shown on the left in Fig. 7.14. A blob originating from the generation region is seen, indicating that a significant fraction of peaks in the total transport corresponds to blobs. On the right hand side

$$\tau = 0.000 \text{ ms}$$
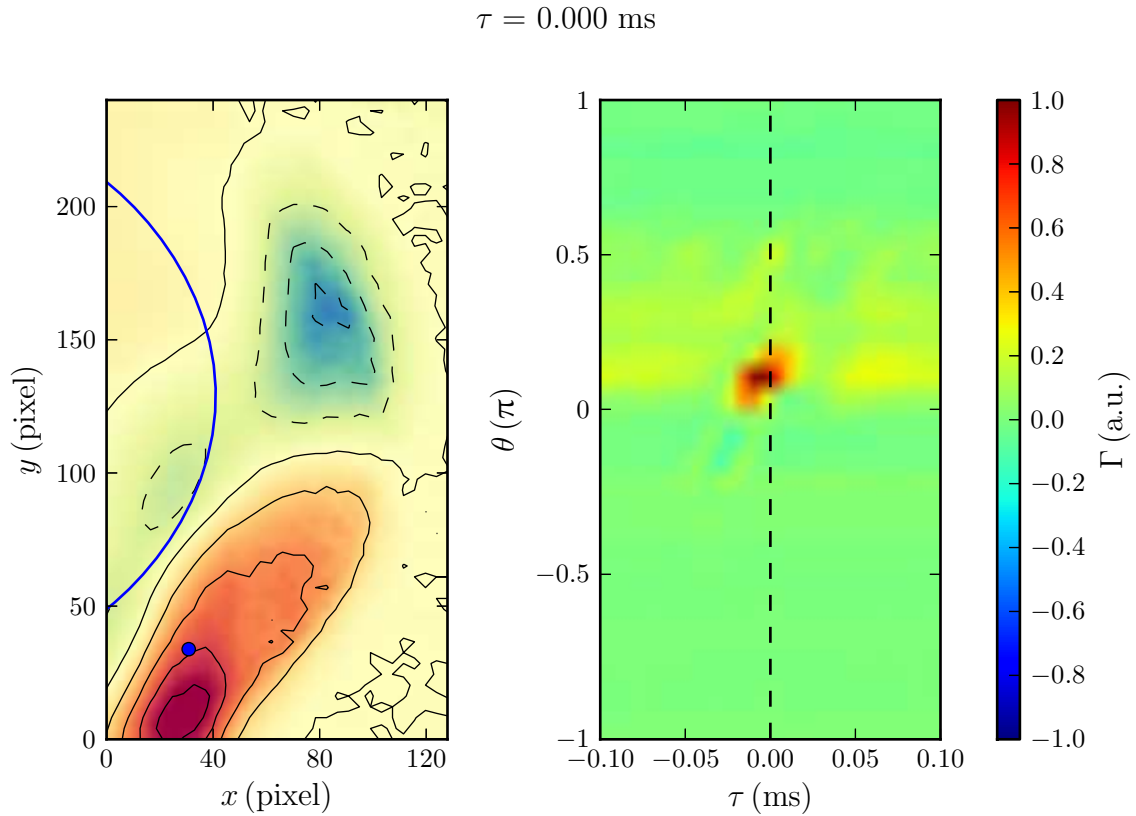
Figure 7.12:   *On the left, the CA of the normalized intensity fluctuations $\tilde{I}_n$ is shown at $\tau = 0\,\mu s$ for #8354. The camera observed the plasma tangentially at port O6. A blob is visible in the SOL. On the right, the CA of the local transport measured by the OPA is shown. The x-axis shows the time lag τ, the y-axis the poloidal angle of the respective OPA probe and the color depicts the local transport Γ_i at that position in arbitrary units scaled to the maximum occuring Γ_i. A localized peak in the transport is associated with the blob. The maximum transport occurs at OPA probe 32 at $\theta = 0.07\pi$. The mapping of this probe position to the camera view is indicated by the dot (blue) in the left figure.*
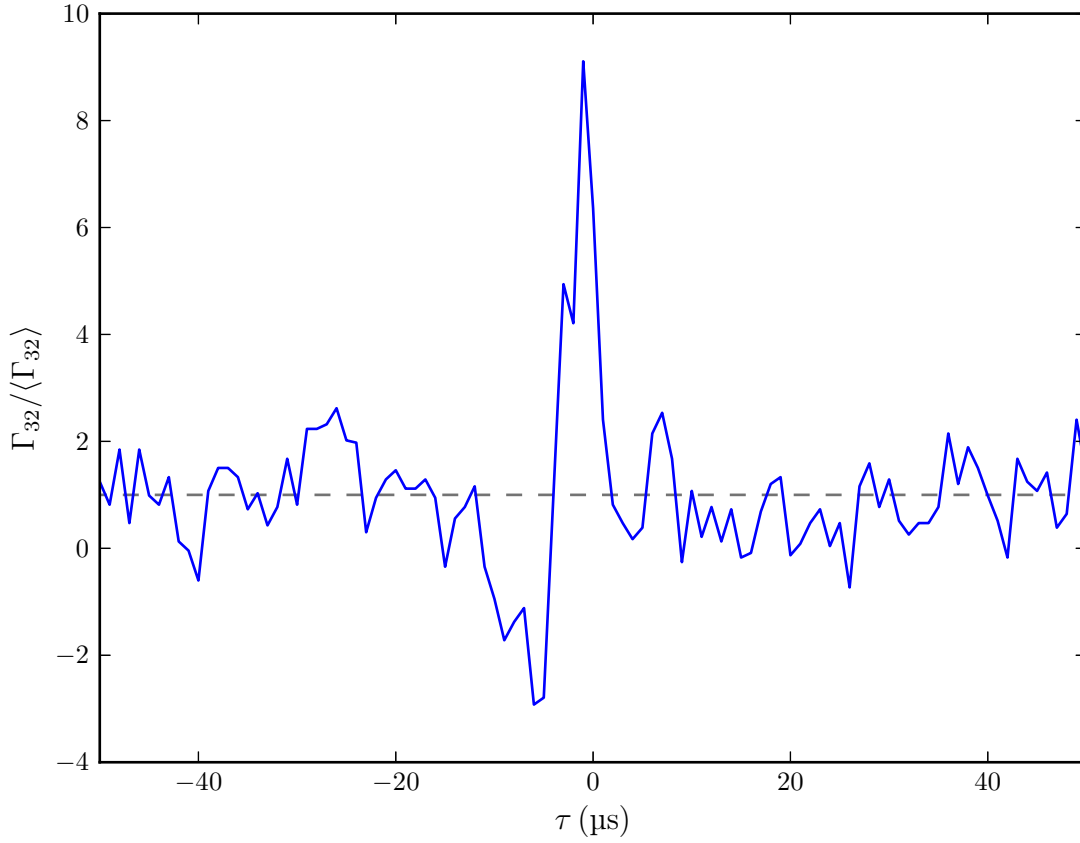
Figure 7.13: *CA of the local transport Γ_{32} at OPA probe 32 ($\theta = 0.07\pi$) normalized to its mean with $\tilde{I}_{\mathrm{n}}$ from the camera data as reference signal for #8354. The dashed line (gray) depicts $\Gamma_{32}/\langle\Gamma_{32}\rangle = 1$, i.e. the average transport level. The local transport is increased during the blob event by a factor of eight.*

Figure 7.14:   *Same representation as in Fig. 7.12, but with the total transport $\Sigma_i\Gamma_i$ as reference is shown for #8354. The results are very comparable. Indicating that local processes play an important role for the total transport.*

of Fig. 7.14, the CA of the local transport is shown. In agreement with the camera data, it resembles the local transport profile already seen in Fig 7.12. Figure 7.15 shows the CA of Γ with itself as reference signal. The total transport during a blob event increases by a factor of five. The relative importance of blobs is estimated by Eq. (7.2). The analysis is done for a helium and a hydrogen discharge (#8355 and #8352). The fraction that large amplitude fluctuations have on the transport is 23 % for helium and 30 % for hydrogen. Hence, blobs indeed do have a significant influence on the total transport in TJ-K. Since the CA only takes largest amplitude events into account, blob induced transport may be of even higher importance.
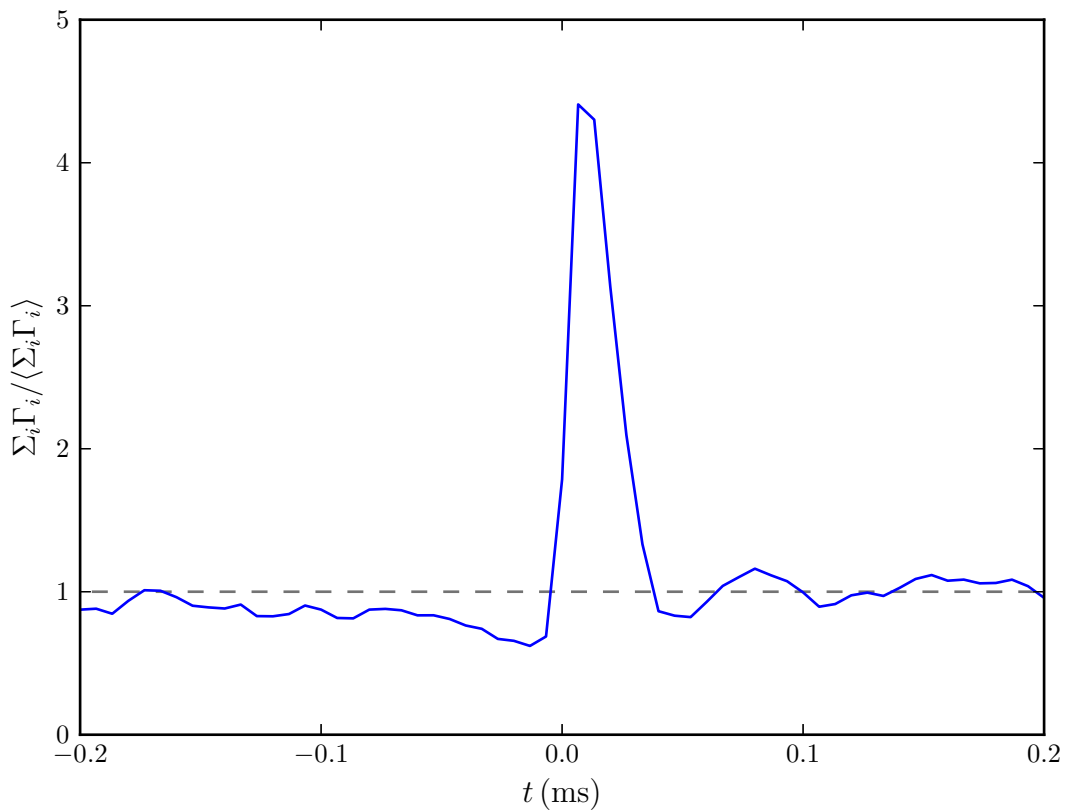
Figure 7.15:   *CA of the relative total transport, i. e. transport summed over all OPA probes and normalized by the mean of this sum, with itself as reference signal (#8354). Fluctuations exist, which increase the net transport temporarily by a factor of five.*

Chapter 8

Blob properties in TJ-K

In this chapter the generation rate together with the waiting-time distribution (WTD), the blobs size δ_b perpendicular to the magnetic field, and the radial blob velocity $v_{r,b}$ are studied. The velocities $v_{r,b}$ are found to agree to a good extent with the theoretical predictions for cold ions (Sec. 3.2.1). This model includes parallel currents along the filaments, which are measured in order to provide further evidence that the observed blob dynamics are indeed well described by this model.

The studies presented had two major goals. The first one was to check the validity of the theoretical predictions for blobs in the stellarator plasma of TJ-K, which features a much more complex magnetic topology than the simple magnetized torus often considered in the analytic treatment of blobs. The second goal was to reveal dependencies of the blob properties that go beyond the present understanding. Especially for the generation rate there is no quantitative prediction, while there are predictions for δ_b for special cases, but almost no experimental effort has been done to verify these. According to Eq. (1.1), understanding of these parameters is crucial to understand and possibly control the turbulent transport caused by blobs. In this work, one focus lies on the connection between the dynamics and properties of the blob and the generating drift wave. Parts of the results on this have already been published in Ref. [123].

The analysis presented here concentrates on blobs originating from the generation region described in Sec. 7.1.5. Since most of the blobs are generated in that distinct region, the number of events detected by the fast camera is high, a few thousands per second, allowing a statistical treatment of the analysed quantities.

8.1 Birth rate of blobs

So far, there is no theoretical prediction for the generation rate of blobs. It is also not clear what influences and determines the generation rate. Prior experiments at TJ-K [48] showed that drift waves in the edge are involved in the blob generation. Hence, the generation rate should be affected by the drift wave turbulence. From the CA, however, it cannot be decided whether each single blob is related to a drift

wave or with what probability an existing drift wave triggers blob ejection. To elucidate this connection, the waiting-time distribution (WTD) and generation rate are compared for drift waves in the edge and blobs in the SOL.
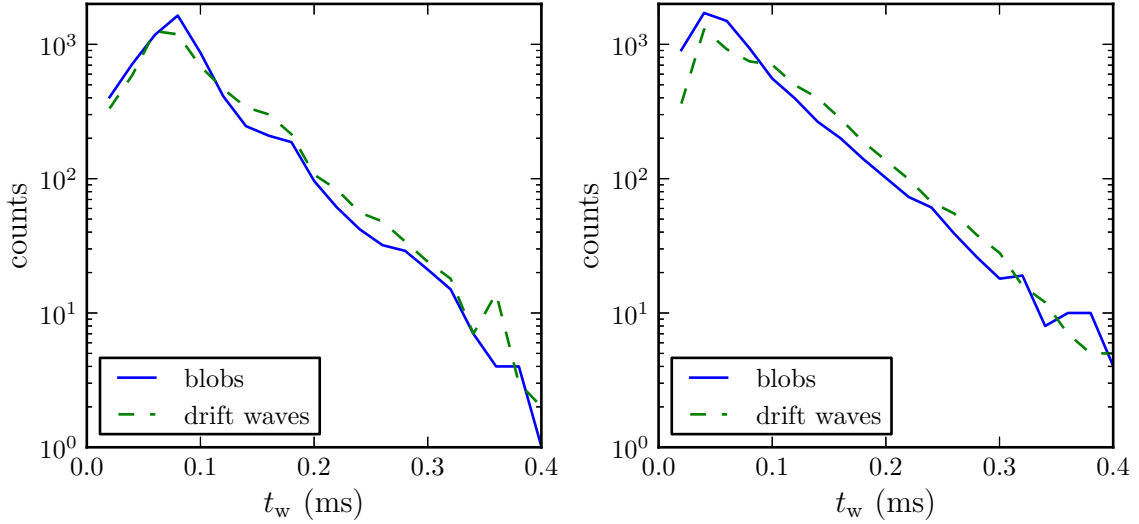
Figure 8.1: *Comparison of waiting-time distributions for blobs and drift waves in a hydrogen (left) and helium (right) low-field discharge (#8213 and #8211) obtained from high-speed imaging.*

The WTD for blobs and large drift waves can be obtained from the image data by the object recognition method described in Sec. 5.6. The occurrence time t_i of structure number i is defined as the time when the intensity amplitude in a small predefined area of the images reaches its maximum during an ongoing event (blob or drift wave). The waiting time between two subsequent events is defined as $t_w = t_{i+1} - t_i$. Figure 8.1 shows the WTDs of blobs and drift waves in low-field hydrogen (left) and helium (right) discharges. For a purely random blob generation process, an exponential decay of the WTD would be expected [124]. Such a behaviour has been found at Alcator C-Mod [125]. In TJ-K, an exponential decay is found for $t_w > 100\,\mu s$. However, there is a clear peak in the WTDs at about $t_w = 90\,\mu s$ (H) and $76\,\mu s$ (He) for both, drift waves and blobs. This feature varies only slightly for discharges with comparable discharge parameters (especially the ion species, magnetic field strength B, and ρ_s), but occurs at different times for the various gases used in TJ-K. For the drift waves in the confined plasma this peak can be understood as follows: If the typical lifetime of the turbulent structures is longer than the time T_t for a complete poloidal transit divided by the poloidal mode number m, the density pattern inside the LCFS recurs after T_t/m due to the poloidal rotation of the drift wave. That this is indeed the case can be seen from Fig. 8.2. It shows two images with a time distance of $\Delta\tau \approx 90\,\mu s$ of the conditionally averaged camera data of a hydrogen discharge. Both images show a comparable density pattern in the confined
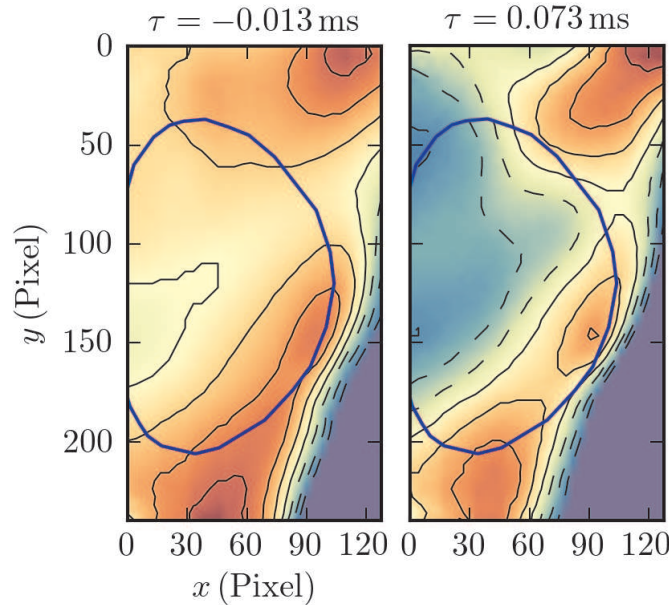
Figure 8.2: *The CA of the camera data reveals a comparable density pattern in the shown hydrogen discharge (#8213) after $\Delta\tau \approx -90\,\mu$s. Both images are scaled to their maximum intensity for better visualization.*

plasma and in the SOL. Experimental values for the dominant poloidal mode number m between three and four, poloidal velocities of the drift waves $\leq 2\,$km/s and a poloidal circumference near the LCFS of $U_{\text{pol}} \approx 50\,$cm yield values for T_{t}/m in the range of 50 to 100 μs, which is in good agreement with the observed peaks in the WTDs. Taking into account the generation mechanism presented in Sec. 6.3.1, it becomes clear that the peak in the WTD for the SOL events is caused by blobs generated at the same location with a time distance of T_{t}/m by separate density maxima of a poloidally rotating drift wave.

This connection is supported even further by comparing the waiting-time distributions for discharges with low and high magnetic field strength. Since the $\mathbf{E} \times \mathbf{B}$ drift velocity scales with $1/B$, the peak in the WTD would have to move to higher values of t_{w}. However, it is also observed that the typical correlation times of drift waves is shorter for the high field discharges with values about $10\,\mu$s. Hence, the lifetime of the drift waves is not sufficient to generate a second blob as described above and the peak should not be present in the WTD at all. The disappearance of the peak in the WTD is illustrated in Fig. 8.3, where a low-field helium discharge (left) and a high-field helium discharge (right) are compared.

Not only the shapes of the WTDs of blobs and drift waves show good agreement, but also the total number of detected events is similar, as can be seen from Fig. 8.1. The detection rates for blobs with intensity amplitudes larger than the standard deviation and density maxima of drift waves are about $10,000$/s for the analyzed discharges. This corresponds to the typical frequency range of a few kHz for the drift-
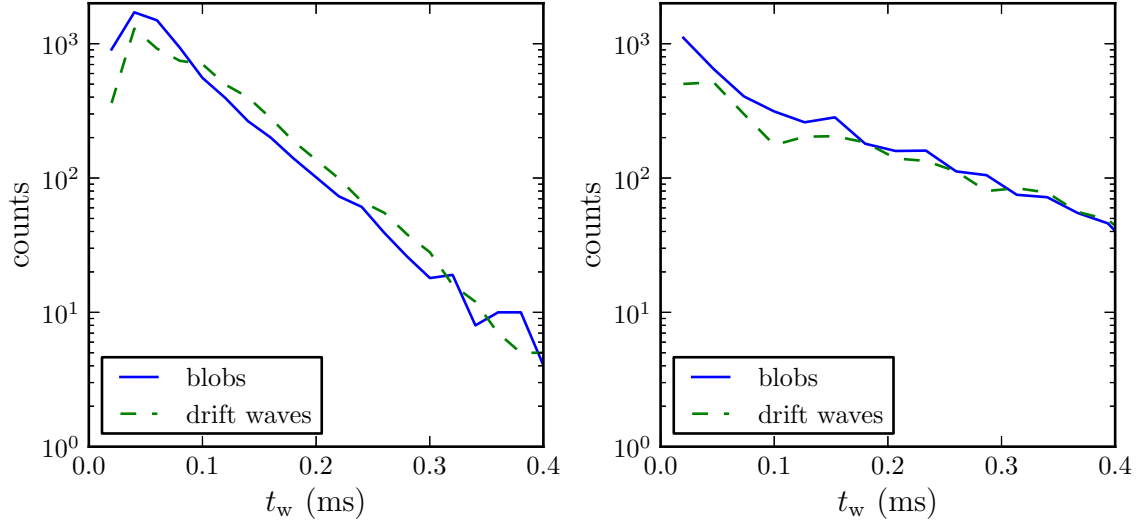
Figure 8.3: *Comparison of waiting-time distributions for blobs and drift waves in a low-field (left) and high-field (right) helium discharge (#8211 and #8212) obtained from high-speed imaging.*

wave turbulence in TJ-K, which reflects that blobs principally appear in conjunction with drift waves.

The results of camera measurements presented here are in agreement with probe measurements in comparable TJ-K discharges, where the peak of the WTD for intermittent structures in the SOL was found close to the drift-wave period [75]. It can be concluded that the generation rate of blobs in the SOL is determined by properties of the drift-wave turbulence in the edge plasma.

8.2   Size scaling

This section investigates the scaling of the structure size δ (perpendicular to the magnetic field) of blobs in the SOL and coherent structures in the edge with the drift scale ρ_s. The results are compared to the prediction from Eq. (3.17) and to the size scaling for coherent structures in the confinement region of TJ-K to study if there is a relation between the size of the blob and the generating drift wave. Prior experiments at TJ-K showed that the size of coherent structures arising from drift-wave turbulence scales as $\delta \propto \rho_s^\alpha$ with $\alpha \approx 0.5$ [70, 126]. However, there were indications that α decreases if the structure size gets too close to the system size, which might be the case for the discharges with limiters presented here.

Here, ρ_s was varied by using different gases (hydrogen, deuterium, helium, neon, and argon) and two different magnetic field strengths. Additionally, for low-field hydrogen and helium discharges, shots with different heating power, and thus different electron temperature, were analyzed. The structure size was determined from

fast imaging data and compared to Langmuir probe measurements, which serve as a cross-check for the sizes deduced from the image data.

It was explained in Sec. 6.3.4 that the camera can measure the blob size δ_{cam} in the observed region and that the resulting quantity is comparable to δ_{p} and δ_{eff} as determined from conditionally averaged ion-saturation current measurements. The background profiles for T_{e} and n_{e} were determined by acquiring Langmuir probe characteristics during a radial probe scan at port O2.

8.2.1   Comparative size scaling

The resulting scalings of the different blob sizes δ_{r}, δ_{p}, δ_{eff}, and δ_{cam} with ρ_s are shown in Fig. 8.4. The different sizes obtained from the probe measurements all yield comparable scaling factors α of about 0.25 and errors of about 0.05 (see Fig. 8.4 for the exact results). The scaling exponent for δ_{cam} is slightly smaller with $\alpha = 0.19 \pm 0.03$. While these differences may arise from the systematic errors of both diagnostics, all scaling exponents agree within the error. The scaling of δ_{r} shows a relatively large scatter, which indicates that there are further influences on the radial size of a blob.

If blobs are generated by drift waves, it is reasonable to assume that blobs also inherit the size properties of drift waves. To elucidate this connection, the drift-wave size scaling was determined. Here, size refers to the typical size perpendicular to the magnetic field of the density maxima of coherent structures arising from drift-wave turbulence. For simplicity this is called drift-wave size in the following.

The resulting scalings for δ_{r}, δ_{p}, δ_{eff}, and δ_{cam} for drift waves are shown in Fig. 8.5. In contrast to the blob sizes, the resulting scaling exponent α is different for δ_{r} and δ_{p}. This behavior has not been observed for drift waves in TJ-K without the limiters [70, 71, 126] and is probably the result of the relatively small cross section of the confinement region in the limiter setup, which also limits maximum structure sizes. Therefore, δ_{r} and δ_{p} may not be resolved properly by the relatively coarse measurement grid of the probe measurements. The effective size δ_{eff}, however, can be determined reliably, since it only depends on the total area covered by the density perturbation. Structure sizes are even smaller in high-field discharges and were not considered in the probe scaling, which mainly served to check the validity of the sizes deduced from the image data.

Since it was observed that the drift-wave size deduced from the camera data, δ_{cam}, agrees particularly well with δ_{eff} (Sec. 6.3.4), those two quantities are most suitable for a comparison of both scalings. For blobs in the SOL, the scaling exponents are $\alpha_{\mathrm{cam}} = 0.19 \pm 0.03$ and $\alpha_{\mathrm{probe}} = 0.27 \pm 0.07$. If the same analysis is repeated for the coherent structures in the confined plasma, the scaling laws with $\alpha_{\mathrm{cam}} = 0.21 \pm 0.03$ and $\alpha_{\mathrm{probe}} = 0.18 \pm 0.05$ are obtained. All exponents are comparable within the error bars. The scaling of the blob size is weaker than the $\alpha = 4/5$ predicted for the most stable blobs according to Eq. (3.17) and weaker than from previous studies, probably due to the reduced size of the confined area. Note, however, that the size
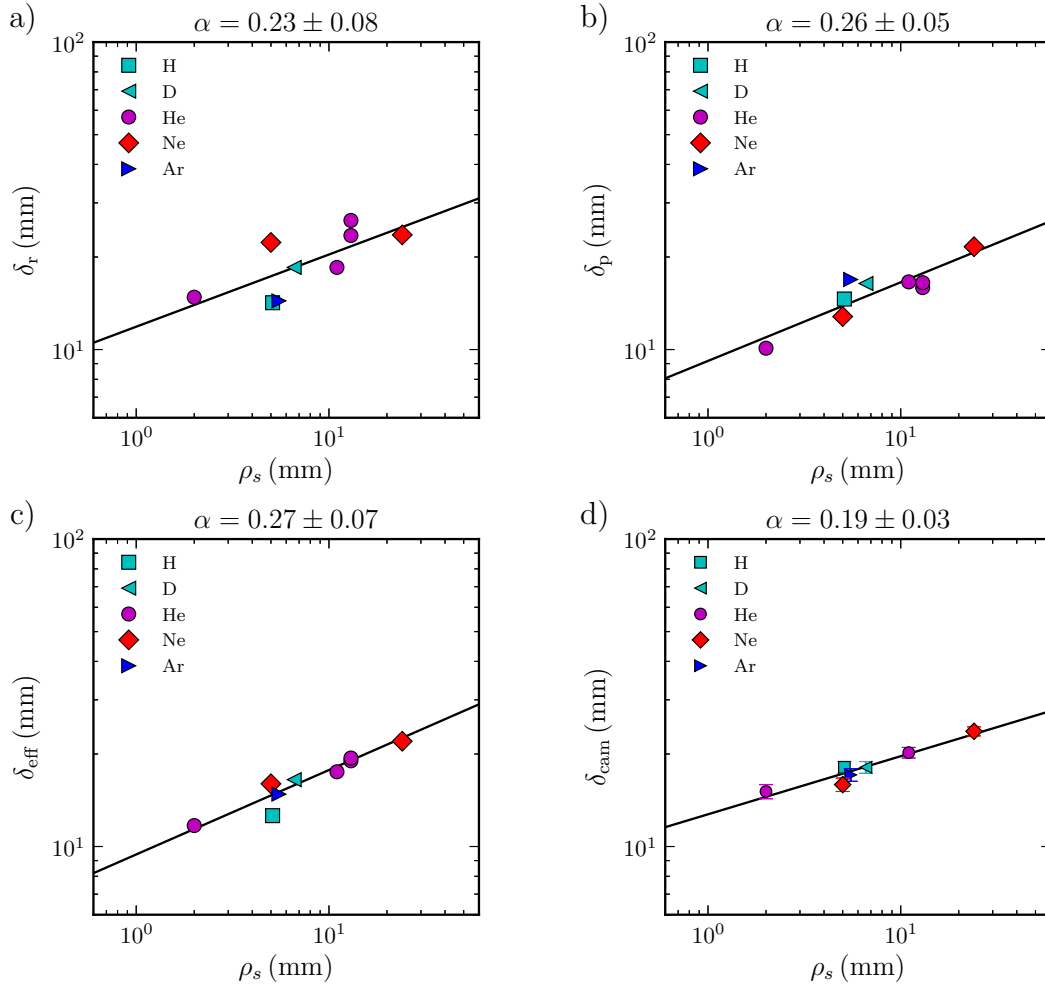
Figure 8.4: *ρ_s-scaling of the different blob sizes δ_r (a), δ_p (b), δ_eff (c), and δ_cam (d). For every blob size, the obtained scaling exponent α is given together with the standard error of the fit. The error bars for the camera measurement are in the range of the symbol size. Since the CA technique is used to determine the size for the probe data, no statistical error is available for the probe measurements.*
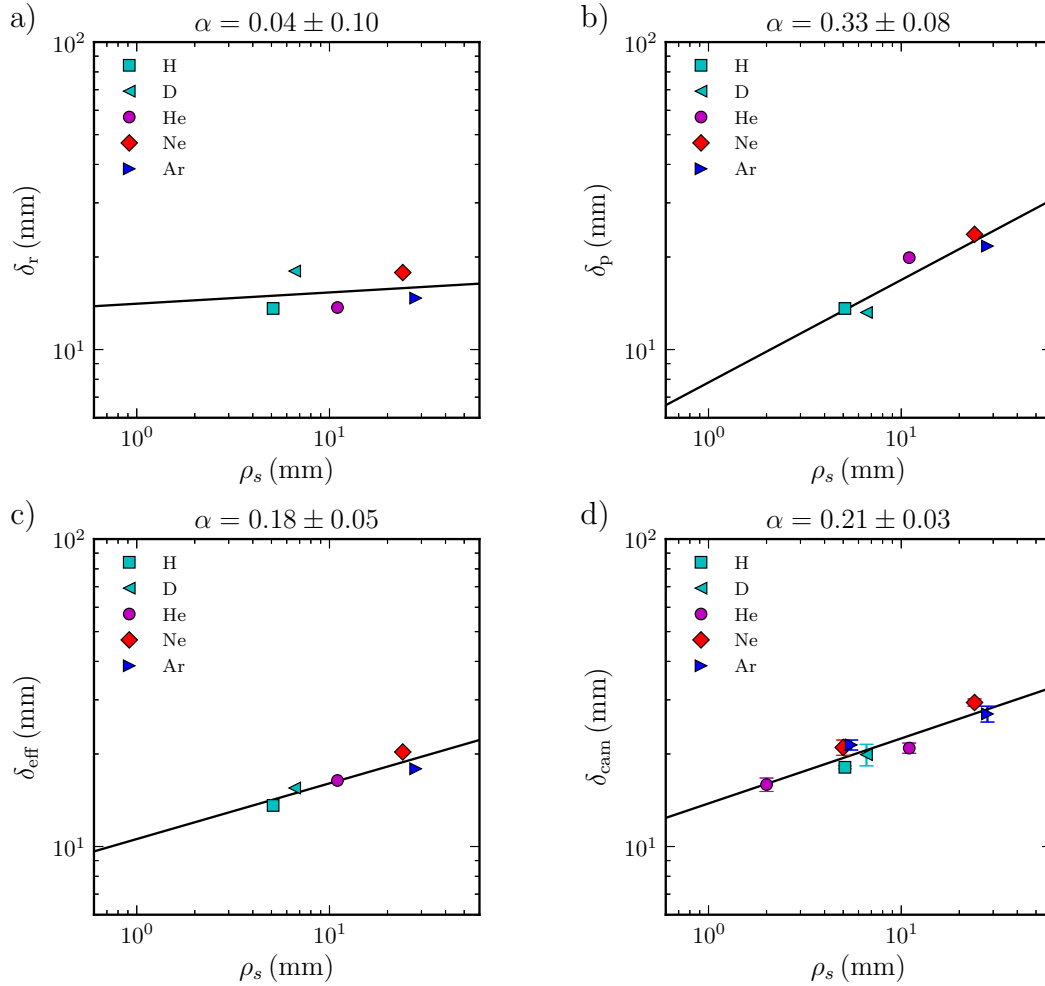
Figure 8.5: ρ_s-scaling of the different drift-wave sizes δ_r (a), δ_p (b), δ_{eff} (c), and δ_{cam} (d). For every blob size, the obtained scaling exponent α is given together with the standard error of the fit. The error bars for the camera measurement are in the range of the symbol size. Since the CA technique is used to determine the size for the probe data, no statistical error is available for the probe measurements.

scaling found corresponds to blobs directly after generation and not necessarily to the most stable ones as required for their predicted ρ_s dependence.

Although the analysis presented above reveals that blobs and drift waves feature the same size scaling with the drift scale ρ_s, it is not clear if the blob size is influenced by the size of the generating drift wave. With the fast camera data it is possible to study single events instead of just the CA and the coupling of the blob and drift-wave size can be confirmed: For every detected blob, the preceding drift wave was analyzed by using the object recognition method and then the sizes of both structures were recorded. Figure 8.6 shows a sample plot of the observed sizes for a neon discharge. For every discharge used for the scaling, a linear regression was performed separately to check if there is a correlation between the different sizes. All analyzed shots showed a weak but positive correlation varying between 0.14 and 0.27 for the single shots. Low correlation values can be caused by a non-linear relation between both sizes or additional effects that influence the blob size simultaneously. Nevertheless, the positive correlations found from the image data for every analyzed discharge indicate that larger drift waves indeed eject larger blobs.

8.3   Velocity scaling

In order to compare experimentally obtained radial velocities v_{exp} with theoretical predictions, the radial outward velocity is defined as

$$v_{\mathrm{exp}} = \frac{\mathrm{d}}{\mathrm{d}t}\, d_{\mathrm{LCFS}} \approx \frac{\Delta d_{\mathrm{LCFS}}}{\Delta t}\,, \tag{8.1}$$

where d_{LCFS} is the distance of the center of the blob to the LCFS. The outward velocity cannot be determined reliably from the image data, since in the observation region systematic errors arising from the integration along the line-of-sight (LOS) influence mainly the radial direction (Sec. 6.3.4). Instead, the radial velocity is determined from the conditionally averaged 2D ion-saturation current measurements.

After the blob in the CA of the ion-saturation current measurements has detached clearly from the LCFS, the time and position of the center of mass of the density perturbation are determined. After 10 sampling intervals (10 µs) the blob position is determined again, yielding the d_{LCFS} needed to evaluate Eq. (8.1).

Additionally, the electron temperature profiles were measured for every discharge to evaluate c_s, ρ_s, and ν_{in} in Eq. (3.8). The term $\delta n/n_0 \approx 1$ was determined from the ion-saturation current measurements and the collision frequency ν_{in} has been calculated from $\nu_{\mathrm{in}} = n_n \sigma (kT_i/m_i)^{1/2}$ using a measured neutral pressure n_n (about $5 \cdot 10^{18}/\mathrm{m}^3$ depending on the discharge), an estimated ion temperature T_i of 1 eV [62, 63], and an estimated neutral-ion cross section of $\sigma = 10^{-15}\,\mathrm{cm}^2$ (which is large compared to values given in e. g. Ref. [127]). Even with the choice of a large σ the resulting collision term in Eq. (3.8) is smaller than 0.01 and, hence, negligible compared to the 1 in the denominator of that equation.
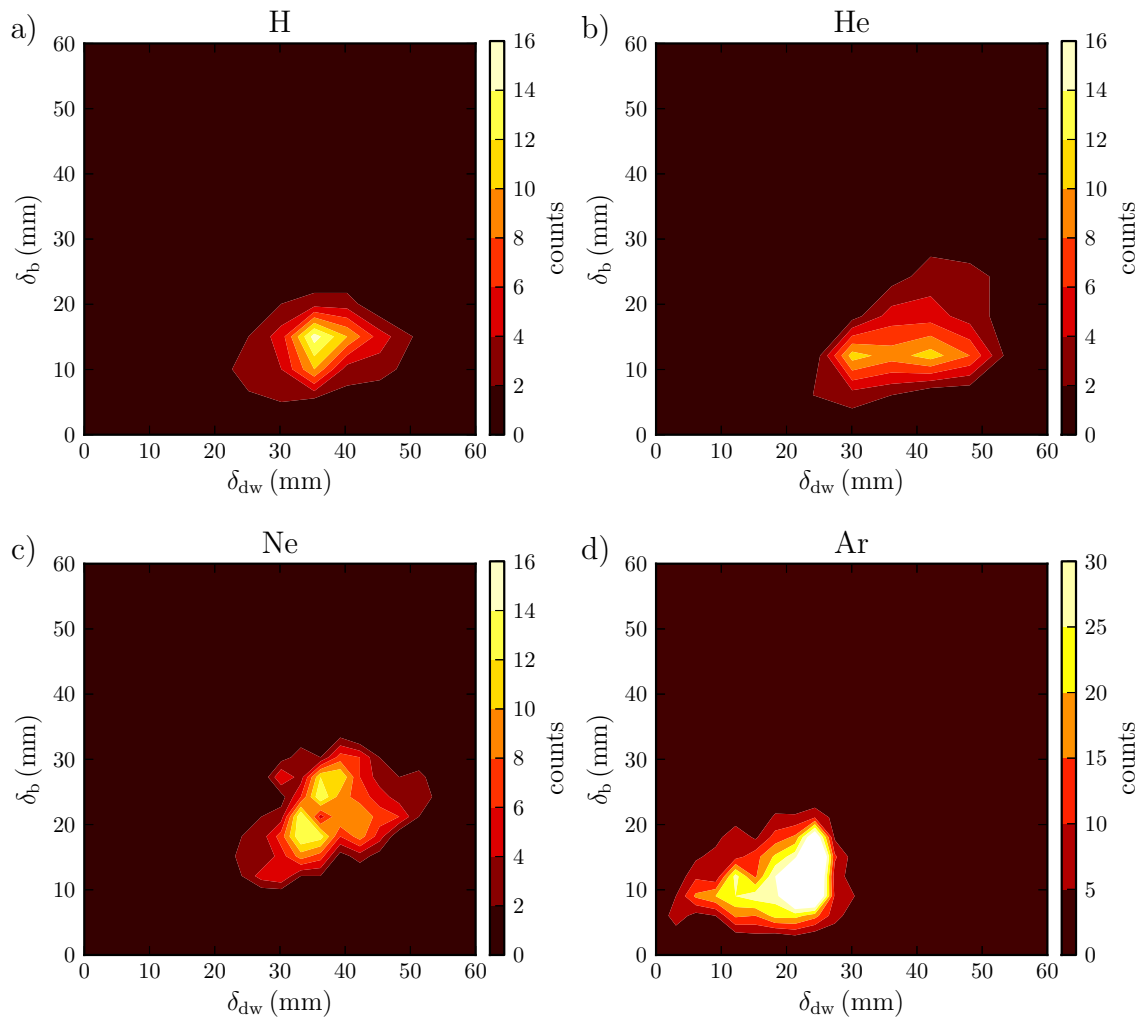
Figure 8.6: *Comparison of detected blob sizes with sizes of density maxima of drift waves right before blob ejection for a) hydrogen (#8213), b) helium (#8211), c) neon (#8219), and d) argon (#8216). While there is relatively low scatter, regression analysis reveals a tendency for larger blobs being generated by larger drift waves.*
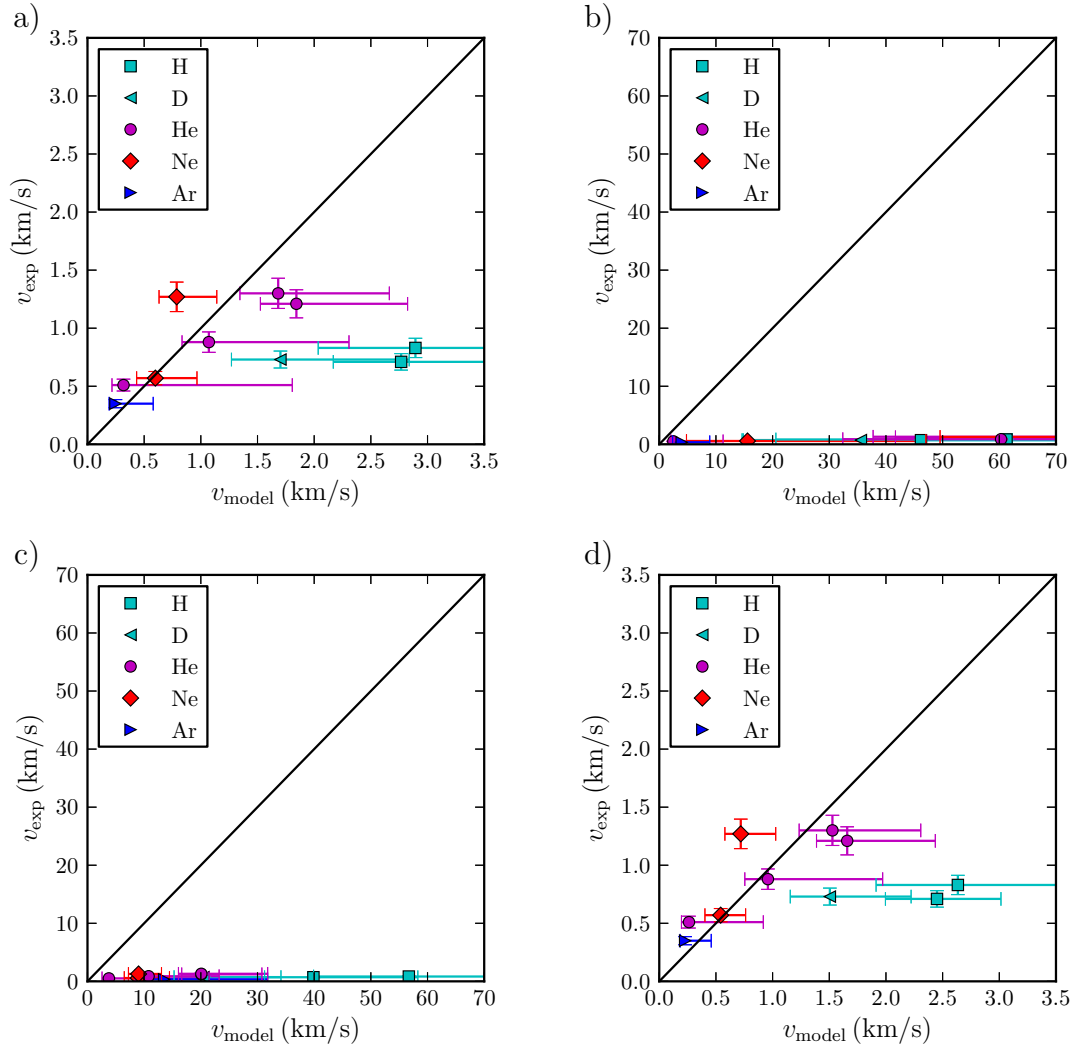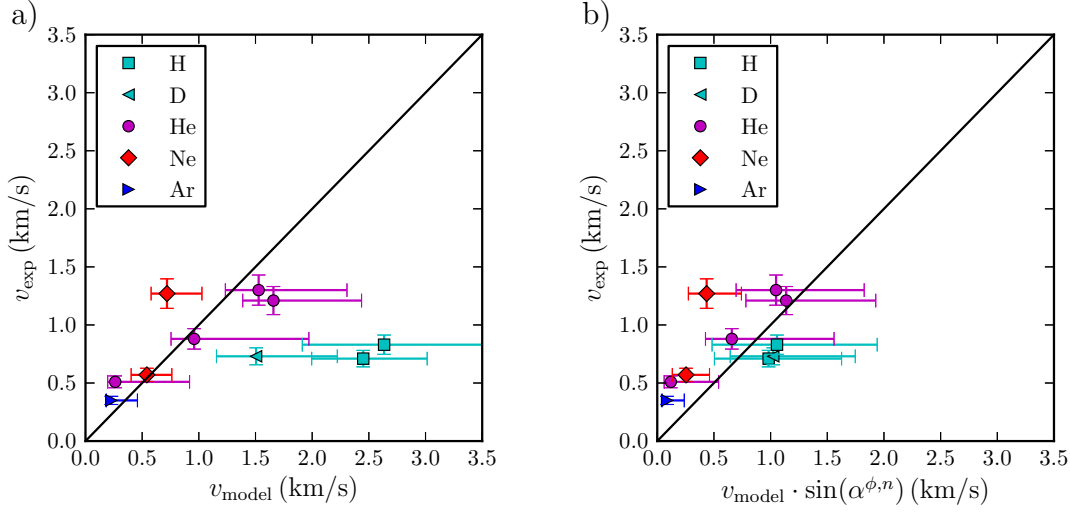
Figure 8.7:   *Comparison of measured blob velocities (v_{exp}) with predicted ones (v_{model}) for the different regimes of Eq. (3.8). Namely when the blob polarization is reduced dominantly by the ion-polarization current (a), sheath currents (b), or neutral collisions (c). In d), all three effects are considered according to Eq. (3.8).*

The experimental velocities v_{exp} are compared to the predicted model velocities v_{model} in Fig. 8.7. As is shown in Sec. 3.2 the velocity prediction according to Eq. (3.8) was obtained by considering sheath currents, ion-polarization currents and ion-neutral collisions as reduction mechanisms for the blob polarization. Three different regimes are presented, where one of the reduction mechanisms clearly dominates Eq. (3.8). The different plots a-c) in Fig. 8.7 show the comparisons with those three regimes according to of Eq. (3.10), Eq. (3.11), and Eq. (3.12). In a) only the term for the ion-polarization current is taken into account, in b) only the sheath current term, and in c) only the collision term. It can be seen that the ion-polarization current regime is best suited to explain the observed velocities and, therefore, the ion-polarization current plays the dominant role in canceling the blob polarization. In the denominator of Eq. (3.8), the first term (ion-polarization current) is 1, the second term (sheath current) is of the order of 0.1 and the last term (neutral collisions) is of the order of 0.01 and is neglected. Figure 8.7 d) shows the comparison of v_{exp} with values for $v_{r,\mathrm{b}}$ calculated from Eq. (3.8), which combines all three effects. Despite the fact that the model is two dimensional and, therefore, does not account for the complex stellarator geometry, a good agreement is found. The experimentally observed velocities are in the range of the calculated values.

Since the variation of the ion mass and the magnetic field has large effects on the plasma parameters, additionally three low-field helium discharges with different heating powers where compared. In agreement with the prediction from Eq. (3.8), the change in δ_{b} and T_e results in an increase of the blob velocity, as can be seen for the different helium measurements displayed in Fig. 8.7 d). However, it is observed that the blob velocity in the hydrogen discharges, and less pronounced in deuterium, is not only significantly smaller than the prediction, but also deviates clearly from the trend observed for the other ion species. The agreement with the model differs for different types of gases. The reason for this deviations are differences in the cross phase between density and potential $\alpha^{\Phi,n}$, which is measured to be significantly smaller for hydrogen than for the other gases. $\alpha^{\Phi,n}$ is estimated from the cross correlation of the CA of the ion-saturation current and floating potential measurements [128]. The blob model from Ref. [35], however, describes blobs as ideal interchange objects with $\alpha^{\Phi,n} = \pi/2$. Any deviation from this should reduce the effectiveness of the interchange drive and, therefore, the velocity of the blobs. In the extreme case of $\alpha^{\Phi,n} = 0$, the radial outward propagation vanishes. To account for this reduction an empirical correction factor of $\sin\left(\alpha^{\Phi,n}\right)$ is introduced to Eq. (3.8).

$$v_{r,\mathrm{b}} = \sin\left(\alpha^{\Phi,n}\right) \cdot v_{\mathrm{model}} \,. \tag{8.2}$$

The comparison with the experimental data is shown in Fig. 8.8 b). For hydrogen and deuterium a much better agreement is obtained if the cross-phase correction is taken into account.

Figure 8.8: *Comparison of measured blob velocities (v_{exp}) with velocities predicted (v_{model}) from a) the prediction for cold ions according to Eq. (3.8) and b) the same prediction but corrected by the phase factor $\sin(\alpha^{n,\phi})$.*

8.4 Parallel currents in blobs

As shown in the previous section the blob velocities in TJ-K can be predicted by the blob model for cold ions. However, as it is shown in the last section, deviations are noticed in hydrogen discharges. These deviations vanish as soon as corrections from cross-phases between density and potential smaller than $\pi/2$ are considered. Further evidence for the applicability of the model will be given in this section by measuring parallel currents along the filaments at the sheath entrance in front of the limiter disks. The parallel current and blob velocity can serve as experimentally independent quantities to check the validity of the blob model. This will provide further evidence that the correction in Eq. (8.2) is indeed a justified extension of the model and does not imply that the before mentioned blob model itself does not properly describe the physics of filaments in TJ-K. First, a prediction for the sheath currents suitable for TJ-K is derived and second, measurements are presented to show that these currents can indeed be observed in the experiment.

8.4.1 Prediction of the parallel current

In Sec. 3.5, an analytical model for the parallel current at the sheath entrance of a plasma facing component oriented perpendicular to the magnetic field lines (e. g. a limiter disk) is presented. In the derivation of this model [55], sheath-limited blobs are assumed, where the parallel sheath currents are the only mechanism to cancel the blob polarization caused by the interchange drive. The investigation on blob velocities in TJ-K (Sec. 8.3) revealed that the ion-polarization current dominates the reduction of the poloidal blob polarization. Hence, it can be expected that the

prediction according to Eq. (3.20), which does not take the ion-polarization current into account, is not suitable in this case. Instead, when deriving the sheath currents from Eq. (3.6), the term proportional to $\Delta\phi$, which represents the divergence of the ion-polarization current, must be kept. Neglecting the influence of neutral collisions, $\nu_{\mathrm{in}} = 0$, which is justified according to the velocity scaling, Eq. (3.6) becomes

$$j_\parallel\big|_{\mathrm{sheath}} = \frac{l_\parallel n m_i}{2B^2}\left(\frac{\partial}{\partial t} + \mathbf{v}_{E\times B}\cdot\nabla\right)\nabla^2\phi - \frac{l_\parallel c_s^2 m_i}{RB}\frac{\partial n}{\partial y}\,. \tag{8.3}$$

In principle, this equation could already be evaluated using conditionally averaged floating potential and ion-saturation current data. However, due to the appearance of the higher-order derivatives in this equation, the result will be strongly affected by noise both from plasma fluctuations and diagnostics.

In Ref. [37], the first term on the right-hand side of Eq. (8.3) was approximated by using the ideal interchange rate, which is also applied in the derivation of the blob velocity in [35]:

$$\frac{n m_i}{B^2}\left(\frac{\partial}{\partial t} + \mathbf{v}_{E\times B}\cdot\nabla\right)\nabla^2\phi \approx -\frac{n m_i}{B^2}\cdot\frac{\sqrt{2}c_s}{\sqrt{R\delta_b}}\cdot\nabla^2\phi\,. \tag{8.4}$$

Plugging this into Eq. (8.3) yields

$$j_\parallel\big|_{\mathrm{sheath}} = -\frac{l_\parallel m_i}{B^2}\cdot\frac{\sqrt{2}c_s}{\sqrt{R\delta_b}}\cdot\nabla^2\phi - \frac{l_\parallel c_s^2 m_i}{RB}\frac{\partial n}{\partial y}\,. \tag{8.5}$$

This equation predicts the parallel blob current to the sheath by making use of the same approximations as in the derivation of Eq. (3.8) for calculating the outward blob velocity $v_{r,\mathrm{b}}$. Parallel current calculations from Eq. (8.5) are more robust with respect to noise (compared to Eq. (8.3)). It can be seen that the density and potential enter Eq. (8.5) directly. Hence, no correction is needed concerning the cross-phase of density and potential $\alpha^{\phi,n}$.

8.4.2 Measurement of the parallel current

In order to evaluate Eq. (8.5), the ion mass m_i, magnetic field strength B, electron sound speed c_s, and the blob size δ_{b} were determined in the same way as for the blob velocity studies (Sec. 8.3). Additionally, the plasma potential and the density enter Eq. (8.5). Since only spatial derivatives of the potential enter this equation, floating potential ϕ_{f} measurements can be used to approximate the plasma potential due to the flat temperature profile. The spatio-temporarily resolved density can be obtained from ion-saturation current measurements by a calibration of the ion-saturation current profile using the line-averaged density (see Sec. 4.4). The parallel current at the sheath entrance can be measured using a single-sided Langmuir probe as it was shown in Ref. [55] and outlined in Sec. 4.4.2.

In the course of a bachelor's thesis [36] at TJ-K, a special probe was designed and built that can measure the parallel current as well as floating potential and ion-saturation current at the same time. For the measurements presented here, the same setup as described in Ref. [36] was used. I. e. the limiter from port O5 is moved close to O6, so that the probe scans the poloidal cross section of TJ-K close to the sheath of the limiter. The measurement grid was chosen with a step size of 0.5 mm in the R and z direction. All quantities were conditionally averaged in order to evaluate Eq. (8.5). The reference probe for the CA was located in the SOL and measured the floating potential in order to obtain comparable results to the study of blob properties. Care has to be taken for the orientation of the blob in the scanned 2D plane; since the derivative of the density in the poloidal direction $\partial n/\partial y$ enters the equation for the sheath current (8.5), the blob must be positioned and oriented such that one of the Cartesian coordinates of the probe scan coincides as well as possible with the poloidal direction in local laboratory coordinates. Figure 8.9 shows the CA of ϕ_f, $j_\parallel$ at the sheath entrance, and $I_{\mathrm{i,sat}}$ for a blob event originating from the generation region for hydrogen (top) and helium (bottom). The dashed line (gray) marks the line at which the predictions are evaluated with the radial direction (x-axis) as the local approximation for the poloidal coordinate. In order to reduce the influence of noise on the derivatives in Eq. (8.5), the derivatives are smoothed by taking the average of the derived signal at every grid point with the directly neighboring grid points. In the following, the experimental results are compared to the prediction according to (3.20) and the prediction according to Eq. (8.3) derived in the present section. Equation (3.20) was derived under the assumption that parallel currents are the only mechanism reducing the blob polarization. This is compared in Fig. 8.10 for hydrogen (top) and helium (bottom). The diamonds mark the measured current density $j_{\mathrm{sheath,exp}}$, the dots the calculated one. The shaded area around both curves marks the error of the measurements, which were calculated by error propagation from the experimental errors in ϕ_{f} and n_{e} for the predictions and from the uncertainty of the probe surface for the measured current.

In accordance with both, prior experiments conducted at TJ-K [36] and experiments performed at TORPEX [55], the predicted currents are smaller than the measured ones when only sheath currents are considered to reduce the blob polarization. The comparison with the prediction according to Eq. (8.5), where in addition the ion-polarization current is taken into account as reduction mechanism, is shown in Fig. 8.11. For hydrogen (top) no improvement is apparent, while for helium both the shape of the curve and the amplitude are better described when the ion polarization current is included in the prediction. To quantify this observation, the pointwise squared difference of the predictions and the measurement is evaluated. For hydrogen the sheath limited prediction yields a value of 10587 and the extended prediction 9898, which means only a marginal improvement. For helium values of 2158 and 1062 are obtained, which means that the match between measurement and prediction is clearly improved when the ion-polarization current is included.
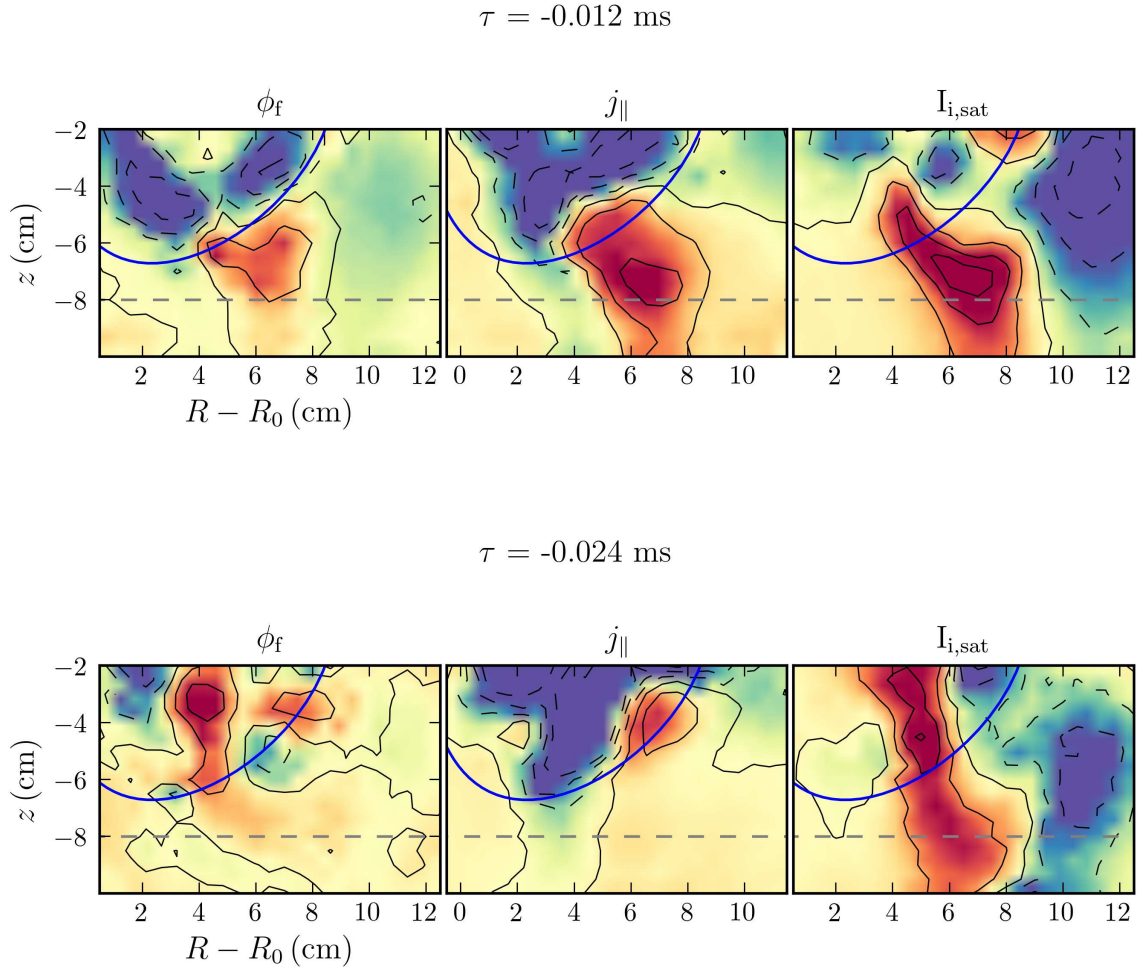
Figure 8.9: *CA of ϕ_f, $j_\parallel$ at the sheath entrance, and $I_{i,sat}$ for a blob event originating from the generation region for hydrogen (top) and helium (bottom) (#9133 and #9130). The line (blue) indicates the LCFS, the dashed line (gray) the line for which the predictive equations are evaluated. All quantities are normalized to the maximum of the CA at $\tau = 0$ for visualization. Positive fluctuations are shown by closed contour lines (red color), negative ones by dashed contour lines (blue color).*
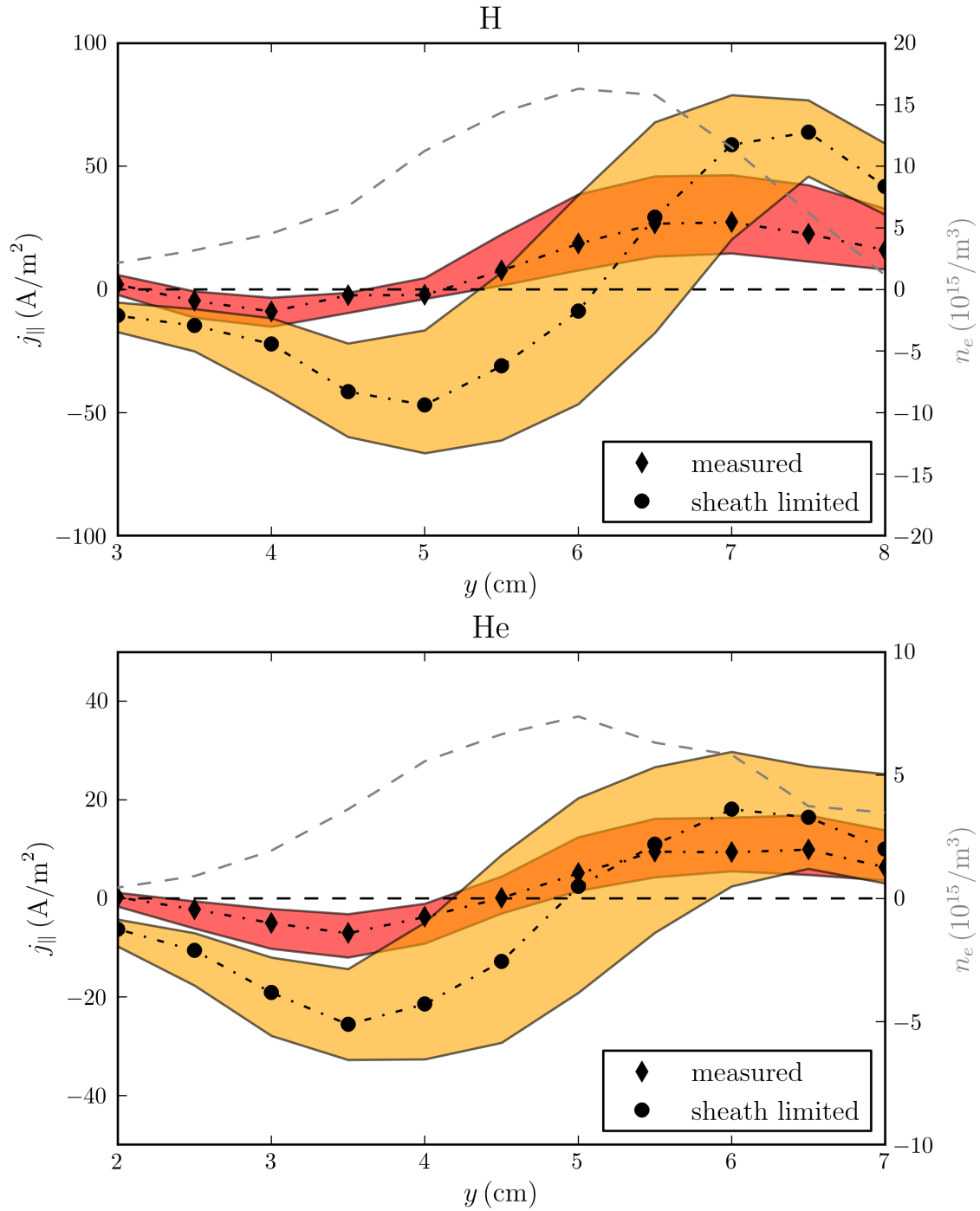
Figure 8.10: *Comparison of measured sheath currents flowing from filaments to a limiter disk with the prediction according to Eq. (3.20) for hydrogen (top, #9133) and helium (bottom, #9130). The gray dashed line shows the density perturbation caused by the blob. The shaded regions mark the error of the measurements and predictions, respectively. In both cases, the measured currents (diamonds) are smaller than the predicted ones (dots).*
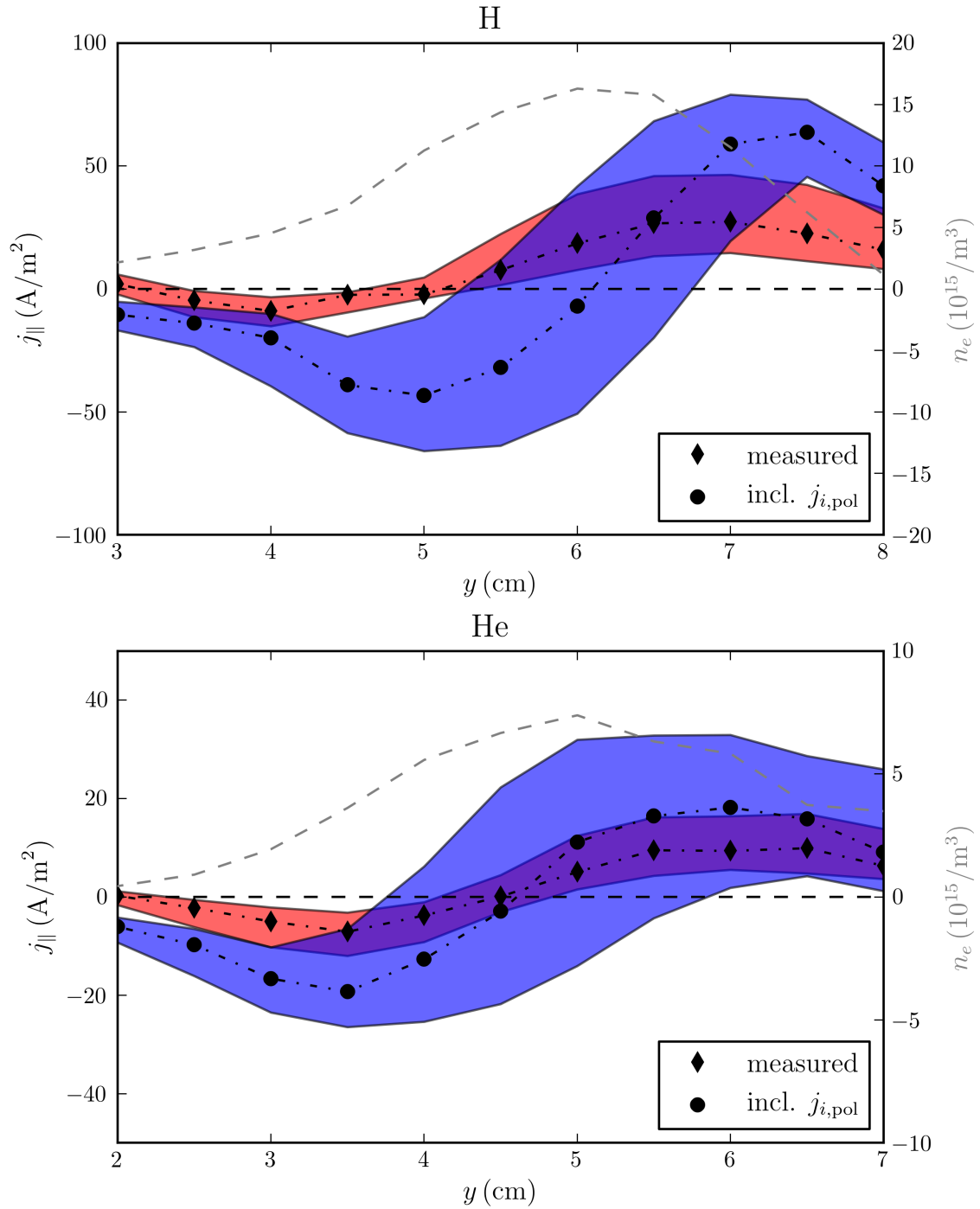
Figure 8.11: *Comparison of measured sheath currents flowing from filaments to a limiter disk with the prediction according to Eq. (8.5) for hydrogen (top, #9133) and helium (bottom, #9130). The representaion is the same as in Fig. 8.10.*

For both ion species, hydrogen and helium, both predictions (with and without the ion-polarization current included) are able to explain the observed dipole-like current profile. This is already a sign that the physics considered by the cold ion blob model can be observed in TJ-K. The inclusion of the ion-polarization current leads to a better agreement between predicted and measured currents. The improvement is only marginal in hydrogen and larger in helium. By comparing the blob velocity $v_{r,\mathrm{b}}$ for hydrogen with the corrected prediction in Fig. 8.8 it can be seen that the predicted velocity is still larger than the measured one by a factor of 2. This means that either the blob drive is overestimated for hydrogen or that there are additional reduction mechanisms for the polarization. The assumption of a larger blob drive as predicted is consistent with the measured larger sheath current. Since $v_{r,\mathrm{b}}$ is proportional to the blob drive (the numerator in Eq. (3.8)), the overestimation can be quantified by the ratio $v_{\mathrm{model}}/v_{\mathrm{exp}} \approx 0.5$. This can be used to reduce the blob drive term in the current prediction (Eq. (8.5)), i.e.

$$j_{\|}\big|_{\mathrm{sheath}} = -\frac{nm_i}{B^2} \cdot \frac{\sqrt{2}c_s}{\sqrt{R\delta_b}} \cdot \nabla^2\phi - \frac{v_{\mathrm{model}}}{v_{\mathrm{exp}}} \frac{l_{\|}c_s^2 m_i}{RB} \frac{\partial n}{\partial y} \,. \tag{8.6}$$

A comparison of sheath currents calculated from this equation with the hydrogen
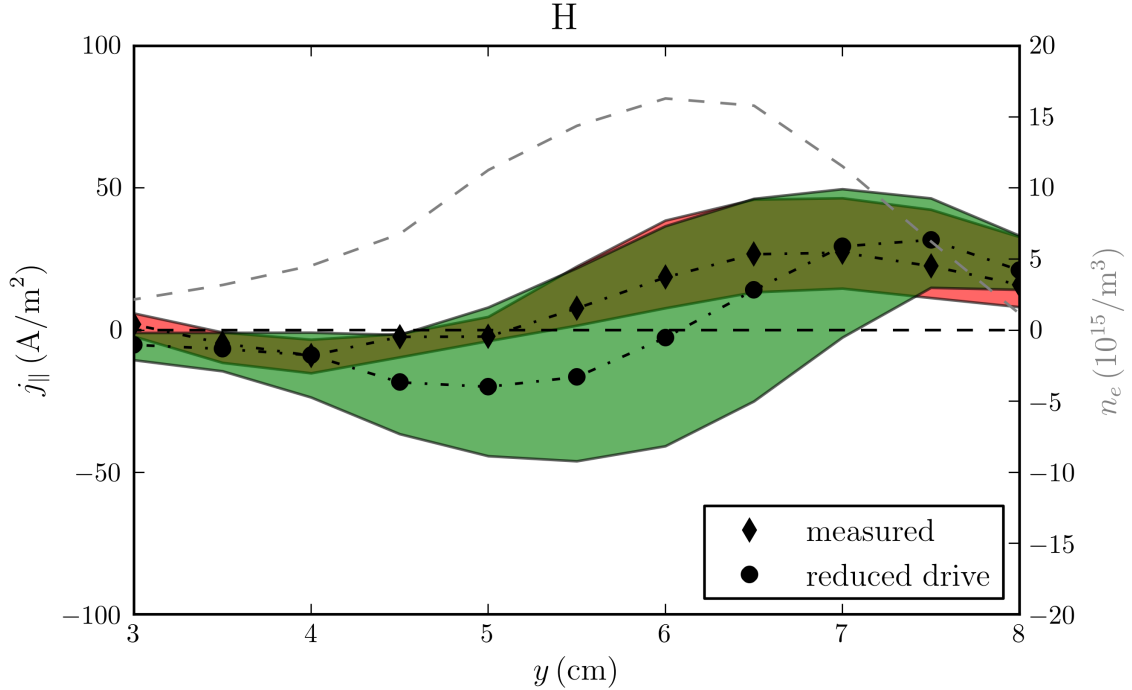
Figure 8.12: *Comparison of the measured sheath current flowing from filaments to a limiter disk with the prediction according to Eq. (8.6) for hydrogen (#9133). The representation is the same as in Fig. 8.10.*

measurements is shown in Fig. 8.12 and indeed a better agreement is observed.

8.5 Conclusions on blob properties

The results obtained from the experiments presented in this chapter can be summed in two major findings:

1. The cold ion model is suitable to understand many aspects of the blob dynamics in TJ-K despite the complex stellarator geometry.

2. The dynamics of the drift wave turbulence in the edge plasma has a strong influence on the blob properties.

Those two points are elucidated in the following in more detail.

As was shown, the observed velocity can be described by the prediction of the cold ion model according to Eq. (3.8). Deviations from the prediction are observed for hydrogen and, less pronounced, also for deuterium. These deviations vanish when the cross-phase $\alpha^{\phi,n}$ between density and potential is taken into account. The model assumes that blobs are perfect interchange objects with a $\alpha^{\phi,n} = \pi/2$. According to the experimental findings the cross-phases are smaller than this value, which leads to a reduced radial propagation velocity. This may be explained by an additional drift-wave-like parallel dynamics, which is not considered by the blob model.

In this model, parallel currents are flowing along the filament and enter the sheath in front of the limiter disks. In this work a prediction for these currents was derived taking into account the ion-polarization current, which was neglected in the model presented in Ref. [55]. The parallel currents were measured and compared with the two different predictions and a better agreement was achieved when the ion-polarization current was included. This is in agreement with the results for the radial velocity and confirm that the model includes the relevant physical processes.

The influence of the drift waves on the blob properties is seen in the waiting-time analysis and the size scaling. The waiting-time distribution (WTD) of the blobs in the SOL reflects exactly the WTD of density maxima of the drift waves in the edge. Keeping in mind the blob generation mechanism presented in Ref. [48] and summarized in Sec. 6.3.1 this result can be interpreted in such a way that every large-amplitude coherent structure arising from drift-wave turbulence triggers blob generation in TJ-K.

During the generation process, also the size of the blobs is influenced by the characteristic size of the density perturbations associated with the drift waves, i. e. their poloidal wavelength, as the comparative size scaling reveals. This does not only influence the density profile of single blobs. Since the radial velocity is size dependent (see Eq. (3.8)), also the propagation of the blobs is influenced by the poloidal wave length of the drift waves.

The close coupling of properties of blobs and coherent structures arising from drift-wave turbulence inside of the LCFS imply that blob properties cannot only be influenced by changing the plasma parameters in the SOL, but also by influencing the turbulence properties just inside of the blob birth region.

Chapter 9

Blob generation at TJ-K

Experimental observations of blob generation in many different fusion experiments indicate that usually two features are involved in the generation process:

1. A radial acceleration of structures of increased density as soon as they reach a certain region (specified below).

2. A shear in the poloidal velocity close to the region of increased radial propagation that leads to a detachment of a part of the initial density perturbation. The detached part forms an isolated structure and is observed as blob.

This seems to be a robust observation, independent from the instability that gives rise to the coherent density structures. The characteristic change of the two velocities is often observed around the separatrix in fusion experiments (Refs. [51, 52]), but can also be observed in experiments that have no confinement region, but only open field lines (Ref. [47]). The radial outward motion appears to be a prerequisite for blob generation. As described in Sec. 3.2, in magnetically confined toroidal plasmas curvature induced interchange-like instabilities can explain such a propagation of the blob. These instabilities depend on the normal curvature κ_n (Sec. 2.2) and it is shown in this chapter that in TJ-K blobs are generated in the SOL region where the mean normal curvature $\langle\kappa_\mathrm{n}\rangle$ is negative.

Furthermore, in some of the discharges analyzed in the course of this work, a zonal flow (explained below) seems to be involved in the blob generation process. A possible explanation for this is given and a future experiment is proposed, which could shed light on this connection.

9.1 Blob generation region

There are two distinct regions for blobs in the SOL of TJ-K: In Sec. 7.1.3 it was shown that there is a *blob region*, in which blobs exist. Inside the blob region there is the smaller *generation* region, where the majority of blobs originates from. This generation region is evident in 2D histograms of blob events detected in the SOL of

TJ-K (e. g. Fig. 7.9). The measurements with the poloidal probe arrays, presented in Sec.7.1.1, revealed that the blob filaments are elongated along the magnetic field lines and extend between the two limiter disks. Hence, the blob generation region follows the magnetic field lines and the observed location of the generation region in a poloidal cross section depends on the toroidal position.

In previous blob studies at TJ-K [48, 73], this generation region was not observed. The blobs seemed to origin mainly from the mid-plane, where the local normal curvature κ_n is high. At that time, fast imaging was not available at TJ-K. Therefore, it cannot be ruled out that a similar feature indeed existed in those experiments, but was not obvious in the performed probe measurements. However, since the limiter setup was different in these experiments (only one limiter disk at port O1), both the parallel length of the blobs $l_\parallel$ and the poloidal profile of $\langle\kappa_n\rangle$ were different. In the following two question will be answered to shed light on what determines the location of the blob generation region:

1. What have the different generation regions in both limiter setups in common?

2. Is there a reason why the generation region discovered in Sec. 7.1.5 has not been observed in the prior experiments?

In Fig. 9.1 the poloidal profile of $\langle\kappa_n\rangle$ is depicted for the setup with two limiter disks (closed line) used in the experiments presented in this work, evaluated at the toroidal position of the probe measurement (port O6). The generation region observed in this setup with the fast camera is marked by "GR$_2$", located inside the region where $\langle\kappa_n\rangle$ is negative and blobs can be generated. Also shown in Fig. 9.1 is the $\langle\kappa_n\rangle$ profile for the setup with just one limiter used in Ref. [48] (dashed line). "GR$_1$" indicates the generation region reported in the reference. Assuming that $l_\parallel$ is also determined by the SOL connection length in this setup with only one limiter disk, the blob generation region should be located again in the region where $\langle\kappa_n\rangle$ is negative, which is indeed the case. So in both cases, the generation region is located in the bad curvature region. This immediately answers the second question, the generation region of the setup with two limiter is located in the good curvature region in the setup with just one limiter disk and, hence, no blob drive exists and blobs should not be generated. It is, however, also apparent from Fig. 9.1 that the generation region is not located at the minimum of $\langle\kappa_n\rangle$, where the effect of the curvature on the blob drive is strongest. The close connection between blob generation and drift waves in the edge of TJ-K implies, however, that the stability of drift waves in the edge plasma plays a major role in the blob generation process. Therefore, the reason for the strongly increased blob detection in the generation region may lie in the confined plasma rather than in the SOL.

Detailed three dimensional measurements of the turbulent transport in TJ-K [110, 129] revealed that, beside the great importance of local quantities like the normal curvature κ_n and the geodesic curvature κ_g, a noticeable toroidal asymmetry in the turbulent transport is observed. The turbulent transport is increased in a small region around a specific magnetic field line. This field line crosses the location where
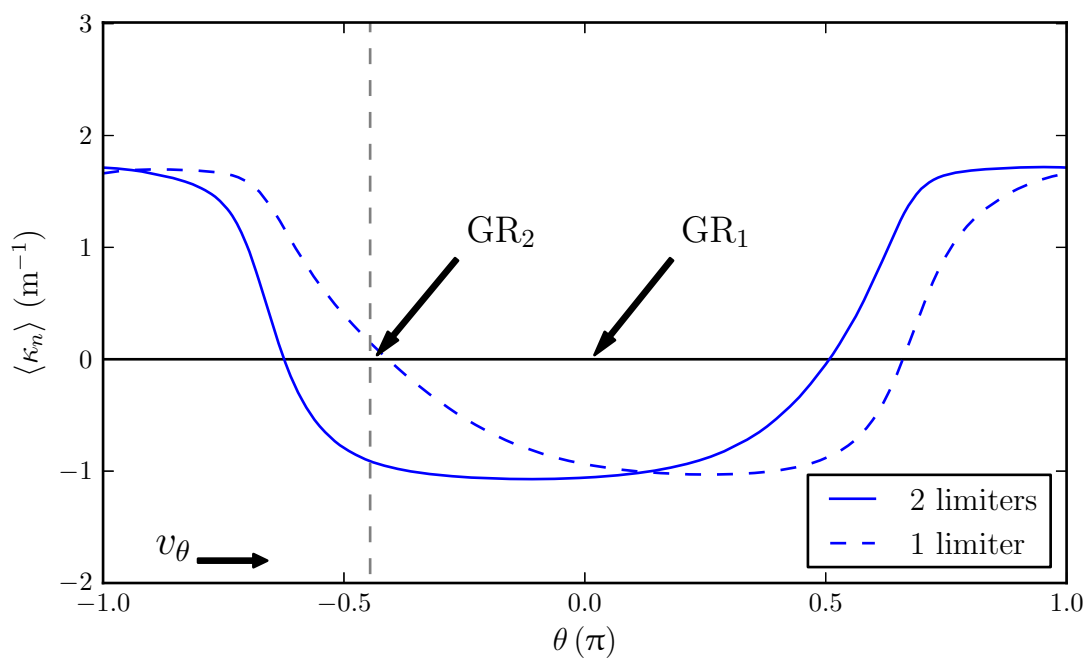
Figure 9.1: $\langle \kappa_n \rangle$ *as a function of the poloidal angle evaluated at the toroidal position of port O6 for the setup used in this work (closed line) and the one used in Ref. [48] (dashed line). GR_1 and GR_2 mark the observed generation regions in the setup with 1 and 2 limiter disks, respectively. The small arrow indicates the poloidal propagation direction.*

the microwave heating mainly deposits its power at the upper hybrid resonance [61] and, therefore, instabilities may be driven due to an interaction of the microwave and the plasma. A possible explanation was given in Ref. [110] namely that trapped particles may exist, which destabilize drift waves and increase the radial transport.

In the limiter setup, this particular field line intersects the limiter plates, therefore, it is unclear if it plays a role for the stability in the confined region. It is noteworthy, however, that the poloidal angle where the generation region is observed at port O6 agrees remarkably well with the poloidal angle where this field line crosses the poloidal plane of O6. If in analogy to the standard setup without limiters instabilities along a particular field line exist in the confinement region, these may indeed be responsible for the generation region.

For the moment this remains as an open question. A possible experiment to assess the role of the localized microwave heating on the generation region would be to heat the plasma in a different toroidal segment and observe if the generation point changes its location in the poloidal cross section.

9.2   Blob generation and zonal flows

A zonal flow in a toroidal magnetically confined plasma is a potential perturbation which features only variations in the radial direction (radial wave number $k_r \neq 0$), but is constant in the poloidal and toroidal direction (wave numbers $k_\phi = k_\theta = 0$) [130, 131]. Therefore, the zonal flow is related to a radial electric field and, hence, a poloidal $\mathbf{E} \times \mathbf{B}$ drift, which does not cause transport due to the absence of a radial component. Note that the terms *toroidal* and *poloidal* are used here for simplicity reasons. Here, "toroidal" refers to the direction parallel to the magnetic field and "poloidal" to the direction perpendicular to the magnetic field and to the gradient of the poloidal magnetic flux (the radial direction).

Due to the radial variation of the zonal flow, this poloidal drift is restricted to a distinct radial region and imposes a shear in the poloidal velocity. Via the so-called Reynolds stress drive, the zonal flow is thought to be fed by the turbulence due to eddy tilting. In turn, the generation of the zonal flow leads to a reduction of the energy contained in the turbulent eddies. This process can cause an oscillatory behavior with a *limit cycle*, where the turbulence feeds the zonal flow, which in turn reduces the turbulence and, hence, its own driving mechanism [130].

There is experimental evidence [49] that zonal flows are related to blob generation. On the one hand a shear flow close to the LCFS induced by the zonal flow assists the shear off of a growing blob structure from the confined plasma. On the other hand the edge turbulence involved in the blob generation is thought to drive the zonal flow via the turbulent Reynolds stress [49, 132, 133], thereby increasing the shear flow but reducing the turbulence and, hence, the blob generation probability.

In TJ-K, zonal flows are observed as well in the standard setup (no limiters
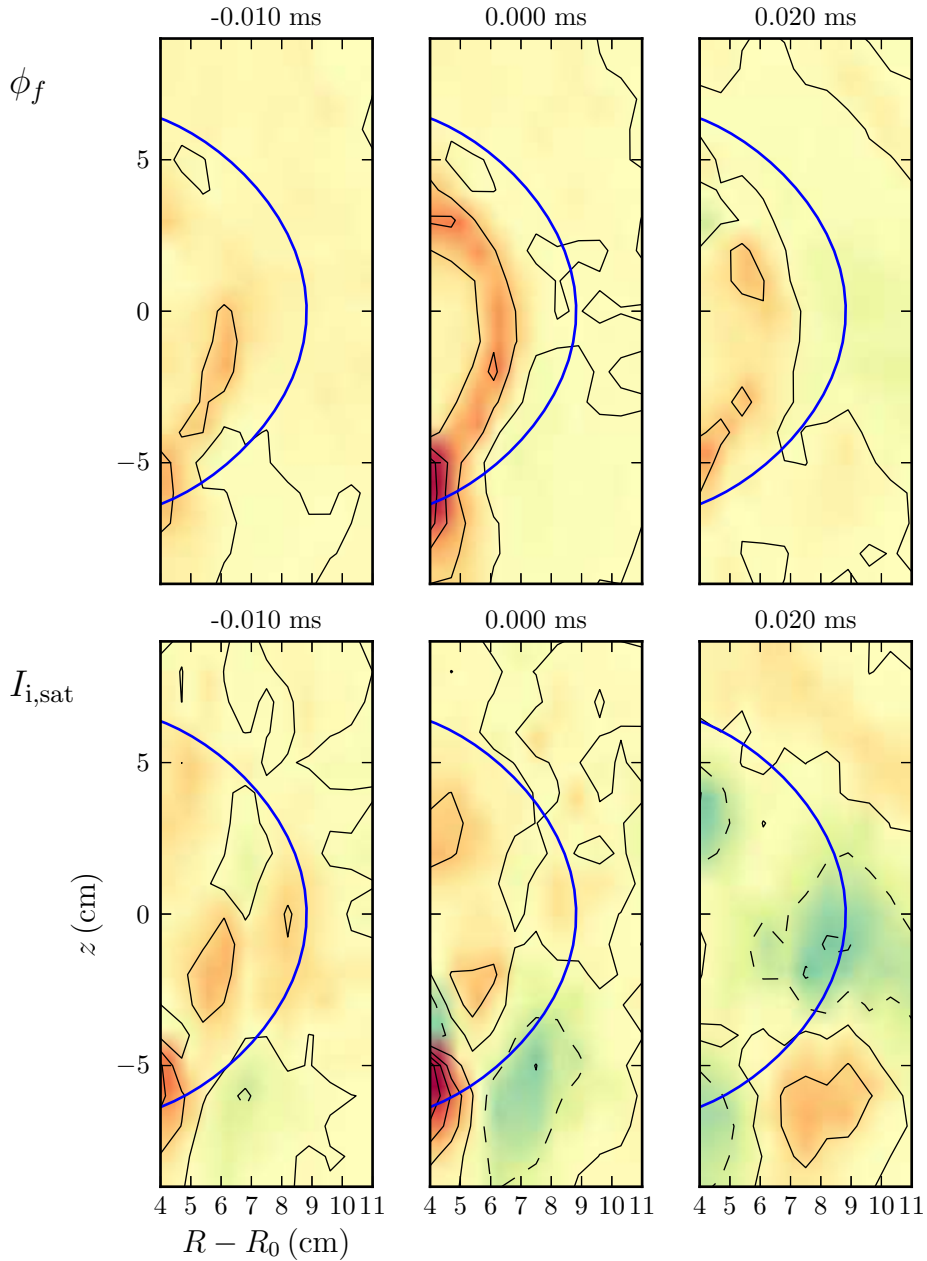
Figure 9.2: *Three time instances of the CA of floating potential (top row) and ion-saturation current fluctuations (bottom row) from #7171. Positive fluctuations are shown in red with closed contour lines, negative ones in blue with dashed lines. The reference probe is located in the edge plasma outside of the measurement region at $R - R_0 = 2$ cm, $z = -5$ cm. From $\tau = -10\,\mu s$, a zonal flow is growing, which reaches its maximum amplitude at $\tau = 0$. At the same time, a density perturbation grows in the bottom of the edge plasma, as can be seen from CA of the ion-saturation current. This density perturbation triggers blob generation. The blob propagates outwards and can clearly be seen in the lower SOL at $\tau = 20\,\mu s$.*
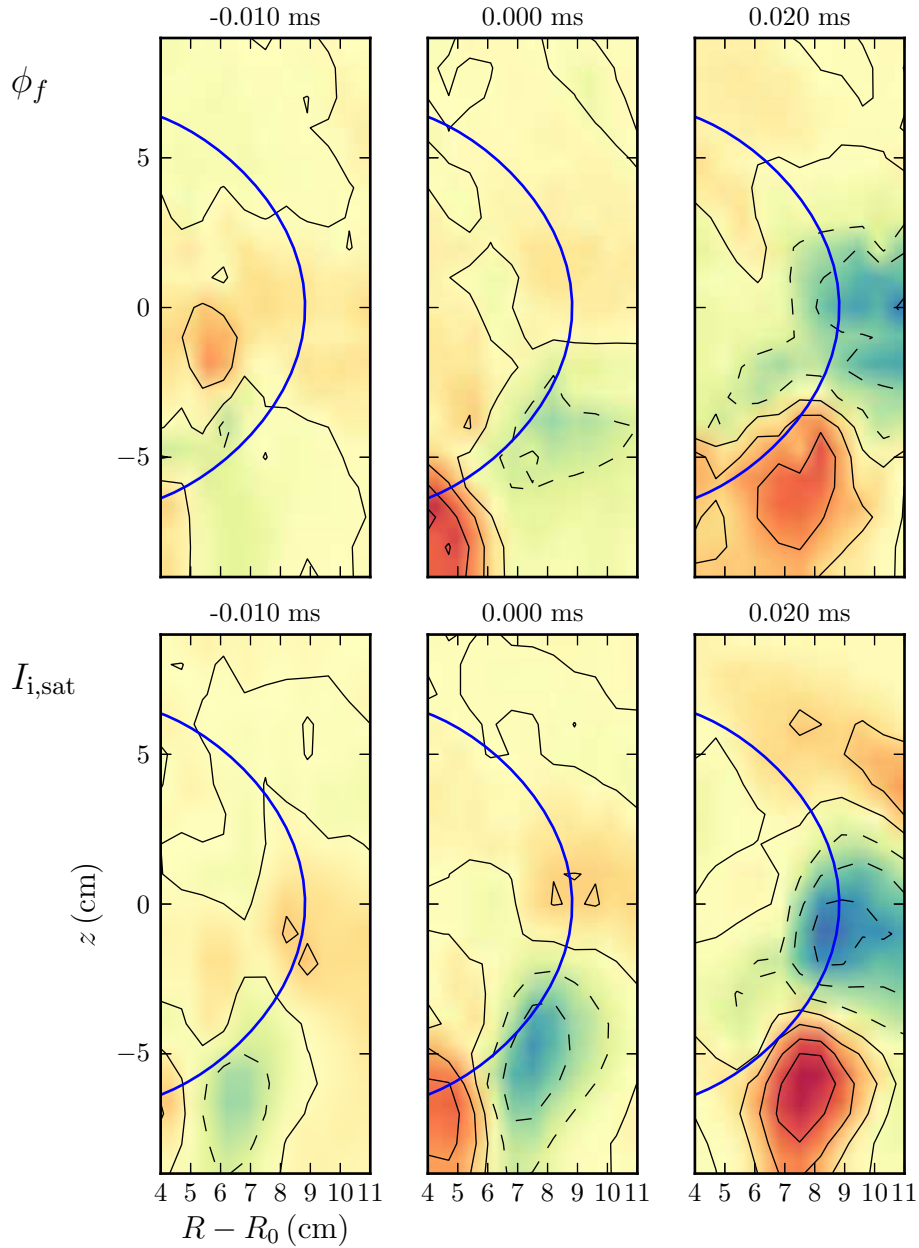
Figure 9.3: *Same representation as in Fig. 9.2, but here the reference probe is located at $R - R_0 = 3$ cm, $z = -7$ cm. A density perturbation grows in the SOL from $\tau = -10\,\mu$s up to $\tau = 0\,\mu$s, before it detaches from the confined plasma and a blob is formed in the SOL. The SOL dynamics are comparable to the one seen in the CA with a reference probe in the edge plasma (Fig. 9.2). In the confined plasma, however, no zonal flow is observed.*

installed) [110, 134] as in the setup with two limiter disks [135]. In both setups, a transport reduction connected to the zonal flow is observed in agreement with the limit cycle [110, 129, 135]. In limited plasmas it was possible to show the occurrence of zonal flows in the conditional average (CA) of a 2D probe scan [135]. Figure 9.2 shows the CA of a floating potential and an ion-saturation current measurement. From $\tau = -10\,\mu s$, a zonal flow grows in the edge plasma before it decays again. The zonal potential can be seen as ring-like structure in the poloidal cross section. At the same time, a density perturbation is growing in the SOL and detaches from the confined plasma. At $\tau = 20\,\mu s$ the structure is clearly detached from the confined plasma. This blob emerges from the generation region (Sec. 9.1). Since the reference probe is located in the edge plasma this provides further evidence that in TJ-K the cause for blob generation is found in the edge.

The simultaneous appearance in the CA of a zonal flow and a blob points to a temporal connection of both phenomena. The analysis was repeated with a reference probe in the SOL, which is not able to detect zonal flows in the edge, but only blobs in the SOL. The result is illustrated in Fig. 9.3. Here, only a blob is observed without the appearance of a zonal flow in the edge, which means that the majority of blobs is not related to zonal flows. There are two possible explanations for the occurrence of both phenomena in the same CA. First, it is possible that zonal flows and potential perturbations associated with blob generating drift waves are two unrelated phenomena, but fulfill the CA threshold at the reference probe comparably frequent. That way, neither blobs nor zonal flows are completely averaged out and coexist in the CA. In prior experiments at TJ-K [135], the zonal flows were observed with a frequency of about 5 kHz, while the drift waves appeared with approximately 20 kHz, which may indeed be close enough to interfere in the CA. Second, it is possible that zonal flows affect the edge dynamics and in turn trigger blob generation. This would, however, not be a necessary prerequisite for blob generation at TJ-K, because otherwise the zonal flow would also be visible when the CA is evaluated for the reference probe in the SOL. Therefore, a small number of blobs exist which are associated with zonal flows while the majority of events is not.

The answer to the relationship between blobs and zonal flows may be found in the limit cycle: In TJ-K, blob generation is triggered by drift waves. Hence, the increase and reduction of the drift wave activity during the limit cycle should be reflected in the probability for blob generation. Future experiments [136] using a poloidal probe array to detect the presence of a zonal flow and simultaneous measurements with a reference probe in the SOL or the fast camera to detect blobs will test this explanation. Since the poloidal probe array can unambiguously distinguish between zonal flows and drift waves it can be avoided that drift waves spuriously trigger the CA condition and, hence, it can be decided if zonal flows and blobs indeed occur simultaneously. The reference probe allows for the investigation of the relation of the limit cycle and an increased probability for blob generation.

Chapter 10

Blob properties at ASDEX Upgrade

In the preceding chapter, detailed studies on blob properties in the stellarator TJ-K are presented. The key findings are the principle validity of the blob model and the influence of edge dynamics on blob properties. In the scrape-off layer (SOL) of fusion experiments like ASDEX Upgrade the ions are not cold ($T_i \gtrsim T_e$ [41]) and the blob dynamics are expected to differ from that in cold plasmas. For both regimes, however, the blob dynamics can be understood from the same theoretical frame work (Sec. 3.2). The identification of a possible influence of the edge dynamics on the blob properties is much more challenging in fusion plasmas than in the low-temperature plasma of TJ-K, since T_e reaches values around $100\,\mathrm{eV}$ already at the separatrix. This high temperature renders both, long-time probe measurements and camera measurements of light emitted by neutrals, impossible.

The experiments performed at ASDEX Upgrade aimed mainly at establishing a gas-puff imaging (GPI) diagnostics for SOL measurements, at using this diagnostics to study the validity of the blob model and at examining differences in the blob properties between L- and H-mode plasmas. The blob properties that are studied are the detection rate together with the waiting-time distribution (WTD), the blob size δ_b perpendicular to the magnetic field, and the poloidal and radial velocity.

10.1   Gas-puff imaging

Gases typically used for gas-puff imaging (Sec. 4.2.2) in the SOL of fusion experiments are deuterium and helium. Since most fusion experiments use deuterium plasmas, a gas-puff with deuterium does not introduce impurities in the SOL. Furthermore, the light intensity emitted by deuterium is high compared to most other gases and, hence, less deuterium is needed. Helium, in contrast, has a high first ionization energy of $24.6\,\mathrm{eV}$ (compared to $13.6\,\mathrm{eV}$ for deuterium) and can penetrate further into the plasma before it is ionized.

10.1.1   Emission range for deuterium

Figure 10.1 displays the light intensity recorded by the fast camera in the SOL during a deuterium gas-puff. The maximum intensity is observed close to the limiter at $\rho_{\mathrm{pol}} \approx 1.065$, thus the separatrix is not located in the imaged region of the SOL.
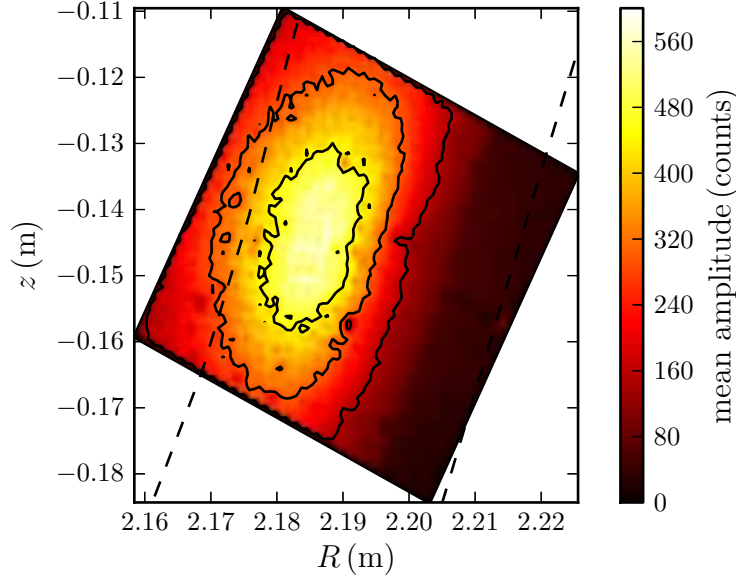
Figure 10.1: *Mean count rate captured by the camera during a deuterium gas-puff. The left dashed line marks the position of $\rho_{\mathrm{pol}} = 1.05$, the right dashed line of $\rho_{\mathrm{pol}} = 1.10$.*

10.1.2   Emission range for helium

Figure 10.2 displays the light intensity recorded by the fast camera in the SOL during a helium gas-puff. The maximum intensity is further inwards of the vessel compared to the deuterium case. Due to a different separatrix position (R_{aus}) the maximum intensity is observed at $\rho_{\mathrm{pol}} \approx 1.09$, but the gas cloud penetrates further into the SOL (compared to deuterium) up to $\rho_{\mathrm{pol}} \approx 1.04$. The separatrix is located in the imaged region of the SOL, however, there is no detectable light emission coming from that position.

10.1.3   Influence of the line integration along the LOS

As described in Sec. 4.2.2, the camera is located outside of the vessel and observes the plasma with a mirror inside an immersion tube that is introduced to the vessel. Due to technical limitations for the positioning of the tube and the mirror the camera does not observe the plasma exactly tangential to the magnetic field lines. Due to
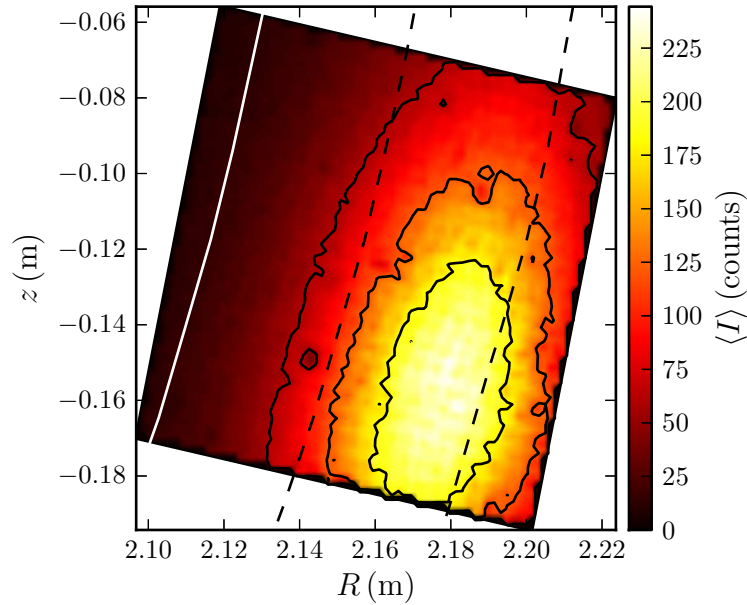
Figure 10.2: *Mean light intensity captured by the fast camera during a helium gas-puff. The left line (white) marks the separatrix position ($\rho_{\mathrm{pol}} = 1.0$), the two dashed lines $\rho_{\mathrm{pol}} = 1.05$ (left) and $\rho_{\mathrm{pol}} = 1.10$ (right).*

the line integration along the line-of-sight (LOS) this leads to a distortion of the structures in the image data. Figure 10.3 shows turbulent structures in the raw GPI data (mean substracted). Due to their extension along the field lines the structures appear elongated in the image data. It can be seen from that figure that the camera measures approximately the size in the poloidal direction. Hence, in the same way as for TJ-K the blobs size δ_b is identified as the poloidal extent of an ellipse fitted to a single structure. In contrary to the measurements at TJ-K, it is observed that this does not have to agree with the minor semi-axis of the ellipse. Hence, to measure the blob size, the poloidal semi-axis of the ellipse is determined from the image data.

10.2 Dynamics in the conditional average

The conditional average (CA) is commonly used to study the characteristic dynamics of coherent structures in turbulent systems both in experiments and simulations. In this section, CA results are shown for the deuterium gas-puff, where the emitted light intensity reaches its maximum in front of the limiter near the segment S13. The CA is compared for an L-mode and H-mode phase in the same discharge.
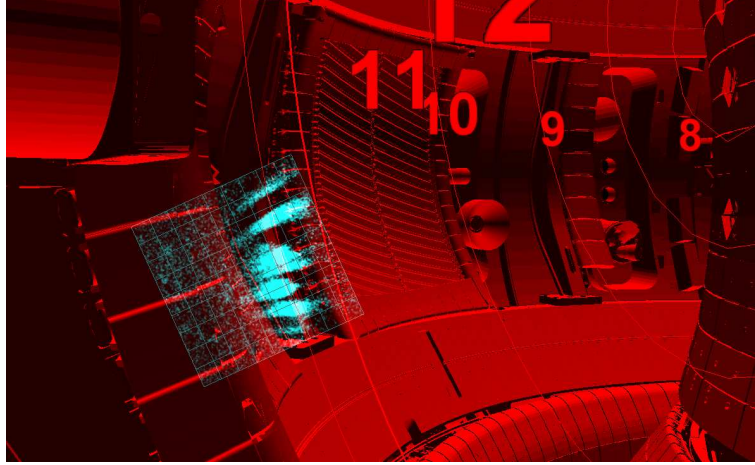
Figure 10.3: *Model of the interior of the ASDEX Upgrade vessel overlayed with a camera image (blue) showing fluctuations in the SOL [137].*

10.2.1 Conditional average of deuterium gas-puff data

Figure 10.4 shows six time instances of the CA of the normalized intensity fluctuations $\tilde{I}_n$ recorded during a deuterium gas-puff in an L-mode phase. The reference pixel is marked by the gray cross, the threshold chosen for the CA was two times the standard deviation. The dashed line indicates the position of the limiter close to S13. The x-axis lies close to the radial direction (ρ), the y-axis close to the poloidal direction, the electron diamagnetic direction (EDD) points to the top of the images and the ion diamagnetic direction (IDD) to the bottom.

A blob is seen in the intensity fluctuations, which propagates radially outwards and poloidally in the electron diamagnetic direction. The observed structure size is about 10 pixels ($\delta_b \approx 1\,\text{cm}$). The structure size will be discussed in more detail in Sec. 10.4. At $\tau = 0\,\mu\text{s}$ (Fig. 10.4 b) the blob features an elliptical shape, which is elongated in the radial direction due to the integration along the line-of-sight (LOS) as has been shown in Sec. 10.1.3. At later times (images d-f) the blob features a more complex shape and develops a tail-like structure. The blob size and velocity cannot be defined clearly at that point. Therefore, size and velocity of the blobs are studied for blobs with locations like the ones shown in in Fig. 10.4 a) or b).

Figure 10.5 shows a CA analysis similar to the one described above, but this time for blobs observed in the H-mode phase of the same discharge. A blob is seen in the captured intensity fluctuations, which also propagates radially outwards. But compared to the L-mode case a smaller poloidal velocity is observed, which even points in the opposite direction. This indicates a change in the radial electric field. Also compared to the L-mode phase the blob size appears to be larger. Apart from these differences the observed structures and dynamics seem to be comparable.
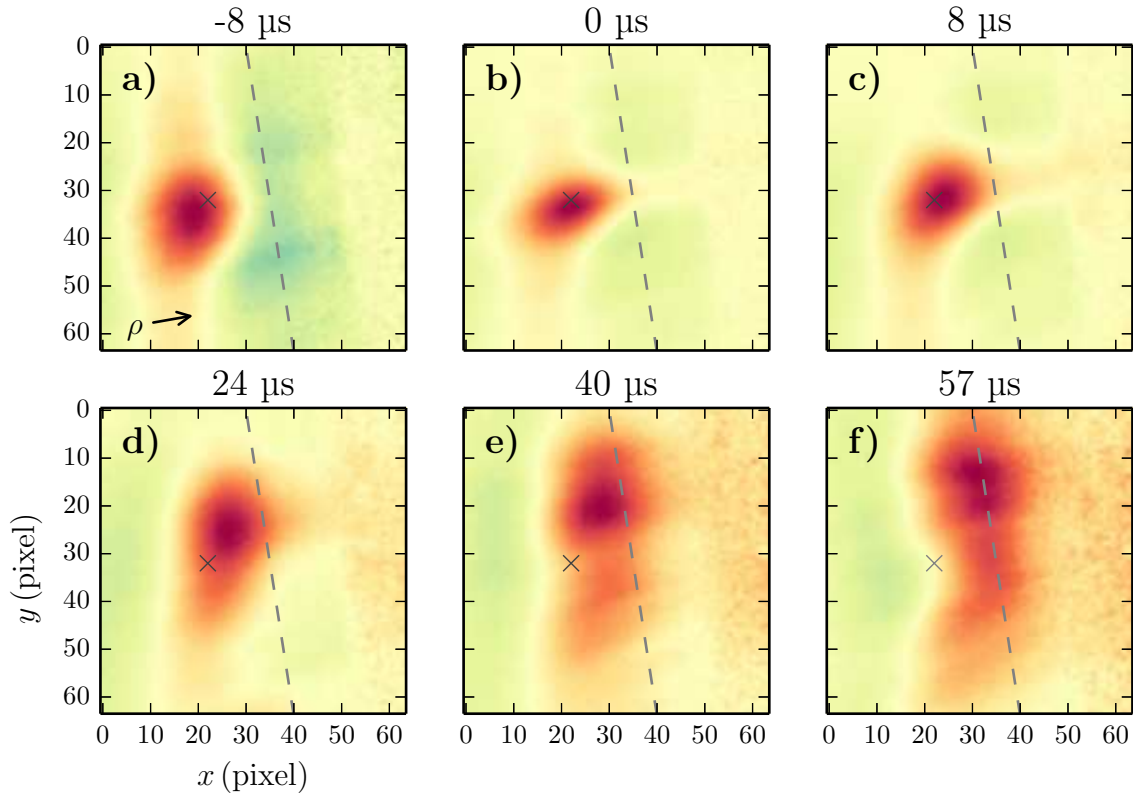
Figure 10.4:   *Conditional average of normalized intensity fluctuations $\tilde{I}_n$ recorded during an L-mode phase of #28769. The cross (gray) marks the location of the reference pixel, the dashed line (light gray) depicts the limiter at port S13, which is visible in the image data. The radial direction ρ (marked by the arrow) agrees approximately with the x direction, the poloidal direction with the y direction. The exact orientation of the images can be seen in Fig. 10.1.*
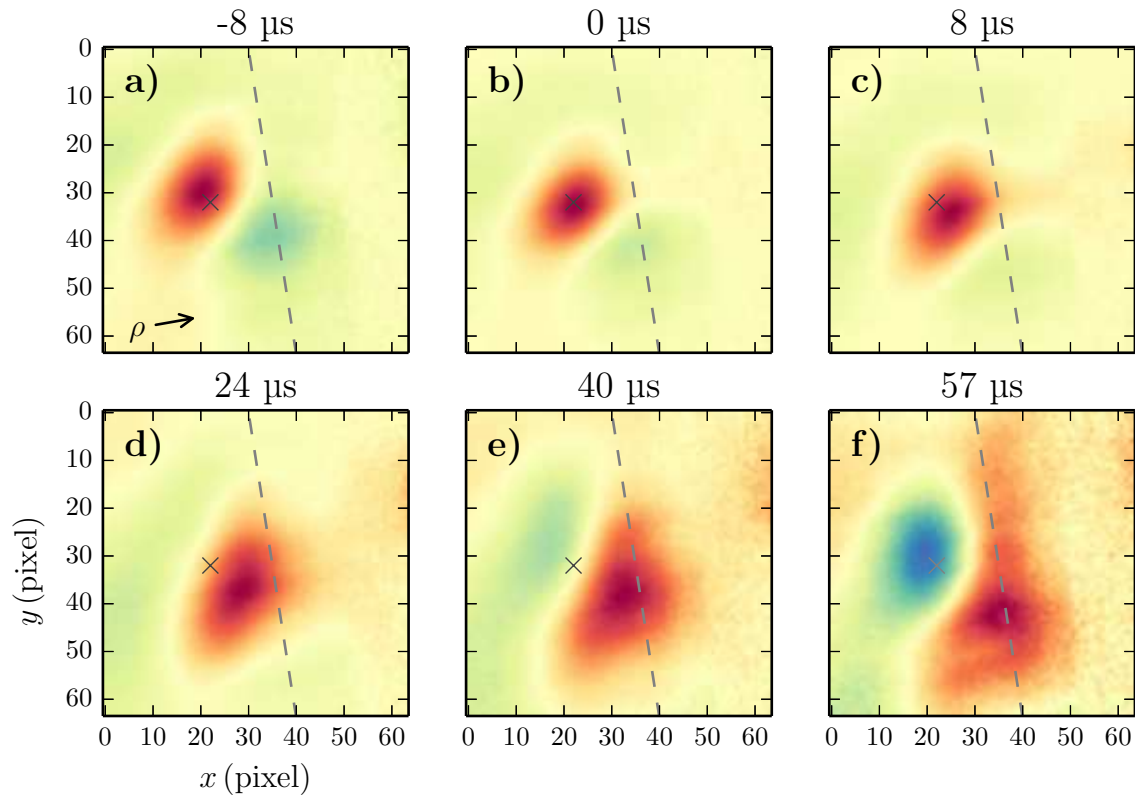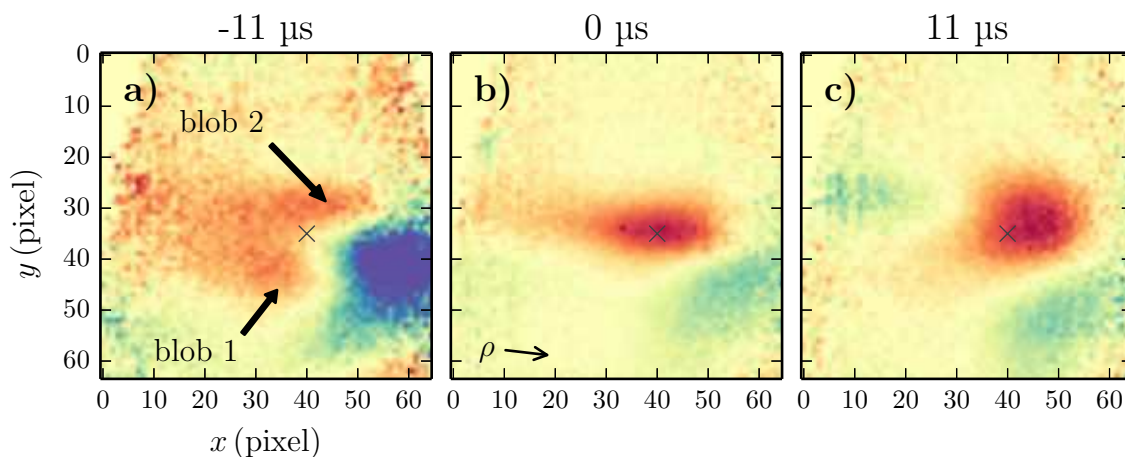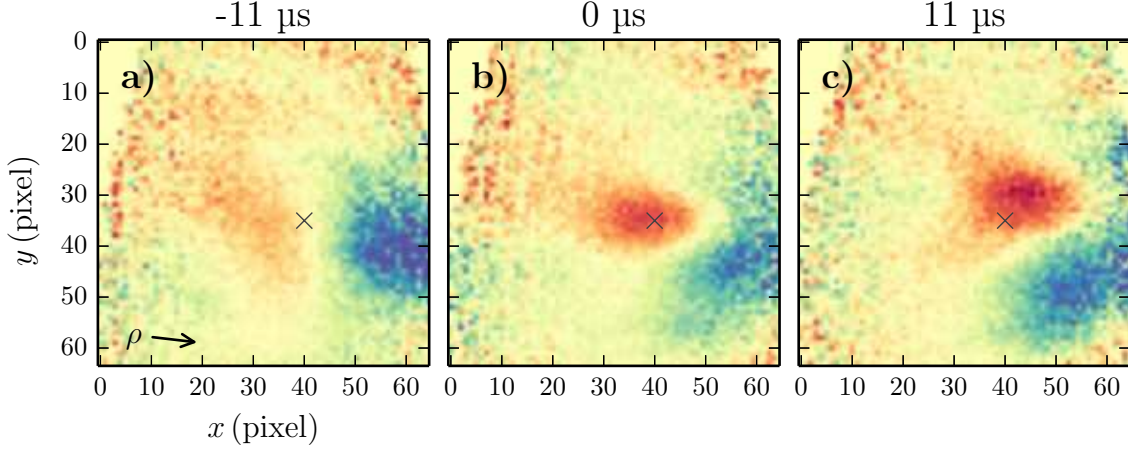
Figure 10.5: *Conditional average of normalized intensity fluctuations $\tilde{I}_n$ recorded during inter-ELM H-mode phases of #28769. The representation is the same as in Fig. 10.4.*

10.2.2 Conditional average of helium gas-puff data

Since the helium gas-puff penetrates further into the SOL the blob dynamics can be studied at a different radial position closer to the separatrix. The emitted intensity peaks approximately 4 cm away from the separatrix.

The CA in L-mode phases with helium gas-puff displays a different dynamics compared to the results from the deuterium gas-puff data, which captures the SOL region in front of the limiter. As can be seen in Fig. 10.6, at $\tau = -11\,\mu s$ two blobs are visible in the CA. These two blobs propagate in different poloidal directions and merge at $\tau = 0\,\mu s$, Fig. 10.6 b), near the reference pixel (gray cross). At $\tau = 11\,\mu s$, Fig. 10.6 c), the resulting blob has moved radially outwards with only a small poloidal propagation velocity.

Figure 10.6: *Conditional average of normalized intensity fluctuations $\tilde{I}_n$ recorded during a helium gas-puff in an L-mode phase of #29520. The cross (gray) marks the location of the reference pixel. The radial direction agrees approximately with the x direction, the poloidal direction with the y direction, see Fig. 10.2 for the exact orientation of the images.*

A more sophisticated analysis of the image data revealed that the CA does not reflect the dynamics of single events, but is a mixture of two different types of events. The object recognition method developed to study blobs at TJ-K was used to introduce a further trigger condition to the CA. A detection region of 10×10 pixels (the typical structure size) is defined, centered around the reference pixel from the analysis above. Whenever the center of mass (COM) of an imaged intensity perturbation of a blob is detected in this region its poloidal velocity is deduced. This velocity can either be positive or negative, resulting in two different CAs, one for each poloidal propagation direction.

Figure 10.7 shows three time instances from the CA for blobs with positive poloidal velocity (upwards in the images). At $\tau = -11\,\mu s$ the light intensity increases at the left (radially inwards) of the reference pixel (gray cross), but no clear quasi-

coherent structure is seen. At $\tau = 0\,\mu s$ (Fig. 10.7 c), a blob is observed near the reference pixel, which propagates radially outwards and poloidally upwards.

Figure 10.7: *Conditional average of normalized intensity fluctuations $\tilde{I}_n$ recorded during a helium gas-puff in an L-mode phase of #29520. Only blobs with positive poloidal (upwards) velocity have been considered as triggering events. The representation is the same as in Fig. 10.6.*

Figure 10.8 shows three time instances from the CA result for blobs with negative poloidal velocity (downwards in the images). At $\tau = 0\,\mu s$ (Fig. 10.8 b), a blob can be seen near the reference pixel position. In Fig. 10.8 c) at $\tau = 11\,\mu s$ two blobs are observed. The first blob (blob 1 in the image) shows a displacement to lower poloidal angles (bottom) and, hence, triggers the CA condition for negative poloidal velocities. The second blob in Fig. 10.8 c) (blob 2) is located at the same position as the blob in Fig. 10.7 c) from the CA for blobs with positive poloidal velocities. The physical interpretation of the observation of the second blob remains an open question. It might result from a splitting of the initial blob at $\tau = 0\,s$.

Figure 10.9 shows three time instances of the CA of the normalized intensity fluctuations $\tilde{I}_n$ recorded in H-mode inter-ELM phases (see Sec. 4.2.1) during a helium gas-puff. A blob can clearly be seen in all three images as it propagates radially outwards and in the negative poloidal direction. Compared to the L-mode phase, the blob features a larger size and moves poloidally in the opposite direction.

10.2.3   Summary of the conditional averaging results

The conditional average analysis of the image data revealed that blobs are observed in L- and inter-ELM H-mode phases. The most obvious difference is the opposite direction of the poloidal propagation. There were also indications that the inter-ELM H-mode blobs feature a larger size perpendicular to the magnetic field. However, due to the observation of blobs moving into opposite poloidal directions, the CA of
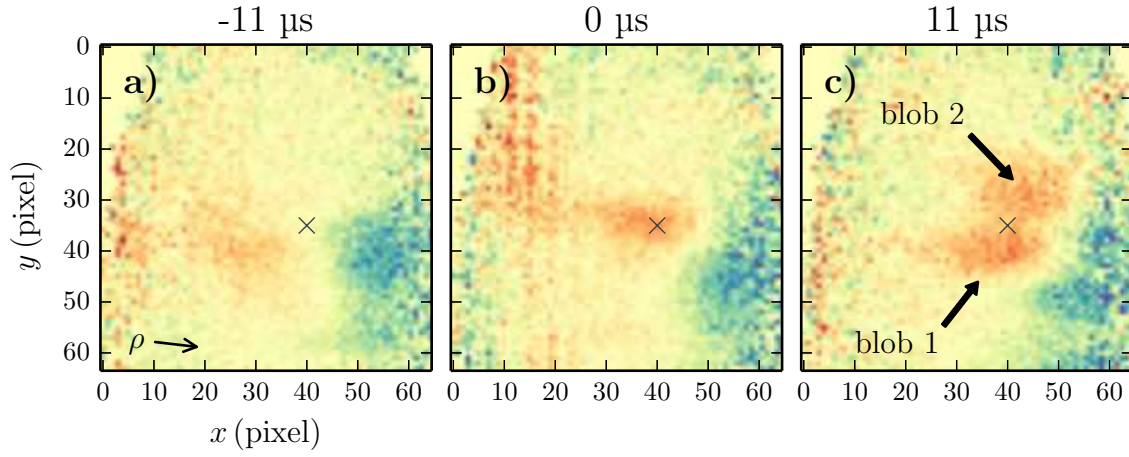
Figure 10.8: *Conditional average of normalized intensity fluctuations $\tilde{I}_n$ recorded during a helium gas-puff in an L-mode phase of #29520. Only blobs with negative poloidal (downwards) velocity have been taken as triggering events. The representation is the same as in Fig. 10.6.*
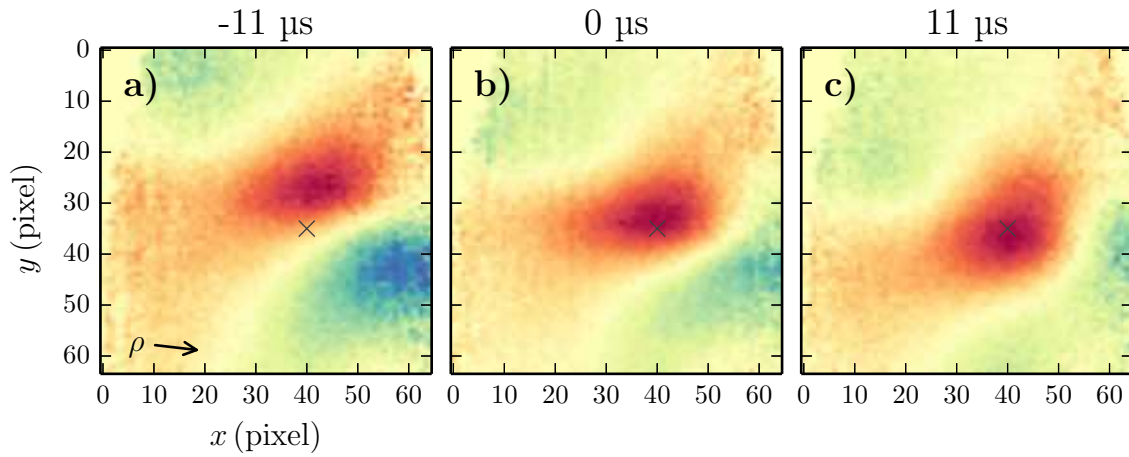
Figure 10.9: *Conditional average of normalized intensity fluctuations $\tilde{I}_n$ recorded during a helium gas-puff in inter-ELM H-mode phases of #29520. The representation is the same as in Fig. 10.6.*

blobs in L-mode phases does not necessarily reflect the dynamics of single events and care has to be taken when using the CA to study the characteristic size and velocity of blobs in the observed region. Instead, in the following single events are analyzed and the obtained sizes and velocities are averaged.

10.3   Detection rate

In Ref. [81] it was observed that blob generation takes place approximately $1\,cm$ outwards of the separatrix. The blobs are not detected in this region, but after propagating into the detection region, where the gas-puff causes sufficiently high light intensities to detect turbulent structures in the SOL. Depending on the typical lifetime of the blobs, the detection rate is not necessarily equivalent to the generation rate. There is, however, no indication that blobs appear spontaneously in the SOL, but that they are generated close to the separatrix and then propagate radially outward. Therefore, changes in the generation rate influence the detection rate. Since the blobs have to propagate through the SOL before reaching the camera view, the detection rate is also influenced by the characteristic trajectory of the blobs and by changes of their lifetime, since the blob may decay before being detected.

Blobs were detected in the raw data by using the object recognition method. Fluctuations in the raw data are considered as blobs when they feature a peak amplitude larger than the standard deviation, which is surrounded by a minimum of 20 pixels detecting a fluctuation amplitude of at least half of the maximum value. The area threshold of 20 pixel serves to prevent spurious blob detection due to noise.

10.3.1   Blob detection rates from deuterium gas-puff data

The deuterium gas-puff produces an emitted peak intensity a few centimeter in front of the limiter at segment S13. A square of 10×10 pixels is chosen as the detection region around a reference position, in order to avoid that the blobs are truncated at the edges of the image or interact with the limiter (see Sec. 10.2). If these two prerequisites are satisfied the resulting waiting-time distribution (WTD) and detection rate change only marginally for different locations of the reference pixel. For the analyses shown below, the reference pixel was chosen at $x = 15$, $y = 30$, i. e. exactly in the middle of the imaged region in front of the limiter.

The resulting WTDs for the L-mode phase and inter-ELM H-mode phases are compared in Fig. 10.10. Since the data sets cover time intervals of different length the count rate per waiting time interval is normalized to the total amount of observed blobs. The corresponding detection rates are 3320 blobs/s for the L-mode phase and 4416 blobs/s for the inter-ELM H-mode phases. The shape of the WTDs and the detection rates compare well for both phases, which indicates that the blob generation mechanism does not change fundamentally. The detection rates are slightly larger in the inter-ELM H-mode. In Sec. 10.4 it is shown, however, that the
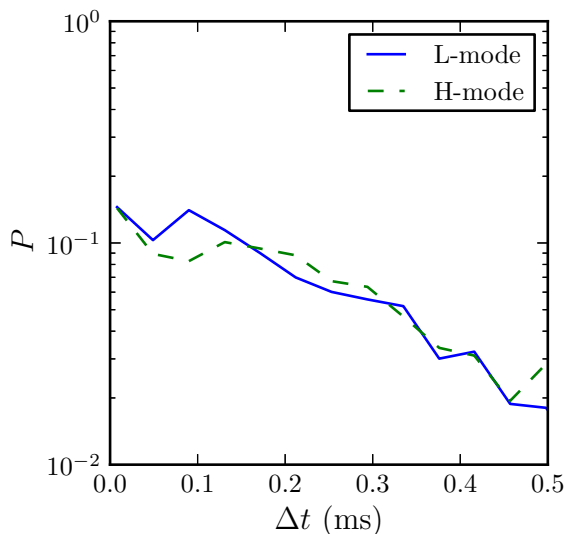
Figure 10.10: *Comparison of waiting-time distributions for blobs observed during a deuterium gas-puff in an L-mode phase and inter-ELM H-mode phases of #28769.*

average blob size is increased in inter-ELM H-mode compared to L-mode. Hence, the higher detection rates in H-mode are probably caused by a larger number of blobs exceeding the area threshold and not necessarily by a larger generation rate.

10.3.2 Blob detection rates from helium gas-puff data

Since the light intensity emitted during the helium gas-puff reaches its maximum closer to the separatrix than during the deuterium gas-puff, the comparison of WTDs and detection rates for two different radial positions in the SOL is possible. Here, the analysis is done for $\rho_{\text{pol}} \approx 1.04$.

Again, the analysis was done for image data captured during an L-mode phase and during inter-ELM H-mode phases. The resulting WTDs are shown in Fig. 10.11 a). The corresponding detection rates are 3736 blobs/s for the L-mode phase and 4623 blobs/s for the inter-ELM H-mode phases. The shape and count rates are comparable, as it is the case for the deuterium gas-puffs which monitor the SOL at a more outward radial position. However, for the helium gas-puff with a more inward observation region the detection rates are higher. A higher blob detection rate also implies shorter waiting times, which is indeed the case as is displayed in Fig. 10.11 b).

But if blobs are generated from turbulent fluctuations in the vicinity of the separatrix, then how does this result agree with the turbulence reduction in the edge plasma in H-mode? The current understanding is that in the pronounced $\mathbf{E} \times \mathbf{B}$ velocity shear layer present in H-mode, turbulence is suppressed by shear decorrelation in the shear flow [138, 139]. This shear layer, however, is not located directly
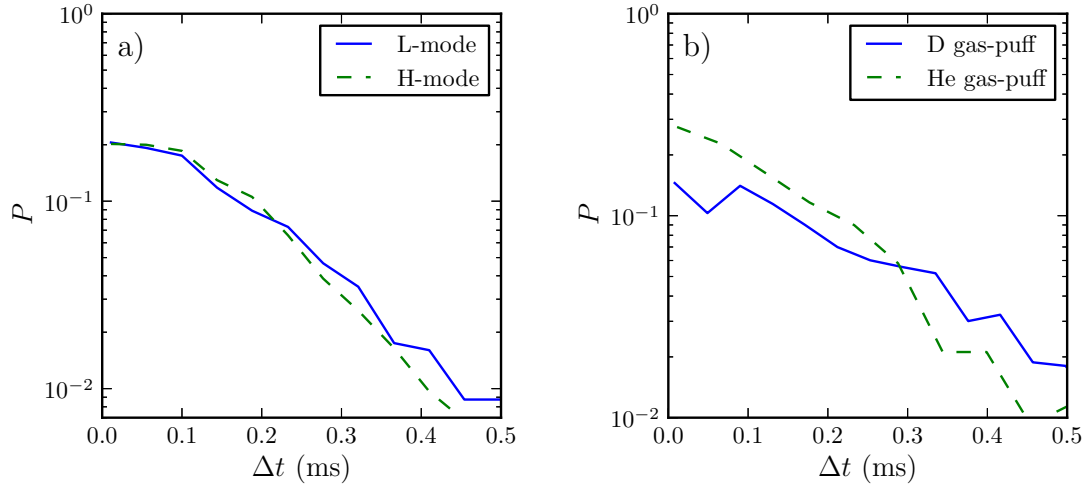
Figure 10.11: *Comparison of the WTD for blobs observed during a helium gas-puff in an L-mode phase from #29520 with the WTD for blobs observed during inter-ELM H-mode phases of the same discharge (a) and with the WTD for blobs also observed in an L-mode phase but with a deuterium gas-puff during #28769 at a more outward radial position (b).*

at the separatrix, but close to it in the edge plasma [140]. Hence, it is not clear how the turbulence just around the separatrix is affected. There are measurements that indicate an unchanged turbulence level directly inside of the separatrix in H-mode phases (compared to L-mode), e.g. at the tokamak DIII-D [24, 141]. Hence, the comparable detection rates in the SOL of ASDEX Upgrade may point to comparable generation rates close to the separatrix and, therefore, no significant change in the turbulence around the separatrix.

10.4   Blob size

With the current optical setup, the poloidal blob size δ_b can be determined from the camera data (Sec. 10.1.3). The analysis of δ_b covers L-mode and inter-ELM H-mode phases of one discharge with a helium and two discharges with a deuterium gas-puff.

10.4.1   Blob sizes from deuterium gas-puff data

From the image data recorded during deuterium gas-puffs in two discharges, the poloidal blob sizes have been deduced by the object recognition method and are compared between L- and inter-ELM H-mode phases. The sizes of blobs with a center of mass (COM) detected in the region between the radial positions $R = 2.175$ and 2.180 m and the vertical positions $z = -0.15$ and -0.145 m are averaged. The detection region is located around $\rho_{pol} = 1.07$.

As an example, the blob size distributions obtained for the L-mode phase (left) and inter-ELM H-mode phases (right) of #28768 are shown in Fig. 10.12. The average size in the L-mode phase is $\delta_{\mathrm{b}} = 6.0 \pm 0.1$ mm and in the inter-ELM H-mode phases $\delta_{\mathrm{b}} = 8.2 \pm 0.1$ mm. The steep edge of the blob size distribution for the L-mode blobs left of the maximum indicates that there are probably blobs with a δ_{b} smaller than 4 mm, which are not properly resolved. Hence, the mean value of δ_{b} obtained from the camera data may be overestimated.
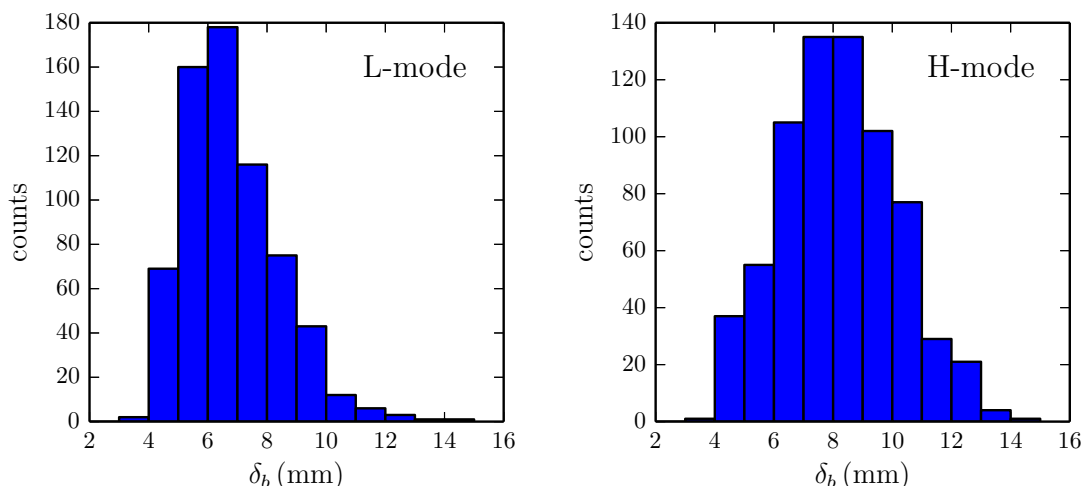
Figure 10.12: *Size distribution (δ_{b}) for blobs around $\rho_{\mathrm{pol}} = 1.07$ in L-mode phases (left) and inter-ELM H-mode phases (right) of #28768.*

Nevertheless, by comparing both the mean value of δ_{b} and the maxima in the size distributions (Fig. 10.12) it can be concluded that δ_{b} is increased in the inter-ELM H-mode phases. However, the change in δ_b of roughly 30 % is small and is even smaller in the second analysed discharge (#28769), where δ_{b} is 6.4 ± 0.2 mm in the L-mode phase and 7.2 ± 0.1 mm in the inter ELM H-mode phases.

Since the blob model presented in Sec. 3.2 and the experiments at TJ-K (Sec. 8.2) indicate a connection between the blob size δ_{b} and the drift scale ρ_{s}, the electron temperature needs to be known. The temperature profiles obtained from a fit to Thomson data are displayed in Fig. 10.13.

It can be seen that for ρ_{pol} larger than 1.07 (where the blob sizes are analyzed) the temperature profiles are flat and comparable for both discharges. At $\rho_{\mathrm{pol}} = 1.07$ an electron temperature of $T_e = 18 \pm 5$ eV is observed in the L-mode phase and of $T_e = 42 \pm 14$ eV in the inter-ELM H-mode phases of #28768. And at the same ρ_{pol} but in #28769 the value for $T_e = 17 \pm 5$ eV (L-mode) and $T_e = 37 \pm 4$ eV (inter-ELM H-mode) are obtained from the temperature fit. This leads to an increased ρ_{s} and, hence, to an increased δ_{b} as can be seen in Fig. 10.14. It should be noted that temperature measurements by Thomson Scattering are not very reliable in the SOL and this result should be cross-checked with temperature
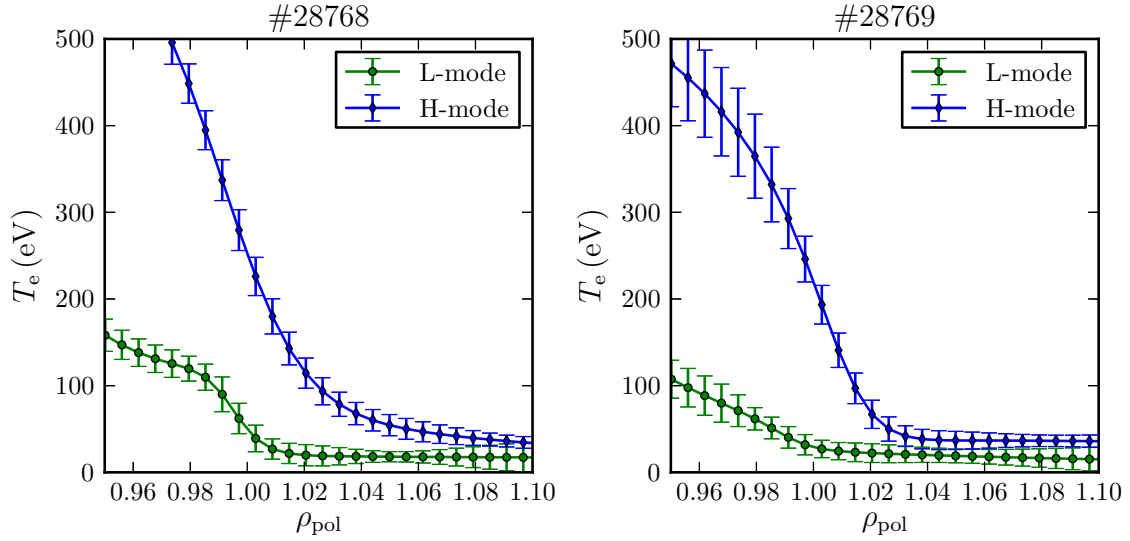
Figure 10.13:   *Temperature profiles in L-mode and inter-ELM H-mode phases of #28768 (left) and #28769 (right).*

measurements using Langmuir probes, which was not available in the presented experiments. However, measurements at ASDEX Upgrade exist, which indicate that T_e can indeed be increased in the SOL in H-mode [142].

In Fig. 10.15 the sizes are compared to the predictions for cold ions, Eq. (3.17), and warm ions, Eq. (3.18). Both models predict blob sizes close to the values for δ_b observed in the experiment. With the assumed $T_i = 3T_e$ the warm ion model predicts the blob sizes almost perfectly. The larger blob sizes in the H-mode phases follow the increase in ρ_s. Furthermore, comparing the inter ELM H-mode phases of #28768 and #28769 increased values of δ_b and ρ_s are also observed together. In the L-mode phases, however, δ_b is smaller in #28768 despite a larger ρ_s. The ion-temperature profiles (T_i), which are also of importance for the blob dynamics, are not available for the analyzed shots. Hence, the influence of T_i on the blob size remains an open question. Furthermore, it was also observed in ASDEX Upgrade that background electron density n_e influences the blobs size [143]. Considering the results obtained at TJ-K, namely that the blob size scaling with ρ_s seems to be influenced by the generating drift waves in the edge plasma, it may also be the case that not only the local ρ_s has to be considered, but also the values at radially more inward positions, where the blobs are generated and propagate through.

10.4.2   Blob sizes from helium gas-puff data

Using helium for the GPI, the blob size was measured at a radially more inward position around $\rho_{pol} = 1.05$. The resulting size distributions for the L-mode phase are shown in the left of Fig. 10.16 and for the inter-ELM H-mode phase on the
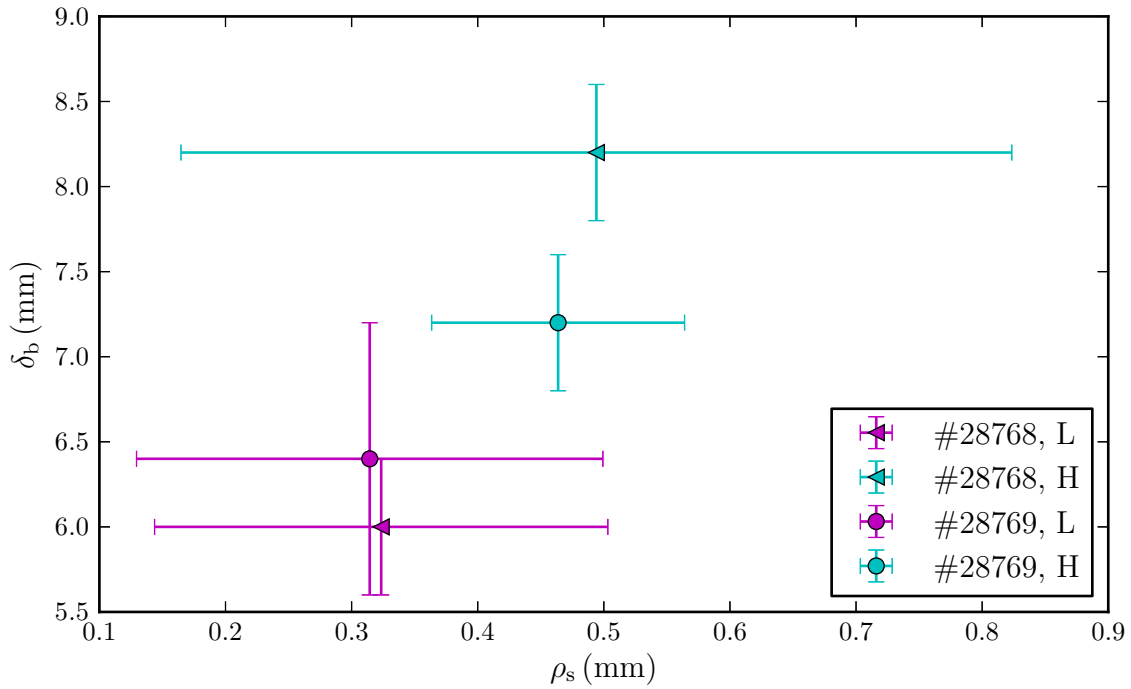
Figure 10.14: *Blob sizes δ_b as a function of ρ_s in L-mode and inter-ELM H-mode phases of #28768 and #28769. There seems to be an increase of δ_b with rising ρ_s, which explains the larger δ_b in H-mode phases.*
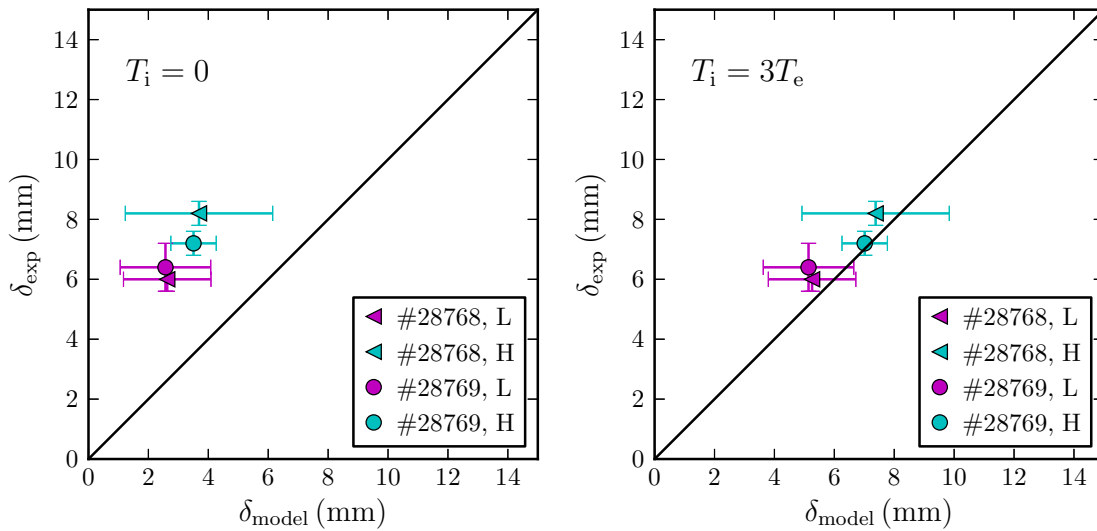
Figure 10.15: *Comparison of the average blob size δ_{exp} with the prediction δ_{model} from a cold ion model (left) and a warm ion model (right).*

right. Due to the short time interval of the gas-puff only a small number of blobs is detected, especially in the inter-ELM H-mode phases, where the time intervals with ongoing ELM activity are not considered in the analysis.
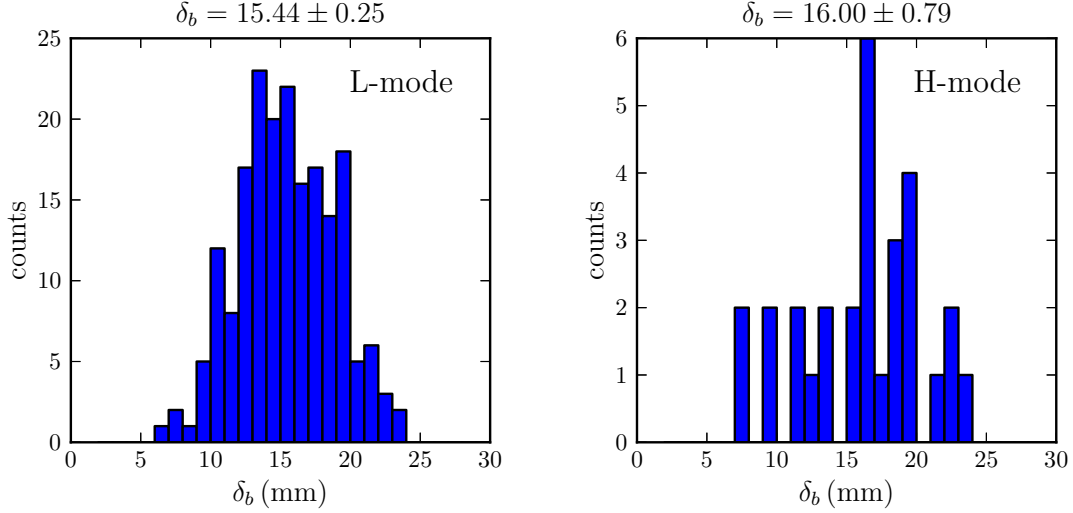
Figure 10.16: *Size distribution (δ_b) for blobs around $\rho_{\mathrm{pol}} = 1.05$ in L-mode phases (left) and inter-ELM H-mode phases (right) of #29520.*

The same trend is observed, namely that the blob size is larger in the inter-ELM H-mode phases, $\delta_{\mathrm{b}} = 15.4 \pm 0.2 \, \mathrm{mm}$ (L-mode) compared to $\delta_{\mathrm{b}} = 16.0 \pm 0.8 \, \mathrm{mm}$ (H-mode), but the error in the H-mode phase is large due to the small number of events. The observed blob sizes are also clearly larger than those observed with the deuterium gas-puff. This indicates that the blobs shrink in size while propagating outwards. Since the radiation emitted by the two gases has different n_{e} and T_{e} dependencies, however, this result needs to be cross-checked by other diagnostics (e. g. lithium-beam spectroscopy). This is planned as one of the next steps for the GPI diagnostics at ASDEX Upgrade.

10.5   Blob velocity

The conditional average of the camera data shown in Sec. 10.2 reveals that both the poloidal and radial velocity are different depending on the location and confinement regime (L- or H-mode). In this section the velocity is analyzed for single events by using the object recognition method. All of these velocities are averaged at the center of mass position of the detected blob. The poloidal magnetic flux Ψ_{p} of magnetic field in ASDEX Upgrade is available for every shot and, hence, the radial (parallel to the gradient of the poloidal flux $\nabla \Psi_{\mathrm{p}}$) and poloidal (perpendicular to $\nabla \Psi_{\mathrm{p}}$ and $\mathbf{B}$) velocity can be determined.

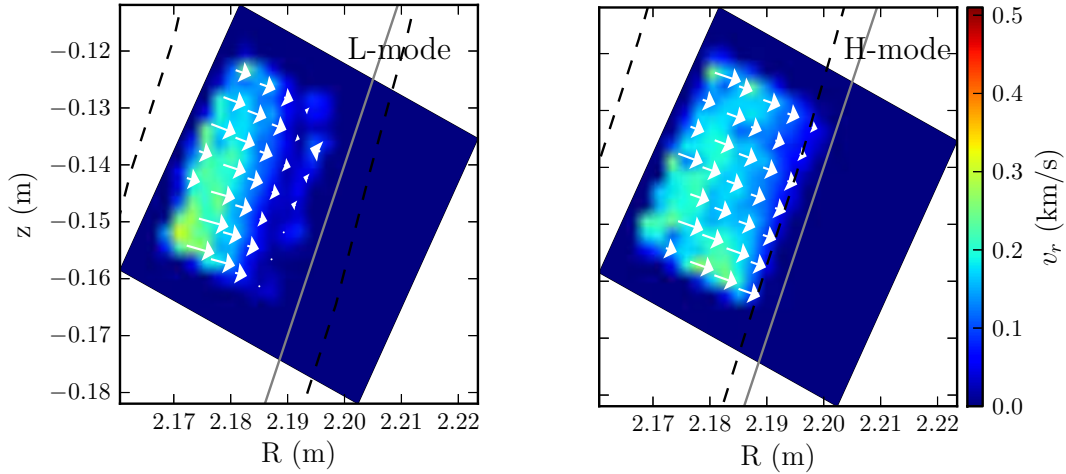### 10.5.1 Blob velocity from deuterium gas-puff data

The spatially resolved poloidal velocity field is compared in Fig. 10.17 for the L-mode (left) and inter-ELM H-mode (right) phases of #28769. While the absolute values are comparable in both phases, between 100 and 300 m/s with a tendency for larger values in the H-mode phase, there is a clear difference in the poloidal propagation direction, which is opposite in the H-mode phase. In the L-mode phase, there is a shear layer in the poloidal velocity at the inner edge of the image data at approximately $\rho_{pol} = 1.06$. A similar feature can be observed by probe measurements of the poloidal velocity in the vicinity of the limiter [82]. In Refs. [27] this shear layer is explained by a change in the plasma potential with connection length and temperature profile, which leads to a reversed $\mathbf{E} \times \mathbf{B}$-drift direction. Such a reversal is observed in ASDEX Upgrade for the radial position where the field lines enter the limiter shadow and no longer end in the divertor, which leads to drastically reduced connection lengths [82]. In H-mode, in contrast, the camera does not see a similar feature. In the experiment Heliotron J a similar poloidal propagation reversal was observed between L- and H-mode phases [144], which gives further evidence that the observation is due to a change in the SOL dynamics, probably due to changes in the radial electrical field E_r, and should be investigated further in future experiments.
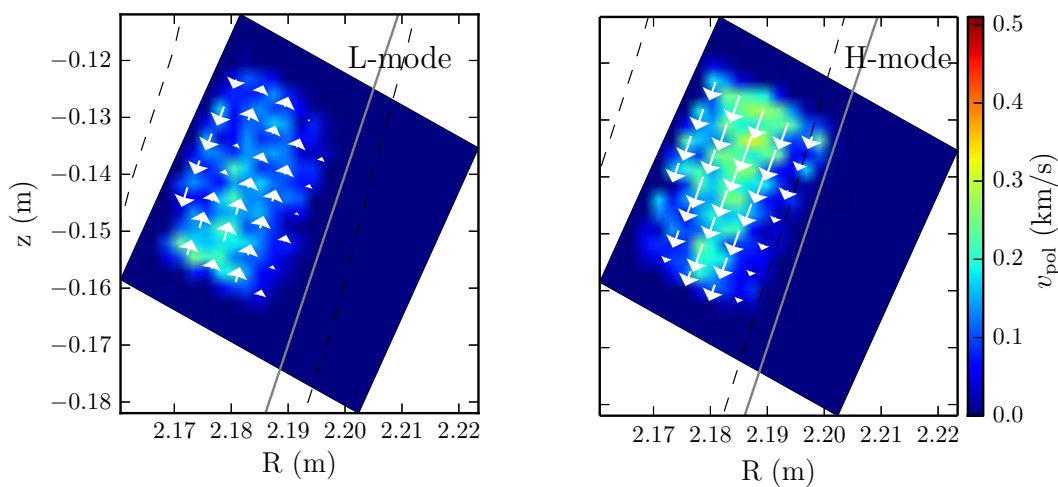
Figure 10.17: *Poloidal velocity fields obtained from camera data during a deuterium gas puff in #28769. The analysis was done for the L-mode phase (left) and the inter-ELM H-mode phases (right). The left dashed line marks $\rho_{pol} = 1.05$, the right one $\rho_{pol} = 1.10$. The line (gray) marks the approximate location of the limiter near S13.*

The radial velocity fields are shown in Fig. 10.18, again for the L-mode (left) and inter-ELM H-mode (right) phases of #28769. Both velocity fields compare well, showing a decrease of the radial velocity in the radial direction from about 200 m/s at the inner edge of the observed region to zero in front of the limiter. Figure 10.19 shows a cut through the radial velocity field of the L-mode phase where this radial

deceleration can clearly be seen. A comparable behaviour is documented for DIII-D in Ref. [145] and was assumed for ASDEX Upgrade, to explain observations from ion-temperature measurements [41]. Furthermore, the radial velocities in Fig. 10.18 appear to be slightly larger in the L-mode phase, as will be shown more clearly in the following section.


Figure 10.18: *Radial velocity fields obtained from camera data during a deuterium gas puff in #28769. The analysis was done for the L-mode phase (left) and the inter-ELM H-mode phases (right).*

10.5.2   Size dependency

Equation (3.8) predicts the radial blob velocity $v_{r,\mathrm{b}}$ under the assumption that the ion temperature T_i is zero. Nevertheless, it was successfully used in Ref. [146] to predict a decreasing $v_{r,\mathrm{b}}$ with increasing δ_b in the SOL of ASDEX Upgrade. In that reference it is stated that $\delta n/n \approx 1$. For characteristic values from ASDEX Upgrade, Eq. (3.8) can be approximated by the scaling according to Krasheninnikov, Eq. (3.10), which predicts the observed decrease of $v_{r,\mathrm{b}}$ with increasing δ_b. This implies that the blob velocity is smaller in H-mode phases due to the larger blob size, when all other parameters are kept constant. This expectation is in agreement with the observed average values as shown in Fig. 10.20. A c/δ_b^2 fit (dashed line) shows no perfect match, indicating that $v_{r,\mathrm{b}}$ does not only depend on δ_b^2.

That this result is indeed explained by a size dependency of $v_{r,\mathrm{b}}$ is shown by determining size and velocity of single blob events from the camera data. A linear regression of $v_{r,\mathrm{b}}$ with $1/\delta_\mathrm{b}^2$ reveals that in both discharges and phases $v_{r,\mathrm{b}}$ decreases with increasing δ_b, in agreement with the trend of the mean values in Fig. 10.20. The correlation values of the linear regression are $0.08\,\%$ in L-mode and $0.11\,\%$ in H-mode. The very low values indicate that δ_b is not the only parameter governing
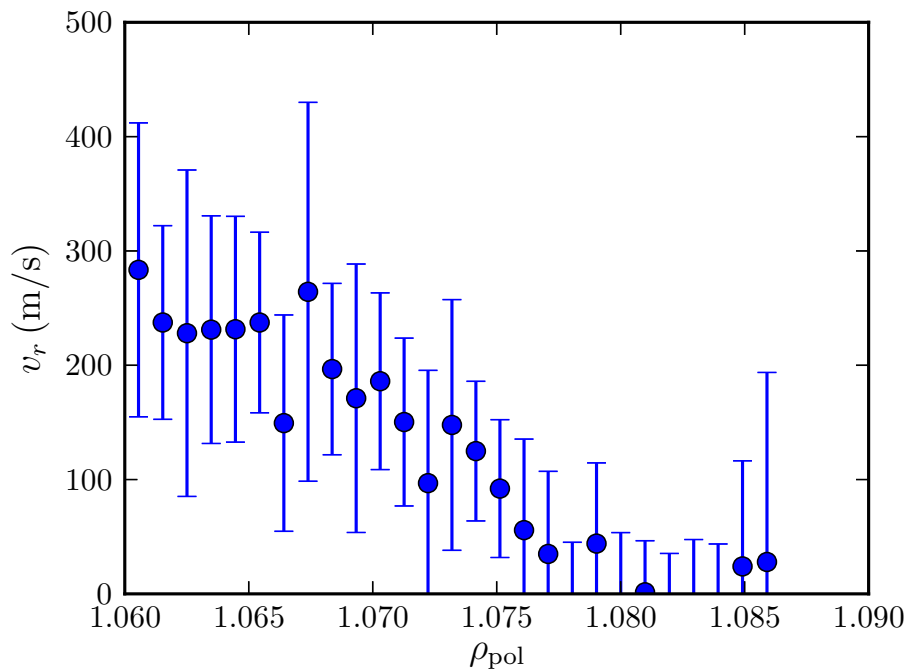
Figure 10.19: *Radial profile of the radial velocity observed in the L-mode phase of #28769 showing the deceleration of the blobs while propagating outwards.*

$v_{r,b}$. Candidates are especially the parallel filament length and the blob pressure amplitude [42].

A comparison of the average value of $v_{r,b}$ with the cold ion scaling according to Eq. (3.10) is shown on the left in Fig. 10.21. It was presented in Sec. 3.2.2, however, that the finite pressure should increase $v_{r,b}$ as can be seen from Eq. (3.14). On the right of Fig. 10.20 $v_{r,b}$ obtained from the fast camera measurements during the discharges with deuterium gas-puffing is compared to the warm ion predictions (assuming $\tau_i = 3$ [68]). Both scalings predict velocities of the right order of magnitude. The cold ion prediction is closer to the observed values than the warm ion prediction, however, the experimental errors are large due to the quadratic dependencies on ρ_s and δ_b. Furthermore, both scalings predict a large difference between the L- and H-mode phases, which is not observed in the experiments. The scaling does, however, correctly predict the decrease of $v_{r,b}$ with δ_b due to an increased blob size.

The collisional scaling according to Eq. (3.15) should not apply, since the collision parameter Λ (Eq. (3.16)) is smaller than 1 (about 0.1 in the L-mode and 0.03 in the H-mode phases) and indeed predicts too small velocities (around values of $10\,\mathrm{m/s}$). It is, however, apparent from other experiments [143] that the background n_e influences the blob velocity, indicating that collisions do play a role. Obviously not all relevant effects seem to be covered by the warm ion scaling, yet.
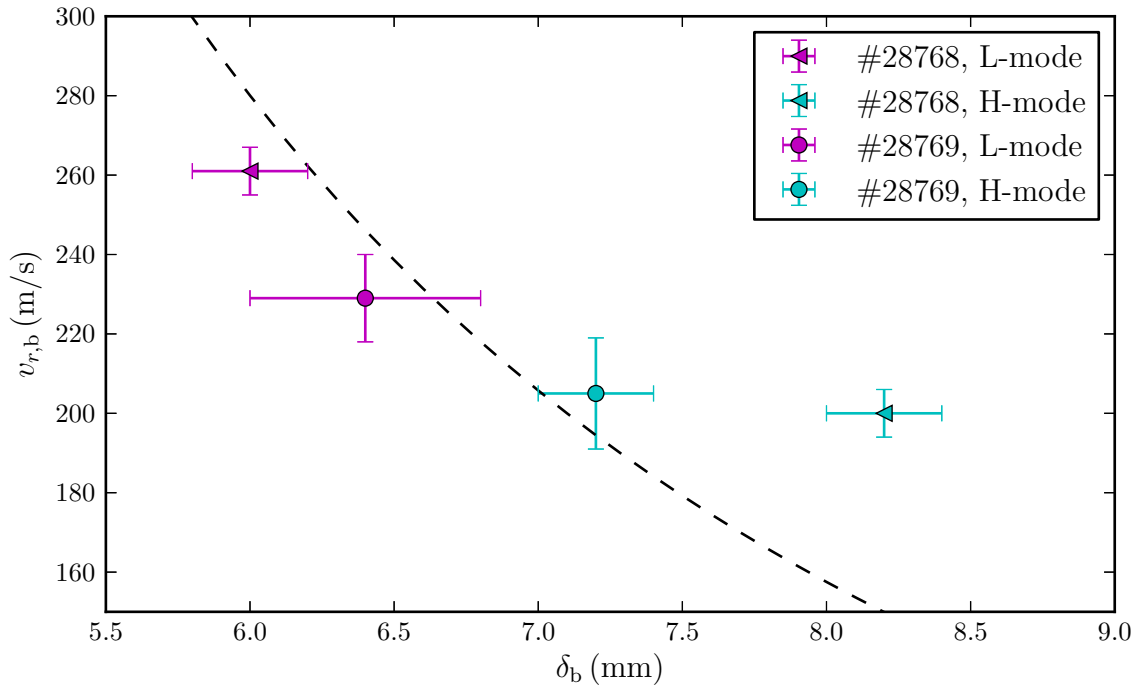
Figure 10.20:   *Radial blob velocitiy $v_{r,b}$ as a function of the mean blob size δ_b at $\rho_{pol} \approx 1.07$ in L-mode and inter-ELM H-mode phases. A c/δ_b^2 fit is shown as dashed line.*
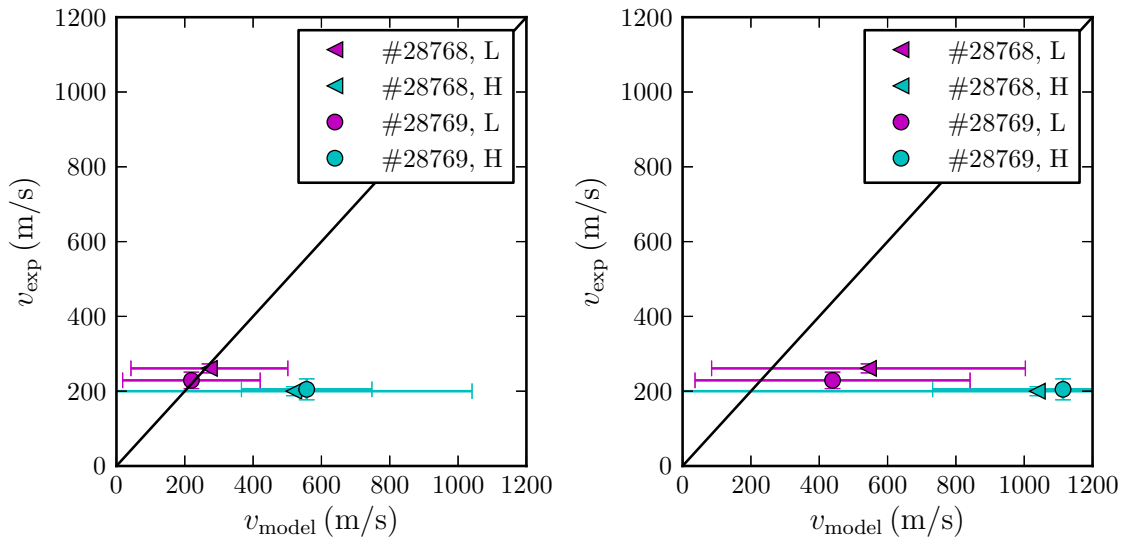
Figure 10.21:   *Comparison of averaged radial blob velocities (v_{exp}) with a cold ion model (left) and a warm ion model (right).*

10.5.3 Blob velocity from helium gas-puff data

The analysis of the poloidal and radial blob velocity field is repeated for discharge #29520 with the helium gas-puff. The poloidal velocity fields are shown in Fig. 10.22. In the H-mode phase (right) the poloidal velocities point downwards (IDD) and are larger (up to $v_{\text{pol}} = 500\,\text{m/s}$) as observed in H-mode in the previous section (Fig. 10.17). The poloidal velocity profile in the L-mode phase (left) shows a large scatter in both, the absolute value and the propagation direction. Different poloidal propagation directions of blobs in the L-mode phase of #29520 are also seen in the conditional average shown in Sec. 10.2. The cause for this feature remains an open question, but may be explained by blobs splitting into smaller structures. A detection problem would also be possible, but seems to be unlikely due to the observations in the CA result shown before in Fig. 10.7.
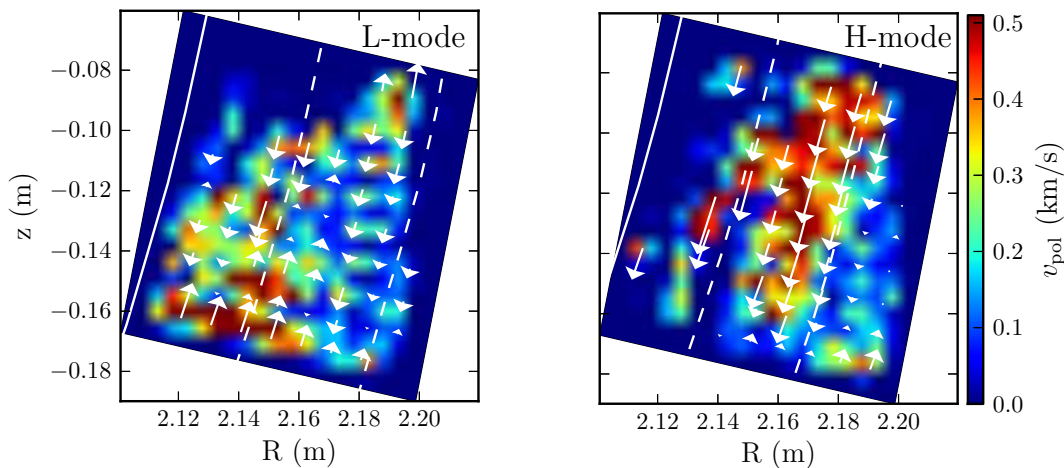
Figure 10.22: *Poloidal velocity fields obtained from camera data during helium gas-puffs in #29520. The analysis was done for the L-mode phase (left) and the inter-ELM H-mode phases (right). The left-most line (white) marks the location of the separatrix ($\rho_{\text{pol}} = 1.00$), the left dashed line marks $\rho_{\text{pol}} = 1.05$, the right one $\rho_{\text{pol}} = 1.10$.*

The radial velocity fields are shown in Fig. 10.23. In both, L- and H-mode phases, the detected radial velocities are higher (up to 600 m/s) than further outward, supporting the observation of a radial deceleration of blobs. However, due to the small number of detected events during the short helium gas-puffs the resulting velocities fluctuate strongly over the observation region, rendering a meaningful comparison of the mean values impossible.
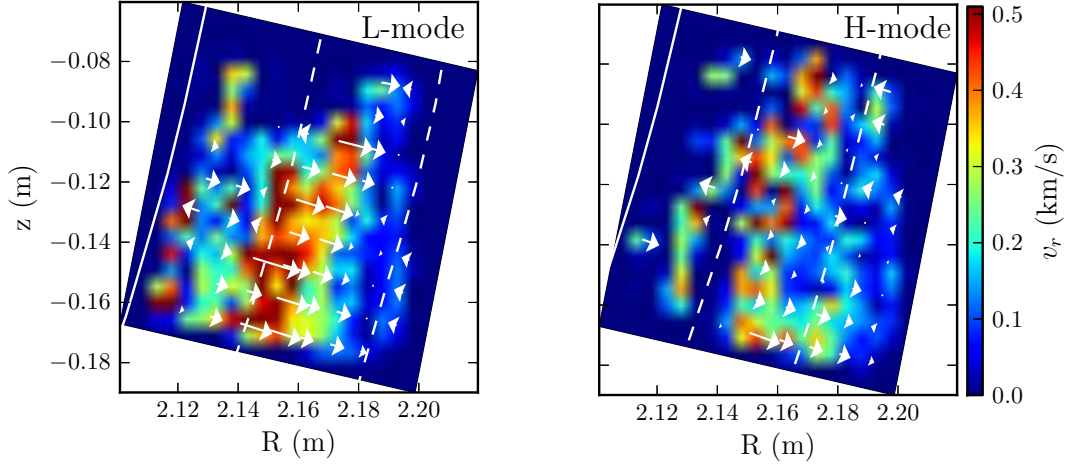
Figure 10.23: *Radial velocity fields obtained from camera data during helium gas-puffs in #29520. The analysis was done for the L-mode phase (left) and the inter-ELM H-mode phases (right).*

10.6   Summary of the ASDEX Upgrade results

The first fast camera measurements in the SOL of ASDEX Upgrade were performed using the technique of gas-puff imaging in order to achieve sufficient light intensities. Two different gases, deuterium and helium, were used for the gas puffs. The advantage of using deuterium is that longer puffing intervals are possible. This is because the bright emission of deuterium allows for low deuterium fluxes and the fact that it does not introduce impurities in the deuterium plasmas of ASDEX Upgrade. However, due to the relatively low ionization energy of deuterium (13.6 eV), it cannot penetrate far into the plasma. Hence, only the outer SOL can be studied with the deuterium puff. In contrast it was seen that helium can almost reach the separatrix. But since the emitted intensity of helium is lower a larger amount of helium is needed, which furthermore is an unwanted impurity in the deuterium discharges. To prevent a change in the SOL dynamics due to helium, only short puffing intervals of about 200 ms are possible, reducing the number of detected events.

All performed discharges were run as purely Ohmically heated L-mode plasmas before additional ECRH triggered the L-H transition. Hence, it was possible to compare the blob detection rate, size δ_b, and velocity (poloidal and radial) between L- and H-mode, where only inter-ELM phases were selected. It was observed that the blobs in H-mode are larger in size and that they have a smaller radial outward velocity. Both changes are not as striking as to indicate a dramatic change in the blob dynamics between L- and H-mode. In accordance with this is the observation that the detection rates and waiting-time distributions (WTDs) remain almost unchanged after the L-H transition. The detection rate is slightly increased in H-mode, but this may be explained by the larger blob size in that phase, which leads to a larger

number of events with sizes exceeding the area threshold. Thus, it cannot be decided if the increase in the detection rate also reflects changes in the generation rate of blobs. Clear differences in the blob dynamics between the L- and H-mode phase were observed in the poloidal velocity profiles. In the outer SOL ($\rho_{\mathrm{pol}} \gtrsim 1.06$) the poloidal propagation is reversed in L-mode. This reversal is not observed in the H-mode phase. Further radially inwards the single blobs show different poloidal propagation directions in the L-mode phase. As a consequence the dynamics deduced from conditional averaging does not reflect the evolution of single events. Furthermore, the camera measurements revealed in both confinement regimes a deceleration of the radial blob velocity $v_{r,\mathrm{b}}$, while the blobs propagate outwards.

The size dependence of $v_{r,\mathrm{b}}$ was studied around $\rho_{\mathrm{s}} = 1.07$. The average values of $v_{r,\mathrm{b}}$ in different L-mode and H-mode phases show a clear decrease with an increasing average δ_{b}. A regression analysis revealed only a weak correlation for single events, which indicates that the blob size δ_{b} is not the only parameter determining $v_{r,\mathrm{b}}$. According to theory (Sec. 3.2.2) the pressure inside the blob (n_{e}, n_{i}, T_{e}, and T_{i}), the parallel length $l_{\parallel}$ of the filament, and δ_{b} determine $v_{r,\mathrm{b}}$. Hence, the size dependence is much clearer for the average values of $v_{r,\mathrm{b}}$, when further influences average out. Comparisons with theoretical scalings explain this size dependence, however, it is also apparent that not all of the relevant physical mechanisms are covered by the scalings discussed in Sec. 3.2.2, yet. This issue has to be addressed in future experiments.

The results show that GPI is a valuable tool to study blob properties in the SOL of ASDEX Upgrade. It is of special interest that the shape and orientation of the structures can be observed directly, which is crucial for the interpretation of measurements from diagnostics without spatial resolution. However, it also became aparent that the interpretation of the camera data relies on quantities that are not accessible from the camera data. Hence, future studies of the SOL turbulence in ASDEX Upgrade should concentrate on a multi-diagnostics approach to measure e. g. temperature and density profiles together with the radial electrical field. Furthermore, it was demonstrated that fast imaging can be employed under very different plasma conditions, like the low temperature plasmas in TJ-K and the much hotter SOL plasma in ASDEX Upgrade using the same methods of data analysis.

Chapter 11

Summary and conclusion

11.1 Summary

Reduction of the energy loss of a fusion plasma is one of the key challenges in the realization of a fusion power plant. Close to the wall, in the scrape-off layer (SOL), a significant contribution to the turbulent energy and particle loss comes from filamentary structures that are generated by turbulent fluctuations in the vicinity of the last closed flux surface. Due to their prominent appearance in many diagnostics they have been called *blobs*. These blobs feature a radial outwards propagation, transporting energy and particles from the plasma edge towards the wall, where they can lead to a serious load on the plasma facing components. The radial propagation of blobs can be understood by a polarization of the filament due to curvature-induced charge separating drifts. The transport and wall load induced by blobs depend not only on the velocity of the filaments, but also on the blob size and their generation rate. Quantitative predictions are available for their size and velocity, but not for the generation rate. The two main objectives of this thesis were to reveal how well the blob properties predicted by the model compare to experimental observations in complex magnetic field configurations of actual fusion experiments and if the turbulence in the confined plasma influences the blob properties during the generation process.

In this thesis, experiments have been carried out on two very different magnetically confined plasmas; a low temperature plasma in the stellarator TJ-K at the University of Stuttgart and a fusion plasma in the tokamak ASDEX Upgrade at IPP. The primary diagnostics used for these experiments was a fast camera. Such a camera is a valuable tool to study dynamic processes in a plasma, since the data are obtained spatially resolved over a large cross section with high time resolution. In plasmas with relatively low temperatures, the remaining background of neutrals allows the direct observation of the emitted visible light. In much hotter fusion plasmas, the neutral density has to be increased locally by gas injection in order to achieve sufficiently bright light emission. Since the light emission depends on both the electron density and temperature at the same time, care has to be taken when

extracting physical information from the raw data.

To study turbulent transport, information about potential fluctuations is required. Hence, supplemental data from other diagnostics were used to obtain a complete picture of the blob related fluctuations. In the case of TJ-K, Langmuir probe measurements were performed. In ASDEX Upgrade, comparable probe studies are not feasible, since the higher SOL temperatures severely limit the lifetime of the probes. The results of the experiments are summarized in the following.

The establishment of fast imaging as new diagnostic tool at TJ-K was one of the aims of this thesis. It was shown that blobs in the SOL and coherent edge structures inside of the LCFS (arising from drift-wave turbulence) can be distinguished and studied with a sufficient time resolution. Furthermore, it was shown that the recorded intensity fluctuations resemble density fluctuations in the plasma.

An object recognition code based on the moment method was written to automatically detect and distinguish blobs and coherent edge structures in the image data. With this code, the size and velocity of the structures can be deduced perpendicular to the projection of the magnetic field lines onto the image data.

For blob sizes measured this way, no agreement with the predictions of the blob model was found: A scaling of the blob size with the drift scale ρ_s revealed a scaling exponent $\alpha \approx 0.25 \pm 0.06$, which is significantly smaller than the prediction of $\alpha = 0.8$. Instead, the scaling exponents agree very well for the size scalings of blobs and coherent edge structures, indicating a size coupling between the two.

For the radial velocity, a fair agreement has been found with theoretical predictions according to Eq. (3.8). However, deviations from the predicted values were observed. It was possible to explain these deviations by a cross-phase between density and potential $\alpha^{\phi,n}$ smaller than the $\pi/2$ assumed in the blob model. The reduced $\alpha^{\phi,n}$, which may be caused by an additional drift-wave-like parallel electron dynamics, leads to a reduced $\mathbf{E} \times \mathbf{B}$ velocity of the blobs. Since the velocity depends on the blob size, the edge dynamics indirectly influence the radial blob velocity.

Further evidence for the validity of the blob model was found by additional probe measurements: First, a prediction for parallel currents (along the blob filament) was derived from the blob model and experimentally verified with a dedicated current probe. Second, it was shown that blobs are generated only in SOL regions of negative mean normal curvature $\langle \kappa_n \rangle$, as expected by the model.

There are no quantitative predictions for the generation rate. Since it is observed that blobs are generated from turbulent fluctuations in the edge, the typical time scales of the edge turbulence should be reflected in the generation rate. The generation rate and the closely related waiting-time distribution (WTD) were determined experimentally for blobs in the SOL and coherent edge structures inside of the LCFS. Both the WTD and the generation rate are the same for both kinds of structure, which indicates that every large-amplitude drift wave triggers blob generation.

At ASDEX Upgrade, gas-puff imaging with a fast camera was implemented. It was shown that turbulent fluctuations in the SOL can be resolved with high spatial localization, since the dimensions of the injected gas cloud are small compared to

the system size. Hence, it was possible to deduce the detection rate, blob size, and radial velocity from the imaging data without assistance of further diagnostics. The observed blob properties were compared to theoretical predictions. Only recently the influence of a finite ion temperature has been treated analytically, which should result in predictions more suitable for fusion plasmas than those from cold ion models. Furthermore, special emphasis was placed on the comparison of blob properties in L- and H-mode phases of the analyzed discharges.

The measured blob sizes agree very well with theoretical predictions of the warm ion model. Both the observed blob size increase from L- to H-mode and also the absolute values are predicted correctly.

For the radial velocity the results are less clear. Both the cold and the warm ion model overestimate the velocity and predict a significantly higher blob velocity in the H-mode phases, which is not observed.

Concerning the poloidal velocity of the blobs, clear differences between L- and H-mode were observed. Not only the absolute values, but also the propagation direction changes between the two confinement regimes. The most obvious explanation would be differences in the radial electric field in the SOL, however, measurements of this field were not available for the analyzed discharges.

The blob detection rates were in the range of a few thousand blobs per second. This agrees well with characteristic time scales of the edge turbulence and, hence, the expectation for blobs generated from turbulent fluctuations in the vicinity of the LCFS. The detection rates are similar for L- and H-mode phases, indicating that there is no drastic change in the blob generation mechanism and blob dynamics.

Comparing the results from TJ-K and ASDEX Upgrade, the following conclusions can be drawn from this work:

Validity of the blob model in stellarator geometry: Although most blob models assume very simple magnetic field geometries (mostly that of the simple magnetized torus), in the stellarator TJ-K a good agreement with predictions from these models is found. Especially the blob velocity, the parallel current along the filament, and the generation in regions of $\langle \kappa_{\mathrm{n}} \rangle < 0$ are well described by present blob models. Unlike in the tokamak ASDEX Upgrade, the blob size was not in good agreement with theoretical predictions. The difference between both experiments is that while the blobs in TJ-K are detected shortly after their generation, the blobs in ASDEX Upgrade propagate over a distance larger than the typical blob size before they are detected. Hence, in TJ-K the size distribution with which blobs are generated is measured, while in ASDEX Upgrade unstable blobs cannot reach the detection region before they decay.

Importance of the cross-phase for the radial velocity: In TJ-K it was shown that the cross-phase between density and potential $\alpha^{\phi,n}$ affects the radial velocity. This is in perfect agreement with general considerations on plasma turbulence, but the effect is not included in the present blob models, where $\alpha^{\phi,n} = \pi/2$ is assumed. In ASDEX Upgrade it is also known from prior measurements that $\alpha^{\phi,n} < \pi/2$ [82]. This may explain the observed blob velocities, which are smaller

than the theoretical prediction. It is proposed to study this effect in numerical simulations for ASDEX Upgrade and to perform simultaneous measurements of the blob velocity in the SOL (e. g. by fast imaging) and, using probes, the cross-phase.

Preliminary confirmation of ion-temperature effects on blob dynamics: A first comparison of blob size and velocity in ASDEX Upgrade with theoretical predictions indicates that the inclusion of a finite ion temperature in the blob model improves the agreement with experimental observations.

Strong influence of edge dynamics on blob properties: For the first time the experiments at TJ-K showed that many blob properties in the SOL are influenced by the turbulence in the confined plasma. In particular the generation rate and blob size showed a strong coupling to the respective properties of coherent edge structures. Since the gas-puff imaging at ASDEX Upgrade does not reach the LCFS, a direct comparison of fluctuations inside and outside of the LCFS is rendered impossible. However, the observed generation rates of a few thousand blobs per second seem to be compatible with the results from TJ-K. An implication of the strong influence of turbulence around the LCFS on blob properties is that the blob dynamics cannot only be influenced by changing the conditions in the SOL, but also by controlling the turbulence close to the LCFS.

Comparable blob dynamics in L- and H-mode: For ASDEX Upgrade, no indications were found from measurements of the generation rate, blob size, and radial blob velocity that the blob generation and dynamics are fundamentally different in both confinement regimes. Only the poloidal velocity profile of the filaments shows a dramatic change after L-H transition, including even a local reversal of the poloidal propagation direction. Measurements of the radial electrical field are necessary to check if this is caused by changes in the background $\mathbf{E} \times \mathbf{B}$ drift.

11.2   Outlook

For TJ-K, the next step will be to search for effects of the stellarator geometry on the blob dynamics. While it was found that the blob models with simple magnetic geometries already describe many aspects of the blob dynamics in TJ-K, additional effects should arise from the complex field geometry. In an experiment that is currently under preparation, the role of the geodesic curvature on the blob trajectory will be studied. In the same way as the normal curvature is responsible for the radial propagation of the filaments, the geodesic curvature should change the spatial structure of the blob polarization and, hence, also add poloidal components to the blob propagation. In ASDEX Upgrade, future experiments will be performed using a multi diagnostics approach to obtain a complete set of blob properties. This allows for a detailed comparison of the measured blob properties with the theoretical predictions, leading to an even better understanding of the dynamics of blobs and their role in the turbulent transport of fusion plasmas.

Appendix A

Discharges and analysis parameters

In the following, an overview is given about the most important TJ-K discharges for the analysis in this thesis. Furthermore, the parameters chosen for the object recognition (see Sec. 5.6) are documented.

Camera calibration discharges

The discharges listed below were diagnosed with the fast camera measurements and/or 2D probe scans to identify useful camera setups and to study how the image data compares to probe measurements.

#	gas	comment	#	gas	comment
7508	He		7517	Ar	
7509	He	probe data only	7518	H	
7512	He		7519	H	
7513	He	probe data only	7682	H	observed O1
7514	Ar				

Discharges with fast imaging and 2D probe scans

These discharges were conducted to study blob dynamics and properties. Three reference probe measured ϕ_f and a movable two pin probe $I_{i,sat}$ and ϕ_f. In the focused plane, the lower left corner of the camera images is located at $(R - R_0, z) = (0, -88.2\,\text{mm})$ and the upper right corner at $(R - R_0, z) = (10.4\,\text{mm}, 78.5\,\text{mm})$. $\alpha_{\min}$ and $\alpha_{\max}$ are the minimum/maximum values for the orientation angle of the major axis (in °) that do not indicate overlap.

#	gas	comment	$\alpha_{\min}, \alpha_{\max}$	#	gas	comment	$\alpha_{\min}, \alpha_{\max}$
8211	He	low field	-80, -40	8217	Ar	high field	-80, -40
8212	He	high field	-70, -40	8218	Ar	low field	-80, -40
8213	H	low field	-80, -40	8219	Ne	low field	-80, -40
8215	H	high field	-80, -40	8220	Ne	high field	-80, -40
8216	Ar	low field	-80, -40	9137	D	low field	-80, -40

Discharges with a movable $j_\parallel$-probe

Listed below are all discharges that were done with the $j_\parallel$-probe (Sec. 4.4.2).

#	gas	comment	#	gas	comment
9130	He	low field	9133	H	low field
9131	He	low field	9134	H	low field
9132	He	low field			

Discharges with probe arrays and fast imaging

The following discharges featured measurements with the poloidal probe arrays and the fast camera.

#	gas	comment	#	gas	comment
8352	He	reversed field	8356	He	
8353	He	reversed field	8357	H	no camera
8354	He		8358	H	no camera
8355	He	no camera	8359	H	

Bibliography

[1] D. Tucker, Proceedings of the Institution of Electrical Engineers **123**, 1026 (1976).

[2] Key World Energy Statistics 2013, IEA (2013), http://www.iea.org/publications/.

[3] F. Chen, *An Indispensable Truth: How Fusion Power Can Save the Planet* (Springer, New York, 2011).

[4] A. S. Eddington, *The Internal Constitution of the Stars* (Cambridge University Press, Cambridge, 1926).

[5] H. A. Bethe, Phys. Rev. **55**, 434 (1939).

[6] R. Gross, *Fusion energy, Wiley Interscience publication* (Wiley, New York, 1984).

[7] I. Kurchatov, Sov. J. At. Energy **1**, 359 (1956).

[8] Institut für Plasmaphysik, www.ipp.mpg.de.

[9] V. Smirnov, Nucl. Fusion **50**, 014003 (2010).

[10] L. J. Spitzer, Phys. Fluids **1**, 253 (1958).

[11] G. Grieger *et al.*, *Plasma Physics and Controlled Fusion Research (Proc. 13th Int. Conf., Washington, DC, 1990), Vol. 3* (IAEA, Vienna, 1991), p. 525.

[12] P. Helander *et al.*, Plasma Phys. Controll. Fusion **54**, 124009 (2012).

[13] C. Federrath and R. S. Klessen, Astrophys. J. **761**, 156 (2012).

[14] W. Fundamenski *et al.*, Plasma Phys. Controll. Fusion **49**, R43 (2007).

[15] J. R. Myra *et al.*, Phys. Plasmas **13**, 092509 (2006).

[16] D. A. D'Ippolito, J. R. Myra, and S. J. Zweben, Phys. Plasmas **18**, 060501 (2011).

[17] D. A. Russell, J. R. Myra, and D. A. D'Ippolito, Phys. Plasmas **14**, (2007).

[18] B. Scott, Plasma Phys. Controll. Fusion **39**, 471 (1997).

[19] X. Garbet, L. Laurent, J.-P. Roubin, and A. Samain, Nucl. Fusion **31**, 967 (1991).

[20] F. D. Halpern *et al.*, Phys. Plasmas **20**, 052306 (2013).

[21] V. Shafranov, Nucl. Fusion **8**, 253 (1968).

[22] W. Horton, Rev. Mod. Phys. **71**, 735 (1999).

[23] E. Martines, M. Hron, and J. Stöckel, Plasma Phys. Controll. Fusion **44**, 351 (2002).

[24] S. J. Zweben *et al.*, Plasma Phys. Controll. Fusion **49**, S1 (2007).

[25] J. R. Angus, M. V. Umansky, and S. I. Krasheninnikov, Phys. Rev. Lett. **108**, 215002 (2012).

[26] T. T. Ribeiro and B. Scott, Plasma Phys. Controll. Fusion **47**, 1657 (2005).

[27] T. T. Ribeiro and B. Scott, Plasma Phys. Controll. Fusion **50**, 055007 (2008).

[28] S. J. Zweben, Phys. Fluids **28**, 974 (1985).

[29] O. Grulke *et al.*, Phys. Plasmas **8**, 5171 (2001).

[30] P. C. Stangeby, *The Plasma Boundary of Magnetic Fusion Devices* (Taylor and Francis Group, New York, 2000).

[31] U. Stroth, *Plasmaphysik: Phänomene, Grundlagen, Anwendungen* (Vieweg+Teubner Verlag, Wiesbaden, 2011).

[32] S. Krasheninnikov, Phys. Lett., A **283**, 368 (2001).

[33] D. D'Ippolito, J. Myra, and S. Krasheninnikov, Phys. Plasmas **9**, 222 (2002).

[34] S. I. Krasheninnikov, D. A. D'Ippolito, and J. R. Myra, J. Plasma Phys. **74**, 679 (2008).

[35] C. Theiler *et al.*, Phys. Rev. Lett. **103**, 065001 (2009).

[36] B. Bätz, *Zur parallelen Dynamik kohärenter Strukturen in der Plasmarand-schicht*, Bachelor's thesis (Universität Stuttgart, Stuttgart, 2012).

[37] O. E. Garcia *et al.*, Phys. Plasmas **12**, 090701 (2005).

[38] C. Theiler *et al.*, Phys. Plasmas **18**, 055901 (2011).

[39] J. R. Myra and D. A. D'Ippolito, Phys. Plasmas **12**, 092511 (2005).

[40] N. Katz *et al.*, Phys. Rev. Lett. **101**, 015003 (2008).

[41] M. Kočan *et al.*, Plasma Phys. Controll. Fusion **54**, 085009 (2012).

[42] P. Manz *et al.*, Phys. Plasmas **20**, (2013).

[43] J. Wesson, *Tokamaks* (Clarendon Press, Oxford, 1987).

[44] G. Yu and S. Krasheninnikov, Phys. Plasmas **10**, 4413 (2003).

[45] D. A. D'Ippolito and J. R. Myra, Phys. Plasmas **10**, 4029 (2003).

[46] N. Bisai *et al.*, Phys. Plasmas **12**, 102515 (2005).

[47] I. Furno *et al.*, Phys. Rev. Lett. **100**, 055004 (2008).

[48] T. Happel *et al.*, Phys. Rev. Lett. **102**, 255001 (2009).

[49] G. Xu *et al.*, Nucl. Fusion **49**, 092002 (2009).

[50] P. Manz *et al.*, Phys. Rev. Lett. **107**, 195004 (2011).

[51] J. Terry *et al.*, Phys. Plasmas **10**, 1739 (2003).

[52] R. Maqueda, D. Stotler, and S. Zweben, J. Nucl. Mater. **415**, S459 (2011).

[53] I. Shesterikov *et al.*, Nucl. Fusion **52**, 042004 (2012).

[54] G. Antar, Phys. Plasmas **10**, 3629 (2003).

[55] I. Furno *et al.*, Plasma Phys. Controll. Fusion **53**, 124016 (2011).

[56] E. Ascasibar, C. Alejaldre, and J. Alonso, Fusion Technol. **27**, 198 (1995).

[57] E. Ascasibar *et al.*, *Plasma Physics and Controlled Fusion Research (Proc. 16th Int. Conf., Montreal, 1996), IAEA, Vienna* (IAEA, Vienna, 1996), p. 183.

[58] E. Ascasibar *et al.*, Nucl. Fusion **37**, 851 (1997).

[59] N. Krause *et al.*, Rev. Sci. Instrum. **73**, 3474 (2002).

[60] U. Stroth *et al.*, Phys. Plasmas **11**, 2558 (2004).

[61] A. Köhn *et al.*, Plasma Phys. Controll. Fusion **55**, 014010 (2013).

[62] S. Enge, *Untersuchung der Ionendynamik in Laborplasmen - Am Beispiel von FLIPS und TJ-K*, Ph.D. thesis (Universität Stuttgart, Stuttgart, 2010).

[63] S. Enge *et al.*, Phys. Rev. Lett. **105**, 175004 (2010).

[64] C. Gourdon, *Programme optimisé de calculs numériques dans les configurations magnetiques toroidales* (CEN, Fontenay aux Roses, 1970).

[65] S. Niedner, B. D. Scott, and U. Stroth, Plasma Phys. Controll. Fusion **44**, 397 (2002).

[66] C. Lechte, S. Niedner, and U. Stroth, New J. Phys. **4**, 34.1 (2002).

[67] N. Mahdizadeh *et al.*, Plasma Phys. Controll. Fusion **49**, 1005 (2007).

[68] G. Birkenmeier, IPP Garching, private communication, (2013).

[69] C. Lechte, *Microscopic Structure of Plasma Turbulence in the Torsatron TJ-K*, Ph.D. thesis (Christian-Albrechts-Universität, Kiel, 2003).

[70] M. Ramisch *et al.*, Phys. Plasmas **12**, 032504 (2005).

[71] E. Häberle, *Skalierung turbulenter Strukturen im Torsatron TJ-K*, Diploma thesis (Universität Stuttgart, Stuttgart, 2008).

[72] M. Ramisch, E. Häberle, N. Mahdizadeh, and U. Stroth, Plasma Sources Sci. Technol. **17**, 024007 (2008).

[73] T. Happel, *Influence of limiters on plasma equilibrium and dynamics in the torsatron TJ-K*, Diploma thesis (Universität Stuttgart, Stuttgart, 2005).

[74] G. Hornung, *Lorentzian Structures in the Torsatron TJ-K*, Diploma thesis (Universität Stuttgart, Stuttgart, 2010).

[75] G. Hornung *et al.*, Phys. Plasmas **18**, 082303 (2011).

[76] G. Fuchert, T. Boettcher, M. Ramisch, and U. Stroth, in *Proceedings of the 38th EPS Conference on Controlled Fusion and Plasma Physics, Strasbourg, France* (The European Physical Society, Strasbourg, 2011), p. P2.120.

[77] N. Mahdizadeh *et al.*, Plasma Phys. Controll. Fusion **47**, 569 (2005).

[78] O. Gruber *et al.*, Nucl. Fusion **49**, 115014 (2009).

[79] A. Herrmann and O. Gruber, Nucl. Fusion **44**, 569 (2003).

[80] B. Nold, *Turbulence Studies in Dimensionally Similar Plasma Discharges*, Diploma thesis (Universität Stuttgart, Stuttgart, 2008).

[81] B. Nold *et al.*, Plasma Phys. Controll. Fusion **52**, 065005 (2010).

[82] B. Nold, *Untersuchung turbulenter Strukturen am Rand magnetisierter Plasmen*, Ph.D. thesis (Universität Stuttgart, Stuttgart, 2012).

[83] F. Wagner *et al.*, Phys. Rev. Lett. **49**, 1408 (1982).

[84] F. Ryter *et al.*, Plasma Phys. Controll. Fusion **40**, 725 (1998).

[85] L. Horton *et al.*, Nucl. Fusion **45**, 856 (2005).

[86] G. Conway *et al.*, *Proc. 5th Int. Workshop on Reflectometry, Toki, Japan, 2001* (NIFS, Toki, 2001), Vol. PROC-49.

[87] T. Happel *et al.*, Phys. Plasmas **18**, 102302 (2011).

[88] F. Wagner, Plasma Phys. Controll. Fusion **49**, B1 (2007).

[89] E. Doyle *et al.*, Nucl. Fusion **47**, S18 (2007).

[90] P. Schneider, *Characterization and scaling of the tokamak edge transport barrier*, Ph.D. thesis (Ludwig-Maximilians-Universität München, München, 2012).

[91] H. Zohm, Plasma Phys. Controll. Fusion **38**, 105 (1996).

[92] W. Suttrop *et al.*, Plasma Phys. Controll. Fusion **53**, 124014 (2011).

[93] N. B. Ayed *et al.*, Plasma Phys. Controll. Fusion **51**, 035016 (2009).

[94] D. Goodall, J. Nucl. Mater. **111-112**, 11 (1982).

[95] S. J. Zweben *et al.*, Nucl. Fusion **44**, 134 (2004).

[96] J. L. Terry *et al.*, J. Nucl. Mater. **390**, 339 (2009).

[97] L. M. Shao *et al.*, Plasma Phys. Controll. Fusion **55**, 105006 (2013).

[98] V. Erckmann and U. Gasparino, Plasma Phys. Controll. Fusion **36**, 1869 (1994).

[99] Y. Sabharwal, Microsc. Anal. **25**, S5 (2011).

[100] H. Tian, B. Fowler, and A. E. Gamal, in *Storage and Retrieval for Image and Video Databases* (SPIE Press, San Jose, CA, USA, 1999).

[101] J. Joubert, Y. Sabharwal, and D. Sharma, Microsc. Anal. Web Features 1 (2011).

[102] A. Rose, J. Opt. Soc. Am. **38**, 196 (1948).

[103] A. Zilch, *Untersuchung von Strahlungsverlusten mittels Bolometrie an einem toroidalen Niedertemperaturplasma*, Diploma thesis (Universität Stuttgart, Stuttgart, 2011).

[104] M. Goto, J. Quant. Spectrosc. Radiat. Transf. **76**, 331 (2003).

[105] G. Y. Antar, J. H. Yu, and G. Tynan, Phys. Plasmas **14**, 022301 (2007).

[106] D. Iraji, I. Furno, A. Fasoli, and C. Theiler, Phys. Plasmas **17**, 122304 (2010).

[107] I. Langmuir, Science **58**, 290 (1923).

[108] H. M. Mott-Smith and I. Langmuir, Phys. Rev. **28**, 727 (1926).

[109] I. H. Hutchinson, *Principles of plasma diagnostics* (Cambridge University Press, Cambridge, 1987), p. 50.

[110] G. Birkenmeier, *Experimentelle Untersuchungen zur Struktur und Dynamik von Driftwellenturbulenz in Stellaratorgeometrie*, Ph.D. thesis (Universität Stuttgart, Stuttgart, 2012).

[111] G. Birkenmeier *et al.*, Plasma Phys. Controll. Fusion **55**, 015003 (2013).

[112] T. Herzog, *Charakterisierung des turbulenten Transports in der Abschälschicht limitierter Plasmen*, Bachelor's thesis (Universität Stuttgart, Stuttgart, 2012).

[113] H. Nobach *et al.*, in *Springer Handbook of Experimental Fluid Mechanics*, edited by C. Tropea, A. Yarin, and J. Foss (Springer, Berlin Heidelberg, 2007), pp. 1337–1398.

[114] D. Block, I. Teliban, F. Greiner, and A. Piel, Physica Scripta **2006**, 25 (2006).

[115] R. J. Adrian, Annu. Rev. Fluid Mech. **23**, 261 (1991).

[116] Y. Feng, J. Goree, and B. Liu, Rev. Sci. Instrum. **78**, 053704 (2007).

[117] L. Rocha, L. Velho, and P. C. Carvalho, Proceedings of the XVII Brazilian Symposium on Computer Graphics and Image Processing 354 (2004).

[118] T. Boettcher, *Vergleichende Turbulenzuntersuchungen mit Hochgeschwindigkeitskamera und Langmuir-Sonde*, Diploma thesis (Universität Stuttgart, Stuttgart, 2011).

[119] N. Mahdizadeh, *Investigation of Three-Dimensional Turbulent Structures in the Torsatron TJ-K*, Ph.D. thesis (Universität Stuttgart, Stuttgart, 2007).

[120] MCC was written by M. Ramisch (University of Stuttgart) in IDL/C/C++.

[121] V. Naulin, A. H. Nielsen, and J. J. Rasmussen, Phys. Plasmas **12**, 122306 (2005).

[122] O. D. Gürcan, P. H. Diamond, T. S. Hahm, and Z. Lin, Phys. Plasmas **12**, 032303 (2005).

[123] G. Fuchert *et al.*, Plasma Phys. Controll. Fusion **55**, 125002 (2013).

[124] O. E. Garcia, Phys. Rev. Lett. **108**, 265001 (2012).

[125] O. E. Garcia *et al.*, Phys. Plasmas **20**, 055901 (2013).

[126] M. Ramisch, *Scaling and Manipulation of Turbulent Structures in the Torsatron TJ-K*, Ph.D. thesis (Christian-Albrechts-Universität, Kiel, 2005).

[127] K. Okuno, NIFS-DATA-100, (2007).

[128] B. A. Carreras *et al.*, Phys. Plasmas **3**, 2664 (1996).

[129] G. Birkenmeier *et al.*, Phys. Rev. Lett. **107**, 025001 (2011).

[130] P. H. Diamond, S.-I. Itoh, K. Itoh, and T. S. Hahm, Plasma Phys. Controll. Fusion **47**, R35 (2005).

[131] K. Itoh *et al.*, Phys. Plasmas **13**, 055502 (2006).

[132] P. W. Terry, Rev. Mod. Phys. **72**, 109 (2000).

[133] P. Manz, M. Ramisch, and U. Stroth, Phys. Rev. Lett. **103**, 165004 (2009).

[134] P. Manz, *Strukturentstehung in Driftwellenturbulenz toroidaler Plasmen*, Ph.D. thesis (Universität Stuttgart, Stuttgart, 2009).

[135] B. Schmid, *Bildung turbulenter Strukturen im Randbereich magnetisch eingeschlossener Plasmen*, Diploma thesis (Universität Stuttgart, Stuttgart, 2011).

[136] B. Schmid, Ph.D. thesis (Universität Stuttgart, Stuttgart, in preparation).

[137] T. Lunt, IPP Garching, private communication, (2012).

[138] S. Coda, M. Porkolab, and K. Burrell, Phys. Lett., A **273**, 125 (2000).

[139] U. Stroth, P. Manz, and M. Ramisch, Plasma Phys. Controll. Fusion **53**, 024006 (2011).

[140] J. Schirmer *et al.*, Nucl. Fusion **46**, S780 (2006).

[141] R. A. Moyer *et al.*, Plasma Phys. Controll. Fusion **41**, 243 (1999).

[142] J. Neuhauser *et al.*, Plasma Phys. Controll. Fusion **44**, 855 (2002).

[143] D. Carralero *et al.*, *Proc. of the 40th EPS Conference on Plasma Physics, Espoo, Finland* (The European Physical Society, Espoo, 2013), p. O4.108.

[144] N. Nishino *et al.*, Plasma Fusion Res. **3**, S1023 (2008).

[145] J. Boedo *et al.*, Phys. Plasmas **8**, 4826 (2001).

[146] G. Birkenmeier *et al.*, *Proc. of the 40th EPS Conference on Plasma Physics, Espoo, Finland* (The European Physical Society, Espoo, 2013), p. P5.105.

Danksagung

Ich möchte mich an dieser Stelle bei all jenen Personen bedanken, die zum Gelingen dieser Arbeit auf ihre Weise beigetragen haben:

Curriculum Vitae

Persönliche Daten

Name	Golo Fuchert
Geburtsdatum/-ort	06.03.1985, Varel, Deutschland
Familienstand	ledig
Nationalität	Deutsch

Schulausbildung

1991–1995	Grundschule Aich, Aichtal
1995–2004	Gymnasium Neckartenzlingen
Juli 2004	Abitur (Profil-/Neigungsfach: Physik und Chemie)

Wissenschaftliche Ausbildung

Okt. 2004–Sep. 2006	Grundstudium Physik (Diplom) an der Eberhard Karls Universität Tübingen
Okt. 2006–Nov. 2009	Hauptstudium Physik (Diplom) am Karlsruher Instiut für Technologie
Okt. 2008–Nov. 2009	Anfertigung der Diplomarbeit mit dem Titel *Modelle für supraleitende Undulatoren an kompakten Synchrotronstrahlungsquellen mit Laser-Wakefield-Beschleunigern* in der Arbeitsgruppe von Dr. A. Bernhard
Nov. 2009	Diplom in Physik
seit Feb. 2010	Promotion an der Universität Stuttgart in der Arbeitsgruppe von Prof. Dr. U. Stroth (später Dr. M. Ramisch)

Versicherung

Hiermit erkläre ich, dass ich diese Arbeit ausschließlich unter Anleitung meiner wissenschaftlichen Lehrer und unter Verwendung der angegebenen Hilfsmittel angefertigt habe. Sie hat weder ganz noch zum Teil an einer anderen Stelle im Rahmen eines Prüfungsverfahren vorgelegen.

Stuttgart, den

_____

Golo Fuchert